

学位論文

Flood history of central Japan during  
the past 7000 years based on  
detrital flux to Lake Suigetsu

(水月湖への碎屑物フラックスに基づく  
中部日本における過去 7000 年間の洪水史)

平成 28 年 12 月博士 (理学) 申請

東京大学大学院理学系研究科

地球惑星科学専攻

鈴木 克明



## **Abstract**

Recently, extraordinary meteorological hazards such as floods and droughts occurring with low frequency gather attentions of many researchers. Especially, in coastal regions, rivers provide rich water resources in one aspect, but they could cause floods that may exert a fatal impact on human society. Therefore, it is important to observe these meteorological hazards and resolve their mechanisms in order to prepare for future occurrences of flood events. Frequency and magnitude of floods are important information to make decision to prevent these hazards. However, it is difficult to observe flood events directly because their occurrences are unpredictable and too dangerous to observe closely. To understand the frequency and magnitude of flood events, collecting the record of flood events in the past is a useful and important approach. However, observational records can only go back to the last few centuries, which is too short to evaluate the frequency and magnitude of flood events. As a potential recorder of flood events going back before observational records, event deposits in sediments are promising. When a flood occurred, significant amount of detrital material was delivered into the sedimentary basin within a geologically instantaneous period and preserved as an “event deposit” within the background sediment. Although sedimentary records have high potential for extending the time range of the flood record, it is difficult to extract quantitative information such as the magnitude of flood events. To improve the quantitative understanding of the flood event preserved in the sedimentary record, a comparison of characters of flood deposits and meteorological data is important. For this purpose, a correlation between sedimentary record and observational and/or historical record is critical.

In this study, I focused on the sediments of Lake Suigetsu, central Japan, that record flood history of the area during the entire Holocene. Sediment of Lake Suigetsu preserve annual lamination (varves) since 1664 and many detrital layers called “event layers”, which were deposited instantaneously based on macroscopic observations. Therefore, sediments of Lake Suigetsu

have high potential to correlate with meteorological record and to extend the flood record back to the entire Holocene. I try to reconstruct a long term and quantitative record of flood events covering the late Holocene using the sediment cores from Lake Suigetsu to establish the method to reconstruct long term floods, and correlate the record with other records on climatic hazard to understand the spatio-temporal variability of flood events in East Asia region.

Based on the observation of sediments and modern sedimentary processes, I estimate the cause and mechanism of sedimentation of event layers in the sediment of Lake Suigetsu. Lake Suigetsu is one of Mikata Five Lakes in Wakasa Bay, Fukui Prefecture, Japan. The drainage area of Lake Suigetsu is relatively small and most of its lake water is supplied from the drainage area of Lake Mikata, which is located immediately upstream of Lake Suigetsu and connected to Lake Suigetsu only by a shallow channel. When flood occurs, large amount of muddy water of Lake Mikata which was supplied from the drainage area of Hasu River, major feeder river of Lake Mikata, flow into Lake Suigetsu. Also landslides occasionally occur in the drainage of Lake Suigetsu. Because Lake Mikata acts as a sediment trap for coarse detrital material from its drainage area, only fine grained detrital material can flow into Lake Suigetsu. I classified the sediment of Lake Suigetsu into two types, background sediments and event layers, and described the occurrence and characteristics of each type of the sediment. The background sediment of Lake Suigetsu are composed of diatom frustules, organic material, detrital material and chemically precipitated minerals such as Fe-Mn oxide, siderite and pyrite. The event layers are distinguished from the background sediment by their colors and a sharp contact with the underlying sediment. Event layers are dominantly composed of fine grained detrital material with less than  $\sim 10 \mu\text{m}$  in diameter.

I unraveled the origin of event layers in the sediment of Lake Suigetsu

accumulated during the last century and revealed the relationship between the scale of flood event and thickness of the event layer based on the correlation with observational meteorological data at Tsuruga, 20km Northeast of Lake Suigetsu. To correlate sedimentary record with the available observational record, I established an age model of the near-surface sediment of Lake Suigetsu based on varve counting, measurement of radioactive nuclides ( $^{137}\text{Cs}$  and  $^{210}\text{Pb}$ ), and fine-tuning by matching of flood events versus event layers with Bayesian error estimation. As a result, high resolution age model of the last century was established within the error of 2 years. Based on the correlation of the near-surface sediment with the observational precipitation record, it is revealed that gray event layers deposited in the last century can be correlated with flood events in this region mainly by strong rainfall due to Typhoon hits. It is also revealed that thickness of gray event layer increases with the amount of rainfall that caused the flood. Because the flux of detrital materials does not have clear relationship with annual precipitation, it is interpreted that the flux of detrital material is mainly controlled by the flood events and frequency of moderately strong rainfall events (30 -100 mm/day).

Because Lake Mikata acts as a sediment trap of coarse grained detrital materials, only fine-grained detrital materials transported as the muddy water from the drainage area would have flowed into Lake Suigetsu and caused the deposition of event layers. However, there are several other sources of detrital materials into Lake Suigetsu such as detritals from surrounding slopes and eolian dusts. Therefore, contribution of fine-grained detrital materials in the bulk sediment and/or bulk detrital materials has to be evaluated with more precise proxy for flood event. To evaluate the origin of detrital material in the sediment of Lake Suigetsu and estimate their contribution, I applied Q-mode factor analysis to the normalized compositional data of major elements that are included only in detrital material (DetXRF data), such as  $\text{Al}_2\text{O}_3$ ,  $\text{TiO}_2$ ,  $\text{MgO}$ ,  $\text{CaO}$ ,  $\text{Na}_2\text{O}$  and  $\text{K}_2\text{O}$  in the samples which are not affected by brackish water from Lake Kugushi. A

comparison of the chemical composition of estimated end members (EMs) with analyzed chemical composition of surface detrital materials sampled from the drainage of Lake Suigetsu and Lake Mikata is also conducted. It is revealed that the major components of detrital materials in Lake Suigetsu are fine grained detrital materials from the drainage area of Lake Mikata (D-EM1), coarse/fine detrital materials from surrounding slope of Lake Suigetsu, and eolian dust from the Asian continent.

I estimated the contents of bulk detrital materials (fine particles from Hasu River, coarse particles from surrounding slope and eolian dust), diatom frustules, organic material and Fe-Mn oxides in the bulk sediment core samples based on multiple regression analysis (MRA) of chemical composition data of the upper part of SG12 core corresponding to the last 7000 years measured in X-ray Fluorescence (XRF). I also estimated flux of each component to the sediment, and discussed about the change of sedimentary environments of Lake Suigetsu during the last 7000 years. Based on these results, I validated the reliability of flux of fine-grained detrital materials from Lake Mikata as a proxy to heavy rainfall. As the base erosion level is higher in the last 1000 years than before, application of flood and rainfall proxies using detrital flux would provide the minimum estimate for magnitude and frequency of flood and rainfall events before 1000 yr B.P. High-stand of D-EM1 flux during the last 1000 years could be explained by tectonic change of geomorphology caused by earthquake or human landuse.

Two proxies are established to estimate the minimum magnitude and frequency of flood events and moderately strong rainfall events in the past 7000 years using the sediment of Lake Suigetsu.

- 1) Occurrence and thickness of gray event layers represent frequency and magnitude of each flood event. Since the Holocene sediment suffers from weak bioturbation, I focused event layers thicker than 1mm (corresponding to heavy rainfall more than 400 mm estimated by the relationship between event layer thickness and rainfall amount in the flood) and used as a proxy

for relatively large flood events.

2) Flux of fine grained detrital materials from the drainage area of Lake Mikata to Lake Suigetsu represents frequency of moderately strong rainfalls (30-100 mm/day) in one year causing flood events in this region. Because flux of fine grained detrital materials in “background sediment” in the Holocene are potentially includes thin event layers erased by bioturbation, this proxy could include relatively small flood events.

Combining these proxies, a semi-quantitative flood record of central Japan during the last 7000 years is reconstructed. The correlation of the record with other paleoclimate records such as discharge from Yangtze River (rainfall induced by East Asian Summer Monsoon: Kubota et al., 2015) and sea surface temperature(SST) record in northwestern Pacific (Isono et al., 2009), it is revealed that in a warm interval, precipitation variability in central Japan and Yangtze drainage agree with each other. In contrast, in a cold period, these two precipitation records do not synchronize. These results suggest that spatial pattern of rainfall and flood events vary along with the change in broader climate pattern, such as SST. It is also revealed that the number of flood events in central Japan increased during the period when SST increase rapidly, indicating that flood events in this region could be influenced by the change of climate pattern, rather than stable states such as warm or cold conditions.

In this study, I established the method to reconstruct semi-quantitative heavy rainfall and flood events distinguishing them with earthquakes based on correlation of sediment versus observation and reconstruction of flux of detrital materials. This method can be applied to the sedimentary sequences with enough precise and high resolution age model especially covering the last century and with weak bioturbation or annual lamination. We could apply this method to other sedimentary sequences to obtain spatio-temporal variation of occurrence and magnitude of hazards such as floods or earthquakes.

## Contents

Abstract .....	i
1. General Introduction .....	1
1-1. Background.....	1
1-2. Existing methods for reconstructing flood history and their problems	2
1-3. Objective and outline of this research .....	3
2. Study site and samples used in this study .....	5
2-1. Geomorphological setting .....	5
2-2. Hydrological setting .....	5
2-3. Geological setting .....	10
2-4. Meteorological setting.....	10
2-5. Samples used in this study .....	12
2-5-1. History of Lake Suigetsu drilling .....	12
2-5-2. SG12 Drilling.....	14
2-5-3. LIMNOS core samples .....	17
2-5-4. Surface samples from the surrounding area .....	17
3. Sediment types and lithology of Lake Suigetsu sediments from SG12 cores .....	19
3-1. Methods .....	19
3-2. Classification and definition of sediment types .....	21
3-2-1. Background sediment.....	21
3-2-2. Event deposits .....	21
3-2-3. Light gray event layers .....	24
3-2-4. Brown event layer .....	25
3-2-5. Tephra layers .....	26
4. Relationship between detrital flux and flood in Lake Suigetsu during the past 100 years .....	27
4-1. Sampling.....	27
4-2. Analytical method .....	28
4-3. Macroscopic and microscopic observation of SG12LM3 core.....	29
4-4. Construction of age model .....	29

4-4-1. Varve counting.....	29
4-4-2. Measurement of radioactive nuclides.....	31
4-4-3. Constraining a varve based age model using the <sup>210</sup> Pb and <sup>137</sup> Cs results.....	33
4-4-4. The correlation between event layers and historical flood events and fine-tuning of varve count age model.....	34
4-4-5. Estimation of age uncertainty using a Bayesian approach.....	36
4-5. Estimation of detrital flux.....	38
4-6. Result.....	41
4-7. Discussion.....	45
4-7-1. Flood vs. gray event layer.....	45
4-7-2. Annual precipitation vs. Background sedimentation.....	51
5. Provenance and flux of detrital material in the sediment of Lake Suigetsu.....	55
5-1. Sample pretreatment.....	55
5-1-1. Core sample.....	55
5-1-2. Surface detrital samples.....	56
5-2. Methods.....	56
5-2-1. Dry bulk density (DBD).....	56
5-2-2. Linear sedimentation rate (LSR).....	57
5-2-3. XRF analysis.....	57
5-3. Results.....	57
5-3-1. Results of XRF analysis.....	57
5-3-2. Results of water content (WC) and DBD measurements.....	64
5-4. Q-mode factor analysis.....	64
5-4-1. Provenance of EM1.....	73
5-4-2. Provenance of EM2.....	75
5-4-3. Provenance of EM3.....	75
5-4-4. Provenance of EM4.....	76
5-5. Multiple regression analysis.....	76
5-6. Results of MRA.....	85

5-7. Flux of components in the sediment of Lake Suigetsu.....	91
5-7-1. Flux of diatom frustules, organic material, Fe-Mn oxide, and sea salt.....	91
5-7-2. Flux of D-EM1 .....	91
5-7-3. Flux of D-EM2 .....	93
5-7-4. Flux of D-EM3 .....	93
5-7-5. Flux of D-EM4 .....	93
5-8. Tectonic and anthropogenic effects.....	95
6. Flood records for the past 7000 years and correlation with other paleoclimatic records .....	99
6-1. Introduction.....	99
6-2. Methods .....	99
6-2-1. Description of event layers in the Holocene sediment.....	99
6-2-2. Flux of D-EM1 as a proxy for flood events .....	99
6-3. Results .....	100
6-4. Discussion.....	104
6-4-1. Comparison between flood records for the last century and those for the last 7000 years .....	104
6-4-2. Correlation with other climatic records for the East Asia region .....	104
7. Conclusion.....	109
Acknowledgement.....	111
References .....	113
Supplementary Data.....	121

# 1. General Introduction

## 1-1. Background

Recently, extraordinary hazards occurring with low frequency gather increasing attention of many researchers [Cai *et al.*, 2014; Cohen *et al.*, 2014; Tang *et al.*, 2014]. Because such hazards cause significant damages to the human society, it is important to know their frequency, magnitude and mechanisms. Also, it is predicted that global warming would increase frequency and/or magnitude of extreme weather such as heavy rain and drought that causes fatal damage to the society [Hirabayashi *et al.*, 2013; IPCC, 2013; Alfieri *et al.*, 2015]. Especially, coastal regions and islands are expected to suffer heavy damages from such hazards because these regions are densely populated. For instance, central and western parts of Japanese Islands have suffered from so many flood events due to heavy rains caused by typhoons and monsoon front activities during the last decade (i. e. heavy precipitation in Hiroshima on August 2014). In the case of typhoon which is the most dominant cause of climatic hazards, it is predicted that the magnitude of Typhoon and frequency of a strong Typhoon would increase in association with the global warming [McDonald *et al.*, 2005; Oouchi *et al.*, 2006]. Although there have been several huge flood events in the historical records, it is not clear whether simple extrapolation of the mechanism and the relationship with meteorological parameters based on the observational records of moderate class hazards are possible or not because the associated meteorological parameters were not recorded by the observational instruments [Luo *et al.*, 2015]. Therefore, understanding and resolving the frequency, magnitude and causative mechanism of hazards in longer time scale beyond the reach of instrumental observation are critical to the human society. However, it is difficult to observe and analyze an extreme flood event individually because they are unpredictable, occur with low frequency and too dangerous to observe directly. Therefore, it is useful to explore geological records of flood events before the instrumental observation records to obtain

such information.

## **1-2. Existing methods for reconstructing flood history and their problems**

Instrumental observations are the most fundamental methods to obtain flood intensity, and their advantages are providing quantitative data with high spatio-temporal resolution, which afford understanding of the causes, process, and effects of the flood event (e.g. *Kay et al., 2009; Gale and Saunders, 2013*). Although the long term record of flood events is necessary to examine the mechanism and frequency of the extreme flood events, observational record can only go back to the last one to few centuries at most [*Yin and Li, 2001; Luo et al., 2015*]. Several approaches are taken to extend the flood record back to several thousand years. One is to examine historical records written in old documents such as diaries [*Glaser and Stangl, 2004*]. These records have high time resolution up to daily or monthly. However, historical records are not easy to confirm in general and causes of hazards are not clear in many cases [*Luo et al., 2015*]. Moreover, these records only go back to the past few thousand years at most. Another approach is to utilize sedimentary records. When a hazard such as earthquake or flood occurs, significant amount of detrital material is delivered into the sedimentary basin, of which process is different from ordinal background sedimentary process [*Sturm and Matter, 1978; Schillereff et al., 2014*]. Consequently, the resulting deposit tends to have different texture, grain size and composition due to different provenance, transport and depositional processes. Such deposits are called ‘event deposits’, which means that their sedimentation occurred geologically instantaneously [*Toomey et al., 2013; Schillereff et al., 2014*]. Sedimentary records tend to have continuity much longer than 1000 years thus easily covering the Holocene. It is generally believed that thickness of an event layer or its mass flux of detrital material increases with the increase in scale of the event [*Schillereff et al., 2014*]. However, in the sedimentary record, the cause of event layer deposition and the scale of the event are not necessarily

clear[Morton *et al.*, 2007]. To improve the quality of reconstruction of the event record preserved in the sediment, it is important to establish the way to estimate scale and cause of event layer deposition. For this purpose, correlation between sedimentary record and observational and/or historical record is critical. To correlate observational record with sedimentary record, a precise age model covering the past century is necessary. Also, to extend the event record to the entire Holocene, continuous and stable background sedimentation setting is desirable.

Lake Suigetsu, in central part of Japan is known as continuous varve (annual lamination) occurrence during the last glacial period and also since 1664 A.D., and continuous sedimentation occurred during the last ~100 kyr [Fukusawa *et al.*, 1994; Marshall *et al.*, 2012; Nakagawa *et al.*, 2012; Schlolaut *et al.*, 2012]. Also, it is known that there are many detrital layers called “event layers” in the sediment of Lake Suigetsu, which are considered to have been deposited instantaneously based on the observations such as sharp bottom contact, high concentration of detrital material and homogeneous appearance[Schlolaut *et al.*, 2014]. These event layers are interpreted as having been deposited as a result of geological events such as flood or earthquake [Schlolaut *et al.*, 2014]. Therefore, sediment of Lake Suigetsu has high potential to correlate with observational record of flood events and extend the flood record back to the entire Holocene.

### **1-3. Objective and outline of this research**

In this study, I try to reconstruct long term and quantitative record of flood events during the late Holocene using sediment cores from Lake Suigetsu. I try to quantify the long term flood record based on correlation between sediment and observational record. I correlate the record with other climate records of surrounding region to understand the mechanism of occurrence and magnitude of flood events. This paper is composed of 7 chapters including Introduction (Chapter 1) and Conclusion (Chapter 7), and contents in other chapters are shown below.

In Chapter 2, hydrological, meteorological and geological settings of Lake Suigetsu are introduced. History of drilling research in the sediment of Lake Suigetsu is reviewed. Sampling and pretreatment methods for this study are also introduced.

In chapter 3, the cause and mechanism of sedimentation of event layers in the sediment of Lake Suigetsu are estimated based on observation of sediments and modern sedimentary process.

In Chapter 4, I unraveled the origin of event layers accumulated in the last century and revealed the relationship between the scale of flood and characteristics of event layers such as thickness and detrital MAR based on comparison of varved sediment with observational flood record. This part is published as Suzuki et al. (2016).

In Chapter 5, I reconstructed the compositional change of detrital material in the core sediments of Lake Suigetsu based on Q-mode factor analysis and multiple regression analysis of major elements composition of sediment core. I applied Q-mode factor analysis to the compositional data of detrital material in the Lake Suigetsu sediment to extract end members and their chemical composition. Then, comparison of the estimated end members' chemical composition with analyzed chemical composition of potential source materials sampled from the drainage of Lake Suigetsu and Lake Mikata is conducted to further characterize end members. Based on the results in Chapter 4 and 5, it is proved that fine-grained detrital flux to Lake Suigetsu can be used as a proxy for total heavy precipitation causing flood event. Additionally, frequency and thickness of event layers caused by flood thicker than 1 mm, a threshold thickness to be preserved after bioturbation in the Holocene sediment, is examined to reconstruct temporal changes in intensity and frequency of a huge flood event.

In Chapter 6, using these two proxies, semi-quantitative flood record is reconstructed for the past 7000 years, and the result is correlated with other precipitation and flood records in the late Holocene reported in surrounding regions.

## 2. Study site and samples used in this study

### 2-1. Geomorphological setting

Lake Suigetsu is one of Mikata Five Lakes near Wakasa Bay, Fukui Prefecture, central Japan (Figure1). Mikata Five Lakes are composed of Lake Mikata, Lake Suigetsu, Lake Suga, Lake Kugushi and Lake Hiruga. Three lakes except for Lake Hiruga are connected to Lake Suigetsu by channels with their depths of less than ~3 m for Lake Mikata and Lake Kugushi and about 15m for Lake Suga. Lake Suigetsu is 34 m in water depth, which is relatively deep considering its small area (4.2 km<sup>2</sup>). This deep water depth is maintained by the movement of Mikata fault, which is running along the eastside of Lake Suigetsu and allow the bottom of Lake Suigetsu to subside with its subsiding rate of ~25m in ~20 kyr [Nakae *et al.*, 2002; Komatsubara, 2006; Okada *et al.*, 2010] that is roughly balanced with the sedimentation rate within the lake (~0.7mm/year). Lake Suigetsu is also characterized by its small direct drainage area of 4.5km<sup>2</sup>, which is almost the same as the area of Lake Suigetsu itself (4.2km<sup>2</sup>). The drainage area of Lake Suigetsu is surrounded by mountains with the hight as high as ~400m at Baijoudake mountain.

### 2-2. Hydrological setting

Thanks to deep water depth and high mountains surrounding the lake, the bottom of Lake Suigetsu is poorly ventilated because it is protected from strong wind. Therefore, sediment of Lake Suigetsu escaped from strong bioturbation and resulted in partly preserved lamination in the Holocene sediment.

Until 1662, outlet of Lake Suigetsu was Kiyama River, flowing out from eastern side of Lake Suga connected with Lake Suigetsu. In 1662 A. D., Kanbun earthquake (M = 7.6: Usami 2003) occurred as a result of the movement of Mikata fault, and resulted in the uplift of eastern side of Mikata Fault consequently caused dry up of Kiyama River [Komatsubara,

2006]. To drain the water spread over the surrounding plain of Lake Suigetsu and Lake Mikata, an artificial river named Urami River was cut on the northeastern side of Lake Suigetsu as an outlet to Lake Kugushi in 1664 A. D.[*Komatsubara, 2006*] Since then, brackish water of Lake Kugushi, originated as freshwater from Lake Suigetsu mixing with the sea water of the Japan Sea, flew into Lake Suigetsu, caused density stratification of the lake water and development of oxygen depleted environment near the lake bottom. Therefore, the sediment without bioturbation and with annual lamination (varve) is preserved in Lake Suigetsu since 1662 A.D.[*Fukusawa et al., 1994; Saito-Kato et al., 2013*]

Since Baijoudake-mountain area is only the area having a river channel that directly flows into Lake Suigetsu, most of detrital material from its direct drainage comes from its slope (Figure 2). Lake Mikata, whose water drains into Lake Suigetsu through a shallow channel on southern side of Lake Suigetsu, has relatively wide drainage of  $\sim 60\text{km}^2$  (Figure2). Therefore, almost all (more than 85% in drainage area) water in Lake Suigetsu is supplied from Lake Mikata and its drainage area. On the other hand, detrital particles larger than coarse silt size cannot be transported into Lake Suigetsu from Lake Mikata and its drainage area because Lake Mikata acts as a sediment trap of coarse detrital materials. Namely, when we assume the mean depth and area of Lake Mikata as 1.5m and  $3.4\text{km}^2$ , respectively, mean residence time of water in Lake Mikata is longer than 0.75 day even when heavy precipitation of 100 mm/day continued for a full day. Within this residence time, detrital grains larger than  $6\mu\text{m}$  are settled down to the bottom of Lake Mikata and only grains finer than  $6\mu\text{m}$  can flow into Lake Suigetsu assuming grain density of detrital material as  $2.65\text{ g/cm}^3$ .

During the flood occurrence, inflow of detrital material from Lake Mikata is actually observed. When a flood occurred in this region, large amount of suspended material flows into Lake Mikata from its drainage. It is observed from aerial photographs that muddy water covers the surface of Lake Mikata and flows into Lake Suigetsu (Figure3A). Considering the trapping effect of

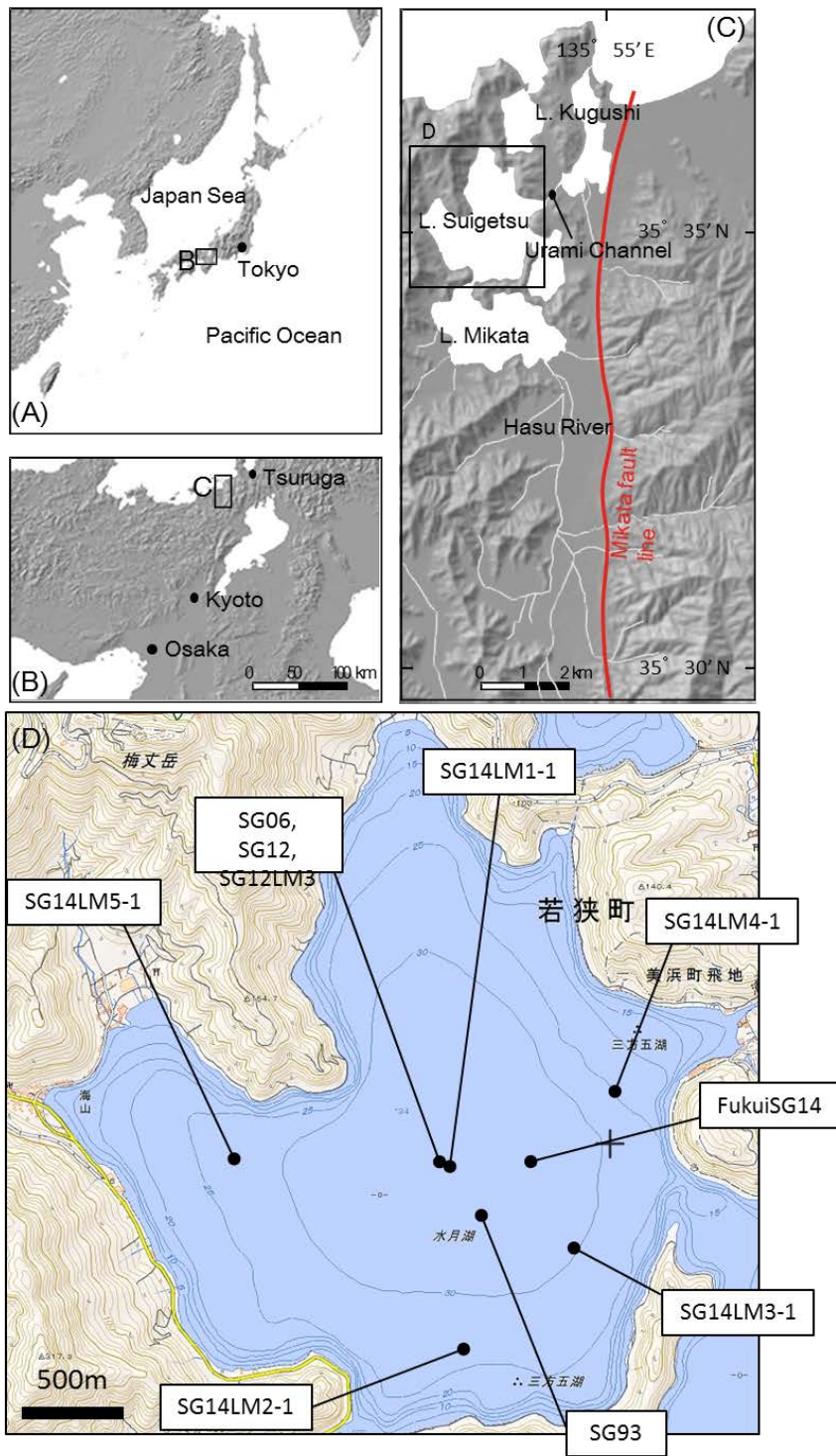


Figure 1  
 (A)(B)(C): Location of Lake Suigetsu.  
 (D) Topographical map and locations of core SG93, SG12, SG12LM3, FukuiSG14 and other coring sites.

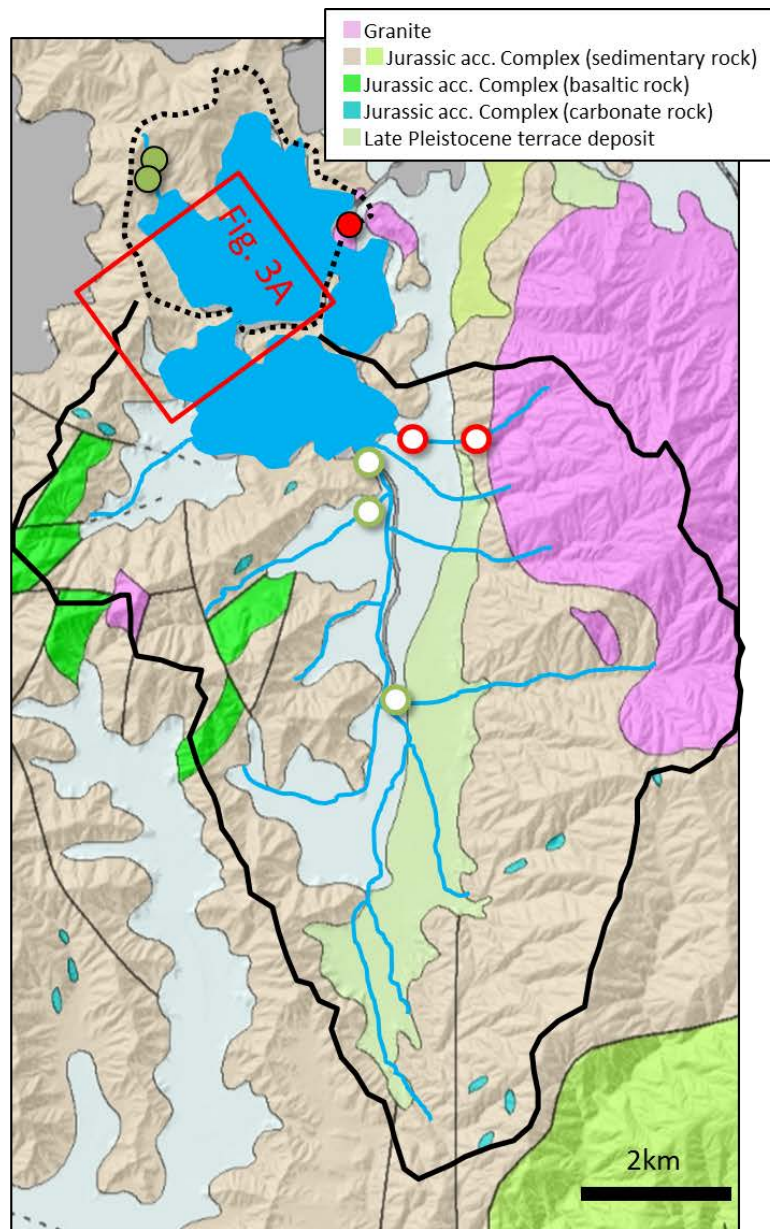
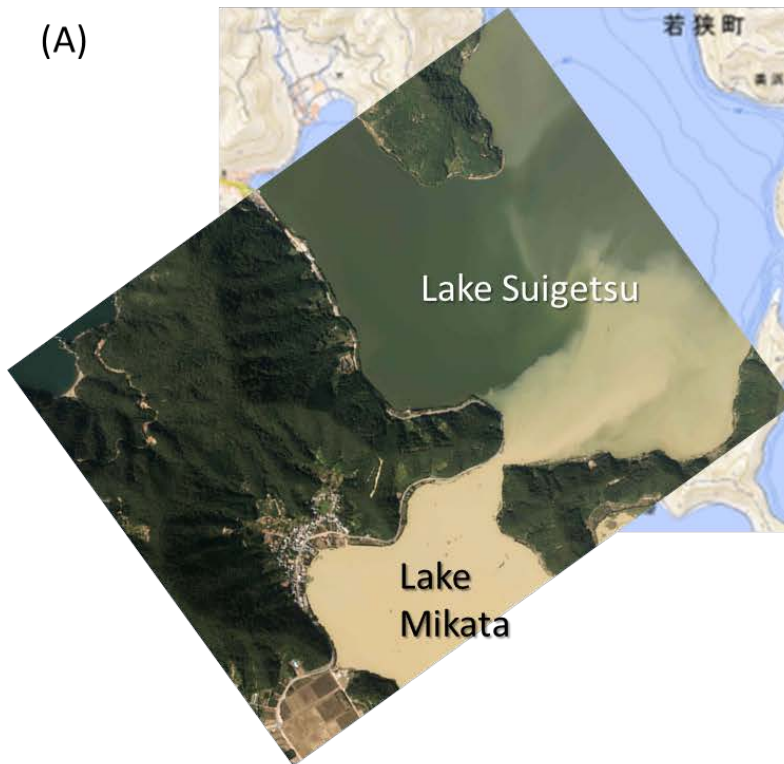


Figure 2

A geological map of Lake Suigetsu and surrounding area. Sampling points of surface sediments are also shown. Black dashed and solid lines represent drainage area of Lake Suigetsu and Lake Mikata. Red/green circles show sampling points in the drainage area of Lake Suigetsu (close circles) and Lake Mikata (open circles). Red indicate samples from localities whose drainage area includes granite basement. Green indicate samples from localities whose drainage area includes only Jurassic accretionary complex.

(A)



(B)



Figure 3  
Aerial photographs taken just after the flood occurred in Sep. 15<sup>th</sup> in 2013. (A) A vertical view from above the lake. Muddy water from Lake Mikata flowing into Lake Suigetsu can be observed. (B) A bird's-eye view from north of Lake Suigetsu. Brownish yellow muddy water spread over Lake Suigetsu. There are landslides on the slope of the southern margin of Lake Suigetsu.

coarse detrital material in Lake Mikata, muddy water should consist mainly of fine silt particles. Together with inflow of muddy water from Lake Mikata, landslides are occasionally observed in the drainage of Lake Suigetsu and Lake Mikata (Figure3B). When landslide occurred within the drainage of Lake Suigetsu, coarse detrital material is discharged to Lake Suigetsu.

### **2-3. Geological setting**

Geologically, the drainage area of Mikata Five Lakes is mainly occupied by accretion complex of Jurassic strata (~90% in area) with a small area of granite complexes (~10% in area) intruded during the late Cretaceous (Figure2,[*Nakae et al.*, 2002]). In the drainage area of Lake Suigetsu, Jurassic accretion complex occupies more than 98% of the area and the rest 2% is granite complex (Kugushi Granite). In the drainage area of Lake Mikata, accretion complex occupies about 85% in area and the rest 15% is granite complex (Kumotaniyama-Granite). In addition, Kumotaniyama-Granite forms high mountains with steep gorges. Therefore, detrital material coming from Lake Mikata into Lake Suigetsu has relatively high contribution from granite terrain compared to that from direct drainage of Lake Suigetsu.

### **2-4. Meteorological setting**

Here, I review the meteorological setting around Lake Suigetsu to understand the causes of floods occurring in this region. Since Lake Suigetsu is located in the Japan Sea side of Honshu Island, surrounding region of Lake Suigetsu receives relatively large volume of rainfall or snowfall during winter (Figure4A: the precipitation record from Tsuruga Observatory (20 km NE of Lake Suigetsu; [obtained from Japan Meteorological Agency, <http://www.data.jma.go.jp/gmd/risk/obsdl/index.php>]). However, when we focus on short but heavy precipitation exceeding 100 mm/day, most of heavy rainfall occurs in summer season from July to October, corresponding to the season of typhoon and Baiu (Figure4B). Practically, most of causes of

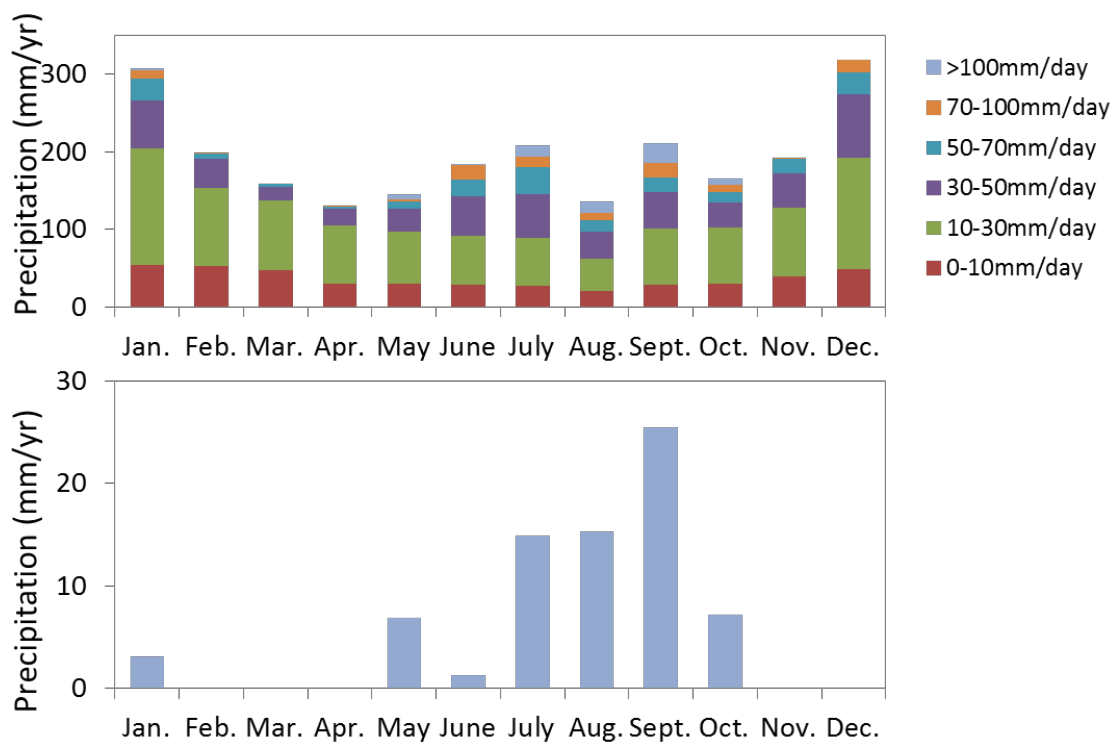


Figure 4  
 (A) Monthly average precipitation with subdivision into 6 categories based on intensity of daily precipitation (mm/day) observed at the Tsuruga observatory (20km east from Lake Suigetsu: Figure 1B) averaged from 1937 to 2012.  
 (B) Same as (A), but for the monthly precipitation exceeding 100 mm/day.

observationally recorded floods in this region are heavy rainfall caused by Typhoon as is summarized in Table 1.

## **2-5. Samples used in this study**

### **2-5-1. History of Lake Suigetsu drilling**

In Lake Suigetsu, there were four drilling projects conducted in 1993, 2006, 2012 and 2014 A.D. To obtain well preserved and continuously accumulated laminated sediment (varve), drillings were conducted at around the center of the lake. In 1993, SG (SG93) site was drilled down to 75m depth below the lake floor at a single hole [Fukusawa *et al.*, 1994; Kitagawa *et al.*, 1995; Yasuda *et al.*, 2004] to extend the calibration curve of  $^{14}\text{C}$  dating beyond the limit of tree ring [Kitagawa and Plicht, 2006]. Because piston coring produces unavoidable core gaps between core sections, SG93 core was not continuous, thus causing problems about establishing an age depth model based on varve counting [Staff *et al.*, 2010, 2013]. In 2006, SG06 cores were drilled down to 73.19m below the lake floor at 4 holes [Nakagawa *et al.*, 2012]. Drilling depth interval of each section were offset at 4 holes so that core gap intervals at one hole are covered by core sections of other holes, so that it is possible to make a perfectly continuous composite column of the sediment core based on correlation of marker layers between neighboring holes [Nakagawa *et al.*, 2012; Schlolaut *et al.*, 2014]. Based on varve counting and  $^{14}\text{C}$  measurements of more than 800 fallen leaves sampled from the composite column, a high resolution and precise age depth model is established for the sediment of Lake Suigetsu [Staff *et al.*, 2011; Bronk Ramsey *et al.*, 2012]. In 2012, SG12 core was drilled at around the same drilling site as SG06 so that the age model of SG06 composite column is projected to SG12 composite column. In 2014, FukuiSG14 core was drilled at the site ~200m to the east of the site of SG12 and SG06. SG12/06 and FukuiSG14 are correlated with each other although thickness of event layers observed in FukuiSG14 (eastern side of Lake Suigetsu) core differ from SG12/06 (the central part of Lake Suigetsu) (Yamada *et al.* submitted).

Table 1 Flood records and their causes compiled by compiled by the staff of Jomon Museum in Wakasa Town (Mikata Town History, 1990;Memoric magazine of 50 anniversary of Kaminaka-Town organization, 2004;Looking back the history of Mikata-Town, 2005)

Date (yr/month/day)	Total precioitation in Tsuruga (mm)	The cause of flood T: Typhoon TD: Tropical depression B: Baiu (rainy season)
2004/10/21	150	T
1999/8/14	149	TD
1998/9/22	130	T
1990/9/20	260	T
1982/8/1	214	T
1976/9/9	124	T
1975/8/23	194	T
1972/9/17	216	T
1972/7/13	477	B
1965/9/17	410	T
1965/9/10	95	T
1959/8/14	258	T
1953/9/25	311	T

## 2-5-2. SG12 Drilling

In 2012, SG12 cores were drilled as a part of Kiban-S project lead by R. Tada (JSPS KAKENHI Grant KIBAN-S Number 23221002) aiming to reconstruct climate changes during the late Holocene with the emphasis on East Asian Summer Monsoon precipitation. Four holes were drilled at SG12 site in the center of Lake Suigetsu (35° 35' 07.93"N, 135° 52' 56.40"E, 34m water depth) by Seibu-Shisui Ltd. using a hydro-pressure thin-walled piston sampler installed on a floating platform. Because a mechanical piston was used for drilling, the top part of each core section was disturbed to cause a core gap. To fill the gaps, 2<sup>nd</sup>, 3<sup>rd</sup> and 4<sup>th</sup> holes (2m south from each neighboring hole drilled before) were drilled in the way of offsetting the drilling depth interval of each core by ~50 cm. In total, 139 core sections were recovered from four holes. In parallel with the drilling operation, retrieved cores were split into halves and high resolution photographs and scan images of an archive half of each section were obtained just after core splitting because the split surface of core started oxidizing and color faded from immediately after splitting. Scanned images were observed and the position of marker layers, which have distinctly different colors such as light gray or brown compared to greenish black background sediment color were marked on the image. The marker layers were used for inter-hole correlation among four holes (Figure5A). Based on the correlation, a perfectly continuous composite column of the sediment of 41.9m in length was made by cutting and pasting of scanned images (Figure5B). After drilling, core samples were sealed by vacuum packs and sent to Univ. Tokyo and stored in a cold room at ~5°C. From 2014 to 2016, top 10m of SG12 cores were sliced into samples with the stratigraphic thickness of 1cm or 2cm. List of samples is shown in Table 2. From each sliced sample, 4-5 cc of sediments was subsampled using a small piston-cylinder to measure the volume of each subsample. These subsamples (of known volume) are used for measurements of water content, dry bulk density and XRF in chapter 5.

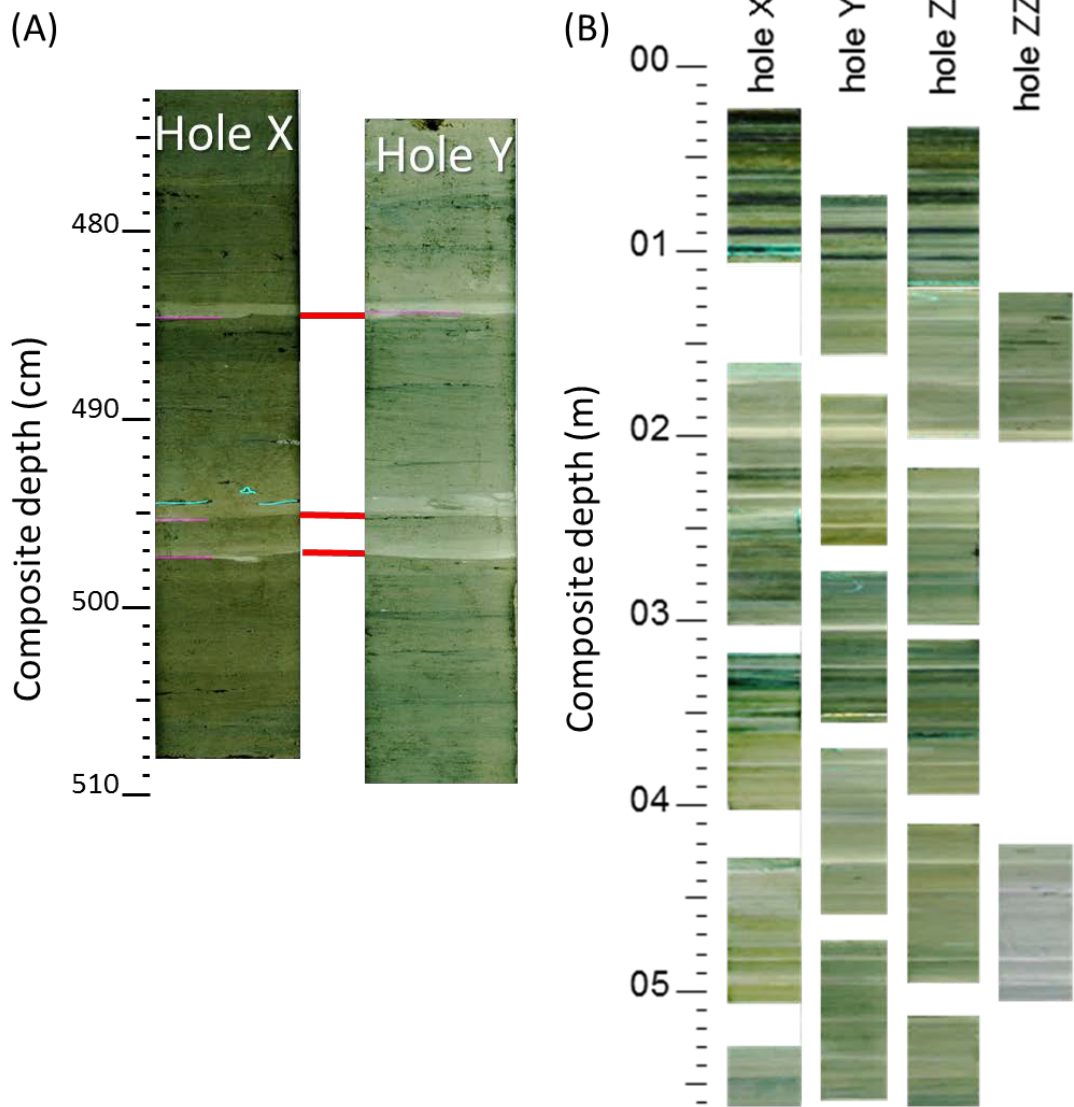


Figure 5  
 (A) An example of inter-hole correlation of SG12 core using scanned images (contrast enhanced). Light gray layers marked by red lines are “marker layers” used for correlation. (B) Inter-hole correlation of 4 holes for the top ~5m of SG12. Core photos are aligned with respect to the composite depth.

Table 2 List of subsampling of SG12 core conducted in this study

Hole	Core number	subsampling interval (cm)	composite depth of section top (cm)	composite depth of section bottom (cm)	top age (yr BP)	bottom age (yr BP)
X	1	1	20	106.8	-53	363
Y	1	1	69.4	156.2	173	595
Z	2	1	119.9	205.2	425	857
Y	2	1	177	261.6	689	1336
Z	3	1	218.6	301.4	969	1657
Y	3	1	271.7	356.3	1419	2058
X	4	1	317.8	403.4	1780	2429
Y	4	2	369.6	460.9	2153	2940
X	5	2	425.5	508.3	2609	3368
Y	5	2	474.2	560.5	3061	3798
X	6	1	528.9	621.4	3536	4261
Y	6	1	573.1	661.1	3905	4554
Z	7	2	615.2	706.6	4216	4922
Y	7	2	683	766.8	4723	5393
X	8	2	738.3	827.7	5164	5869
Y	8	2	784.4	867.5	5532	6210
Z	9	2	832.8	921.7	5911	6775
Y	9	2	891.3	969.4	6438	7264

### **2-5-3. LIMNOS core samples**

In general, mechanical drilling fails to retrieve the top part of the sediment immediately below the sediment/water interface because near surface sediment is soft and can be easily disturbed by mechanical drilling. To obtain the sediment immediately below the sediment/water interface without disturbance, LIMNOS core sampler [*Kansanen et al.*, 1991] was used.

Sampling was conducted in July 2012 and June 2014. In 2012, LIMNOS core samples were obtained from the drilling ship of SG12 by K. Yamada of Museum of Natural and Environmental History, Shizuoka. In 2014, LIMNOS samples were obtained at 6 sites in Lake Suigetsu and 2 sites in Lake Suga by boat in cooperation with K. Yamada, Y. Nakai of Hokkaido University and J. Kitagawa of Fukui Prefecture Satoyama-Satoumi Research Institute. Sampling locations are shown in Figure1C and their GPS coordinates are listed in Table 3. SG12-LM3, collected at the center of Lake Suigetsu close to site SG12 is used to fill the top ~30cm of SG12 core. LIMNOS samples are used in Chapter 4.

### **2-5-4. Surface samples from the surrounding area**

To examine the provenance of detrital material in the sediments of Lake Suigetsu, surface sediment samples were collected from rivers and river beds in the drainage area of Lake Suigetsu and Lake Mikata. River suspended materials was also sampled from Hasu River, a major river of the drainage area of Lake Mikata. Samplings were conducted in field surveys from 2012 to 2014, mainly helped by H. Kojima of Jomon Museum in Wakasa Town and K. Nagashima of JAMSTEC. Sampling locations are shown in Figure2 (Red and green circles) and their GPS coordinates are listed in Table 3. An eolian dust sample corrected by T. Irino at Hokkaido University in 2002 is also analyzed for comparison. These materials are used in chapter 4 and 5.

Table 3 List of sampling point of LIMNOS cores and surface detrital sample.

Sample Name	Type of sample	Sampling date (year/month/day)	Latitude	Longitude	water depth	Details of sampling point
SG12LM3	LIMNOS core	2012/7/6	35.586383	135.88233	34	Taken from the drilling ship of SG12 core
SG14LM1-1	LIMNOS core	2014/6/21	35.58488056	135.8832861	34.7	Taken at the center of Lake Suigetsu
SG14LM2-1	LIMNOS core	2014/6/21	35.57868889	135.8827222	26.8	Taken at the south part of Lake Suigetsu
SG14LM3-1	LIMNOS core	2014/6/21	35.58172222	135.8877861	31	Taken at the western part of Lake Suigetsu
SG14LM4-1	LIMNOS core	2014/6/21	35.5878	135.8902583	25.3	Taken at the eastern part of Lake Suigetsu
SG14LM5-1	LIMNOS core	2014/6/21	35.58580833	135.8734583	29.2	Taken at the northeastern part of lake Suigetsu
SG140219-01d	Surface detrital material	2014/2/19	35.596944	135.865192	-	Slope in the drainage of Ikabachi-River(a stream flowing into Lake Suigetsu)
SG131009-01	Surface detrital material	2013/1/09	35.596727	135.864336	-	Slope in the drainage of Ikabachi-River.
140621-1-2	Surface detrital material	2014/6/21	35.59735	135.865603	-	Slope in the drainage of Ikabachi-River.
140219-03a	Surface detrital material	2014/2/19	35.564006	135.902413	-	Riverbed of Kammon-River
140621-11'	Surface detrital material	2014/6/21	35.526622	135.903578	-	Riverbed of Oya-River (Upper branch of Hasu River)
140621-5'	Surface detrital material	2014/6/21	35.562909	135.90137	-	Riverbed of Kammon-River
140622-6	Surface detrital material	2014/6/22	35.559918	135.897111	-	Riverbed of Hasu-River near Jonnon museum
140620-3-2	Surface detrital material	2014/6/20	35.588701	135.896325	-	Shore of Lake Suigetsu near outcrop of Kugusshi Granite Rock
140219-03b	Surface detrital material	2014/2/19	35.564006	135.902413	-	Riverbed of Kammon-River
140622-8'	Surface detrital material	2014/6/22	35.542821	135.87646	-	Riverbed of Takase-River (western branch of Hasu-River)

### **3. Sediment types and lithology of Lake Suigetsu sediments from SG12 cores**

Based on macroscopic observation of core surface and scanned images of SG12 cores, Lake Suigetsu sediment from SG12 cores can be classified into three types, background sediments, event deposits and Tephra layers (Figure6). In this section, I describe occurrences, characteristics such as color, grain size, grain components and sedimentary structures.

#### **3-1. Methods**

To characterize the sedimentary types, macroscopic/microscopic observation and color measurement were conducted. Grain size measurement of detrital material isolated from each sedimentary type was also conducted.

**Macroscopic Observation:** Macroscopic observation was conducted using scanned images (Figure 6) of half split sections and composite column made in Chapter 2-5-2.

**Microscopic Observation:** Microscopic observations using smear slides were conducted on the top ~2m part of SG12 core. Small amount of sediments were taken by toothpicks from typical sedimentary types and smear slides made from these samples. Components of particles in the sediment, their grain size, shapes and mixing ratio were described based on observation of smear slides under the microscope.

**Color Measurement:** Color measurement was conducted by the members of SG12 project just after the scanning of each section, scraping off the surface part of half split surface whose color is faded. Thin plastic film was put on the surface of a half split core and a spectrophotometer KONICA MINOLTA CM-700d equipped with the window of 8mm diameter was deployed. Measurements was conducted in 1cm intervals from the top of the core (1cm, 2cm, 3cm, 4cm...) and after that, measurements in 1cm intervals were conducted again offsetting 5mm from the first measurement(0.5cm, 1.5cm, 2.5cm, 3.5cm...). Combining the two measurements, color data is obtained with 0.5cm intervals. The result of color measurement is shown in ( $L^*$ ,  $a^*$ ,

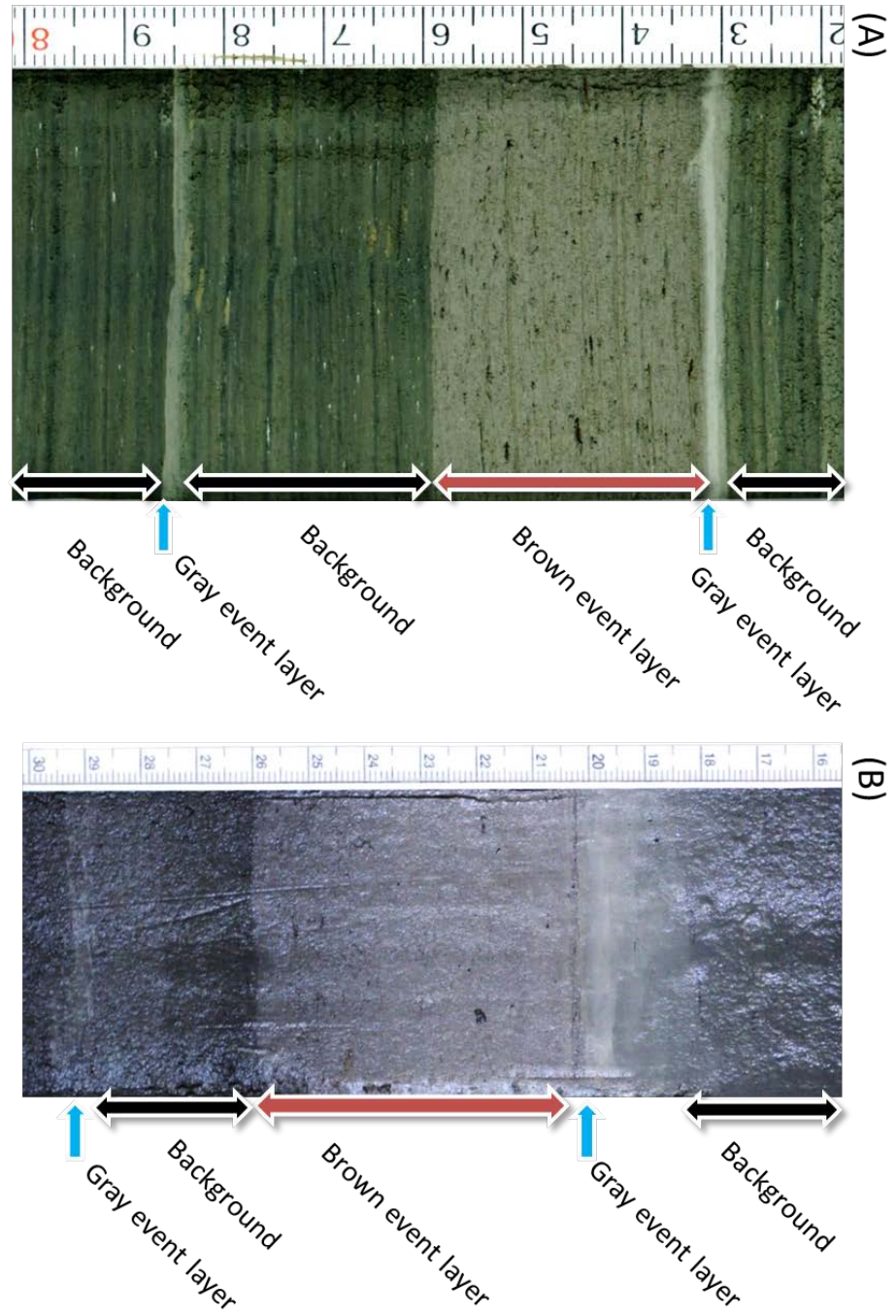


Figure 6  
Core photographs(contrast enhanced) which shows the 3 representative sediment facies in the sediment of Lake Suigetstu: background sediments, gray event layer, brown event layer.  
(A) SG12Z14 (72~80cm of distance from section top, corresponding to 1430~1438cm composite depth).  
(B) SG12Y2 (16~30cm of distance from section top, corresponding to 192.87~206.45cm composite depth).

b\*) coordinates for D65 light source in Figure 7.

Grain Size Analysis: Grain size measurement is conducted using laser diffraction grain size analyzer (Malvern MasterSizer 2000) after extraction of detrital material by chemical treatment that decomposes organic material, and dissolves diatom frustules, Fe-Mn oxides and carbonates after *Nagashima et al.* (2016) . Grain size measurement was conducted on 20–30mg of isolated detrital materials using a laser diffraction scattering grain size analyzer (Malvern, Mastersizer 2000) at the Univ. Tokyo. The analyzer has 52 detectors, which reproduce the diameter range from 0.01 to 10,000  $\mu\text{m}$ .

### **3-2. Classification and definition of sediment types**

#### **3-2-1. Background sediment**

Background sediments of Lake Suigetsu are defined by their dark-green color with  $(L^*, a^*, b^*) = (25-40, -1-0.5, 0-6)$ (Figure 7), fine grain size (less than  $\sim 10\mu\text{m}$ ), and either laminated or homogeneous appearance. Millimeter to centimeter-scale lamination is occasionally well preserved. Based on smear slide observation, background sediment is composed of several kinds of particles such as diatom frustule, detrital material, organic material and authigenic or hydrogenous mineral (Fe-Mn oxide or pyrite)(Figure8B). Mean grain size of detrital material in the background sediment (Figure8A) is 5 to 8 micrometers corresponding to suspended particles that are able to pass through Lake Mikata and flow into Lake Suigetsu assuming residence time of  $>18$  hours described in the Chapter 2-3. This observation indicates that fine detrital material from drainage area of Lake Mikata could be the source of detrital material in the background sediment.

#### **3-2-2. Event deposits**

An event layer is defined as a layer that has a sharp bottom contact with the sediment underneath and shows distinctly different color of either light gray or dark reddish brown with  $(L^*, a^*, b^*) = (35-45, -1.4-0.7, 2-8)$ (Figure 7, in contrast to the background sediment. Generally, event deposits have

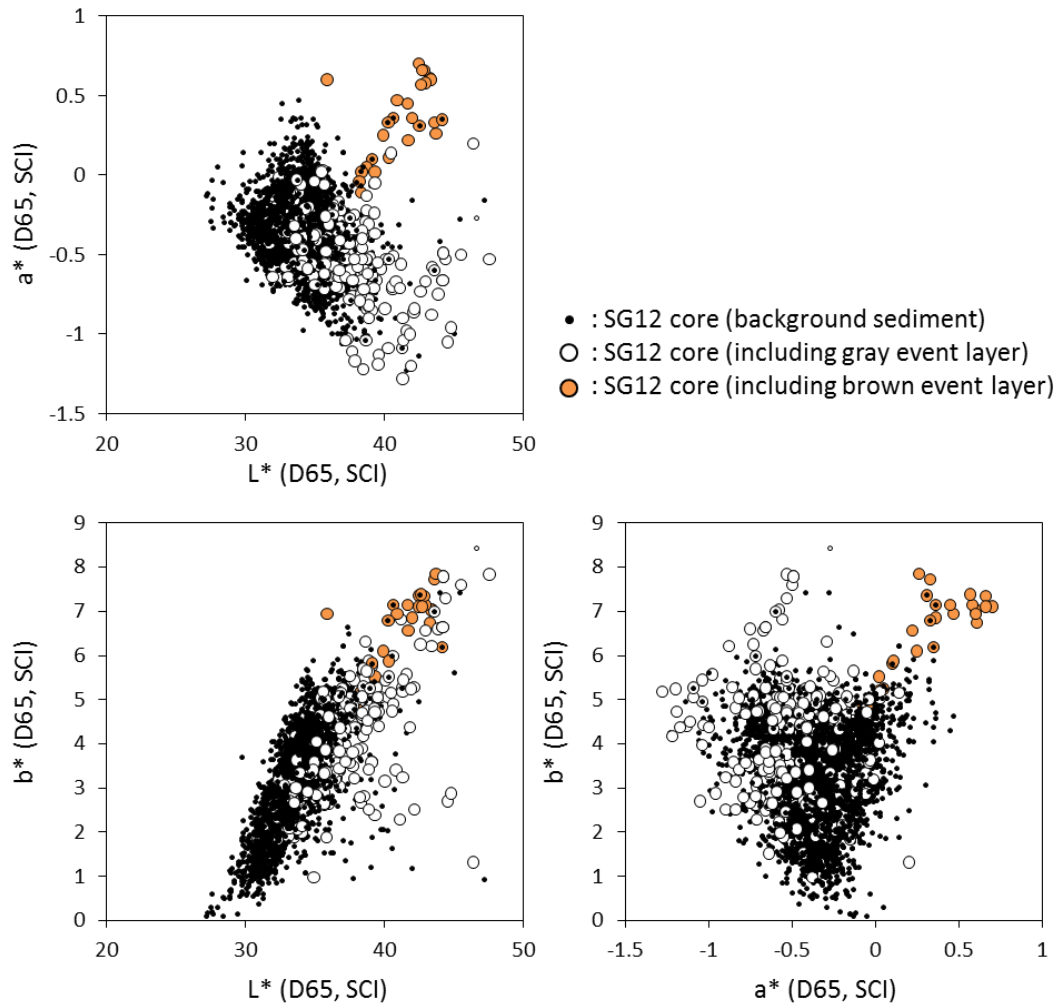


Figure 7  
 Cross plots of color measurement data in the top 10m of SG12 core.  
 Black dots, white circles and orange circles correspond to samples of  
 background sediment, samples including gray event layers and samples  
 including brown event layer, respectively.

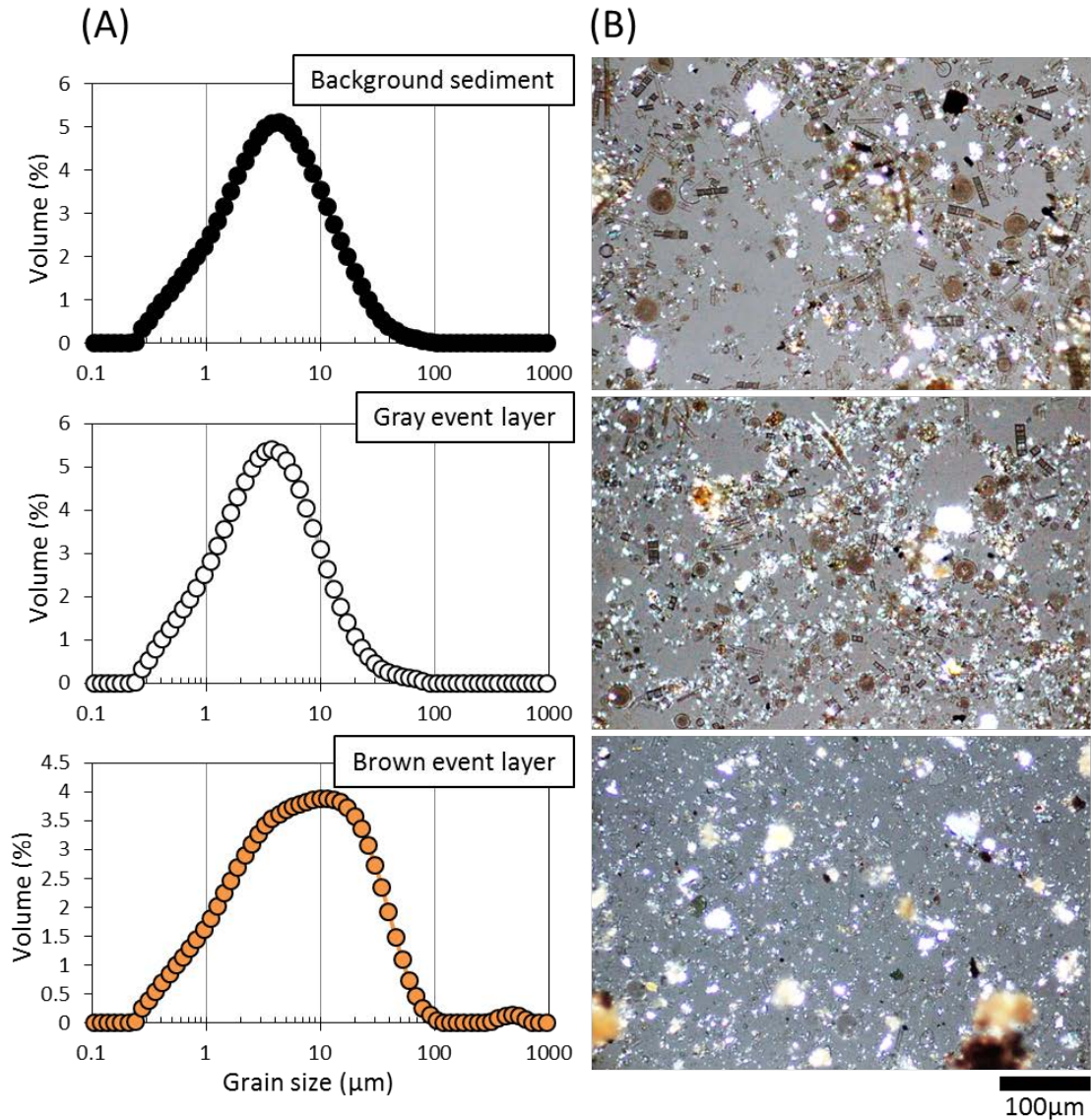


Figure 8

(A) Grain size distribution of detrital material in each sediment facies\* observed in the sediment of Lake Suigetsu.

(B) microscopic photograph of each facies taken in crossed-Nicol.

\*Each facies are taken from samples below.

Background sediment: SG12-HoleZ-section2 (53.22-54.23cm)

Gray event layer: SG12-HoleZ-section2 (71.49-72.5cm)

Brown event layer: SG12-HoleY-section2 (21.4-22.4cm)

sharp bottom contact[*Schillereff et al.*, 2014]. In case of Lake Suigetsu sediments, many event deposits can be observed as layers. Event layers in Lake Suigetsu are also characterized by their thickness of more than ~1mm, thicker than annual lamination in the background sediment. Sharp bottom contact suggests that these layers deposited within a short time. Event layers in the sediment of Lake Suigetsu can be subdivided into two types, light gray event layers and brown event layers based on their color, thickness and grain sizes.

### **3-2-3. Light gray event layers**

A light gray event layer is defined as an event layer with its light gray color distinctly different from background sediment ( $L^*$  is generally more than 35 in color measurement). Although their thickness observed on scanned image of split core surface has large variation, most of them are about 1 mm thick, but some layers have thickness in excess of 1cm. According to macroscopic observation, top part of some gray event layers thicker than ~1cm have color grading from light gray to background dark greenish gray color with the decrease in detrital material content. Thin event layers less than ~1cm thick does not show color grading in general. In smear slides, gray event layers are rich in fine silt sized (4-16 $\mu$ m) detrital material and other materials such as diatom frustules, organic material are rare compared to the background sediment(Figure8B). Mean grain size of detrital material in gray event layers is about ~6 $\mu$ m and coarse sized detrital material exceeding ~10  $\mu$ m are less than ~5% of total detrital material (Figure8A). Thus, light gray event layer is composed mostly of fine silt to clay sized detrital materials based on smear slide observation. Considering the result of grain size analysis and estimation of residence time of river water in Lake Mikata described in chapter 2-3, Lake Mikata and its drainage area can be interpreted as the main source of fine-grained detrital material in gray event layers. Light gray silty clay event layers occur every centimeter to meter interval in the background sediment.

### 3-2-4. Brown event layer

A brown event layer is defined by a sharp bottom contact with background sediment, and their brown color varies widely but always slightly reddish comparing to the background sediment with  $(L^*, a^*, b^*) = (35-45, 0-0.8, 5-8)$ (Figure 7). Thickness of brown event layers has wide variation ranging from 1cm to ~10cm, much thicker than a gray event layer. As is also seen in a brown event layer occurring at the depth of 3.5m (Figure6B), a gray event layer occurs on the top of a brown event layer. Since there are no background sediments in between and the bottom of the gray event layer is sharp, it is interpreted that these two layers are deposited sequentially during one event. Based on the observation of smear slides, brown event layers are mainly composed by coarse (10-100 $\mu$ m) semi-angular detrital materials with rare occurrence of other components (Figure8B). Since coarse detrital material from the drainage of Lake Mikata is trapped in Lake Mikata, surrounding slopes of Lake Suigetsu is considered as the only source of coarse(> ~16 $\mu$ m: such coarse grain would settle to the bottom of Lake Mikata in 2 hours, which corresponds to unrealistic heavy precipitation more than 800mm/day, 1.5 times of larger than the heaviest rainfall in one day observed in Japan) detrital material to Lake Suigetsu except for eolian dust from Asian continent with it diameter 6 to 21 $\mu$ m[Osada *et al.*, 2014]. Therefore, it is concluded that their main source is rivers flowing from surrounding slopes that directly flow into Lake Suigetsu since detrital grains in brown event layers is much larger than those of other detrital sources. Grain size distribution of detrital material in the brown event layer matches with the result of microscopic observation, having modal grain size of 10-20 $\mu$ m in grain size distribution (Figure8A). However, fine-grained detrital material is also present approximately the same amount as coarse detrital material based on grain size analysis (Figure8A). Brown event layers are rare and occur every ~10m intervals or so in average. For instance, only 1 brown event layer occurs within top 10m interval of SG12 core.

### **3-2-5. Tephra layers**

Tephra layers are defined by sharp basal contact and concentration of volcanic ash observable with naked eyes. Samples including tephra layers observed by naked eyes and on core photographs are listed in Table S5 with facies 3. As it is obvious that tephra layers are originated from outside of hydrological system of Lake Suigetsu, I eliminated samples including tephra layers from data analysis to avoid the effect of tephra layers. Tephra layers in Lake Suigetsu sediment are described and determined their origins and ages by *Smith et al.* (2013)

## **4. Relationship between detrital flux and flood in Lake Suigetsu during the past 100 years**

In this chapter, I aim to understand the relationship between event layers and occurrence and magnitude of flood events in Lake Suigetsu. For this purpose, I correlate observational record with sedimentary record using near surface sediment covering the last century. For this purpose, I construct a high resolution age-depth model to correlate the sedimentary record with historical and observational meteorological record of this region.

### **4-1. Sampling**

In this section, I introduce samples and their pretreatment. In this study, I use LIMNOS core SG12LM3, which is taken from the center of Lake Suigetsu (Figure1D). GPS coordinates and water depth of SG12LM3 core are shown in Table 3.

Because LIMNOS core is too soft to handle due to its high water content just after the sampling, SG12LM3 core is kept in standing position with sponge forms at the top and bottom of the sediment and stored in cold room of The University of Tokyo for about half a year since the coring to allow sediments to be compacted and then split into halves. Scanned images were taken using an “archive” half. From a working half, slab samples (20 × 5 × 0.7 cm) were taken for soft-X ray analysis. The remaining part of working half and “archive half” were sliced into subsamples with thicknesses of 6 mm, corresponding to a time resolution of 2–3 years. Slicing positions of working half and “archive half” were coincided with each other based on the correlation of lamination within the error of  $\pm 1$ mm and sliced samples of two halves were mixed.

To determine the chemical composition of the suspended particulate material from the Hasu River, 100 liters of river water was collected at the mouth of the Hasu River on October 1, 2012, immediately after the strong precipitation event that occurred during the 17th typhoon in 2012. This typhoon passed through the central part of Honshu Island. The water was

filtered using a Millipore filter (pore diameter = 0.45 $\mu$ m), and the filtered suspended particulate material of the Hasu River was washed from the filtrating paper using deionized water.

#### 4-2. Analytical method

Slab (20  $\times$  5  $\times$  0.7 cm) samples were subject to soft X-ray analysis using a SOFTEX CMB-2 with the filming condition of 40 kV / 2 mA / 5 minutes exposure time. The sliced samples were weighed in wet condition (Wet weight (g) is described as  $W_w$ ) and then freeze-dried for more than 30 h. The dried samples were weighed (Dry weight (g) is described as  $W_d$ ) again. Weighing errors of  $W_w$  and  $W_d$  are  $\pm 0.0005$ g. Grain density (GD, g/cm<sup>3</sup>) was calculated by weight ( $W_d$ ) and volume ( $V_d$ ) of dried sample by equation (1).

$$GD = W_d / V_d \quad (1)$$

$V_d$  is measured using a He pycnometer (AccuPyc 1330, Micrometrics Instrument Co.) at the Atmospheric and Ocean Research Institute, the University of Tokyo. Measurement error of  $V_d$  is  $\pm 0.00005$  cm<sup>3</sup>.

X-ray fluorescence (XRF) analysis was conducted to determine the concentrations of 10 major elements (Al<sub>2</sub>O<sub>3</sub>, SiO<sub>2</sub>, TiO<sub>2</sub>, Fe<sub>2</sub>O<sub>3</sub>, MnO, P<sub>2</sub>O<sub>5</sub>, Na<sub>2</sub>O, CaO, MgO, and K<sub>2</sub>O) using an XRF spectrometer (PANalytical Axios) equipped with an Rh tube in Department of Earth and Planetary Science the University of Tokyo. From each dried sample, ~0.6 g was split and used to make a glass bead for XRF analysis. Before making the glass bead, each sample was ignited, and the loss on ignition (LOI: wt%) was calculated using the weight after drying ( $W$ ) and the weight after ignition ( $W_i$ ) by following equation (2).

$$LOI = \left(1 - \frac{W_i}{W}\right) \times 100 \quad (2)$$

Relative error of LOI is  $\pm 0.2\%$ . Measurement conditions of XRF are 32kV / 125 mA for 7 elements (Al<sub>2</sub>O<sub>3</sub>, SiO<sub>2</sub>, P<sub>2</sub>O<sub>5</sub>, Na<sub>2</sub>O, CaO, MgO, and K<sub>2</sub>O), 60kV / 66mA for 2 elements (Fe<sub>2</sub>O<sub>3</sub> and MnO) and 40kV / 100mA for TiO<sub>2</sub>. The 10

values of the measurements were  $\pm 0.046$  % for  $\text{SiO}_2$ , 0.0035 % for  $\text{TiO}_2$ , 0.019 % for  $\text{Al}_2\text{O}_3$ , 0.0067 % for  $\text{Fe}_2\text{O}_3$ , 0.0018 % for  $\text{MnO}$ , 0.0058 % for  $\text{MgO}$ , 0.003 % for  $\text{CaO}$ , 0.0072 % for  $\text{Na}_2\text{O}$ , 0.0057 % for  $\text{K}_2\text{O}$ , and 0.0035 % for  $\text{P}_2\text{O}_5$ .

#### **4-3. Macroscopic and microscopic observation of SG12LM3 core**

The SG12LM3 core is 24.8cm in length and upper 17cm preserves fine paralleled lamination. In the lower part, lamination is not well preserved compared to the upper part. Based on the observation of smear slides, SG12LM3 core is dominantly composed of diatom frustules, clay to fine silt-sized detrital materials, organic materials, and black-colored minerals showing grain aggregation which is considered as siderite or pyrite formed within the water column (Figure8B). Clear ~mm-scale lamination observed in upper 17cm of the core is composed of alternation of black-gray laminae mainly composed of diatom frustules and organic material, brown laminae mainly composed of diatom frustules and aggregated siderite, and gray laminae mainly composed of detrital material. Light-gray fine-grained event layers with thicknesses of a few millimeters are also observed every a few centimeter intervals.

#### **4-4. Construction of age model**

Based on five procedures described below, an age model for SG12LM3 core is constructed with high resolution and precision.

##### **4-4-1. Varve counting**

Varve counting was conducted using soft X-ray images to construct an annual resolution age model for the SG12-LM3 core. In general, varve (annual lamination) has laminae corresponding to each season. Therefore, we could recognize one set of varve based on stacking of 4 different kinds of laminae in fixed orders as is described below. Each varve is defined as a set of a lower light (dense) layer and an upper dark (less dense) layer observed on the soft X-ray images. A lower light layer on soft X-ray image represents

siderite and/or clay layer accumulated during winter [*Schlolaut et al.*, 2012]. An upper dark layer in soft X-ray image represents organic amorphous material accumulated during summer and diatom frustules accumulated during spring and autumn. The basal boundary of varve is defined as the base of light layer (winter), so that one varve represents one year starting from winter till the next autumn (approximately from the beginning to the end of one year).

The basal boundary of each varve was determined as the steepest point of the change in brightness from the underlying dark (low-density) layer to the overlying light (high-density) layer on soft-X images; the former represents the organic amorphous material accumulated during summer and diatom frustules accumulated during spring and autumn., and the latter represents the siderite and/or fine-silt layer. When a light and dark layer couplet does not have clear density contrast or is not horizontally continuous within slab samples (5cm width), hereafter I call it as unclear varve and I treat it as representing per  $0.5 \pm 0.5$  years following the varve counting method for Lake Suigetsu sediments by *Schlolaut et al.* (2012) . This method assumes unclear layer as representing even possibility to be a varve (1 year) or not a varve (0 year).

The lamina with sharp basal contacts with the underlying layers and with light gray to white color on scanned images are identified as event layers. Event layers have distinct characteristics on the soft X-ray images, sharp basal contact and higher density (light gray to white on the soft X ray images) than adjacent laminae. Event layers were excluded from annual layer counting because they are considered to have accumulated rapidly because suspended detrital material with their diameter of  $4\mu\text{m}$  would settle to the bottom of Lake Suigetsu (34m water depth) within  $\sim 26$  days when calculating the settling velocity based on Stokes' law. Because there was no clear lamination in the depth interval from 17.3 to 19.1 cm, we considered this interval as bioturbated and interpolated the mean sedimentation rate ( $2.5 \pm 1.2\text{mm/yr}$ ) of background sediment based on the average varve

thickness in the top 17cm interval( $2.5 \pm 0.8$  mm) and the interval between 19.1cm and 24.6cm( $0.2 \pm 0.1$  mm). On the basis of the varve counting with the assumption that the top of the core represent 2012 yr A.D. (the time of the core retrieval), we estimated the age of each varve in the SG12-LM3 core. Preliminary counting error of each varve is estimated based on piling up of errors estimated on unclear varves from the top of the core. The results are shown as age versus depth plot in Figure 9C and Table S1.

#### 4-4-2. Measurement of radioactive nuclides

Radioactive nuclides of  $^{137}\text{Cs}$ ,  $^{210}\text{Pb}$ , and  $^{214}\text{Pb}$  were measured for 14 selected samples using an ORTEC GWL-120230-S HPGe (High-Purity Germanium) coaxial well photon detector system with an inner diameter of 17 mm and an active well depth of 40 mm at Hokkaido University by T. Irino.  $^{137}\text{Cs}$  is a radioactive nuclide ( $T_{1/2} = 30.1$  yr) produced by nuclear fission of  $^{235}\text{U}$ , generally produced by nuclear testing and extremely rare in natural condition. It is known that  $^{137}\text{Cs}$  concentration in atmosphere has a peak corresponding to the peak age of nuclear testing in 1963 A.D. and the onset of its concentration increase corresponds to a start of nuclear testing in 1954 A.D. according to the record of nuclear testing[*Pennington et al.*, 1973; *Delaune et al.*, 1978]. Therefore, fallout  $^{137}\text{Cs}$  in the sediment provides us the age constraints of 1954 and 1963 A.D.

Excess  $^{210}\text{Pb}$  (Bq/g), which is defined as the difference between the radioactivities of measured  $^{210}\text{Pb}$ (Bq/g) and  $^{214}\text{Pb}$ (Bq/g) as is given in the equation (3).

$$\text{Excess } ^{210}\text{Pb} = ^{210}\text{Pb} - ^{214}\text{Pb} \quad (3)$$

Here,  $^{210}\text{Pb}$ ( $T_{1/2} = 22.3$  yr) is assumed to come from the decay of  $^{226}\text{Ra}$  in the sediment itself and fallout product originated from  $^{222}\text{Rn}$  (gas) in the atmosphere produced by the decay of  $^{226}\text{Ra}$  of the ground surface. On the other hand,  $^{214}\text{Pb}$  ( $T_{1/2} = 26.8$  min) only come from  $^{226}\text{Ra}$  in the sediment. Therefore, Excess  $^{210}\text{Pb}$  represents the contribution from  $^{222}\text{Rn}$  decay (?) in the atmosphere. Assuming a constant mass accumulation rate ( $\text{g}/\text{cm}^2/\text{year}$ ) of the sediment, constant production of  $^{222}\text{Rn}$  and the radiation equilibrium of

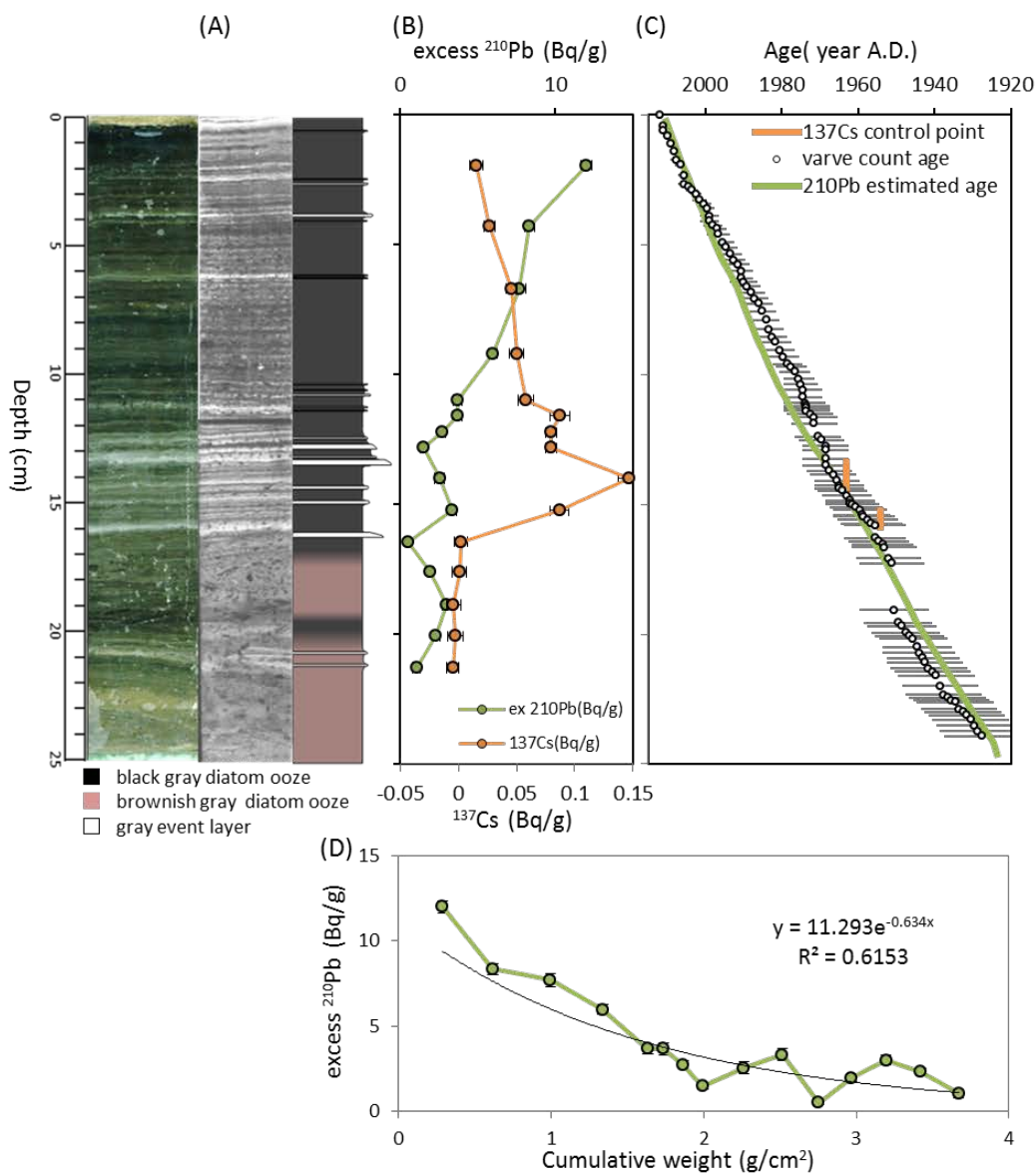


Figure 9

(A) A scanned image (color intensified), a soft X-ray image (color intensified and length adjusted with the scanned image) and a columnar section of the SG12LM3 core.

(B)  $^{210}\text{Pb}$  (Bq/g) and  $^{137}\text{Cs}$  (Bq/g) excess profiles of the SG12LM3 core plotted by green and orange circles, respectively.

(C) varve count age of the SG12LM3 core (white circles with gray error ranges). The  $^{137}\text{Cs}$  control points (orange points) and estimated ages based on  $^{210}\text{Pb}$  (green line) are also shown. Varve based age model matches with the result of the age estimations by radioactive nuclides.

(D) The  $^{210}\text{Pb}$  decay curve against the cumulative weight ( $\text{g}/\text{cm}^2$ ) of every samples by compiling dry weight of each slice of the core.

$^{210}\text{Pb}$  and  $^{214}\text{Pb}$ , we can estimate mass accumulation rate of the sediment [Kato *et al.*, 2003]. One to two grams of each frozen dried sample was weighed within an error of  $\pm 0.5$  mg and placed into a plastic tube. The tube was then placed in the well-shaped Ge detector. The measurement time was 48 h. The gamma-ray spectra were obtained using a Seiko EG&G MCA7600 multichannel analyzer. The analytical errors (detection limits) of  $^{137}\text{Cs}$ ,  $^{210}\text{Pb}$ , and  $^{214}\text{Pb}$  were 0.006 (0.018) Bq/g, 0.28 (0.83) Bq/g, and 0.010 (0.030) Bq/g, respectively. Results of  $^{137}\text{Cs}$  content and excess  $^{210}\text{Pb}$  are shown in Figure 9B and listed in Table S2. In chapter 2-4-3, they are used as constraints of a varve based age model.

#### **4-4-3. Constraining a varve based age model using the $^{210}\text{Pb}$ and $^{137}\text{Cs}$ results**

I used  $^{210}\text{Pb}$  and  $^{137}\text{Cs}$  to further constrain an age model based on varve counting. Figure 9B shows the depth profiles of excess  $^{210}\text{Pb}$  and  $^{137}\text{Cs}$  concentrations in SG12-LM3 core. The result of measurement of  $^{137}\text{Cs}$ ,  $^{210}\text{Pb}$ ,  $^{214}\text{Pb}$  and Excess  $^{210}\text{Pb}$  are listed in Table S2. The depth profile of Excess  $^{210}\text{Pb}$  shows generally decaying trend excepting the samples corresponding to 12.5-13cm and 16-16.5cm depth. These parts are characterized by frequent occurrence of gray event layers. As gray event layers is considered have high sedimentation flux, less contents of Excess  $^{210}\text{Pb}$  in these parts is interpreted less concentration of fallout products caused by high sedimentation rate. The profile of 15 Excess  $^{210}\text{Pb}$  data against mass accumulative weight ( $\text{g}/\text{cm}^2$ ) was fit by a decaying curve, as is shown in Figure 9D. The age model based on Excess  $^{210}\text{Pb}$  (Figure 9C) shows an age of 1925 A.D. ( $\pm 3$  varve count years) at the bottom of the core. At the same point, varve counting suggested an age of 1930 A.D. ( $\pm 10$  varve count years). Therefore, the  $^{210}\text{Pb}$ -based age depth model agrees with the varve count age model within the error. The depth profile of  $^{137}\text{Cs}$  shows highest value of 0.14 Bq/g at 14cm depth and has nearly zero values in samples below 16.45 cm depth. The first appearance of  $^{137}\text{Cs}$  is known to correspond to the beginning of nuclear testing in 1954 A.D., and the peak  $^{137}\text{Cs}$  concentration corresponds to 1963 A.D., when nuclear

testing was at its peak [Delaune et al., 1978]. In Figure 9B,  $^{137}\text{Cs}$  appears (1954 A. D.) in the depth interval between 15.4 and 15.8 cm, while the varve count age of 1954 A.D. is in the depth interval between 15.2 and 20.4 cm when taking into account of the error of varve counting.  $^{137}\text{Cs}$  has a clear peak (1963 A. D.) in the depth interval between 14.0 and 15.2 cm, while the varve count age of 1963 A.D. is in the depth interval between 13.4 and 15.8 cm when taking into account of the error of varve counting. These results show that the varve count age model is consistent with the  $^{137}\text{Cs}$ -based ages within the error of varve counting (Figure 9C).

#### **4-4-4. The correlation between event layers and historical flood events and fine-tuning of varve count age model**

The result of 4-4-3 revealed that the varve count age model is accurate for the past 90 years within an error of  $\pm 5$ -10 years. To further constrain the age model, I correlated the ages of event layers with historical flood events. All of event layers found in the SG12-LM3 core were assumed to have been formed by short-term high precipitation events causing floods, as inferred from their sharp basal contact and normal grading. Smear slide observation revealed that gray event layers correlated with flood events are mainly composed of detrital materials and diatom frustules, siderite and pyrite are absent (Figure 8B). On the other hand, flood events that damaged human properties in this region were compiled by the staff of Jomon Museum in Wakasa Town (Editing Committee of Mikata-Town history, 1990; Center of Kaminaka Town residents, 2004; PR magazine of Mikata-Town, 2005).

There are 17 event layers identified in SG12-LM3 core and 13 historically recorded flood events during the last 90 years (Table 4). As shown in Table 4, event layers and flood events are given numbers from E1 to E13 and F1 to F19, respectively, in descending order. I assume an event layer can be correlated to a flood event if the varve based age of the event layer agrees with the calendar age of the flood event within the error of varve-based age model. I use calendar ages of the flood events to tune the age of flood events. At each fine-tuning point at which an event layer matches with a

Table 4 List of age control points based on the correlation between the event layers and historically recorded floods. Gray shades indicate the pairs used as age control points. These pairs are consistent with the estimated varve count age for each event layer, except those symbolized as asterisks, which require further constraining (see the bottom of this table).

Event layer Number	List of event layer			List of historically recorded flood				The cause of flood T: Typhoon TD: Tropical depression B: Baitu (rainy season)
	bottom depth of event layer (distance from core top, cm)	Varve count age (additional constraint from 137Cs) (A.D.)	Event layer thickness (mm)	Flood Number	Date (yr/month/day)	Total precipitation in Tsuruga (mm)		
E1	0.6	2009-2011	1.1	-	-	-	-	-
E2	2.45	2004-2007	0.65	F1	2004/10/21	150	T	T
E3 <sup>*1</sup>	3.9	1996.5-2001.5	0.95	F2	1999/8/14	149	TD	TD
E4 <sup>*1</sup>	4.2	1996.5-2001.5	0.65	F3	1998/9/22	130	T	T
E5	6.3	1987.5-1993.5	1.05	F4	1990/9/20	260	T	T
-	-	-	-	F5	1982/8/1	214	T	T
E6 <sup>*2</sup>	10.38	1972.5-1979.5	0.55	F6	1976/9/9	124	T	T
E7	10.6	1969.5-1979.5	0.3	-	-	-	-	-
E8 <sup>*3</sup>	10.88	1969.5-1979.5	0.9	F7	1975/8/23	194	T	T
E9 <sup>*4</sup>	11.3	1967.5-1979.5	0.6	F8	1972/9/17	216	T	T
E10 <sup>*4</sup>	11.4	1967.5-1979.5	1.15	F9	1972/7/13	477	B	B
E11	12.52	1963.5-1975.5	1.1	-	-	-	-	-
E12	12.9	1962.5-1974.5	1.5	-	-	-	-	-
E13 <sup>*4,5</sup>	13.24	1962.5-1974.5	1.8	F10	1965/9/17	410	T	T
E14 <sup>*4,5</sup>	13.4	1962.5-1974.5	2.85	F11	1965/9/10	95	T	T
E15	14.4	1958.5-1971.5	1.5	-	-	-	-	-
E16 <sup>*6</sup>	15.05	1954.5-1968.5	0.65	F12	1959/8/14	258	T	T
E17	16.15	1947.5-1963.5 (older than 1954)	3.55	F13	1953/9/25	311	T	T

\*1: Two neighboring event layers in the range of 5 years are compared to two floods occurred in 1998 and 1999.

\*2: Based on varve re-counting from E5, age of E6 ranges from 1976 to 1977.

\*3: Based on varve re-counting from E6, ages of E8 ranges from 1973 to 1976.

\*4: Two neighboring event layers without no varve between the layers are compared to two floods occurred in one year (1972 and 1965).

\*5: Based on varve re-counting from E16, age of E14 ranges from 1965 to 1967.

\*6: Based on varve re-counting from E17, age of E16 ranges from 1958 to 1960.

flood event, the error of age estimation is set as  $\pm 0.5$  year that corresponds to the uncertainty in the position of event layer in a varve. Namely, from the core top, event layer E2 is correlated with historically recorded flood event F1 within the error of the varve based age model. This set is used as a first fine-tuning point from the top of SG12-LM3 core. After this pair is correlated, errors of age estimation in the parts of the SG12LM3 core below E2 are revised from the first fine-tuning point. The revised error becomes narrower than that of the initial varve based age model. After this error reducing effort, E3 is correlated to F3 that occurred in 1998. The same process is repeated downward throughout SG12-LM3 core and 12 sets of fine-tuning points are fixed (Figure 10 and Table 4). Using the 12 fine-tuning points and 2 points constrained by the occurrence and peak of  $^{137}\text{Cs}$  listed in Table 4, we fine-tuned the varve based age model to explain the time interval between two neighboring fine-tuning points by reevaluating unclear varve ( $0.5 \pm 0.5$  years in the preliminary age model) to count (as 1 year) or not count (=0 year) to make the revised varve based age consistent with ages of 14 fine-tuning points.

#### **4-4-5. Estimation of age uncertainty using a Bayesian approach**

To verify the reliability of the fine-tuned age model, Bayesian analysis is conducted by T. Omori at The University Museum of Univ. Tokyo based on *Ramsey* (2009) using OxCal software (<http://c14.arch.ox.ac.uk>). Sets of varve counts and their errors sandwiched by two neighboring fine-tuning points (a set is called “si = sample interval”, Table S3) are defined. The age differences between centers of neighboring “si” are used for Bayesian analysis. In Bayesian analysis, varve based age model and the error estimated in 4-4-2 is used as prior probability (constraint condition). Ages of fine-tuning points (Table 4) are used for constraints of Bayesian probability. As output (posterior probability) of Bayesian analysis, age errors of every “si” are calculated based on prior probability and constraints, namely, without constraints determined by the re-counting of age error conducted in 4-4-4. Comparison between the output and error estimation conducted in 4-4-4

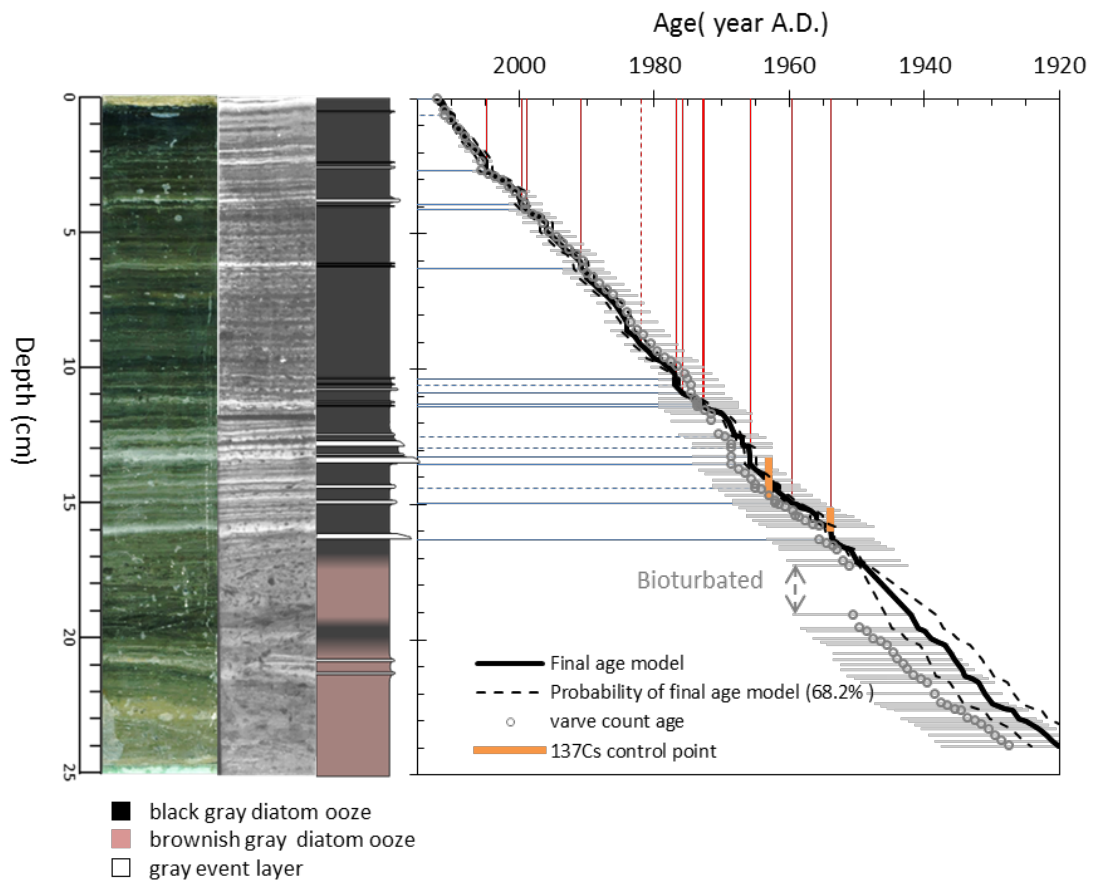


Figure 10

Fine-tuned age model of SG12LM3 (black thick line). Probability range (dashed line) is estimated based on Bayesian analysis. Varve count age (open gray circles),  $^{137}\text{Cs}$  control points (orange), and 12 pairs of event layers (blue solid lines) used for fine-tuning and historically recorded flood events (red solid lines) are also shown. Blue and red dashed lines represent positions of event layers and the age of flood events which could not be correlated.

(fine-tuned age model) is shown in Figure S1 and Table S3. Age error estimations based on varve counting (open ranges) and those estimated by Bayesian analysis (close ranges) matches with each other and varve based error estimations have broader range than those of Bayesian analysis. This result indicates that the error estimation of fine-tuned age model in 4-4-4 is in agreement with the posterior probability estimated by the Bayesian analysis. Therefore, it is verified that the fine-tuned age model is acceptable. I use fine-tuned age model for putting age values to each varve because Bayesian age model does not provide annual resolution. For the error estimation, I adopted a probability estimation based on Bayesian analysis because it narrows the age estimation error (Figure S1, Table S1) without re-counting the error conducted in 4-4-4.

#### 4-5. Estimation of detrital flux

The flux of detrital material ( $F_{\text{det}}$ , mg/cm<sup>2</sup>/yr) was calculated for each sample of SG12-LM3 core using equation (4) so as to compare with observational precipitation record at Tsuruga observatory (20 km east of Lake Suigetsu) to examine the relationship between  $F_{\text{det}}$  and precipitation

$$F_{\text{det}} = \text{DBD} \times \text{SR} \times C_{\text{det}}, \quad (4)$$

where DBD (g/cm<sup>3</sup>) is the dry bulk density estimated from grain density (GD: g/cm<sup>3</sup>) and water content (WC: wt%), SR is sedimentation rate (cm/yr) based on the fine-tuned age model, and  $C_{\text{det}}$  is the weight fraction of detrital material in the sample. SR is estimated as thickness of each sliced sample (cm) divided by the age difference between the top and bottom of each sliced sample. Since the position of the boundary between background sediment and event layer is not taken into account while slicing SG12-LM3 core, time intervals (and error) for each sample varies widely. The samples with extremely short intervals (less than 1 year) were excluded in the following discussion because of the large estimation error of the  $F_{\text{det}}$  due to the large uncertainty of the SR (SG12-LM3-22, depth = 12.55 to 13.1 cm, red shaded in Figure12).

WC was calculated from the dry ( $W_d$ ) and wet ( $W_w$ ) weight of the sample using the following equation (5).

$$WC = \frac{W_w - W_d}{W_w} \times 100 \quad (5)$$

DBD was calculated based on following equations (6) - (8).

$$DBD = \frac{W_d}{V_{water} + V_g} = \frac{GD}{(V_{water}/V_g) + 1} \quad (6)$$

where  $V_{water}$  is volume of water in the sample and  $V_g$  is grain volume.  $V_{water}/V_g$  can be written as equation (7) using WC and GD.

$$\frac{V_{water}}{V_g} = \frac{(W_w - W_d)}{W_d/GD} = \frac{WC}{100 - WC} \times GD \quad (7)$$

Combining (6) and (7), DBD can be written using GD and DBD by equation (8).

$$DBD = \frac{GD}{\frac{WC}{100 - WC} \times GD + 1} \quad (8)$$

$C_{det}$  (wt %) was estimated from the  $Al_2O_3$  and  $SiO_2$  content of each sample determined by XRF. Based on the observation of flood events (Section 2-2) and correlation of event layers and flood events (Section 4-4-4), it is suggested that suspended material from Hasu River is the major source of detrital material. To verify the source detrital material of event layers, chemical composition of suspended detrital material sampled from Hasu River is plotted with the data of SG12LM3 on the cross plot diagram of  $Al_2O_3$  and  $SiO_2$  (Figure 11). SG12LM3 data shows negative correlation and they are mostly plotted on a mixing line between the points at  $(SiO_2, Al_2O_3) = (90, 0)$ , which represents biogenic silica, and  $(53.5, 20.6)$ , which represents suspended detrital material from Hasu River (Figure11). A clear negative correlation between  $Al_2O_3$  and  $SiO_2$  suggests that  $Al_2O_3$  and  $SiO_2$  contents of the samples represent a mixing ratio of diatom frustules and suspended detrital material. Therefore, I estimate the concentration of detrital material ( $C_{det}$ : wt%) for each sample based on the equation (9)

$$C_{det} = \frac{Al_2O_3}{20.6} \times \frac{100-LOI}{100} \times 100, \quad (9)$$

where  $Al_2O_3$  and  $SiO_2$  are the concentrations (in wt%) in each sample after

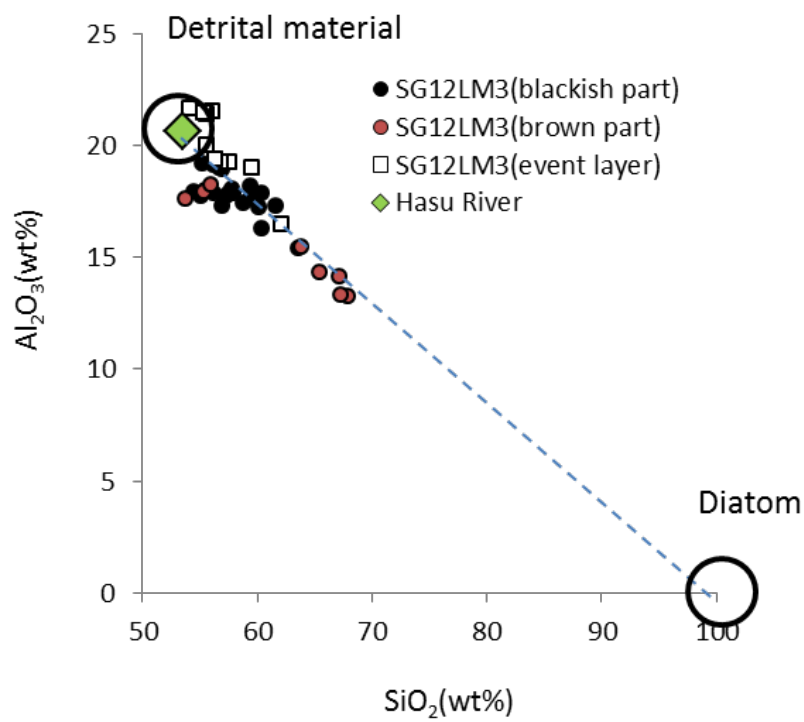


Figure 11  
 X–Y plot of  $SiO_2$  and  $Al_2O_3$  content for SG12LM3 samples and suspended material taken from Hasu River. Black circles represent the measured value of Hasu River and assumed value of diatom frustule.

ignition measured by XRF (Figure11).

#### 4-6. Result

The XRF data,  $C_{det}$ , and DBD of samples from SG12LM3 are listed in Table 5. The depth profiles of  $C_{det}$ , SR, DBD and  $F_{det}$  are shown in Figure 12. The values of  $C_{det}$  (Figure 12A) are higher (ca. 60%) in samples that contain event layers compared to other samples that contain only background sediments whose  $C_{det}$  is 40% to 50%. The sedimentation rate (Figure 12C: cm/yr) tends to be higher ( $\sim 0.7$  cm/yr) in samples containing event layers and lower in other samples covering background sedimentation ( $\sim 0.2$  cm/yr). DBD (Figure 12B) shows an increasing trend from the top of the core ( $\sim 0.1$  g/cm<sup>3</sup>) to the bottom ( $\sim 0.25$  g/cm<sup>3</sup>), primarily due to increasing compaction downward. The DBD also tends to be higher in samples containing event layers ( $\sim 0.25$  g/cm<sup>3</sup>) corresponding to higher content of detrital material ( $C_{det}$ ).  $F_{det}$  varies widely from 10 to 100 mg/cm<sup>2</sup>/yr (Figure 12D). Especially in samples containing event layers,  $F_{det}$  shows values ranging from 10 to 100 mg/cm<sup>2</sup>/yr, whereas it ranged from 10 to 35 mg/cm<sup>2</sup>/yr in samples that do not contain event layers.  $F_{det}$  reached the maximum value at the depth of 13cm that coincides with E10 (= F9). On that flood event, this region received over 400 mm of continuous precipitation within one week (the precipitation record from Tsuruga Observatory: JMA). This was the most significant precipitation event in the past 100 years and was caused by two typhoons that directly hit the area (JMA). In contrast,  $F_{det}$  in background sediment has relatively narrow variation ranging from 10 to 40 mg/cm<sup>2</sup>/yr (Figure 12D) and oscillates in short cycle (1-2 samples). Small variation of  $F_{det}$  in background sediment suggests that if the event layer deposition does not occur, flux of detrital material into Lake Suigetsu is relatively stable. Variations in background  $F_{det}$  are closely associated with that of SR. In contrast,  $C_{det}$  and DBD do not have such short term variation (Figure 12 A, B). Therefore, SR (nearly equal to the varve thickness) is supposed to have a stronger effect on  $F_{det}$  than does  $C_{det}$  or DBD in the background sedimentation. The flux of total

Table 5 XRF data of the SG12LM3 samples and suspended material from the Hasu River

SG12LM3	distance from core top (cm)		XRF data (wt%)														Cdet(wt%)	DBD (g/cm <sup>3</sup> )
	top	bottom	LOI	SiO <sub>2</sub>	TiO <sub>2</sub>	Al <sub>2</sub> O <sub>3</sub>	Fe <sub>2</sub> O <sub>3</sub>	MnO	MgO	CaO	Na <sub>2</sub> O	K <sub>2</sub> O	P <sub>2</sub> O <sub>5</sub>					
SG12LM3-02	0.5	1.1	33.40	62.09	0.77	16.45	7.74	0.10	3.15	1.02	4.49	3.54	0.63	41.78	0.12			
SG12LM3-03	1.1	1.7	35.93	60.46	0.72	16.27	8.85	0.17	3.16	1.01	5.04	3.74	0.58	38.83	0.11			
SG12LM3-04	1.7	2.2	28.14	59.41	0.84	17.60	9.64	0.21	3.13	0.92	4.56	3.29	0.40	47.28	0.13			
SG12LM3-05	2.2	2.8	27.97	61.60	0.81	17.27	8.18	0.21	2.99	0.91	4.44	3.17	0.42	47.63	0.14			
SG12LM3-06	2.8	3.4	27.67	56.96	0.77	18.93	10.50	0.23	3.02	0.91	5.28	3.03	0.38	50.43	0.13			
SG12LM3-07	3.4	4	24.01	56.06	0.90	21.51	9.57	0.26	2.96	0.83	4.35	3.18	0.37	61.53	0.16			
SG12LM3-08	4	4.6	34.20	57.54	0.83	17.83	9.02	0.23	3.53	1.30	5.28	4.02	0.41	42.93	0.11			
SG12LM3-09	4.6	5.2	29.43	60.21	0.79	17.22	9.07	0.23	3.02	1.01	4.80	3.28	0.38	45.66	0.14			
SG12LM3-10	5.2	5.8	26.25	58.81	0.80	17.39	10.32	0.23	3.06	0.91	5.11	3.05	0.32	47.43	0.15			
SG12LM3-11	5.8	6.4	22.63	59.57	0.86	19.00	9.43	0.21	3.00	0.79	3.93	2.94	0.27	56.08	0.18			
SG12LM3-12	6.4	7	26.25	60.46	0.80	17.83	8.27	0.23	3.02	0.87	4.94	3.27	0.30	49.98	0.16			
SG12LM3-13	7	7.6	27.91	57.97	0.81	17.87	10.54	0.30	3.01	0.91	4.87	3.38	0.33	47.43	0.13			
SG12LM3-14	7.6	8.2	28.25	56.94	0.80	17.28	10.64	0.33	3.16	1.19	5.75	3.61	0.31	44.66	0.13			
SG12LM3-15	8.2	8.9	24.33	59.39	0.84	18.13	9.25	0.32	2.94	0.86	4.61	3.37	0.29	51.64	0.13			
SG12LM3-16	8.9	9.5	24.61	57.85	0.87	18.01	10.64	0.36	3.05	0.94	4.90	3.10	0.28	49.99	0.15			
SG12LM3-17	9.5	10.1	28.22	56.25	0.88	17.84	10.89	0.37	3.14	1.05	5.77	3.46	0.36	46.06	0.14			
SG12LM3-18	10.1	10.7	24.45	56.37	0.88	19.38	10.90	0.39	2.95	0.83	4.62	3.36	0.32	53.82	0.16			
SG12LM3-19	10.7	11.3	21.70	55.61	0.95	19.98	11.31	0.39	3.08	1.02	4.29	3.05	0.31	57.43	0.19			
SG12LM3-20	11.3	11.9	22.66	56.21	0.95	19.08	11.57	0.40	3.14	0.97	4.45	2.94	0.29	53.94	0.17			
SG12LM3-21	11.9	12.55	20.54	57.57	0.98	19.23	11.35	0.39	3.04	0.81	3.47	2.83	0.33	56.95	0.20			
SG12LM3-22	12.55	13.1	17.01	55.66	1.05	21.39	11.28	0.35	3.13	0.74	3.34	2.77	0.29	66.41	0.23			
SG12LM3-23	13.1	13.7	17.96	55.37	1.02	21.47	11.37	0.36	3.10	0.79	3.42	2.80	0.31	65.70	0.24			
SG12LM3-24	13.7	14.3	20.40	56.80	1.00	19.20	11.84	0.50	3.19	0.82	3.60	2.79	0.26	56.39	0.21			
SG12LM3-25	14.3	14.95	20.36	56.31	1.00	19.37	11.92	0.57	3.17	0.82	3.74	2.83	0.27	56.66	0.21			

Table 5 (continued)

	distance from core		XRF data (wt%)																DBD (g/cm <sup>3</sup> )
	top	bottom	LOI	SiO <sub>2</sub>	TiO <sub>2</sub>	Al <sub>2</sub> O <sub>3</sub>	Fe <sub>2</sub> O <sub>3</sub>	MnO	MgO	CaO	Na <sub>2</sub> O	K <sub>2</sub> O	P <sub>2</sub> O <sub>5</sub>	Cdet(wt%)					
SG12LM3																			
SG12LM3-26	14.95	15.55	23.79	56.72	0.93	18.96	11.44	0.65	3.07	0.91	4.00	3.03	0.30	53.07	0.20				
SG12LM3-27	15.55	16.2	19.77	54.14	1.01	21.63	12.26	0.65	3.00	0.74	3.34	2.93	0.31	63.82	0.22				
SG12LM3-28	16.2	16.7	25.15	55.31	0.93	19.15	12.61	0.74	3.02	0.88	4.06	2.96	0.35	51.80	0.19				
SG12LM3-29	16.7	17.3	26.46	54.52	0.88	17.91	14.33	0.76	2.96	0.95	4.31	3.03	0.36	46.30	0.18				
SG12LM3-30	17.3	17.9	27.41	55.49	0.89	17.99	13.01	0.69	3.02	1.12	4.24	3.04	0.49	46.59	0.18				
SG12LM3-31	17.9	18.55	27.45	55.36	0.89	17.88	13.49	0.64	3.02	0.91	4.58	2.88	0.35	46.13	0.17				
SG12LM3-32	18.55	19.2	28.59	53.72	0.86	17.57	14.68	0.64	3.03	0.88	5.05	3.22	0.35	43.42	0.17				
SG12LM3-33	19.2	19.75	28.11	55.15	0.88	17.69	14.22	0.60	2.95	0.88	4.35	2.94	0.34	44.96	0.18				
SG12LM3-34	19.75	20.4	25.61	57.31	0.89	17.69	12.96	0.47	2.85	0.80	4.05	2.66	0.33	47.92	0.19				
SG12LM3-35	20.4	21	24.26	63.60	0.77	15.40	10.54	0.34	2.48	0.66	3.56	2.36	0.28	44.72	0.20				
SG12LM3-36	21	21.6	21.17	67.21	0.71	14.10	9.14	0.27	2.26	0.58	3.29	2.20	0.24	43.89	0.21				
SG12LM3-37	21.6	22.2	19.12	67.91	0.67	13.23	9.58	0.25	2.17	0.57	3.44	1.95	0.24	42.14	0.22				
SG12LM3-38	22.2	22.7	21.99	67.29	0.67	13.33	9.68	0.24	2.16	0.58	3.42	2.38	0.25	40.70	0.22				
SG12LM3-39	22.7	23.3	21.60	56.03	0.91	18.25	13.17	0.52	3.00	0.83	4.15	2.84	0.31	51.60	0.20				
SG12LM3-40	23.3	23.9	21.16	63.84	0.78	15.43	10.37	0.30	2.45	0.65	3.44	2.48	0.27	46.80	0.21				
SG12LM3-41	23.9	24.5	21.63	65.43	0.73	14.29	10.22	0.28	2.32	0.62	3.51	2.34	0.26	43.34	0.22				
Hasu River																			
SG121001-01	-	-	16.20	53.53	1.55	20.61	13.41	0.53	3.98	1.83	1.62	2.33	0.60	-	-				

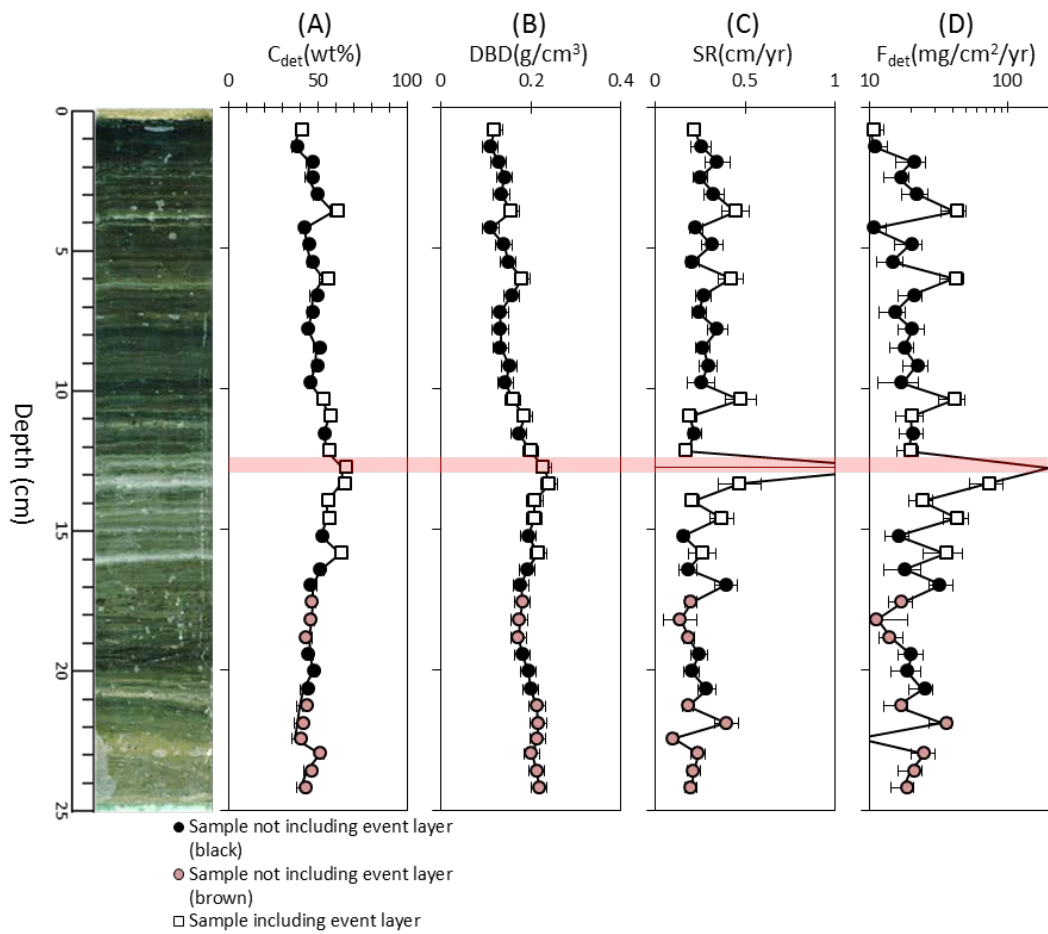


Figure 12  
 Depth profiles of (A) weight fraction of detrital material ( $C_{det}$ ), (B) dry bulk density (DBD), (C) sedimentation rate (SR), and (D) flux of detrital material ( $F_{det}$ ) of SG12LM3. A sample with its interval less than one year (Sg12LM3-22: 12.55~13.1cm) is shown with red shade.

detrital material calculated here covering the last 90 years is 5- to 10-times larger than the eolian dust fluxes in SW Honshu and the south-central part of the Sea of Japan, which were estimated as less than 1 mg/cm<sup>2</sup>/yr by observation in Toyama, 100km northeast from Lake Suigetsu [Osada *et al.*, 2014] and analysis of sediment cores from Japan Sea sediment [Irino and Tada, 2000; Nagashima *et al.*, 2007], respectively. Therefore, in Chapter 4, I regard eolian dust is a minor component of the detrital flux in SG12-LM3 core.

#### 4-7. Discussion

##### 4-7-1. Flood vs. gray event layer

The gray event layers, characterized by detrital flux maxima, are directly correlated to the historical flood records. I further examine the relationship between event layer thickness and total observational precipitation associated with the historically recorded flood events to test whether the event layer thickness record intensity of the extreme precipitation. Figure 13A shows plots of gray event layer thickness versus cumulative precipitation amount during a flood event recorded at Tsuruga observatory. Cumulative precipitation during each flood event is calculated by integrating the amount of precipitation at Tsuruga observatory from the start to the end of precipitation event covering the date of flood which is generally around 2 days. We find a strong positive correlation with the linear relationship described as equation (10)

$$T = 0.34 + 0.0023 \times P \quad (R = 0.74) \quad (10)$$

where T is thickness of an event layer(mm) and P is total precipitation during one flood event (mm) for all event layers except for E14 and E17, which are exceptionally thick (2.85 and 3.5 mm, respectively) relative to small amount of cumulative precipitation. We examined whether the characteristics of these two event layers are distinctly different from those of the other layers. Figure 13C shows scanned images of LIMNOS cores taken in 2014 from 5 sites and correlation of event layers among these sites. Event

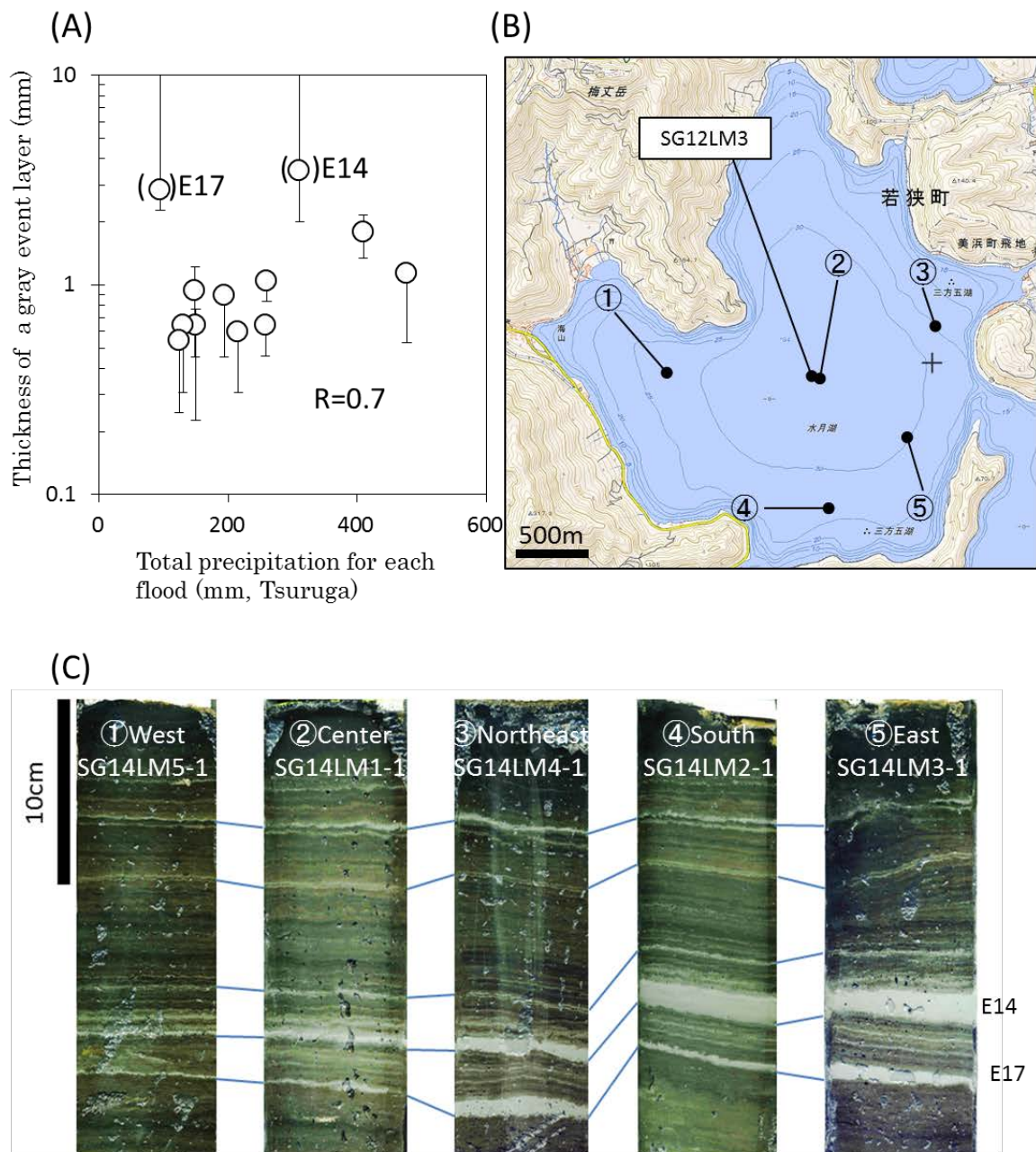


Figure 13  
 (A) A cross plot of total precipitation during historical floods and thickness of gray event layers which were correlated with historical floods. E14 and E17 are outliers with extreme thick event layer relative to weak precipitation during corresponding floods.  
 (B)(C) Scanned images of LIMNOS cores retrieved from Lake Suigetsu in 2014. The location of each core is shown in (B).

layers including E2 to E17 could be correlated among five sites indicating that event layer deposition spread over the entire lake. When focusing on the thickness distribution of event layers, most of event layers except for E14 and E17 have thickness variation of less than 40% (except for E2 and E3: extremely soft part of the sediment) and tend to be thickest at the center of the lake (Figure 14). This suggests that most of the event layers were deposited from a suspended sediment cloud that spread more or less homogeneously all over the lake. In contrast, E14 and E17 show large variation in thickness with more than 60%, and thinner in the central part (3mm and 2.7mm, respectively) and the thickest in the southern part for E14 (14.6mm) and in eastern part for E17 (8.3mm), respectively. This indicates that E14 and E17 include large amounts of detrital materials that were supplied through different processes than those of other event layers. I compared precipitation record during flood events with observational sea tide change and wind speed data (Figure 15). Although the clear difference could not be found, high level of sea tide and the peak of hourly precipitation occurred simultaneously in F11(E14) and F13(E17). Because wind data was not taken on the period of F13(E17), I could not verify the effect of the wind. In this study, I could not specify the cause of “extremely thick” gray event layers such as E14 and E17. However, if we correlate the cores taken from different points such as SG12 and FukuiSG14, we can characterize the difference of event layer in different position in the lake and treat these layers as outliers.

Number of typhoons that hit Japan without causing floods is much larger than those causing flood events in the study area. To characterize typhoons that cause floods recorded as event layers in Lake Suigetsu sediments, I summarize the routes of typhoons that are considered to have caused flood events (F1, F3-8 and F10-13 of Table 4). These typhoons hit the middle part of Honshu Island and moved to the north afterward, passing through the western side of the island (Figure 16). Because typhoons are known to gain vapor from areas neighboring the typhoon center [Fudeyasu *et al.*, 2008],

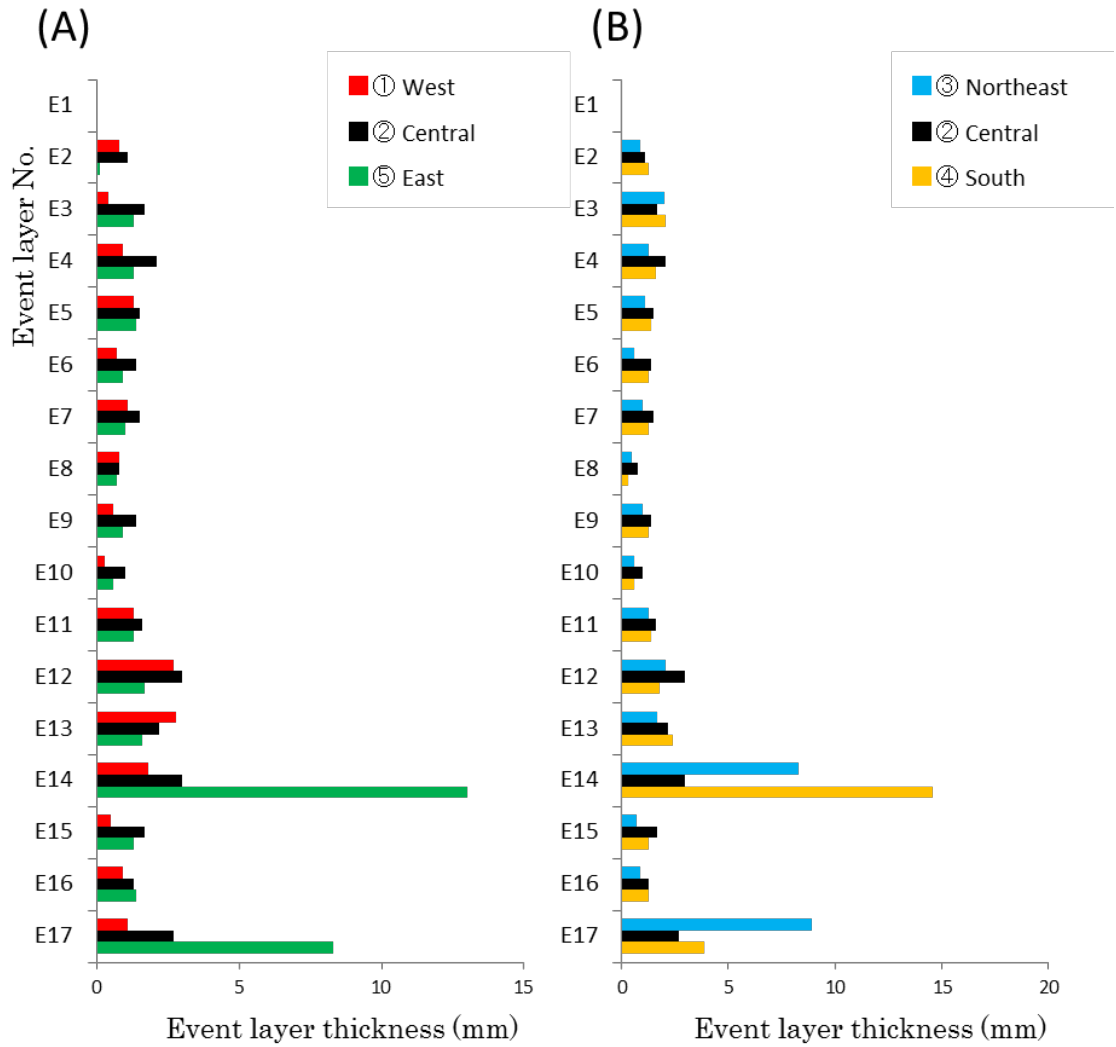
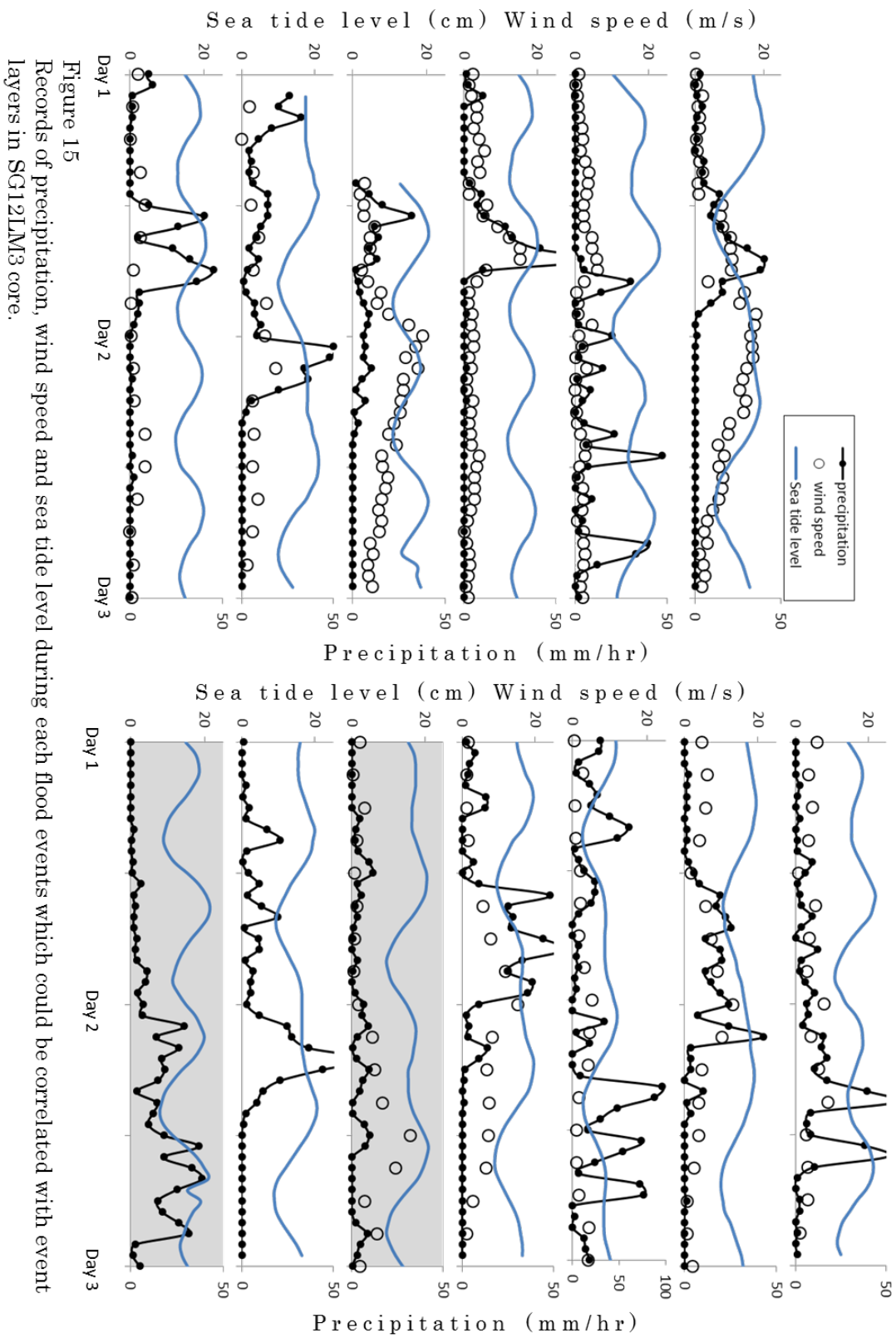


Figure 14

(A) West-east profiles of the event layers thicknesses.

(B) North-south profiles of the event layers thicknesses.

E14 and E17 are thicker in eastern areas and thickness in central part is less than 30% of thickest part. The rest of the event layers are thickest in central part or thickness in central part is more than 70% of thickest part.



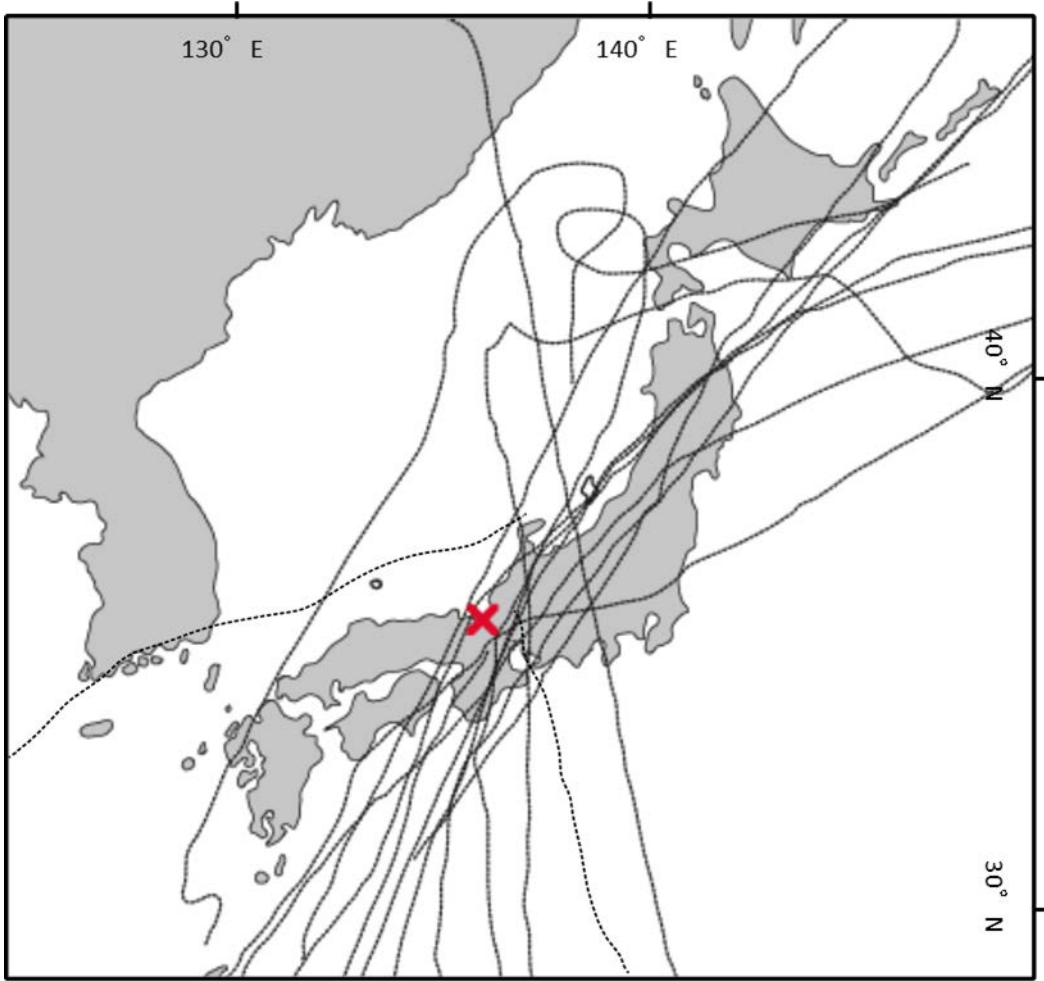


Figure 16  
Tracks of Typhoons (dashed line) causing flood in surrounding  
area of Lake Suigetsu(red cross mark).

typhoons taking the routes passing Japan Sea side should have received enough vapor from the Japan Sea to cause heavy precipitation on the Japan Sea side of the island. In contrast, ordinal typhoons that did not cause flooding around Lake Suigetsu in spite of hitting the site, passed through the southern and eastern sides of Honshu Island. Furthermore, event layers were deposited only when total precipitation in one event exceeds ~100 mm at Tsuruga observatory (Table 4). As is shown in Figure 4B, precipitation exceeding 100mm/day was caused mainly by typhoon (64%) rather than by Baiu (22%). These results indicate that gray event layers were deposited during strong precipitation and their thickness increased with precipitation, and that heavy precipitation in this region is primarily caused by typhoon, at least in the last 80 years.

#### **4-7-2. Annual precipitation vs. Background sedimentation**

I compared  $F_{det}$  and observed precipitation at Tsuruga observatory, which are expected to have exponential relationship based on the empirical relationship between sediment load of a river and river water discharge (nearly equal to precipitation in the drainage area in humid region) that is known as “rating curve” [Kazama *et al.*, 2005; Yang *et al.*, 2007; Sadeghi *et al.*, 2008; Kaji and Nihei, 2014].

Figure 17A shows mean annual precipitation versus  $F_{det}$  plot for samples that do not contain event layers. Mean annual precipitation (P: mm/yr) for each sample was estimated by total amount of precipitation during the time interval calculated from ages of the top and bottom of each sample and the precipitation record from Tsuruga Observatory (20 km NE of Lake Suigetsu; [obtained from Japan Meteorological Agency, <http://www.data.jma.go.jp/gmd/risk/obsdl/index.php>] Figure 1B) divided by duration of the interval. The  $F_{det}$  values for samples of pure background sedimentation showed a very weak positive correlation ( $R^2 = 0.199$ ,  $F_{det} = 0.0106P - 0.3473$ ) with averaged annual precipitation.

To further explore the relationship between  $F_{det}$  and precipitation, I focus on daily and relatively strong precipitation. Rating curve can be written by

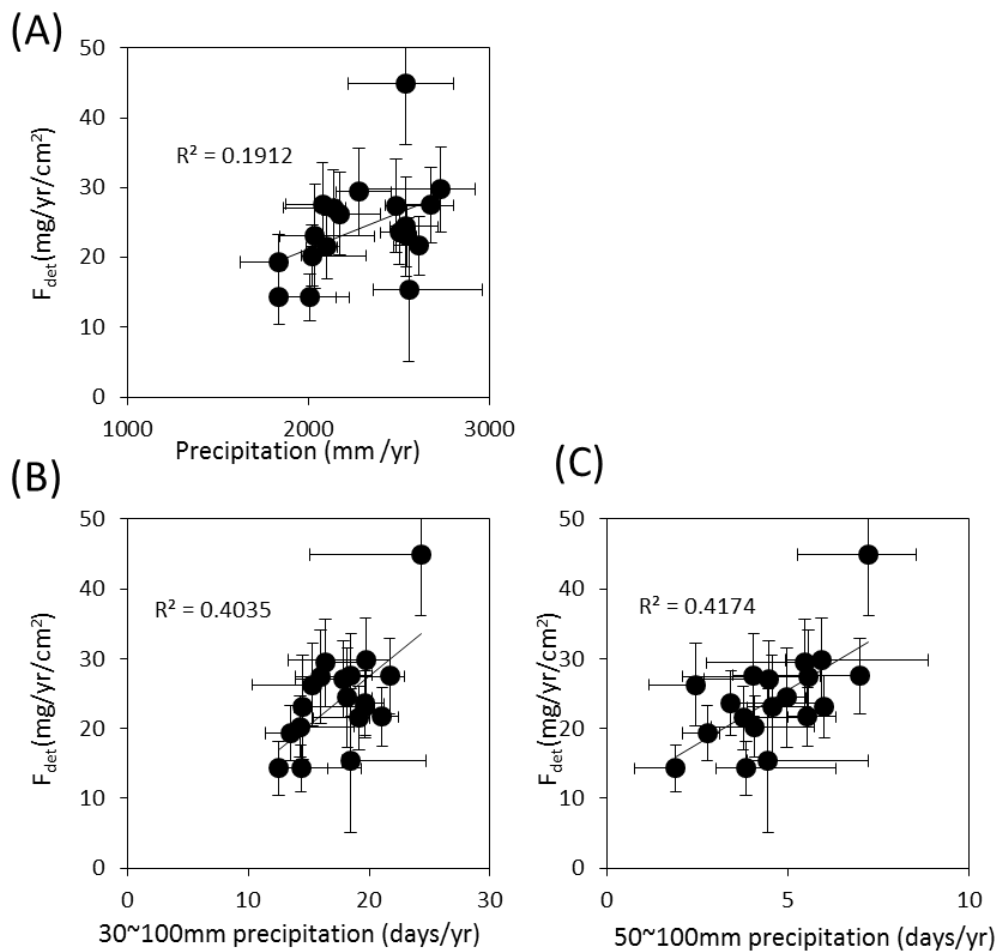


Figure 17

(A) X-Y plot of the annual precipitation (excluding >100 mm/day) at Tsuruga [JMA, <http://www.data.jma.go.jp/gmd/risk/obsdl/index.php>] and corresponding detrital flux of SG12LM3 background sedimentation for SG12LM3 samples excluding those including gray event layers. The detrital flux shows a weak relationship with the annual precipitation.

(B) X-Y plot of detrital flux versus frequency of rainy days more than 30mm.

(C) X-Y plot of detrital flux versus frequency of rainy days more than 50mm.

Frequency of “relatively strong rainfall” have clearer relationships than that of annual precipitation with  $F_{det}$ .

equation (11) using  $F_{det}$  (mg/cm<sup>2</sup>/ time unit), precipitation P: mm/time unit) and constants (a and b) specific to river system.

$$F_{det} = a \times P^b \quad (11)$$

As the river system of Lake Suigetsu including drainage of Lake Mikata is small, time scale of river discharge is considered as about 1 day or so [Milliman and Syvitski, 1992]. Therefore, it is supposed that river system of Lake Suigetsu is sensitive to strong rainfall. I compared  $F_{det}$  with frequency of strong rainfall, based on the days recording rainfall more than 30mm and 50mm but less than 100mm in one day. Frequency of “relatively strong rainfall” is calculated by number of rainy days with more than the threshold value of precipitation (30 and 50mm) divided by the time interval of each sample. Figure 17 B and C show relationship between  $F_{det}$  and frequency of “relatively strong rainfall”. When I compare  $F_{det}$  with frequency of rainfall stronger than 30mm/day or 50mm/day (Figure 17B, C), correlation coefficient becomes better ( $R^2 = 0.404$  for 30-100mm/day precipitation and 0.417 for 50-100mm/day precipitation) than that of  $F_{det}$  versus annual precipitation ( $R^2 = 0.191$ ) (Figure 17A).

These two results suggest that detrital flux in the background sediment represents frequency of relatively strong rainfall (for instance, more than 30mm per one day), even though the rainfall event is not strong enough to cause the flood event.



## **5. Provenance and flux of detrital material in the sediment of Lake Suigetsu**

To estimate the flux of fine-grained detrital material derived from the drainage area of Lake Mikata as a proxy of heavy rainfall, as discussed in Chapter 4, its content in the sediment of Lake Suigetsu has to be determined. However, bulk detrital material may contain material from several other sources such as coarse material from the slopes surrounding Lake Suigetsu and eolian dust from the Asian continent [*Schlögl et al.*, 2012; *Nagashima et al.*, 2016].

As a proxy of flood events, river-suspended particles have to be distinguished from those derived from other sources. In addition, the Holocene sediment of Lake Suigetsu has been weakly mixed by bioturbation.

Consequently, thin gray event layers, which could serve as a proxy of flood events, might have been erased. Therefore, it is important to determine the content of fine-grained detrital material within the sediment, which may contain event layers dispersed as a result of bioturbation.

In this chapter, I have attempted to measure the content of fine-grained detrital material transported from the drainage area of Lake Mikata by floods on the basis of Q-mode factor analysis (QFA) of the composition of the major elements in the sediment. By comparing the elemental compositions of extracted factors (end members [EMs]) with those of potential sources of the detrital material sampled from local rivers and eolian dust, I estimated the elemental compositions of the EMs. By estimating the elemental compositions of these detrital EMs, as well as those of other EM components of the sediment such as biogenic silica, organic material, and Fe-Mn oxide, I conducted multiple regression analysis (MRA) of the elemental compositions of bulk sediments to estimate the content of each EM.

### **5-1. Sample pretreatment**

#### **5-1-1. Core sample**

In this chapter, I used the top 10 m of the SG12 core, which covers the last

7000 years according to the  $^{14}\text{C}$  age model of the SG06 core projected to SG12 [Staff *et al.*, 2010, 2013; Bronk Ramsey *et al.*, 2012]. Half split cores that constitute a composite column were continuously sliced at intervals of 1 or 2 cm and subjected to measurements of dry bulk density (DBD) and X-ray fluorescence (XRF). The samples analyzed are listed in Table S5.

### **5-1-2. Surface detrital samples**

Fine-grained sediment samples were collected from riverbeds in the drainage areas of Lake Suigetsu and Lake Mikata and were analyzed by XRF for comparison with the estimated compositions of the EMs in order to specify the origin of the EMs. Grain size separation was conducted for each sample to evaluate the effects of grain size and transportation processes in lakes and rivers on the elemental compositions of the sediments. Grain size separation was conducted using a settling method [Gee and Or, 2002], and grains were separated into four fractions, namely,  $<4\ \mu\text{m}$ ,  $4\text{--}8\ \mu\text{m}$ ,  $8\text{--}16\ \mu\text{m}$ , and  $16\text{--}64\ \mu\text{m}$ . The fraction of  $>64\ \mu\text{m}$  was not analyzed, because the results of the grain size analysis conducted in Chapter 3 show that detrital material coarser than  $64\ \mu\text{m}$  is not present in gray event layers. A dust sample collected at Hokkaido University was also analyzed without grain separation.

## **5-2. Methods**

### **5-2-1. Dry bulk density (DBD)**

For the core samples, the DBD was calculated from the wet volume and dry weight of each sample. From each sliced sample, a sample of about  $5\ \text{cm}^3$  was subsampled using a small plastic syringe with grid lines, of which the head was cut off to make a piston cylinder. The volume of each subsample was quantified by reading the gridlines with a precision of  $\pm 0.1\ \text{cm}^3$  ( $\sim 2\%$ ). The subsamples were pushed out from the cylinders, frozen in a freezer, and dried with a freeze-dryer for 2–3 days. After freeze-drying, the dry weight ( $W_d$ ) was measured with a precision of  $\pm 0.001\ \text{g}$  ( $\sim 0.2\%$ ). The DBD was calculated using equation (12) below with a relative error of  $\sim 2\%$ .

$$\text{DBD} = W_d/V \quad (12)$$

### 5-2-2. Linear sedimentation rate (LSR)

The linear sedimentation rate (LSR) (cm/yr) for the top 10 m was calculated using the age–depth model established on the basis of  $^{14}\text{C}$  dating conducted by *Staff et al.* (2011) and *Saito-Kato et al.* (2013) in the SG93 and SG06 cores [*Kitagawa and Plicht, 2006; Nakagawa et al., 2012*]. The age control points used here and their positions in the core are shown in Table S6. The LSR of the  $N^{\text{th}}$  interval ( $\text{LSR}_N$ ) (cm/yr) bounded by two neighboring control points,  $C_N$  and  $C_{N+1}$ , was assumed to be constant and was calculated using the ages ( $A_N$  and  $A_{N+1}$ ) (yr BP) and the event-free depths ( $\text{EFD}_N$  and  $\text{EFD}_{N+1}$ ) (cm) of  $C_N$  and  $C_{N+1}$  using equation (13):

$$\text{LSR}_N = \frac{\text{EFD}_{N+1} - \text{EFD}_N}{A_{N+1} - A_N} \quad (13)$$

Here, the event-free depth was used, which involved excluding the thickness of event layers thicker than 5 mm from the composite depth to minimize the effect of instantaneous huge sedimentation events [*Staff et al., 2011*].

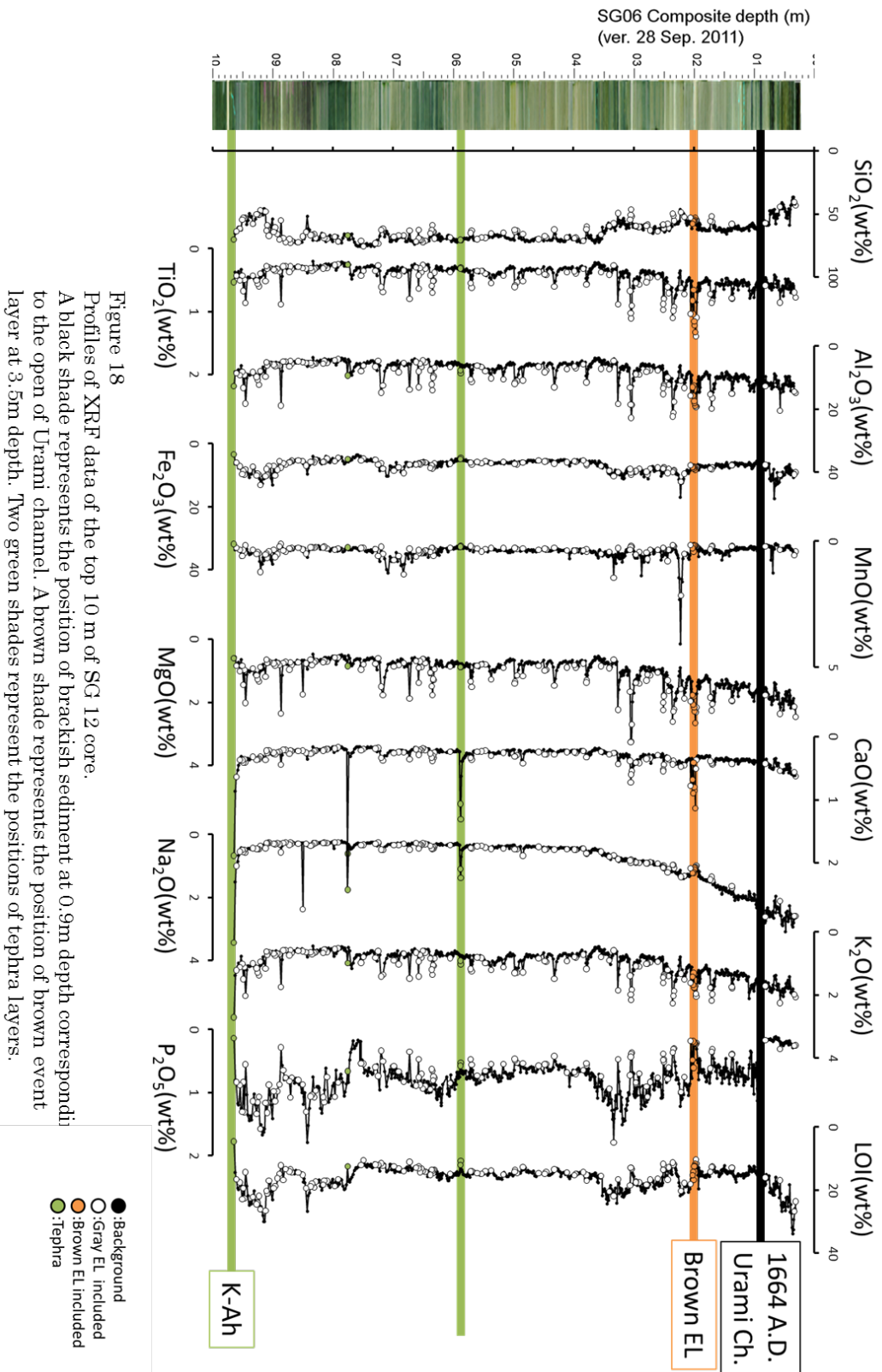
### 5-2-3. XRF analysis

XRF analysis was conducted on 711 core samples and 12 surface samples. The methods of pretreatment and measurement were the same as those described in Section 4-2.

## 5-3. Results

### 5-3-1. Results of XRF analysis

The results of XRF analysis of the top 10 m of the SG12 core are listed in Table S7. Depth profiles of elemental concentrations are shown in Figure 18, cross-plots of  $\text{Al}_2\text{O}_3$  versus other elements are shown in Figure 19, and the cross-correlation coefficients of 10 elements and loss on ignition (LOI) are listed in Table 6. On the basis of Figures 18 and 19 and the correlation coefficients listed in Table 6, I separated these 10 elements and LOI into three groups, namely, 1) an Si group ( $\text{SiO}_2$ ), 2) an Al group ( $\text{Al}_2\text{O}_3$ ,  $\text{TiO}_2$ ,



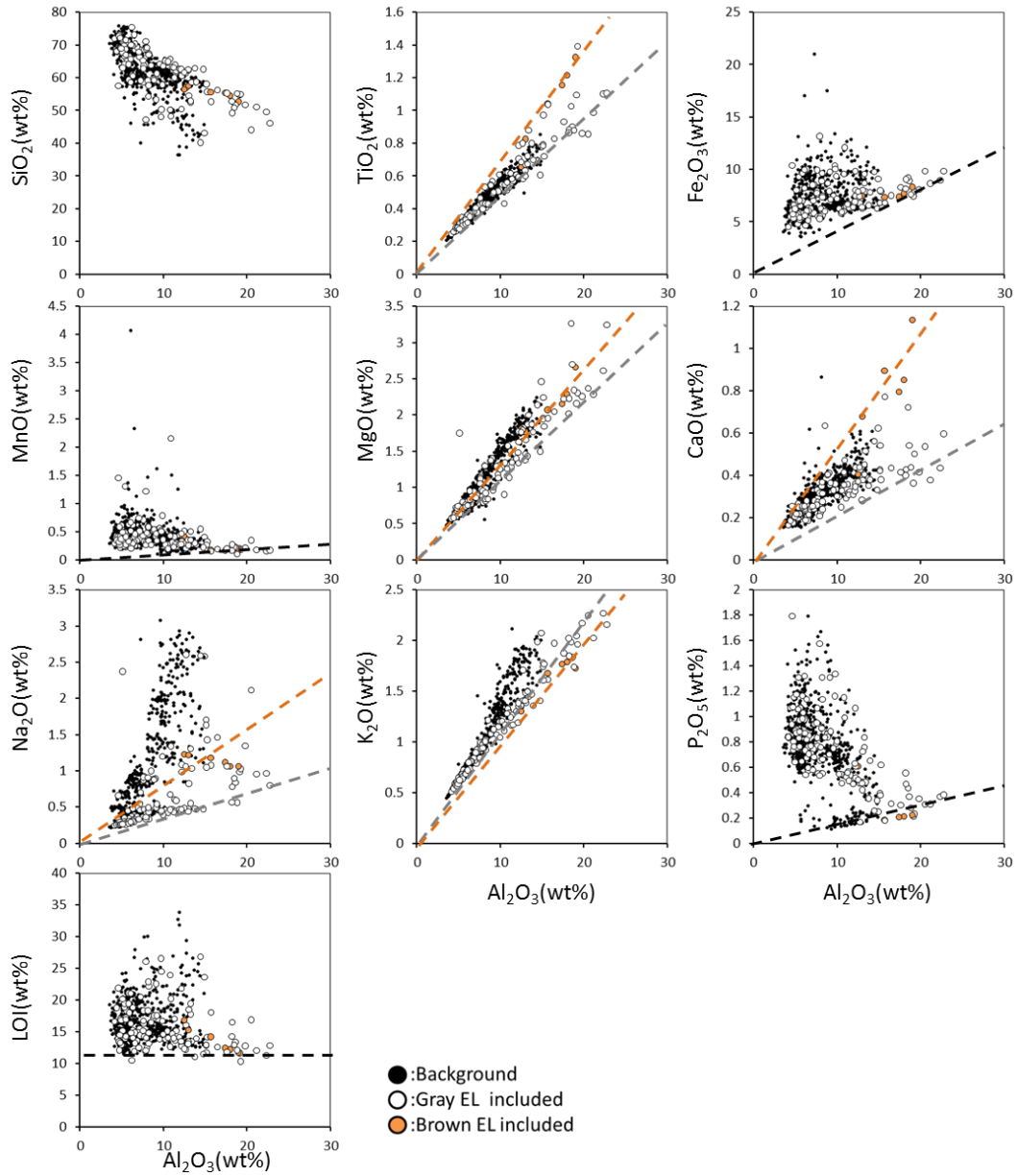


Figure 19  
 Cross plots of  $\text{Al}_2\text{O}_3$  (horizontal axis) content versus contents of other elements and LOI (vertical axis) of XRF data of SG12 core samples. Gray and brown dashed lines show gradients of composition of gray and brown event layers, respectively. Black dashed lines show lower envelope of gradients of Fe group.

Table 6 Correlation coefficients(R) of major elements measured by XRF data of SG12 core (n=715) and relative error of XRF measurement for each elements

	SiO <sub>2</sub>	TiO <sub>2</sub>	Al <sub>2</sub> O <sub>3</sub>	Fe <sub>2</sub> O <sub>3</sub>	MnO	MgO	CaO	Na <sub>2</sub> O	K <sub>2</sub> O	P <sub>2</sub> O <sub>5</sub>	LOI
SiO <sub>2</sub>	1.000										
TiO <sub>2</sub>	-0.645	1.000									
Al <sub>2</sub> O <sub>3</sub>	-0.684	0.961	1.000								
Fe <sub>2</sub> O <sub>3</sub>	-0.791	0.314	0.310	1.000							
MnO	-0.175	-0.171	-0.209	0.501	1.000						
MgO	-0.745	0.927	0.939	0.394	-0.169	1.000					
CaO	-0.499	0.559	0.600	0.234	-0.084	0.550	1.000				
Na <sub>2</sub> O	-0.665	0.568	0.629	0.339	-0.115	0.740	0.597	1.000			
K <sub>2</sub> O	-0.719	0.874	0.937	0.324	-0.212	0.916	0.666	0.821	1.000		
P <sub>2</sub> O <sub>5</sub>	0.120	-0.475	-0.538	0.180	0.425	-0.525	-0.341	-0.497	-0.597	1.000	
LOI	-0.672	-0.061	-0.026	0.603	0.267	0.086	0.061	0.233	0.060	0.311	1.000
Relative error (%)	0.07299	0.77838	0.23239	0.09207	0.43115	0.51856	0.93537	0.77733	0.54974	0.4636	

MgO, CaO, Na<sub>2</sub>O, and K<sub>2</sub>O), and 3) an Fe group (Fe<sub>2</sub>O<sub>3</sub>, MnO, P<sub>2</sub>O<sub>5</sub>, and LOD). I described the characteristics of these groups based on observations of their profiles and estimated the major carrier(s) of each element by taking into account the observations of sediment components described in Chapter 3.

1) Si group: In general, the SiO<sub>2</sub> content has a negative correlation with that of other elements and tends to be slightly lower in samples that contain event layers. Although SiO<sub>2</sub> is present in detrital material, the lower content of SiO<sub>2</sub> in event layers suggests that SiO<sub>2</sub> is largely in the form of diatom frustules, which are abundant in background sediments, as observed in smear slides.

2) Al group: It is obvious from Figure 18 that the Al group is present at higher levels in the samples containing event layers, and its members have high correlation coefficients with one another (Table 6; minimum value is R = 0.550 for MgO versus CaO and maximum value is R = 0.961 for Al<sub>2</sub>O<sub>3</sub> versus TiO<sub>2</sub>), which suggests that these elements are enriched in gray event layers. Because gray event layers are enriched with detrital material, these elements are considered to be predominantly present in detrital material. However, on the multi-meter scale, MgO, CaO, Na<sub>2</sub>O, and K<sub>2</sub>O display decreasing trends in background sediment from the top of the core downward to a depth of 3.5 m, which corresponds to ~2 ka (Figure 18). In particular, Na<sub>2</sub>O exhibits an exponentially decreasing curve down the core with a much greater amplitude than those of the peaks corresponding to event layers. Because these elements are present in seawater, and the top 90 cm of the core corresponds to the period when brackish water is intruded from Lake Kugushi, these background trends are interpreted as resulting from the intrusion of seawater into the bottom of Lake Suigetsu and its downward diffusion through the pore water. At a depth of 90 cm, there is a thick black layer containing a large amount of pyrite, which corresponds to the period of the inflow of seawater into Lake Suigetsu caused by the opening of the Urami channel in 1664 [Komatsubara, 2006]. Before 1664 A.D., there is no

historical evidence of the inflow of seawater to the lake bottom. Therefore, the decreasing trend in the Na<sub>2</sub>O content from 2–3% at a depth of 90 cm to 0.4–0.6% at 350 cm indicates that some Na of seawater origin was supplied by diffusion into the sediment below a depth of 90 cm.

On the x-y plots of the Al group in Figure 19, gray and brown dashed lines have been drawn to connect the plots of the pure gray and brown event layers with the origin (0, 0). In the plots of TiO<sub>2</sub> and CaO versus Al<sub>2</sub>O<sub>3</sub>, the core data are effectively scattered within a triangle and the two dashed lines correspond to envelope lines of the core data, which suggests that the detrital materials in the background sediments can be explained in terms of a mixture of the detrital materials in the gray and brown event layers, which are diluted by non-detrital components to various degrees. On the other hand, in the plots of MgO, Na<sub>2</sub>O, and K<sub>2</sub>O versus Al<sub>2</sub>O<sub>3</sub> the distributions of the core data are not enclosed by the two dashed lines, which suggests that the detrital materials present in the gray and brown event layers cannot explain the variations in these elements and that there should be additional contributions from other sources such as sea salt or eolian dust.

3) Fe group: Fe<sub>2</sub>O<sub>3</sub>, MnO, P<sub>2</sub>O<sub>5</sub>, and LOI have similar trends, with high values in the intervals of 2–3.5 m, 6.3–7.3 m, and 8.9–9.6 m. P<sub>2</sub>O<sub>5</sub> and LOI have another enriched interval at 7.8–8.7 m (Figure 18). In Figure 20, cross-plots of the Fe group are shown. The positive trends seen in all plots and smear slide observations of Fe-Mn oxide in Chapter 3 suggest that the elements in this group are present together in the form of Fe-Mn oxide and associated organic matter. Nevertheless, the correlation coefficient of Fe<sub>2</sub>O<sub>3</sub> and MnO is not so high ( $R = 0.501$ ), which indicates that the ratios of Fe, Mn, and organic matter may be variable, possibly in association with changes in bottom water conditions [Davis, 1982; Williams and Scherer, 2004]. On the x-y plots of Al<sub>2</sub>O<sub>3</sub> versus Fe<sub>2</sub>O<sub>3</sub>, MnO, and P<sub>2</sub>O<sub>5</sub> there seem to be minimum gradients with zero intercepts, and samples of the pure gray event layers are plotted on these gradients (black dashed lines in Figure 19). This observation suggests

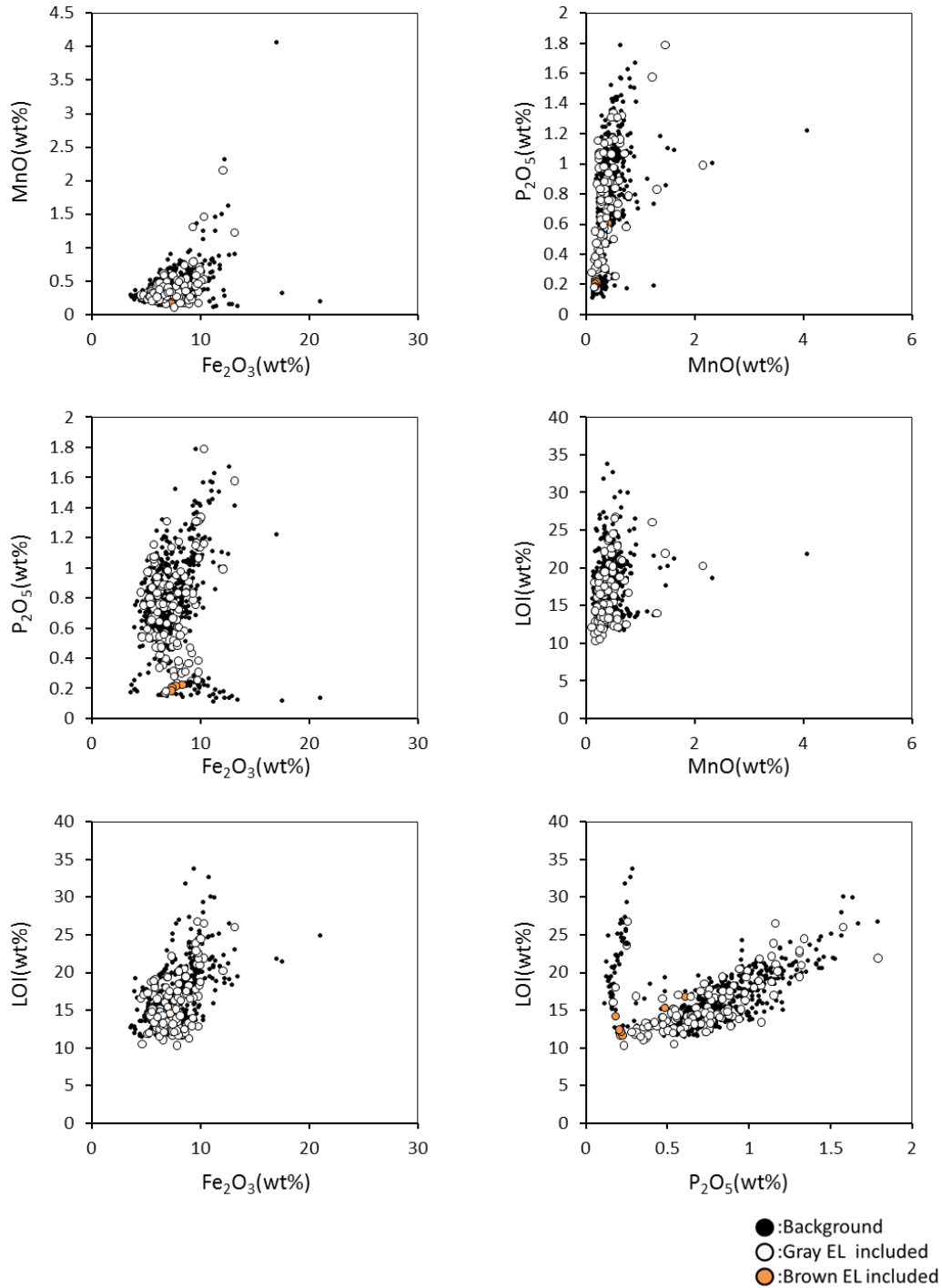


Figure 20  
 Cross plots of Fe-group of XRF data of SG12 core samples.  
 Three elements and LOI have positive relationships with each other.

that these elements are also present in the pure gray event layers, of which the major component is detrital material, and the content of these elements in detrital material could be estimated on the basis of the minimum gradients.  $P_2O_5$  levels are much lower in the top 90 cm than in the interval below, which suggests the effect of the intrusion of brackish water and subsequent changes in bottom water conditions.

### **5-3-2. Results of water content (WC) and DBD measurements**

The results of measurements of water content (WC) and DBD and calculations of GD are shown in Figure 21 and Table S5. LSR values are also shown in Figure 21. Basically, WC and DBD display opposing trends. On the centimeter to decimeter scale, DBD (WC) has high (low) values in samples containing event layers that contain a large amount of detrital material with higher density and lower porosity than other components of the sediment. On the meter scale, DBD displays increasing trends in the intervals of 0.3–2.0 m and 7.6–8.9 m and a decreasing trend in the interval of 2.0–3.5 m. DBD exhibits a discontinuous rise from 0.2–0.23 g/cm<sup>3</sup> to 0.28–0.32 g/cm<sup>3</sup> at a depth of 3.5 m. WC displays opposing trends to those of DBD, with decreasing trends in the intervals of 0.3–2.0 m and 7.6–8.9 m and an increasing trend in the interval of 2.0–3.5 m. WC exhibits a discontinuous decline from 80–85% to 72–75% at a depth of 3.5 m. GD tends to have constant values of between 1.5 and 2.0 g/cm<sup>3</sup> and higher values (2.0–2.5 g/cm<sup>3</sup>) in the samples that include event layers. As there is no distinct change in GD at a depth of 3.5 m, the stepwise change in DBD at a depth of 3.5 m is caused by a change in the content of pore water.

### **5-4. Q-mode factor analysis**

QFA was conducted for the elements  $TiO_2$ ,  $Al_2O_3$ ,  $MgO$ ,  $CaO$ ,  $Na_2O$ , and  $K_2O$ , which were analyzed by XRF and are only present in the detrital component of the sediment of Lake Suigetsu. For QFA, I used XRF data of these elements, which is normalized by their total values, for samples from depths of 350–1000 cm. Here this dataset is referred to as DetXRF data. On

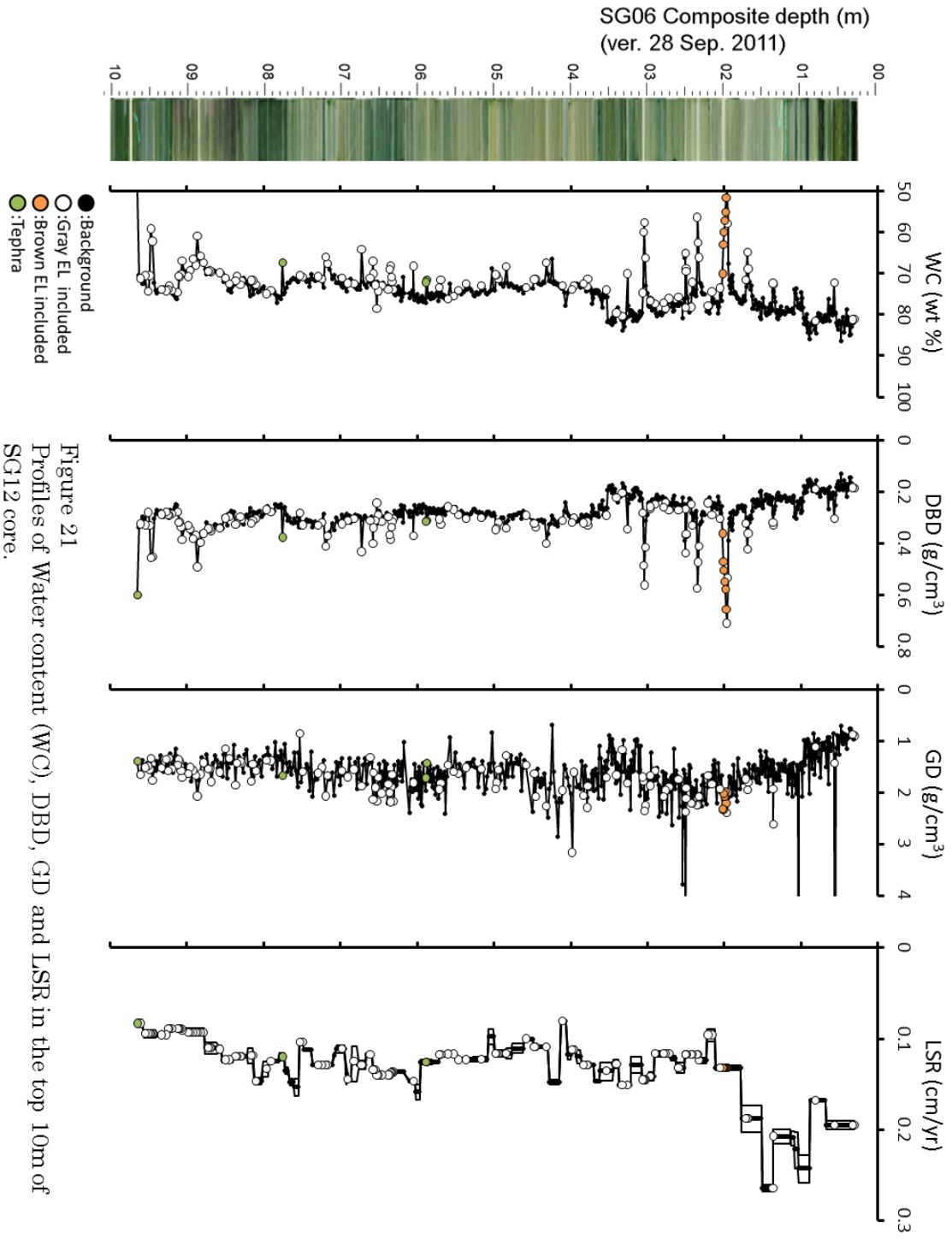


Figure 21  
Profiles of Water content (WC), DBD, GD and LSR in the top 10m of SG12 core.

the basis of the observation of sediment particles in smear slides, the sediment of Lake Suigetsu contains diatom frustules (rich in SiO<sub>2</sub> and LOI), Fe-Mn oxide (enriched in Fe<sub>2</sub>O<sub>3</sub>, MnO, P<sub>2</sub>O<sub>5</sub>, and LOI), and organic material (enriched in P<sub>2</sub>O<sub>5</sub> and LOI), together with detrital material (enriched in TiO<sub>2</sub>, Al<sub>2</sub>O<sub>3</sub>, MgO, CaO, Na<sub>2</sub>O, and K<sub>2</sub>O). I excluded the other elements, quantified TiO<sub>2</sub>, Al<sub>2</sub>O<sub>3</sub>, MgO, CaO, Na<sub>2</sub>O, and K<sub>2</sub>O by normalizing the sum of these six elements to 100%, and conducted QFA to determine the EMs of detrital materials. On the basis of observations of the depth profiles of DBD and XRF results, samples from the top 3.5 m of the composite column were not used for QFA because these samples are subject to the influence of sea salt diffused from the lake bottom into the sediment. QFA was conducted based on previous procedures [*Klovan and Imbrie, 1971; Klovan and Miesch, 1976; Walden et al., 1992; Irino and Tada, 2000*]. The minimum number of EMs and their chemical compositions and contents can be determined by QFA. In QFA, the composition loading matrix A and the composition score matrix F can be obtained from the sample data matrix (S) by equation (14):

$$\begin{aligned}
 S &= AF = \begin{pmatrix} a_{11} & \cdots & a_{1n} \\ \vdots & \ddots & \vdots \\ a_{l1} & \cdots & a_{ln} \end{pmatrix} \begin{pmatrix} f_{11} & \cdots & f_{1m} \\ \vdots & \ddots & \vdots \\ f_{n1} & \cdots & f_{nm} \end{pmatrix} \\
 &= \begin{pmatrix} a_{11} & \cdots & a_{1n} \\ \vdots & \ddots & \vdots \\ a_{l1} & \cdots & a_{ln} \end{pmatrix} \begin{pmatrix} \vec{f}_1 \\ \vdots \\ \vec{f}_n \end{pmatrix} \quad (14)
 \end{aligned}$$

where S is an  $l \times m$  matrix composed of matrix elements of the form  $s_{ik}$ , which represents the concentration of the  $k^{\text{th}}$  element in the  $i^{\text{th}}$  sample, A is an  $l \times n$  matrix composed of matrix elements  $a_{ij}$ , which represents the content of the  $j^{\text{th}}$  EM in the  $i^{\text{th}}$  sample, and F is an  $n \times m$  matrix composed of matrix elements  $f_{jk}$ , which represents the concentration of the  $k^{\text{th}}$  element in the  $j^{\text{th}}$  EM. The  $m$ -dimensional row vector  $f_j$  is a reference vector and refers to the elemental composition of the  $j^{\text{th}}$  EM.

As the first step of QFA, the number of EMs ( $n$ ) is determined by increasing

the number of EMs until more than 99.0% of the total variance can be explained. A threshold value of 99% is selected because a residual after QFA of less than 1% is equal to the maximum relative error of XRF measurements (Table 6: 0.94% for CaO). A normalized data matrix S' is used to estimate the number of EMs. The data matrix (S) is normalized to S' so that the maximum and minimum values of each element would take values of 1 and 0, respectively. S' is normalized again to a matrix S'' using the vector length of each sample. The normalization steps can be written as equation (15) using an n-dimensional matrix N' and an l-dimensional matrix N'' corresponding to the first and second step of normalization, respectively.

$$S'' = N'' S' = N'' S N' \quad (15)$$

After normalization, the eigenvalues of S'' ( $e_1, e_2 \dots e_m$ ) and the corresponding eigenvectors are calculated. If the number of EMs is set at n, the percentage of the data explained by QFA in the total variance of the data (V) (%) is defined by equation (16):

$$V = (\sum_{i=1}^n e_i) / (\sum_{i=1}^m e_i) \times 100 \quad (e_i \geq e_{i+1}) \quad (16)$$

where  $e_i$  is the  $i^{\text{th}}$  largest eigenvalue of S''.

After determination of the number of EMs, the composition loading (content of EMs) matrix A and the composition score (chemical composition of EMs) matrix F are calculated using equations (17) and (18):

$$F = \begin{pmatrix} f_{11} & \cdots & f_{1m} \\ \vdots & \ddots & \vdots \\ f_{n1} & \cdots & f_{nm} \end{pmatrix} = \begin{pmatrix} e_{11} & \cdots & e_{1m} \\ \vdots & \ddots & \vdots \\ e_{n1} & \cdots & e_{nm} \end{pmatrix} N' \quad (17)$$

$$A = A F F^T (F F^T)^{-1} = S F^T (F F^T)^{-1} \quad (18)$$

where  $e_{jk}$  represents the value of the  $k^{\text{th}}$  element in the  $j^{\text{th}}$  eigenvector corresponding to the  $j^{\text{th}}$  largest eigenvalue.

As the second step, the chemical compositions and contents of the EMs are determined by oblique rotation of compositional vectors of factors [Leinen and Pisiyas, 1984]. The oblique rotation matrix can be written in the form of

an n-dimensional matrix  $R$ , and the composition loading matrix  $A'$  and composition score matrix  $F'$  after oblique rotation can be obtained by equations (19) and (20):

$$A' = A R \quad (19)$$

$$F' = R^{-1} F \quad (20)$$

For the oblique rotation, I set the constraints that the contents of the EMs and the elemental composition of each EM must be in the range of 0–100% and that the total value of the elements in each EM must be 100% to ensure realistic values. Within these constraints, there could still be multiple solutions for the chemical compositions and mixing ratios of EMs. Here, I show two cases of solutions of QFA, which are denoted as cases A and B.

Case A: the minimum value of EM contents in samples is maximized.

Case B: the maximum value of the content of each EM in samples is maximized, which means that the chemical composition of the EMs approaches the centroid of the DetXRF data.

As a result of QFA, it was revealed that three or four EMs can explain more than 99.0% of the total variance of the DetXRF data (Figure 22). The DetXRF data and the chemical compositions of four EMs before oblique rotation are shown in Figure 23. Before oblique rotation, the chemical composition of EM1 (black triangle) is plotted at the centroid of the DetXRF data. After oblique rotation, the chemical compositions of the four EMs are plotted surrounding the DetXRF data in all plots. Typical chemical compositions of the four EMs after oblique rotation corresponding to cases A and B described above are shown in Figure 24 and listed in Table 7. Because QFA cannot provide unique solutions for the compositions of EMs, these values lie within certain ranges. Here, the chemical compositions of the four EMs corresponding to cases A and B are shown in Figure 24, but the actual values of the chemical compositions of the four EMs would lie between the values for these cases. The ranges of the chemical compositions of the four EMs corresponding to cases A and B are shown in Figure 24, together with

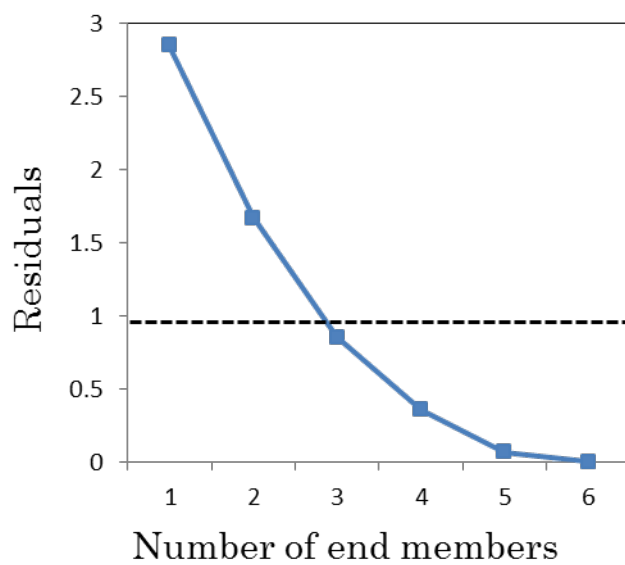


Figure 22  
Change of residuals of DetXRF data after QFA-adopted with increase of the number of end members. Residuals get lower than 1.5% when we put 3 end members, meaning that 3 EMs can explain 98.5% of total variance of DetXRF data.

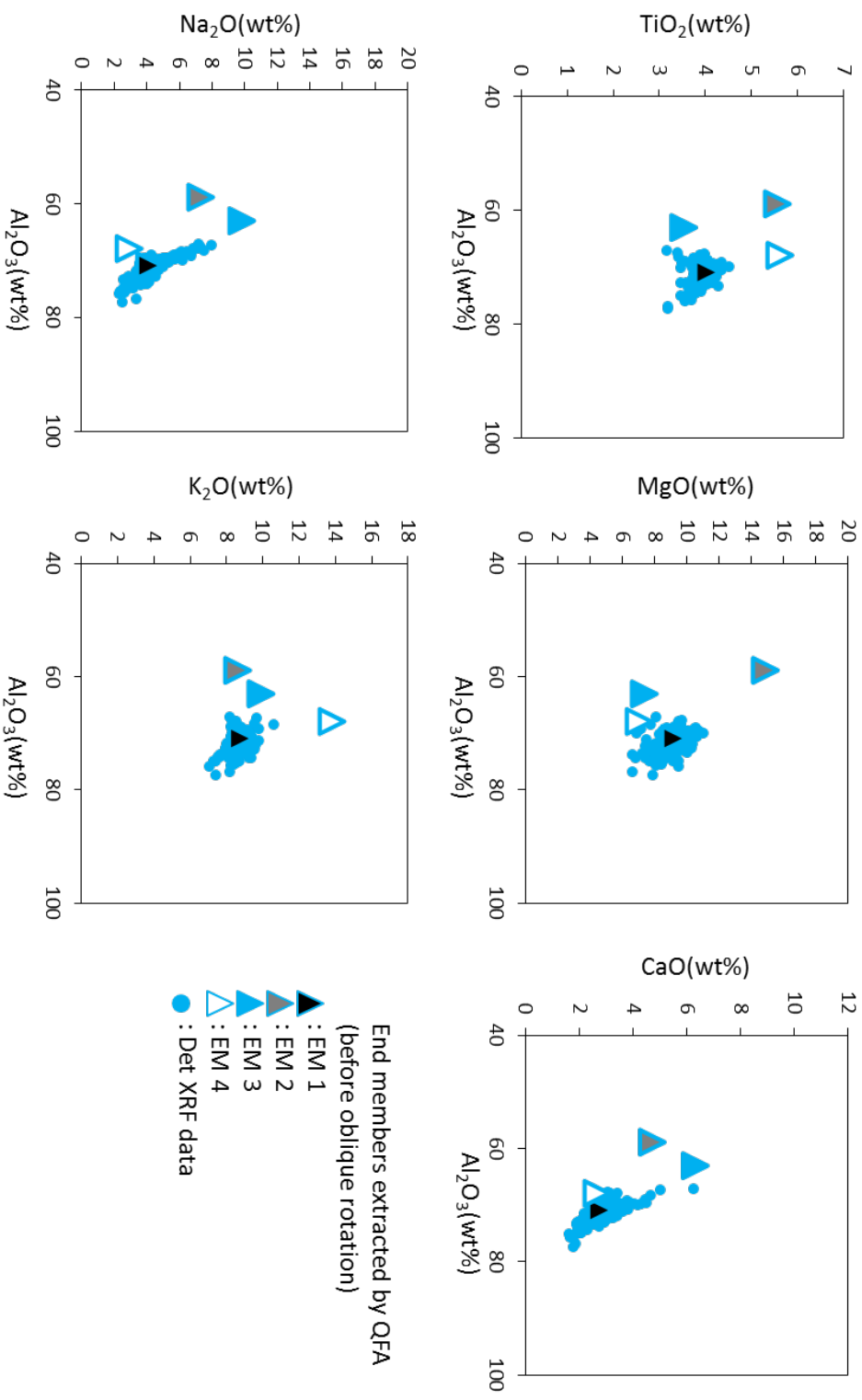


Figure 23  
Result of QFA showing DetXRF data (blue circles) and Extracted end members (triangles) before oblique rotation.

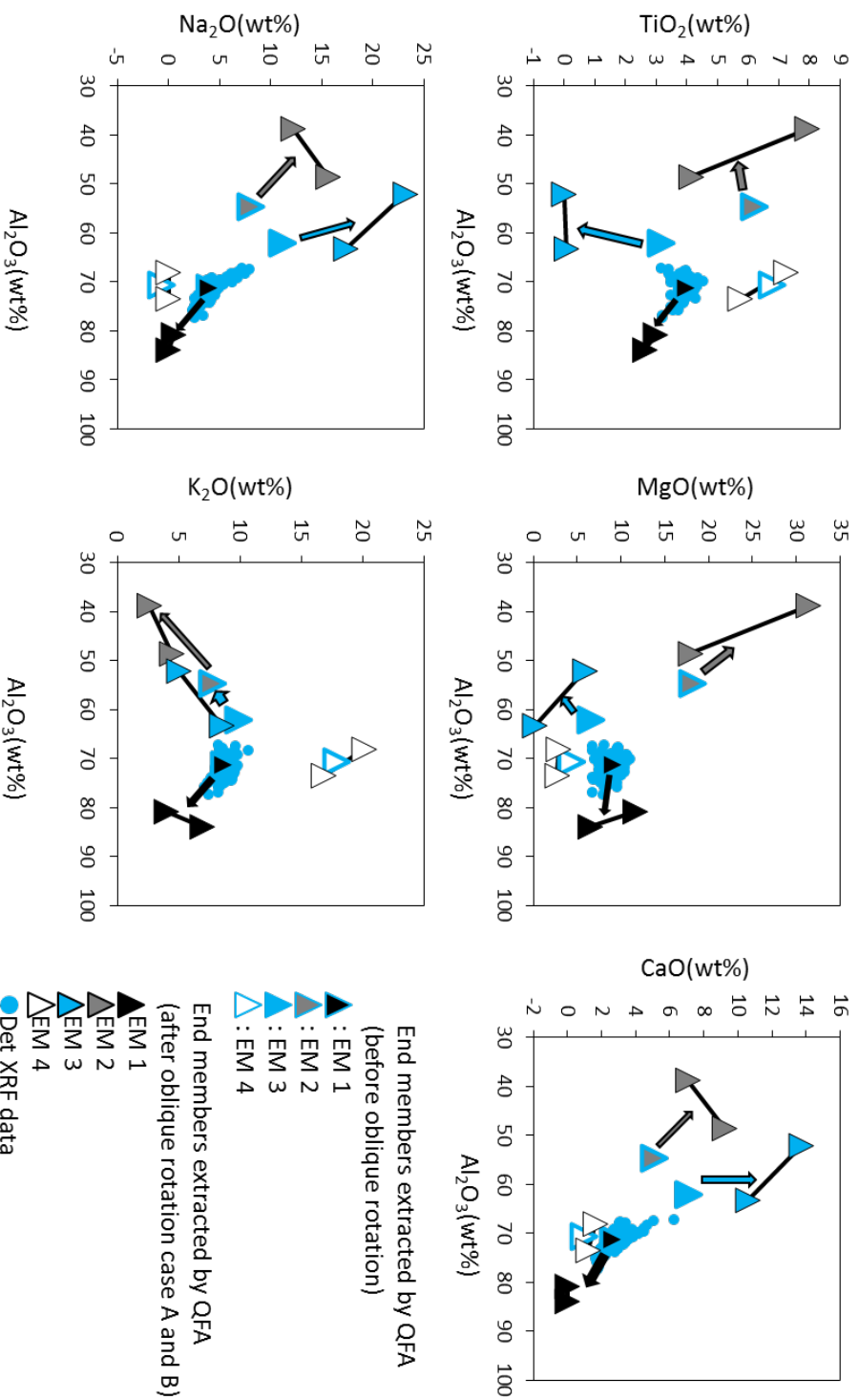


Figure 24

Result of QFA showing DetXRF data (blue circles) and Extracted end members (triangles) before oblique rotation(blue borders) and after oblique rotation(black borders). Det XRF data is surrounded by 4 EMs after oblique rotation (case A and B) meaning that content of each EM in each sample takes the value within the range of 0-100 wt% in both cases.

Table 7 Typical chemical compositions (wt %) of four EMs extracted by QFA

		TiO <sub>2</sub>	Al <sub>2</sub> O <sub>3</sub>	MgO	CaO	Na <sub>2</sub> O	K <sub>2</sub> O
Case A	EM1	2.64	83.90	6.53	0.00	0.00	6.93
	EM2	7.93	38.76	31.40	7.08	12.21	2.62
	EM3	0.00	52.12	5.93	13.73	23.19	5.03
	EM4	7.24	68.08	2.88	1.66	0.00	20.13
Case B	EM1	2.98	80.81	11.66	0.00	0.53	4.01
	EM2	4.15	48.59	17.95	9.23	15.62	4.45
	EM3	0.08	63.25	0.19	10.60	17.36	8.53
	EM4	5.75	73.45	2.74	1.23	0.00	16.83

the chemical compositions of the core samples, which are subdivided into pure background, pure gray event layers, and a pure brown event layer.

The chemical composition of EM1 is characterized by an  $\text{Al}_2\text{O}_3$  content of up to ~80%, which is the highest of the four EMs, and low contents of  $\text{TiO}_2$  (2–3%),  $\text{CaO}$  (~0%),  $\text{Na}_2\text{O}$  (~0%), and  $\text{K}_2\text{O}$  (4–7%). The chemical composition of EM2 is characterized by the highest content of  $\text{MgO}$  (17–30%) among the four EMs. The contents of  $\text{CaO}$  (7–9%) and  $\text{Na}_2\text{O}$  (12–16%) are also high but that of  $\text{K}_2\text{O}$  (4–7%) is low. The chemical composition of EM3 is characterized by the highest contents of  $\text{CaO}$  (10–14%) and  $\text{Na}_2\text{O}$  (17–23%) and the lowest contents of  $\text{TiO}_2$  (~0%) and  $\text{MgO}$  (0–6%) among the four EMs. EM4 has the highest contents of  $\text{TiO}_2$  (5–7%) and  $\text{K}_2\text{O}$  (16–20%) and the lowest content of  $\text{Na}_2\text{O}$  (~0%) among the four EMs.

I compared the chemical compositions of these four EMs in case B with those of surface detrital material sampled in the drainage area and an eolian dust sample, which are considered to be potential sources of the detrital material in Lake Suigetsu. For comparison, the chemical compositions of the core samples representing pure background, gray event layers, and a brown event layer were also plotted with those of the EMs. By a comparison of the chemical compositions of the EMs with those of potential sources, I estimated the source and composition of each EM. In the x-y plots shown in Figure 25, the chemical compositions of the four EMs (triangles), core samples from three lithofacies (circles), and the centroid of the DetXRF data (red cross) are plotted. In Figure 25, the background samples are essentially plotted on a mixing line of the gray and brown event layers except for  $\text{MgO}$  and  $\text{K}_2\text{O}$ . This indicates that the detrital material in background sediment is a mixture of the detrital material in the gray and brown event layers. The exceptions in the cases of  $\text{MgO}$  and  $\text{K}_2\text{O}$  indicate other sources of the detrital material in background sediment such as eolian dust.

#### **5-4-1. Provenance of EM1**

The chemical composition of EM1 (black triangle) is plotted on the mixing line between background sediment and gray event layers (Figure 25). When

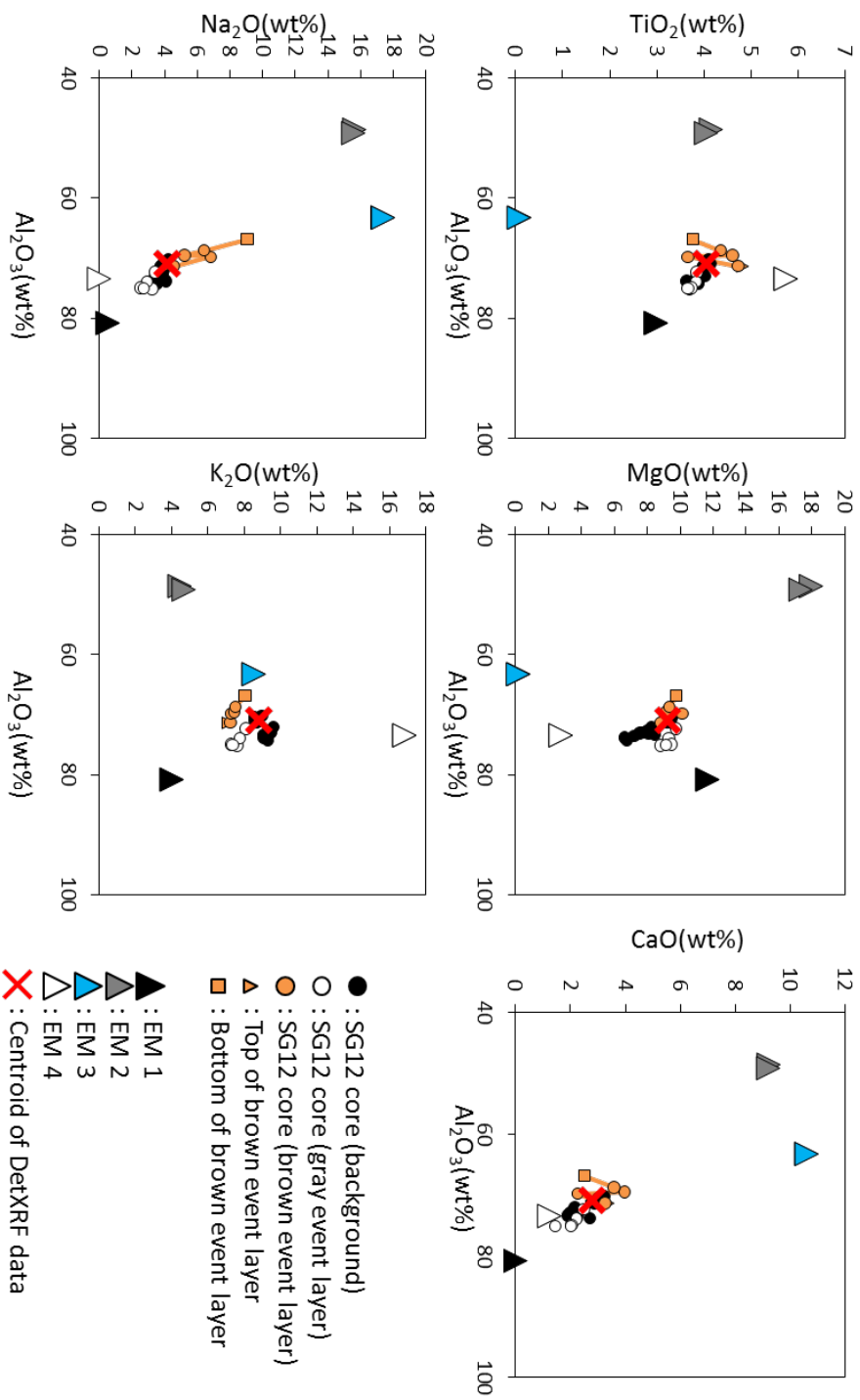


Figure 25

End members of QFA after oblique rotation (triangles with black bordering) are plotted with typical chemical composition of sediment types shown in black(background), white (gray event layer) and brown (brown event layers) colors. Centroid of DetXRF data is shown as a red cross.

we plot the data for surface detrital material finer than 4  $\mu\text{m}$  sampled from the drainage area of Lake Mikata (corresponding to the grain size of suspended particles passing through Lake Mikata on the basis of estimations described in Section 2-4), background samples, and gray event layers, together with EM1, they fall close to one another and the data for surface detrital samples effectively extend from the centroid toward those for EM1 (Figure 26). Therefore, EM1 is interpreted as representing suspended detrital particles of less than 4  $\mu\text{m}$  in diameter supplied from rivers in the drainage area of Lake Mikata.

#### **5-4-2. Provenance of EM2**

As observed in Figure 25, the chemical composition of EM2 (gray triangle) is characterized by its high contents of MgO, CaO, and Na<sub>2</sub>O and low content of Al<sub>2</sub>O<sub>3</sub>. These characteristics suggest that the provenance of EM2 is relatively coarse material such as eolian dust or coarse detrital material from the drainage area of Lake Suigetsu. As eolian dust, which originated from the Asian continent, is relatively poor in MgO, coarse detrital material from the drainage area of Lake Suigetsu can be expected to be the provenance of EM2. To confirm this estimate, fractions of 16–64  $\mu\text{m}$  from the drainage area of Lake Suigetsu are plotted in Figure 27 (green squares). As the general characteristics of EM2 relative to the DetXRF centroid match those of the green squares in Figure 27, EM2 is interpreted as representing coarse detrital material from the slopes surrounding Lake Suigetsu.

#### **5-4-3. Provenance of EM3**

As observed in Figure 25, the chemical composition of EM3 (blue triangle) is characterized by its low contents of Al<sub>2</sub>O<sub>3</sub>, TiO<sub>2</sub>, and MgO and high contents of CaO and Na<sub>2</sub>O. As its low Al<sub>2</sub>O<sub>3</sub> content suggests that EM3 is coarse material, I compared the chemical composition of EM3 with those of eolian dust samples measured in this study (one sample, measured by XRF) and those measured by Inoue and Naruse (1987) (eight samples, calculated on the basis of chemical treatment) (Figure 28). The general trends of the data for EM3 and eolian dust relative to the DetXRF centroid are in accordance

with each other, although the contents of  $\text{TiO}_2$  and  $\text{MgO}$  in EM3 are too low. Therefore, EM3 is interpreted as representing the contribution of eolian dust.

#### **5-4-4. Provenance of EM4**

As observed in Figure 25, the chemical composition of EM4 (white triangle) is characterized by its high contents of  $\text{Al}_2\text{O}_3$ ,  $\text{TiO}_2$ , and  $\text{K}_2\text{O}$  and low contents of  $\text{MgO}$ ,  $\text{CaO}$ , and  $\text{Na}_2\text{O}$ . As the residual provenance of detrital material is fine-grained particles from Lake Suigetsu and the characteristics of EM4 suggest fine-grained detrital material, I compared the chemical composition of EM4 with that of the fraction of  $<4 \mu\text{m}$  in samples taken from the drainage area of Lake Suigetsu (green squares in Figure 29). Although the green squares show a large variance in the  $\text{TiO}_2$ ,  $\text{MgO}$ , and  $\text{K}_2\text{O}$  contents, the characteristics of a high  $\text{Al}_2\text{O}_3$  content and low  $\text{CaO}$  and  $\text{Na}_2\text{O}$  contents are in accordance with those of EM4. Figure 30 shows the vertical change in the grain size distribution of detrital material in the brown event layer seen at a depth of 3.5 m, which shows normal grading. With respect to the vertical change in the brown event layer in Figure 29 (orange square to orange triangle), normal grading tends to correspond to the shift in the orange plot from near EM2 (lower  $\text{Al}_2\text{O}_3$  content) toward EM4 (higher  $\text{Al}_2\text{O}_3$  and  $\text{TiO}_2$  contents and lower  $\text{MgO}$  and  $\text{Na}_2\text{O}$  contents). Therefore, EM4 is interpreted as representing fine-grained detrital material from the drainage area of Lake Suigetsu.

#### **5-5. Multiple regression analysis**

To reconstruct the flux of EM1, it is necessary to specify the composition of EM1 in the bulk sediment and multiply its content by its mass accumulation rate (MAR). I estimated the chemical compositions of diatom frustules, organic material, sea salt, Fe-Mn oxide, and detrital materials (fine detrital particles from the drainage area of Lake Mikata, coarse and fine detrital particles from the drainage area of Lake Suigetsu, and eolian dust with a particle size of  $\sim 10 \mu\text{m}$  from the Asian continent), which are considered to be

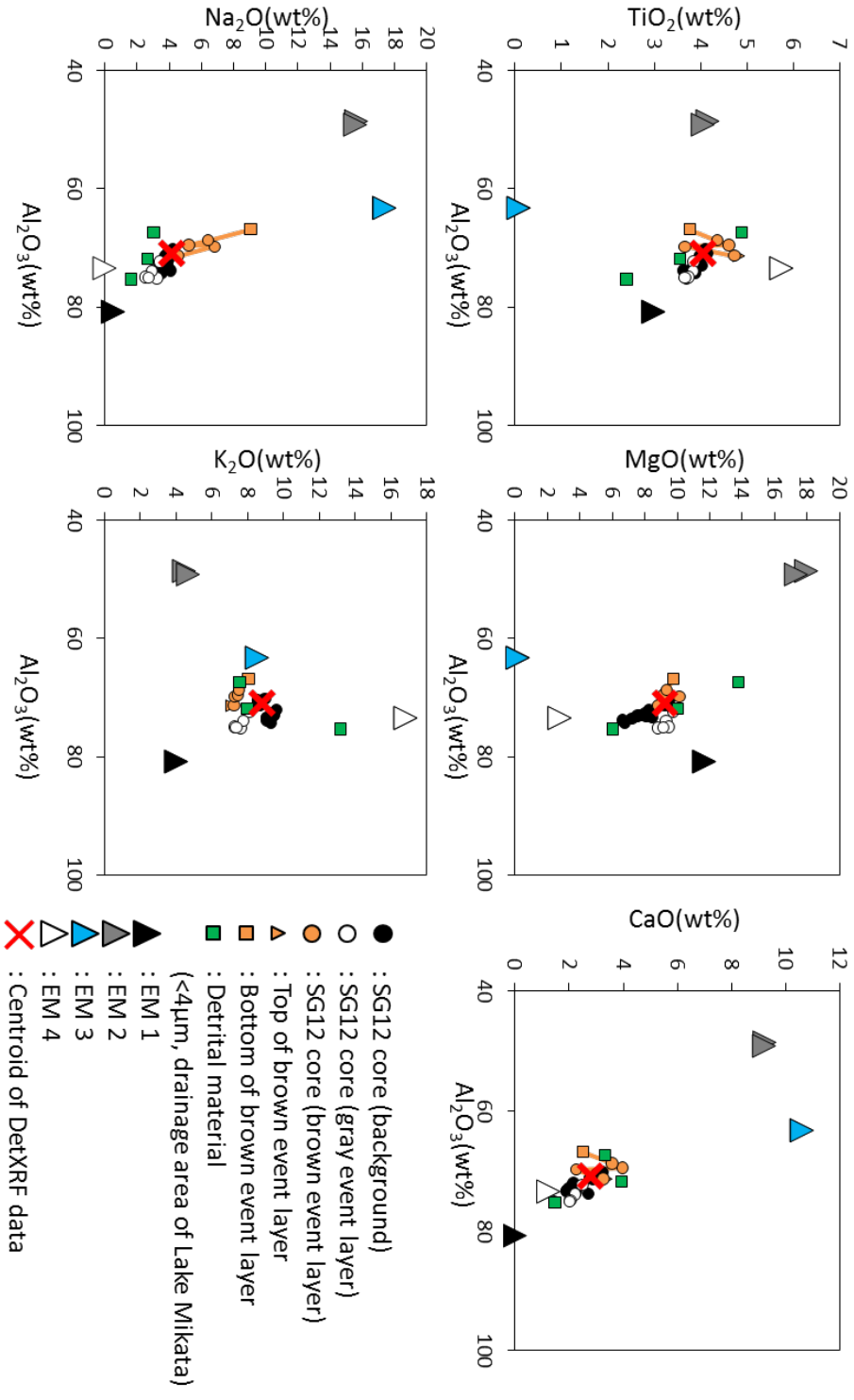


Figure 26  
 Detrital material from the drainage area of Lake Mikata (<4 $\mu\text{m}$  fraction: green square) is plotted on Figure 25.

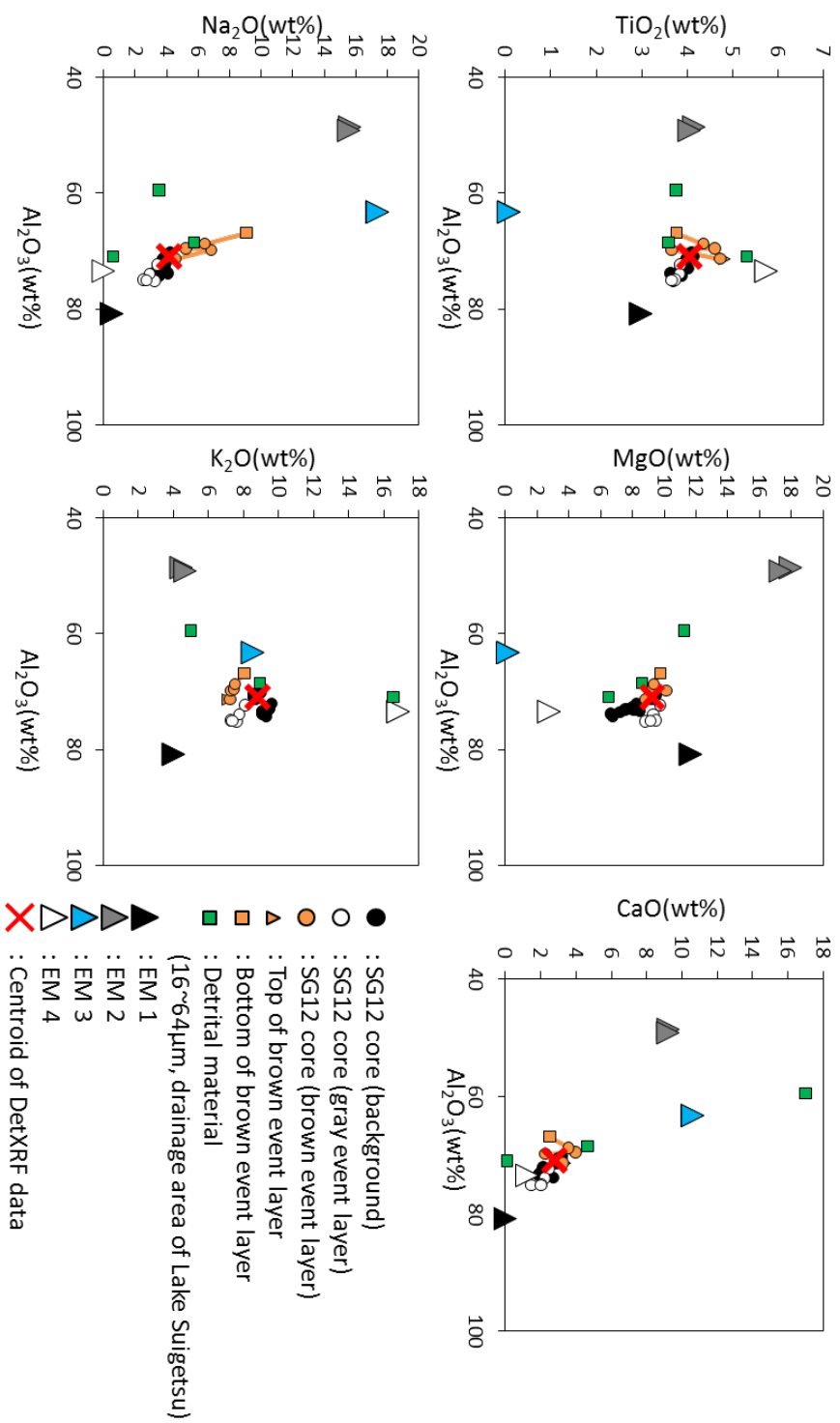


Figure 27  
Detrital material from the drainage area of Lake Suigetsu (16~64µm fraction: green square) is plotted on Figure 25.

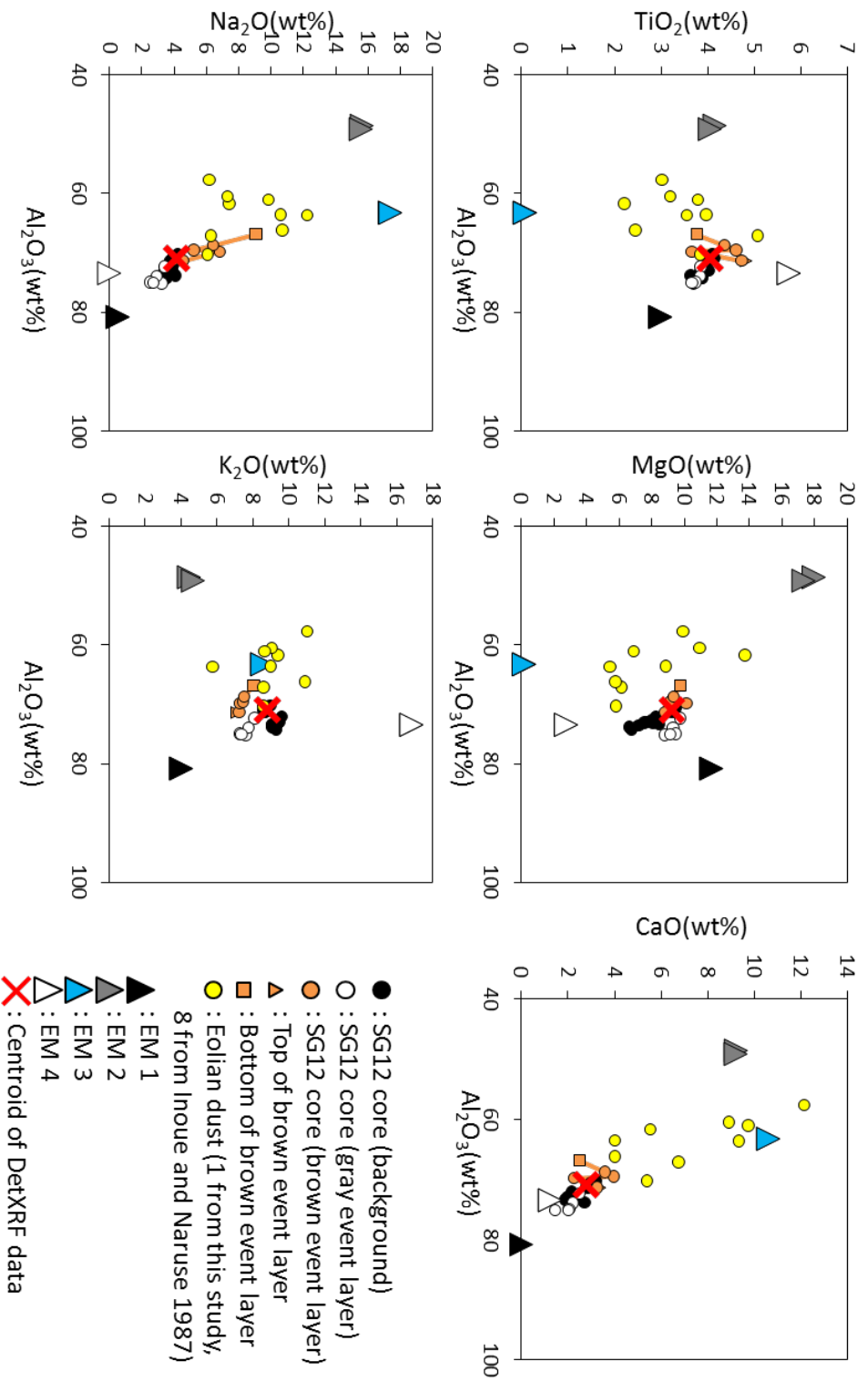


Figure 28  
Eolian dust data (yellow circle) is plotted on Figure 25.

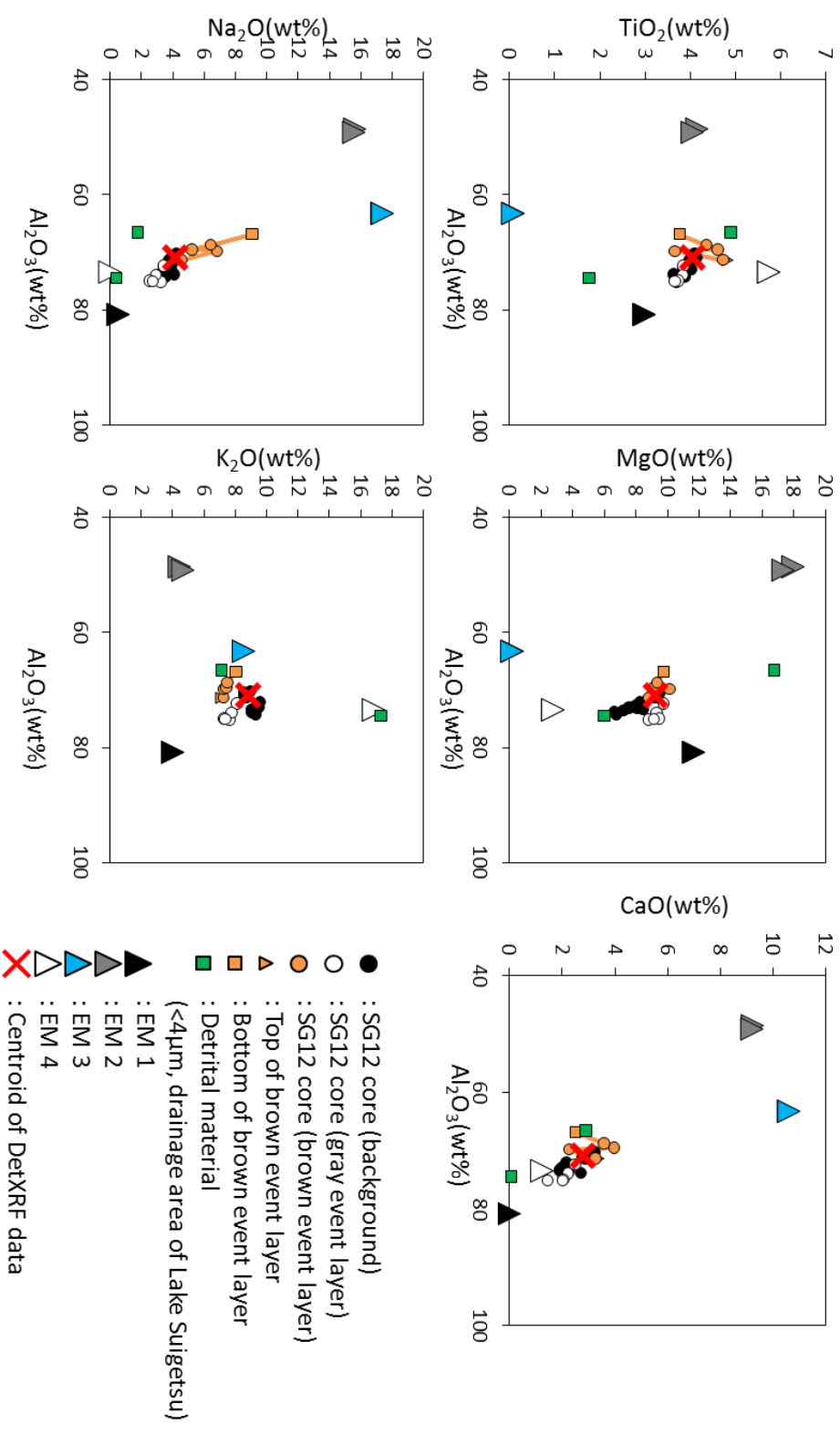


Figure 29  
Detrital material from the drainage area of Lake Suigetsu (<4 $\mu\text{m}$  fraction: green square) is plotted on Figure 25.

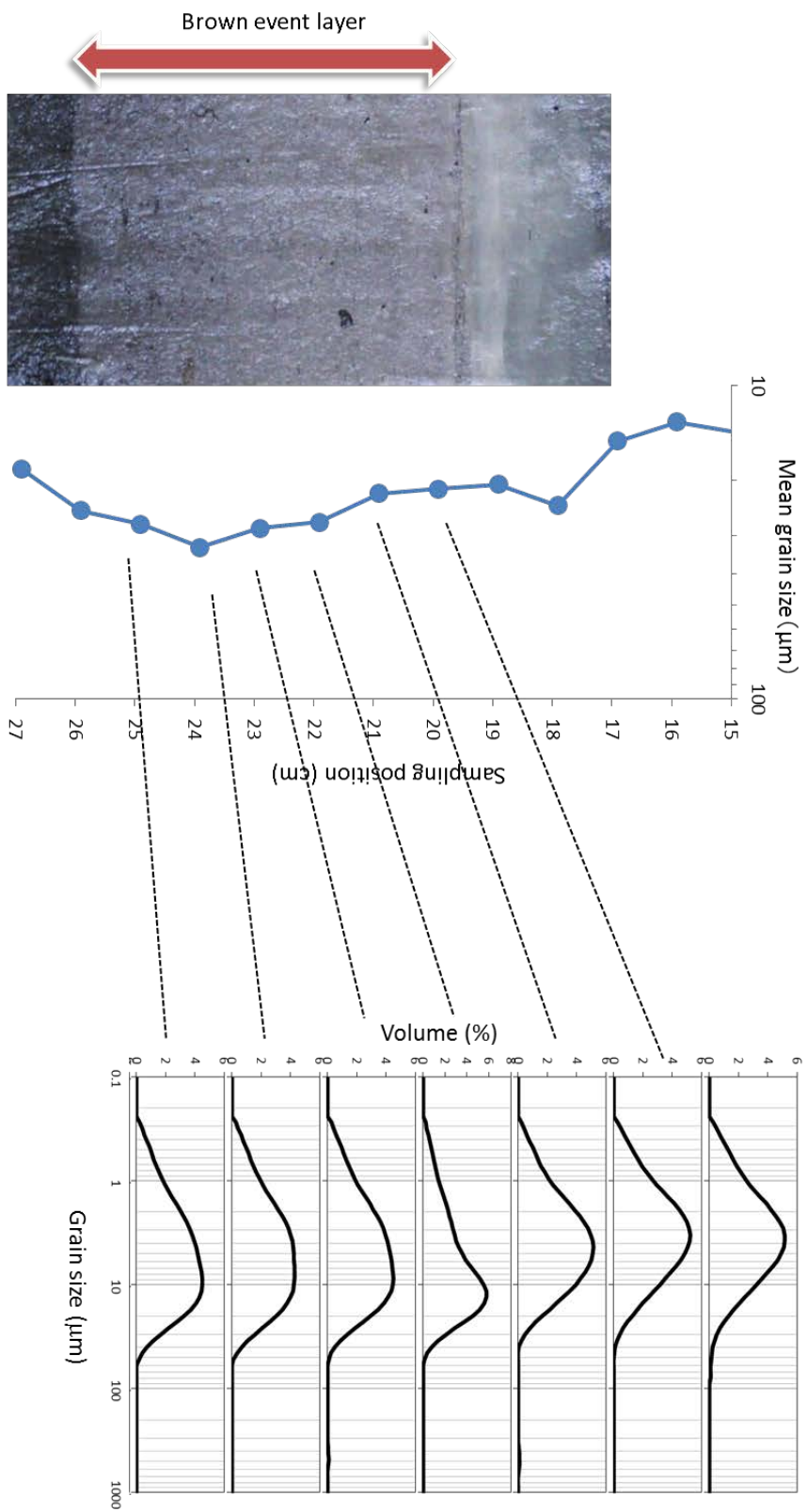


Figure 30  
Vertical change in grain size distribution of detrital material in brown event layer at 3.5m depth.

major detrital components of Lake Suigetsu sediment on the basis of observations of smear slides described in Chapter 3. MRA was conducted to estimate the contents of these materials in each sample using the following equations (21) and (22):

$$S = AF = \begin{pmatrix} a_{11} & \cdots & a_{1n} \\ \vdots & \ddots & \vdots \\ a_{l1} & \cdots & a_{ln} \end{pmatrix} \begin{pmatrix} f_{11} & \cdots & f_{1m} \\ \vdots & \ddots & \vdots \\ f_{n1} & \cdots & f_{nm} \end{pmatrix} \quad (21)$$

$$A = AFF^T (FF^T)^{-1} = SF^T (FF^T)^{-1} \quad (22)$$

where S is an  $l \times m$  matrix composed of matrix elements  $s_{ik}$ , which represents the concentration of the  $k^{\text{th}}$  element in the  $i^{\text{th}}$  sample, A is an  $l \times n$  matrix composed of matrix elements  $a_{ij}$ , which represents the content of the  $j^{\text{th}}$  sediment component in the  $i^{\text{th}}$  sample, and F is an  $n \times m$  matrix composed of matrix elements  $f_{jk}$ , which represents the concentration of the  $k^{\text{th}}$  element in the  $j^{\text{th}}$  sediment component. For this MRA, the chemical composition of each component (matrix element in F) is estimated on the basis of the following reasoning.

(1) Diatom frustules: Because the chemical composition of diatom frustules is generally in the range of  $\text{SiO}_2 = 85\text{--}90\%$  and  $\text{LOI} = 10\text{--}15\%$  [*Kamatani and Oku, 2000*], in the x-y plot of  $\text{SiO}_2$  versus  $\text{Al}_2\text{O}_3$  shown in Figure 31A the dashed line indicates a mixing line between diatom frustules ( $\text{SiO}_2, \text{Al}_2\text{O}_3 = 85, 0$ ) and pure gray event layers ( $\text{SiO}_2, \text{Al}_2\text{O}_3 = \sim 45, \sim 24$ ), which are mostly composed of fine detrital material. Because the upper envelope of data plots of the core samples is in accordance with the mixing line of diatom frustules (assumed) and gray event layers, I assumed that the  $\text{SiO}_2$  and LOI contents of diatom frustules are 85% and 15%, respectively.

(2) Organic material: The major elements that constitute organic material are P, C, H, O, and N, among which C, H, O, and N are assumed to be present in LOI and P as  $\text{P}_2\text{O}_5$ . To estimate the ratio of  $\text{P}_2\text{O}_5$  to LOI in organic material in the sediment from Lake Suigetsu, the chemical composition of terrestrial organic materials compiled by McGroddy et al. (2004) was used.

Assuming that the molar ratio of C:N:P in terrestrial organic material is 922:26:1 and C, H, and O are present as CH<sub>2</sub>O in organic material, the mixing ratio of P<sub>2</sub>O<sub>5</sub> and LOI as a weight fraction is estimated to be 395:1. A cross-plot of P<sub>2</sub>O<sub>5</sub> versus LOI (Figure 31E) shows an upper envelope with a gradient equal to this estimate.

(3) Sea salt: As described in Section 5-3-1, brackish water at the bottom of Lake Suigetsu has diffused into the sediment to a depth of ~3.5 m. The major elements that constitute sea salt are assumed to be the same as the mean composition of seawater, which is (MgO, CaO, Na<sub>2</sub>O, K<sub>2</sub>O) = (11.8, 2.9, 82.7, 2.6) (wt%) (<http://www.seafriends.org.nz/oceano/seawater.htm>).

(4) Fe-Mn oxide: The major components of Fe-Mn oxide are Fe<sub>2</sub>O<sub>3</sub>, MnO, P<sub>2</sub>O<sub>5</sub>, and LOI. Because there are large variances in its composition associated with changes in the sediment environment, the residual values for these elements after MRA may have larger variances than those for other elements (see the results shown in Figure 35). For MRA, I assumed that the contents of the four elements in Fe-Mn oxide are constant and then added the residual values after MRA. The Fe<sub>2</sub>O<sub>3</sub>/MnO ratio in Fe-Mn oxide was estimated from the envelope line for the core samples drawn on an x-y plot of Fe<sub>2</sub>O<sub>3</sub> versus MnO (Figure 31B). Although the rate of absorption of organic material by Fe-Mn oxide could have changed in association with changes in the oxygenation conditions of the bottom water, it is difficult to estimate the contents of LOI and P<sub>2</sub>O<sub>5</sub> in Fe-Mn oxide. Therefore, in MRA the minimum contents of P<sub>2</sub>O<sub>5</sub> (0.1%) and LOI (10%) from the data for the core samples were assumed to be their concentrations in Fe-Mn oxide (Figure 31C and D).

(5) Detrital materials: On the basis of QFA as applied to DetXRF data in Section 5-4, it was confirmed that the four major components of detrital material in the sediment of Lake Suigetsu are as follows: fine-grained detrital material (predominantly <4 μm) from the drainage area of Lake Mikata, eolian dust (predominantly 4–16 μm) from the Asian continent, coarse-grained detrital material (predominantly 16–64 μm) from the slopes surrounding Lake Suigetsu, and fine-grained detrital material

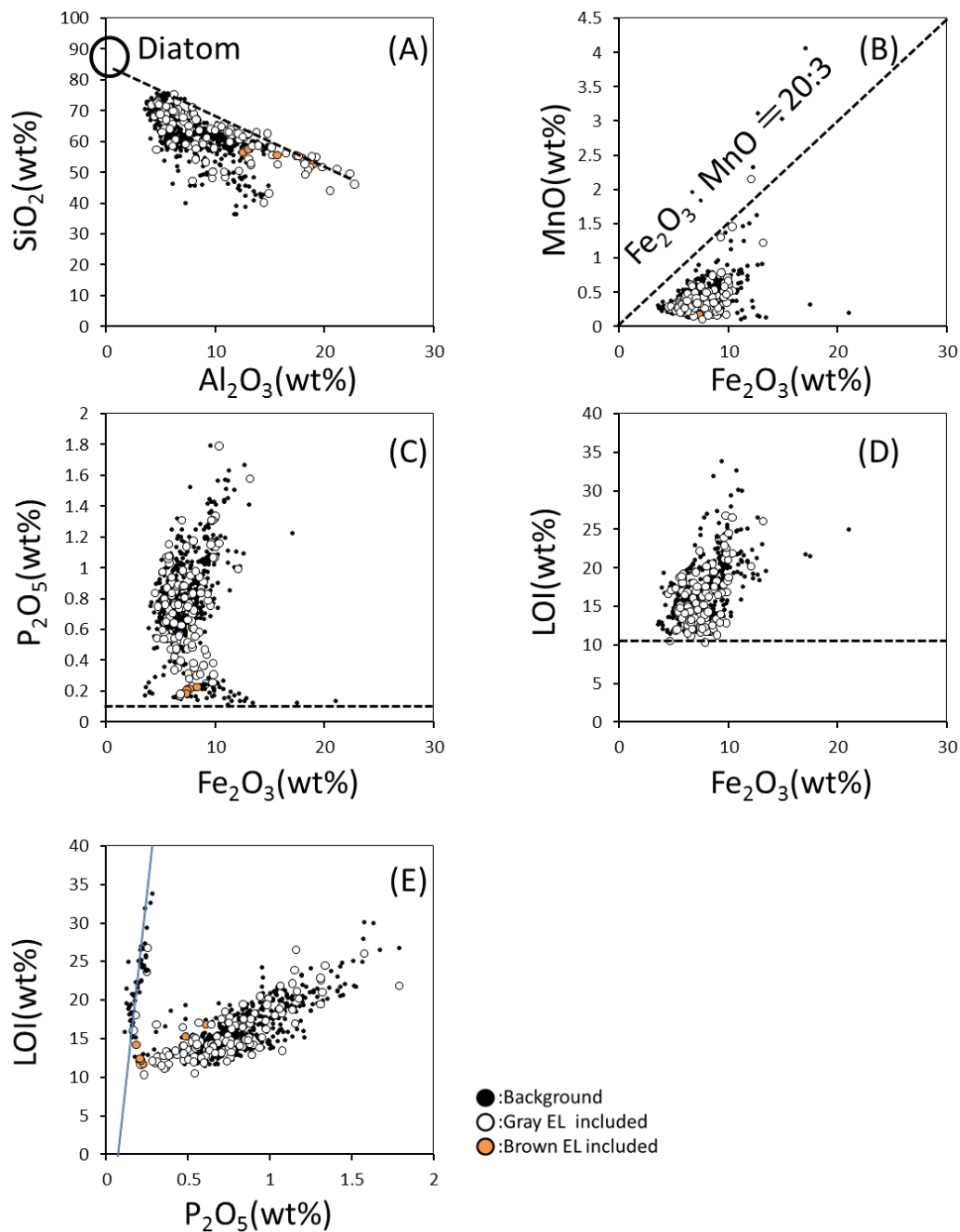


Figure 31  
 X-y plot of (A) Al<sub>2</sub>O<sub>3</sub> vs. SiO<sub>2</sub>, (B) Fe<sub>2</sub>O<sub>3</sub> vs. MnO, (C) Fe<sub>2</sub>O<sub>3</sub> vs. P<sub>2</sub>O<sub>5</sub> and (D) Fe<sub>2</sub>O<sub>3</sub> vs. LOI for evaluation of chemical composition of diatom frustules and Fe-Mn oxide.

(predominantly  $<4 \mu\text{m}$ ) from the slopes surrounding Lake Suigetsu. Here, I refer to these materials as D-EM1, D-EM2, D-EM3, and D-EM4, respectively. Although the chemical compositions of the D-EMs are different from each other, these differences are minor in comparison to the differences from the chemical compositions of other sediment components. Therefore, in MRA I assumed the chemical composition of the pure gray event layer with the highest  $\text{Al}_2\text{O}_3$  content and estimated the bulk content of detrital material in the sediment. After MRA, I estimated the content of each D-EM in the sediment by multiplying the mixing ratio of the four D-EMs calculated using QFA by the result of MRA after excluding the effect of sea salt by subtracting the contribution of sea salt (content  $\times$  chemical composition).

#### **5-6. Results of MRA**

In Figures 32 and 33, the chemical compositions of sediment components estimated in MRA and core data obtained by XRF are plotted on x-y plots of  $\text{Al}_2\text{O}_3$  versus other elements and LOI. As the chemical composition of sediment components in MRA is intended to explain the chemical composition of SG12 core data, it can be observed that SG12 core data were successfully plotted among the components estimated in MRA. Depth profiles of the estimated content of each component of the sediment based on MRA are shown in Figure 34. The relative errors in the contents of sediment components were calculated on the basis of propagation of errors in the chemical composition of each sediment component (assumed to be  $\pm 1\%$ ), residuals after MRA, and the ranges of D-EM contents as the output of QFA for detrital material. The relative errors in the contents of sediment components are also shown in Figure 34.

The content of D-EM1 (fine detrital material from the drainage area of Lake Mikata) reaches high values (40–60%) in the samples, including those from gray event layers. The contents of D-EM1 in background sediment are rather constant at around 10–15% in the interval from 3.5 m to 10.0 m and around 20% in the top 3.5 m.

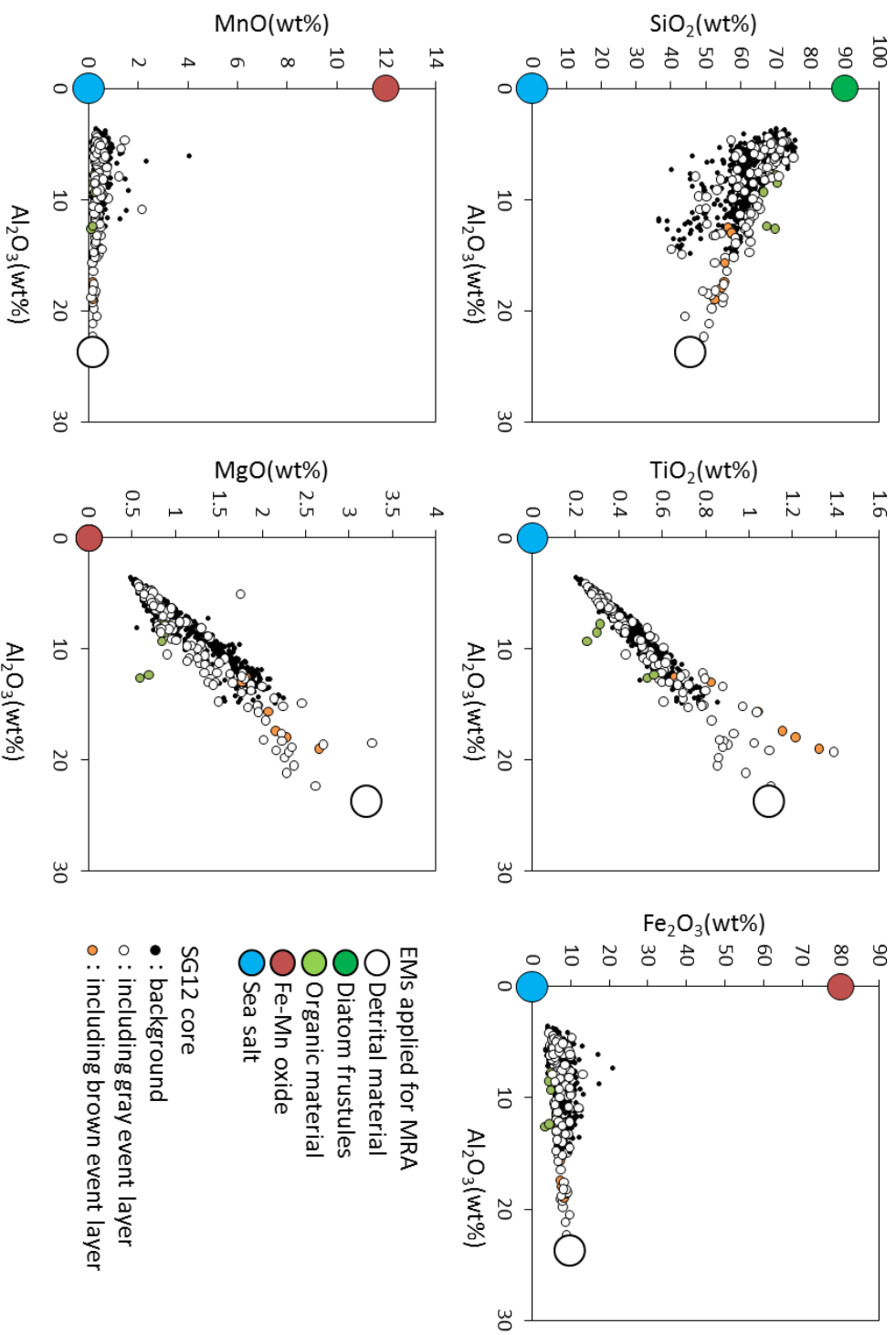


Figure 32 X-y plot of XRF data of SG12 core, dust samples and EMs for MRA ( $\text{Al}_2\text{O}_3$  vs.  $\text{SiO}_2$ ,  $\text{TiO}_2$ ,  $\text{Fe}_2\text{O}_3$ ,  $\text{MnO}$  and  $\text{MgO}$ ).

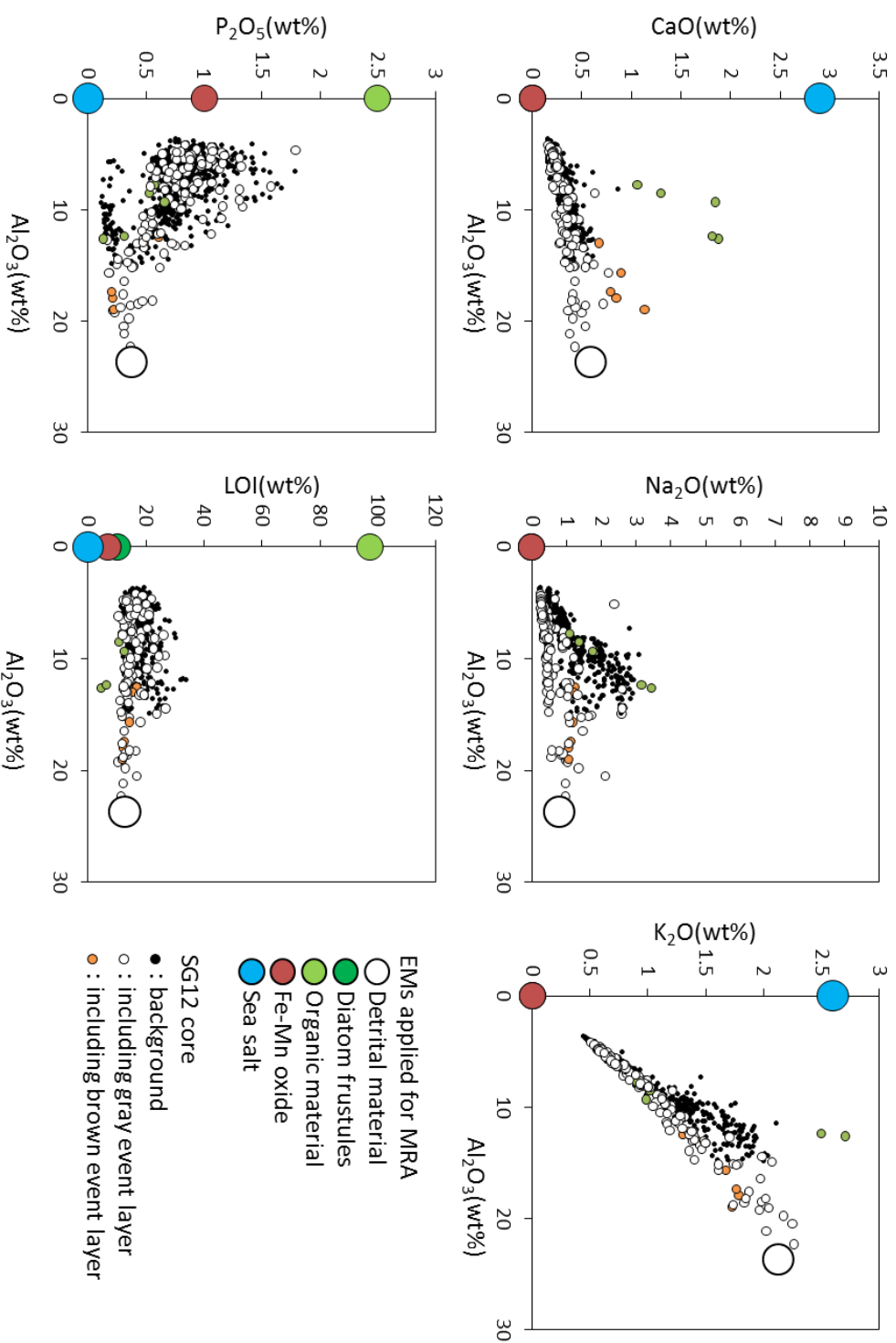


Figure 33  
 X-y plot of XRF data of SG12 core, dust samples and EMS for MRA (Al<sub>2</sub>O<sub>3</sub> vs. CaO, Na<sub>2</sub>O, K<sub>2</sub>O, P<sub>2</sub>O<sub>5</sub> and LOI).

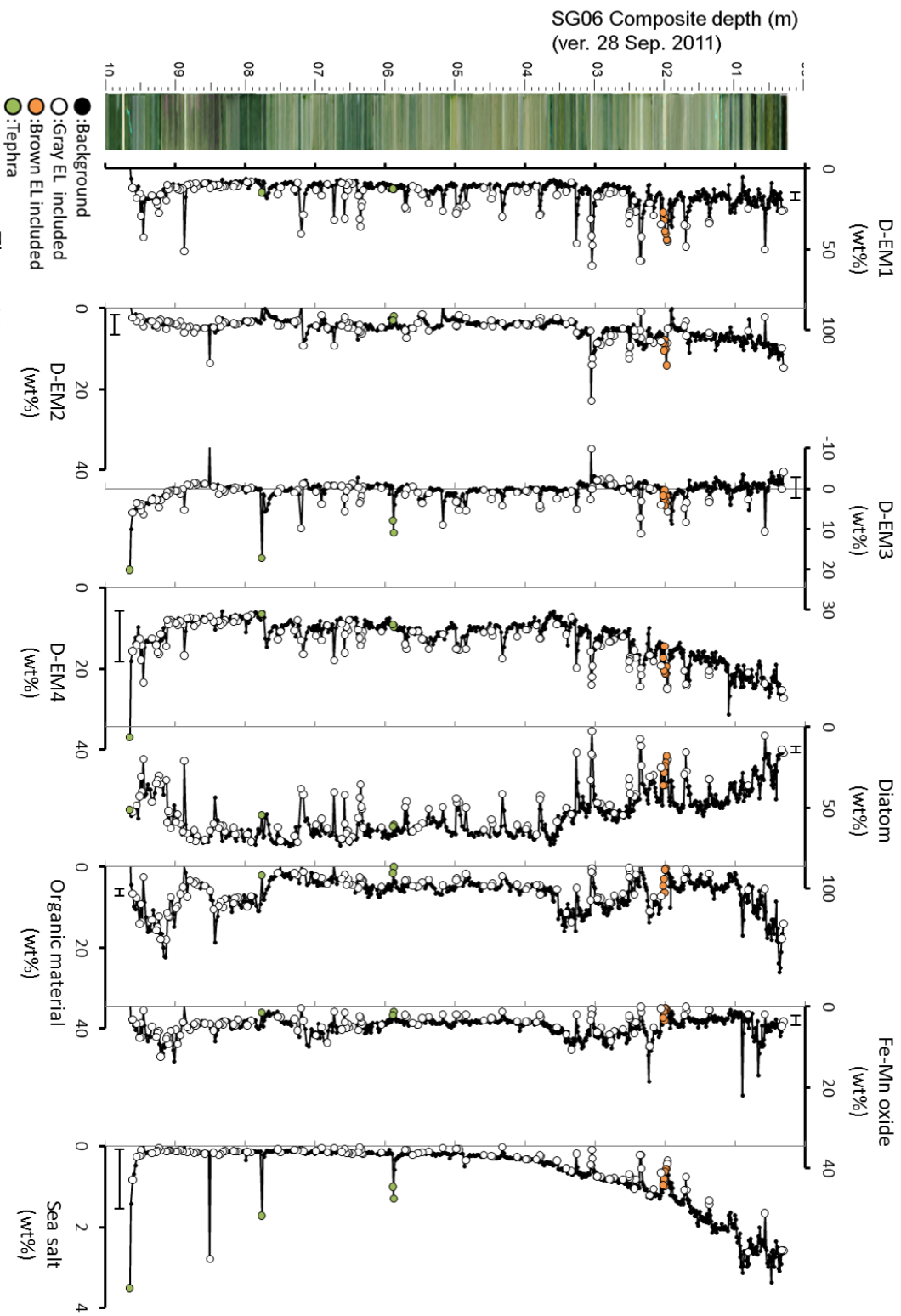


Figure 34  
Depth profiles of contents of sediment components estimated by MRA in the top 10m of SG12 core.

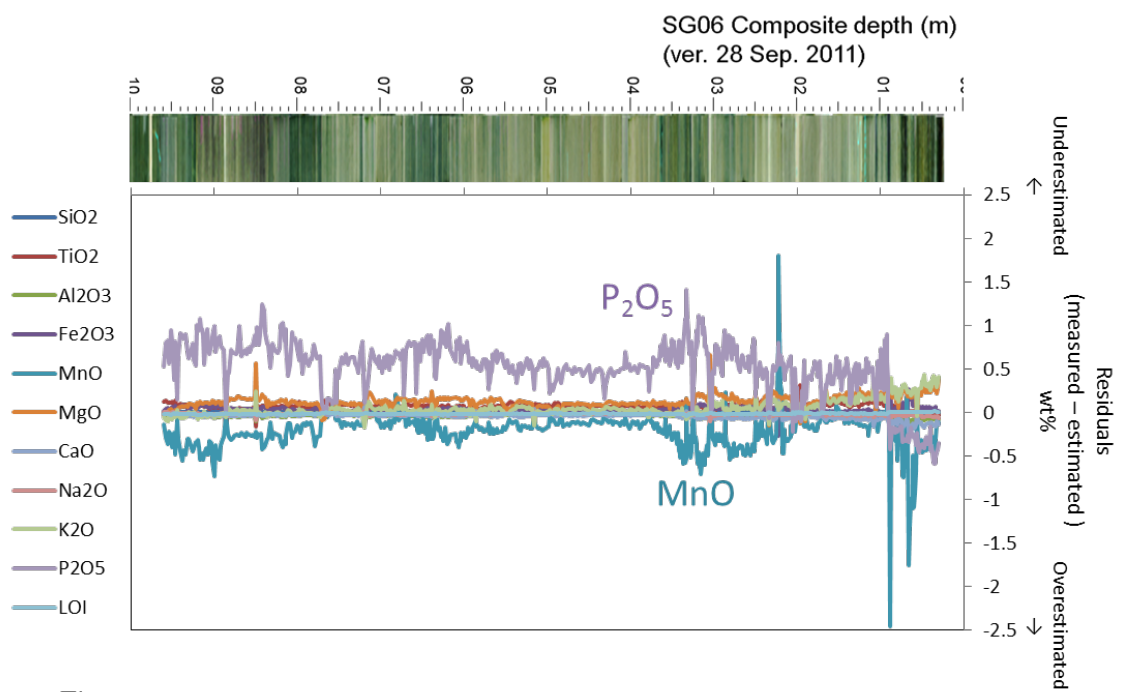


Figure 35  
Residuals of each elements after MRA, calculated as differences between measured XRF data and estimated compositional data by mixing ratio of sedimentary components.

The contents of D-EM2 (coarse detrital material from the slopes surrounding Lake Suigetsu) have high values in the brown event layer of up to ~20% and also in some gray event layers (i.e., the gray event layer at a depth of 3.1 m). On the other hand, in background sediment and the other gray event layers the content of D-EM2 is very low at around 5%. This result agrees with the result of the grain size analysis of each facies in Chapter 3, i.e., that coarse detrital particles are not present in background sediment or gray event layers but are present in brown event layers.

The contents of D-EM3 (eolian dust) generally have values of ~0% but have peaks in samples containing event layers. Contamination from event layers could occur when estimating the content of eolian dust by this method.

The contents of D-EM4 (fine detrital material from the slopes surrounding Lake Suigetsu) have high values in event layers in the same way as D-EM1. The content of D-EM4 in background sediment gradually decreases from the top of the core (~25%) to a depth of 3.5 m (~10%) and has a constant value in the interval between 3.5 and 10 m (10–15%).

The content of diatom frustules is higher in background sediment and lower in event layers, as a result of the large contribution of detrital material in samples containing event layers. The content of diatom frustules in background sediment displays a stepwise increasing trend downward, namely, ~30% in the top 1 m, 40–50% in the interval between 1.0 and 3.5 m, and ~70% in the interval between 3.5 and 8.8 m. In the interval between 8.8 and 10.0 m, the content of diatom frustules decreases downward to 30–40%. The contents of organic material and Fe-Mn oxide are relatively similar other than in the top 90 cm and the interval between 6.7 and 7.3 m, which indicates that these two components are effectively transported together. Because the top 90 cm corresponds to the period of inflow of seawater, it is supposed that the conditions of precipitation of Fe and Mn had changed. In the intervals of 2.0–3.5 m, 7.8–8.4 m, and 8.8–9.5 m, the contents of organic material and Fe-Mn oxide have high values (~10%, 5–10%).

### 5-7. Flux of components in the sediment of Lake Suigetsu

The flux of each component in the sediment of Lake Suigetsu was calculated from the content of each component and its DBD ( $\text{g}/\text{cm}^3$ ) and LSR ( $\text{cm}/\text{yr}$ ) using the following equation (23):

$$F_N = (C_N/100) \times DBD \times LSR \times 1000 \quad (23)$$

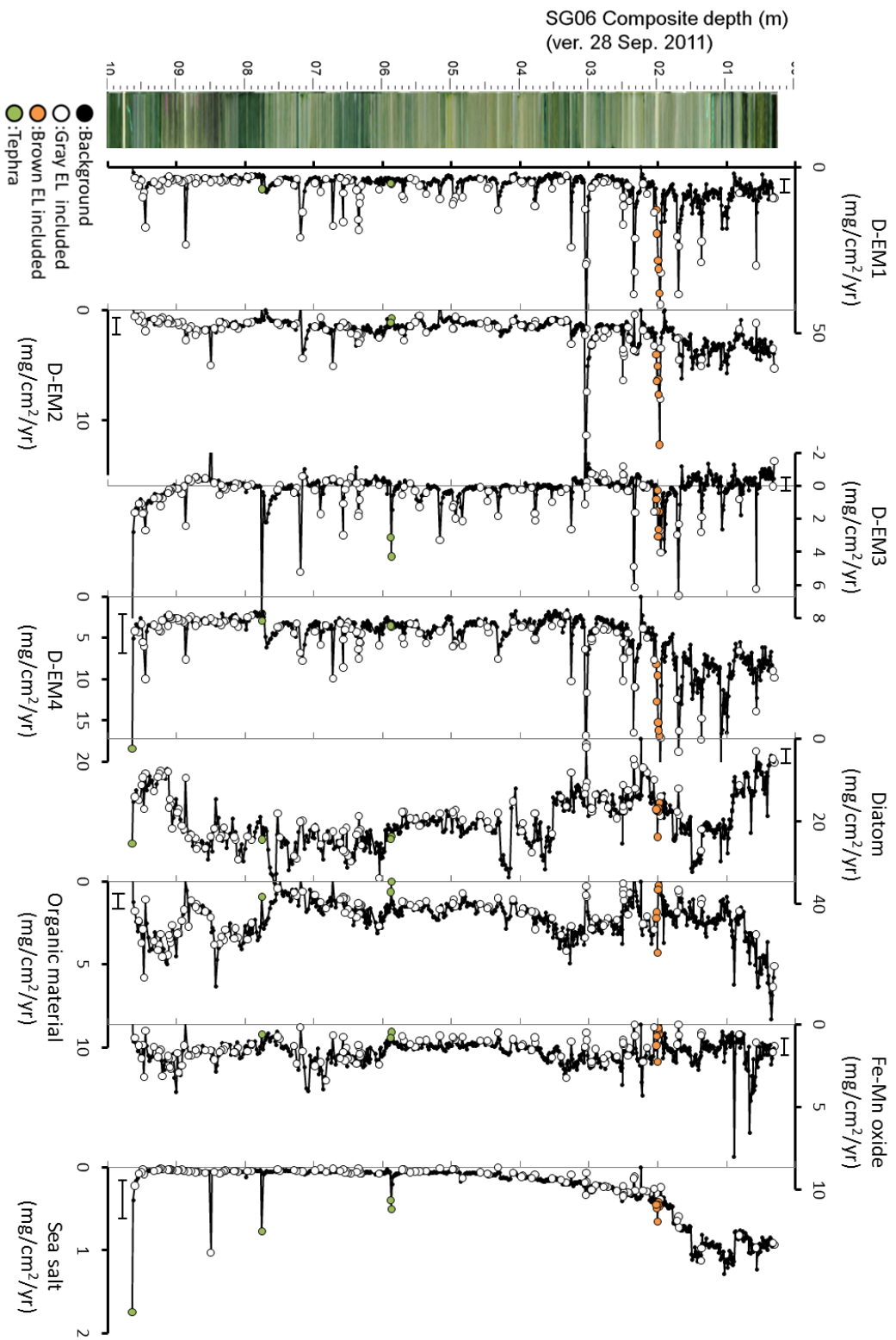
where  $F_N$  and  $C_N$  are the flux ( $\text{mg}/\text{cm}^2/\text{yr}$ ) and content (wt%) of the  $N^{\text{th}}$  component in the sediment assumed in MRA. The LSRs of the samples were based on the age–depth model described in Section 5-2 and are listed in Table S7. Because the average interval between neighboring age datum points based on  $^{14}\text{C}$  dating is about 100 years, the resolution of the LSRs is  $\sim 100$  years. However, the measurements of EM1 content and DBD were conducted with a higher resolution of an average of  $\sim 10$  years. The flux profile (Figure 36) of each component in the sediment is shown, which corresponds to a resolution of  $\sim 10$  years assuming that the LSR is constant between two neighboring age control points (equation 13). Temporal changes in the calculated fluxes of components in the sediment of Lake Suigetsu are shown in Figure 36. The relative error in the  $F_N$  values shown in Figure 36 was estimated from the propagation of the errors in  $C_N$  (estimated as 5–6%), DBD (10% error in measurements), and LSR ( $\sim 3\%$  on average).

#### 5-7-1. Flux of diatom frustules, organic material, Fe-Mn oxide, and sea salt

The flux of diatom frustules shown in Figure 36 displays stepwise decreases upward at 5.9 m, 3.5 m, and 0.9 m. Between these points, the flux of diatom frustules displays a gradual increasing trend upward. The fluxes of organic material and Fe-Mn oxide have higher values in the intervals between 7.8 and 9.5 m and 0.3 and 3.5 m, and that of Fe-Mn oxide also has higher values in the interval between 6.0 and 7.2 m. The flux of sea salt has higher values ( $0.5\text{--}1.0 \text{ mg}/\text{cm}^2/\text{yr}$ ) in the top 1.7 m and displays an exponential decreasing trend in the interval of 1.7–3.5 m.

#### 5-7-2. Flux of D-EM1

The flux of D-EM1 in background sediment has a high value of 5–10  $\text{mg}/\text{cm}^2/\text{yr}$  at a depth of  $\sim 2.0$  m. In the interval from 2.0 m to 10 m, the



background value is slightly lower than in the upper part and oscillates between 3 and 5 mg/cm<sup>2</sup>/yr with peaks every 1.8–2.2 m. On a shorter scale of ~10 cm, the flux of D-EM1 exhibits high-amplitude peaks at intervals of several tens of cm, most of which correspond to samples containing gray event layers. After removing samples containing event layers, some peaks still remain (blue horizontal lines in Figure 37B). These peaks are subdivided into peaks with longer duration (blue solid bands in Figure 37B) and shorter duration (blue dashed lines in Figure 37B). These peaks are characterized by rapid increases and slower decreases. The scale of the decreasing trends ranges from ~1 cm (shorter duration) to ~10 cm (longer duration). The peaks in the flux of D-EM1 with longer duration (more than 100 years) indicate that the influx of fine-grained detrital material from the drainage area of Lake Mikata suddenly increased owing to events such as floods or earthquakes, and higher levels of detrital flux continued. Therefore, the asymmetry of the peaks, especially those with longer duration, can be ascribed to the prolonged effect of events on the level of surface erosion.

#### **5-7-3. Flux of D-EM2**

The flux of D-EM2, which mainly corresponds to the coarse fraction of detrital material from the slopes surrounding Lake Suigetsu, has high values just above the position of the brown and gray event layers at a depth of 3.1 m. Most of these peaks relate to samples containing event layers.

#### **5-7-4. Flux of D-EM3**

The flux of D-EM3, which mainly corresponds to eolian dust, displays a long-term trend of oscillations between ~0 and ~1 mg/cm<sup>2</sup>/yr, which is generally within the order of estimates of the dust flux in the sediment in the Sea of Japan [*Nagashima et al.*, 2007].

#### **5-7-5. Flux of D-EM4**

The flux of D-EM4 reaches high peaks in event layers, which match peaks in the flux of D-EM1. The background flux of D-EM4 increases from a depth of 3.0 m (~4 mg/cm<sup>2</sup>/yr) to a depth of 0.9 m (~10 mg/cm<sup>2</sup>/yr).

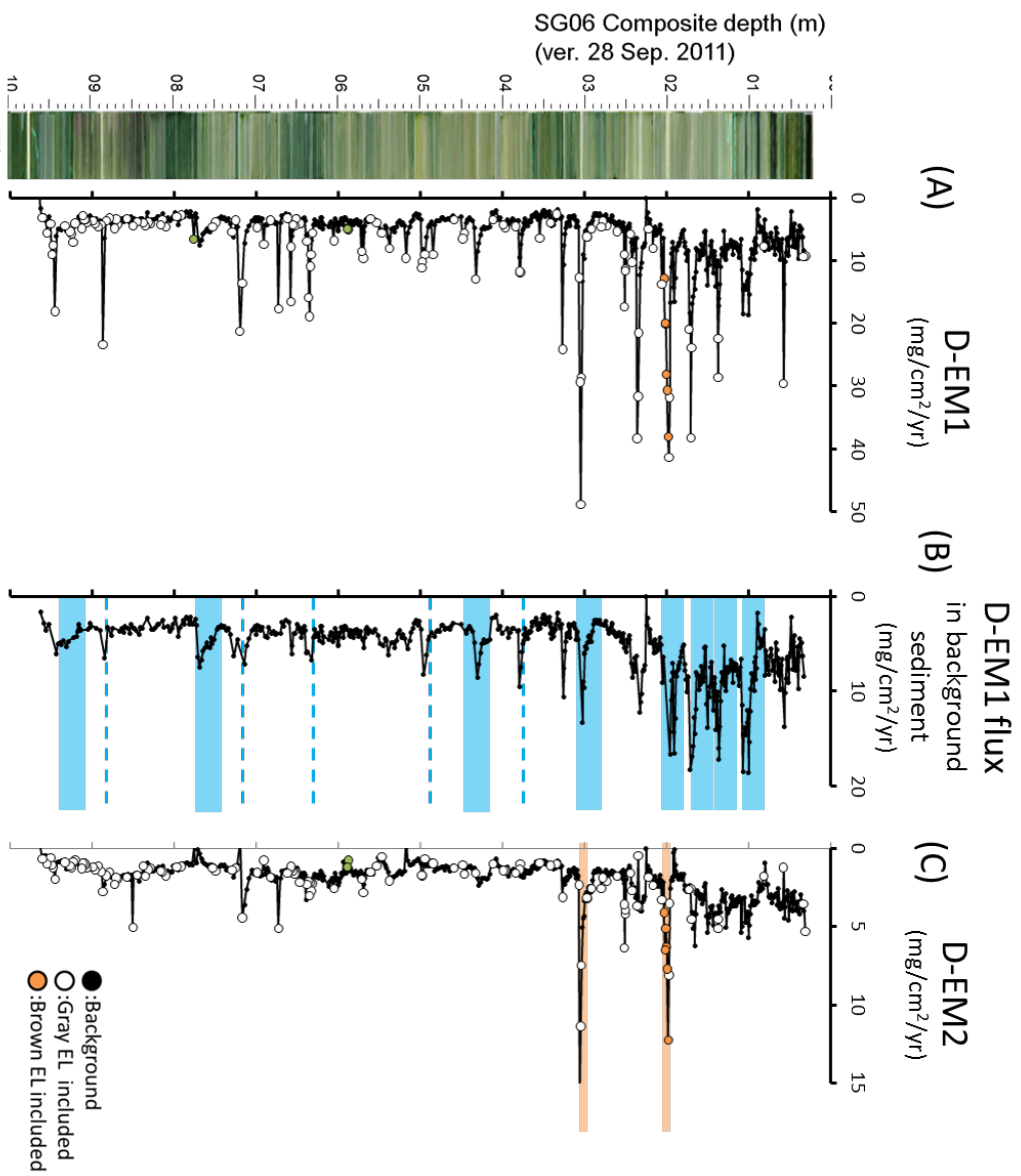


Figure 37  
Depth profiles of D-EM1 flux of (A) all samples, (B) D-EM1 flux of background samples and (C) D-EM2 flux in the top 10m of SG12 core.

## 5-8. Tectonic and anthropogenic effects

There is a possibility that the baseline level of erosion of the ground surface changed after huge landslides or the development of farming. To discuss the history of floods based on the flux of D-EM1 derived from the drainage area and supplied by surface erosion, we have to properly evaluate the effects of such processes. In Figure 38, the fluxes of D-EM1 (fine-grained detrital material from Lake Mikata) and D-EM2 + D-EM3 (coarse detrital material including eolian dust) are shown and correlated with the record of earthquakes, agriculture, and the flux of elemental carbon (EC) reconstructed by Nakai (2016 MS) using the SG12 core. The fluxes of D-EM1 and coarse material increase gradually between the depths of 3.0 and 2.0 m (1650–850 yr BP), increase suddenly at a depth of 1.9 m to reach a highstand between the depths of 2.0 and 0.9 m (850–290 yr BP), and then suddenly decrease at a depth of 0.9 m to reach a lowstand. At a depth of 2.0 m a brown event layer is observed (Figure 6B), and at a depth of 0.9 m a thick black layer is observed, which is considered to be deposited by the inflow of seawater caused by the opening of the Urami channel [Fukusawa *et al.*, 1994]. According to historical records for this region (Editing Committee of Mikata Town history, 1990; Usami, 2003; Center of Kaminaka Town residents, 2004; PR magazine of Mikata Town, 2005), two earthquakes have affected this region. One of these, the Kanbun Earthquake (moment magnitude [M]  $\sim 7.6$ ) in 1662 A.D., caused the uplift and drying-up of the Kiyama River, the former outlet of Lake Suigetsu, and an increase in the lake level, and subsequently caused flooding of farmland in the area surrounding Lake Suigetsu and Lake Mikata. To reclaim the flooded farmland, the Urami channel, the new outlet of Lake Suigetsu, was cut to lower the lake level, which caused seawater to intrude into Lake Suigetsu. The Kanbun Earthquake is estimated to have been caused by the movement of the Hiruga and Hanaore faults, which are very close to the Mikata Five Lakes region [Nishiyama *et al.*, 2005; Komatsubara, 2006]. The other was the Bunchi Earthquake (M  $\sim 7.4$ ) in 1174 A.D., which occurred around the

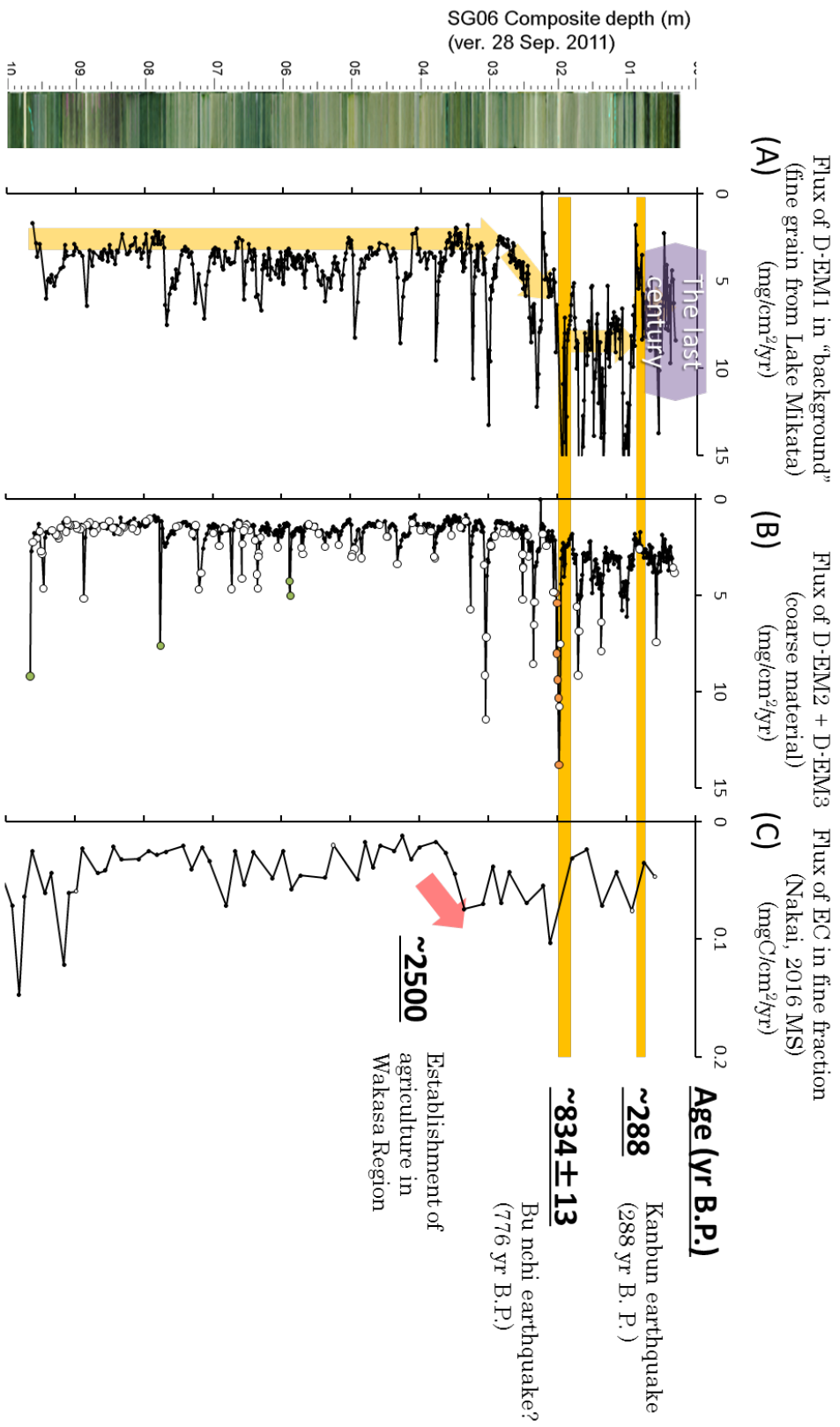


Figure 38  
 Depth profiles of (A) D-EMI1 flux of background samples, (B) D-EMI2 + D-EMI3 (coarse detrital material) flux and flux of Elemental Carbon (EC) in fine fraction reconstructed by Nakai (2016 MS) in the top 10m of SG12 core.  
 Historical events are also shown with the age.

Kyoto region, ~50 km south of Lake Suigetsu. Although the epicenter of the Bunchi Earthquake has not been confirmed, it has been estimated to be either the Lake Biwa West Coast fault or the Nankai Trough (Usami, 2003). Although there is no record in local historical documents of whether this earthquake caused any damage in the Mikata Five Lakes region, the age of this earthquake matches that of a brown event layer (depth of 19.2–26 cm in the SG12 Y2 section) within the range of error of the age model. After the deposition of the brown event layer, the flux of D-EM1 in the background sediment was at higher levels (10–20 mg/cm<sup>2</sup>/yr) for the subsequent ~800 years than in the lower interval (<10 mg/cm<sup>2</sup>/yr). Considering that the brown event layer can be correlated with the Bunchi Earthquake, this high level of flux of D-EM1 could have been caused by uplift in the drainage area, which in turn caused a change in the shape of the drainage area, of which the effect (higher flux of detrital material) continued on a much longer timescale than that of slope failure. In turn, this suggests that the effects of earthquakes and subsequent changes in landscape morphology could be detected by sudden changes in the influx of detrital material into the sedimentary basin.

In this region, farming has been established since ~2500 yr BP according to historical records (Fukui Prefecture, 2003), and *Nakai* (2016 MS) detected a sudden increase in the flux of EC around this period on the basis of analysis of the SG12 core. Although agriculture could increase the flux of detrital material from the basin by decreasing its vegetation cover, the increase in detrital flux (Figure 38) did not coincide with, but was later than, the increase in the flux of EC. Considering that farmlands are established in plains, whereas detrital material is supplied from mountainous areas, this difference in age between the fluxes of detrital material and EC could represent a change in land use by society, such as the deforestation of mountainous areas.

Considering that the baseline erosion level after the deposition of the brown event layer was higher than before, extrapolation of the flood proxies found in Chapter 4 could underestimate the magnitude of flood or precipitation

events. Therefore, flood records before 1 ka in Chapter 6 have to be considered as minimum estimates of the frequency and magnitude of flood events.

## **6. Flood records for the past 7000 years and correlation with other paleoclimatic records**

### **6-1. Introduction**

As described in Chapter 3, the Holocene sediment in Lake Suigetsu has suffered from slight bioturbation, which has obscured sedimentary structures such as varves and thin event layers. However, we can still recognize many event layers in half split surfaces of core sections with thicknesses of greater than 1 mm. As was discussed in Chapter 4, thickness of a gray event layer reflects the scale of the flood event that caused its deposition. Therefore, by counting the number of event layers that avoided bioturbation and measuring their thickness, it was possible to reconstruct the frequency of flood events larger in scale than a flood that resulted in a gray event layer with a thickness of 1 mm and to estimate their magnitude from the thickness of the respective event layer.

### **6-2. Methods**

#### **6-2-1. Description of event layers in the Holocene sediment**

To examine the frequency and magnitude of each flood event that caused the deposition of an event layer with a thickness of >1 mm, we described the position and thickness of event layers with a thickness of >1 mm in the sediment corresponding to the last 7000 years. Because the Holocene sediment in Lake Suigetsu is slightly bioturbated and its primary sedimentary structure has been disturbed, there is a possibility that thin event layers have been erased owing to bioturbation and mixed into the background sediment. To reduce this effect as far as possible, we only extracted event layers with a thickness of >1 mm, which is thicker than the annual lamination if it is well preserved.

#### **6-2-2. Flux of D-EM1 as a proxy for flood events**

As discussed in Section 4-7-2, the flux of detrital material increases with the frequency of moderately heavy rainfall (30–100 mm/day) on the

assumption that the relationship over the last century was maintained in previous periods. Here, I examined whether this relationship holds if the flux of detrital material is separated into four EMs, as was carried out in Chapter 5. In Figure 39, cross-plots of the flux of D-EM1 versus the amount of precipitation and frequency of heavy rainfall (30–100 mm/day and 50–100 mm/day) are shown. On comparing the correlation coefficients shown in Figure 38 with those in Figure 17, these were higher when the flux of D-EM1 (based on the results of MRA and QFA) was selected as the Y-axis than when the total detrital flux (estimated in Chapter 4) was chosen. Therefore, the flux of D-EM1, namely, fine-grained detrital flux from the drainage area of Lake Mikata, can be used as a proxy to represent the frequency of heavy rainfall. In addition, even if thin event layers are bioturbated and erased, the increase in the influx of D-EM1 caused by the deposition of gray event layers can be detected as an increase in the flux of D-EM1. Therefore, the flux of D-EM1 reconstructed in Chapter 5 represents the sum of background sedimentation due to moderately heavy rainfall and thin (<1 mm) event layers. In this chapter, I used the flux of D-EM1 in “background” sediment (including erased gray event layers) as a semi-quantitative proxy to reflect the frequency of moderately heavy rainfall (30–100 mm/day) and excluded “former event layers” in each sample if the relationship over the last century was maintained in previous periods.

### **6-3. Results**

Figure 40A shows a histogram that represents the distribution of the duration between the deposition of each event layer and the deposition of the previous event layer. Figure 40B shows the temporal changes in the duration between the deposition of each event layer and the deposition of the previous event layer. Figure 40C shows the temporal changes in the frequency of gray event layers in a 500-year interval (black dashed line) and the thickness of each event layer (red lines). A list of event layers in the top 10 m of the SG12 core is shown in Table S8. The histogram of the duration between two event

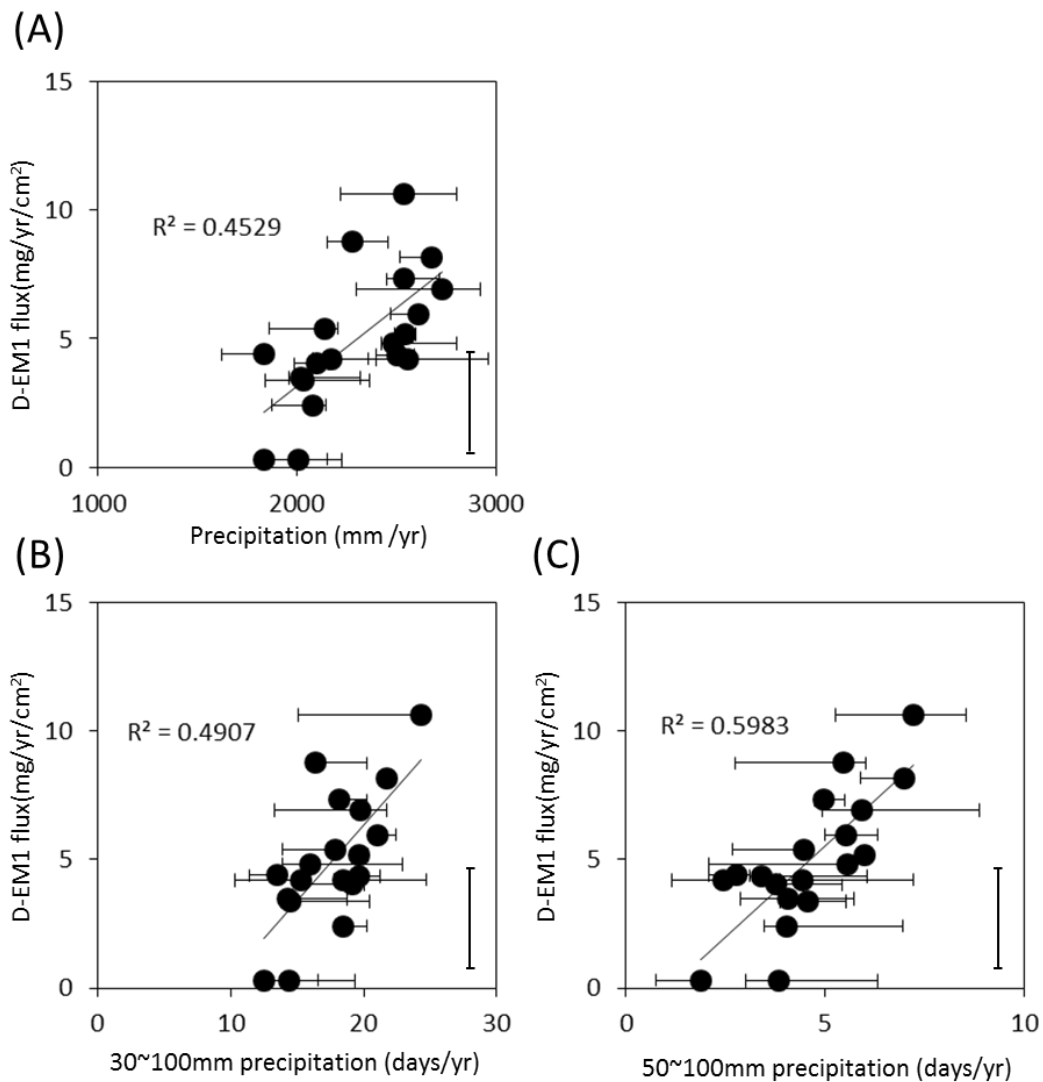


Figure 39

(A) X–Y plot of the annual precipitation (excluding >100 mm/day) at Tsuruga [JMA, <http://www.data.jma.go.jp/gmd/risk/obsdl/index.php>] and corresponding flux of D-EM1 in the background samples of SG12LM3 core excluding those including gray event layers. (A) The flux of D-EM1 shows a weak relationship with the annual precipitation.

(B) X–Y plot of detrital flux versus frequency of rainy days more than 30mm.

(C) X–Y plot of detrital flux versus frequency of rainy days more than 50mm.

Frequency of “relatively strong rainfall” have clearer relationships than that of annual precipitation with  $F_{det}$ .

Comparing with Figure 17 (correlation of  $F_{det}$  versus precipitation), correlation coefficients become better in every plot.

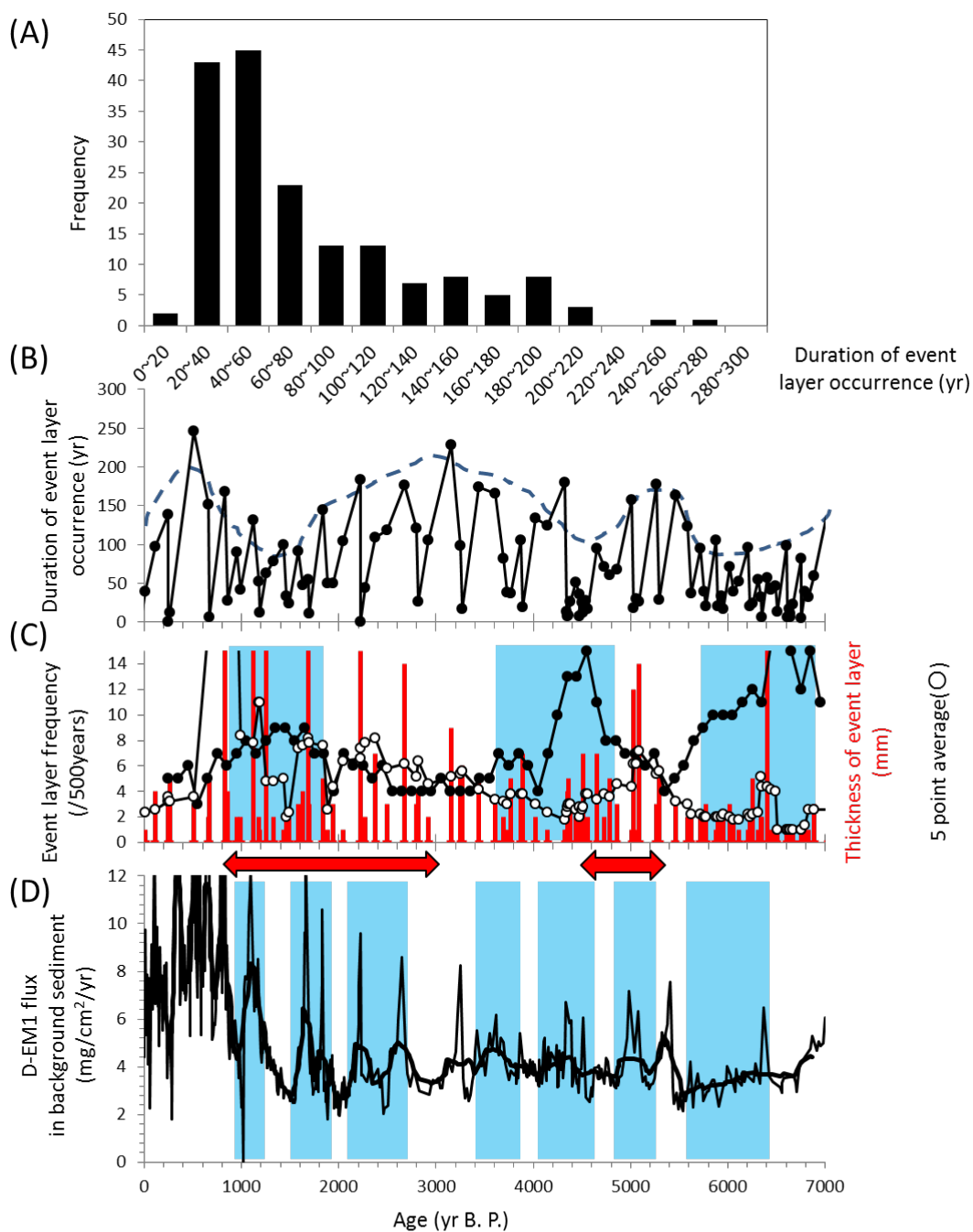


Figure 40

- (A) A histogram showing distribution of duration of each event layer deposition since the deposition of previous event layer.
- (B) Temporal change in duration of each event layer deposition since the deposition of previous event layer.
- (C) Temporal changes in frequency of gray event layers in 500 years interval (black dashed line) and thickness of each event layer (Red lines)
- (D) Temporal changes in flux of D-EM1.

layers (Figure 39A) has one peak at 20–60 years (10–25 times per 500 years) and a small secondary peak around 180 years (2–3 times per 500 years). The duration between the depositions of event layers (Figure 39B) over the last 7000 years oscillates with a high amplitude over a relatively short cycle (200–400 years). The maximum value in each cycle ranges from ~80 to 250 years, whereas the minimum value ranges from ~10 to ~50 years. This indicates that if one event layer is deposited the deposition of another event layer often occurs, which continues until the deposition of the last event layer.

In Figure 40C, the frequency of event layers per 500 years (250-year intervals) is shown as a black dotted line, and the thickness of each event layer (mm) is shown as a red line. The background level of the frequency of event layers is about 4–6 times per 500 years (every ~100 years) with positive anomalies in the intervals of 7–5.5 ka (8–14 times per 500 years), 4.8–4.2 ka (8–14 times per 500 years), and 1.8–0.8 ka (6–8 times per 500 years) (indicated by the blue bands in Figure 40C). This trend is in accordance with the troughs in the envelope line drawn in the profile of the duration between the depositions of event layers (dashed line in Figure 39B). The event layers described here have a thickness of greater than 1 mm. If we simply apply the relationship between the thickness of gray event layers and the amount of heavy precipitation that causes flood events (equation (9) in Section 4-5), a thickness of 1 mm can be interpreted as representing one event of precipitation with ~300 mm within one or two days. Therefore, these intervals can be characterized by the frequent occurrence of flood events with rainfall of more than 300 mm. On the other hand, the thickness of each event layer (5-point average: open circles in Figure 40C) displays a different trend from the other two variables, having high levels in the intervals of 5.2–4.4 and 3.4–0.4 ka. These periods can be characterized by the occurrence of huge flood events. Figure 40D shows the flux of D-EM1 excluding visible event layers (= “background” flux of D-EM1) as a gray line and its 15-point moving average as a black solid line. The background flux of D-EM1 has high values

in the intervals of 6.4–5.6, 5.2–4.8, 4.6–4.0, 3.8–3.5, 2.7–2.1, 1.9–1.5, and 1.2–0.9 ka (shown as blue bands in Figure 40D), with peak values of around 8–12 mg/cm<sup>2</sup>/yr. Considering that the background flux of D-EM1 over the last century is around 5–10 mg/cm<sup>2</sup>/yr (Section 6-2-2 and Figure 39), the background sedimentation of D-EM1 was consistently at a much lower level over the last 7000 years than in the last century.

#### **6-4. Discussion**

##### **6-4-1. Comparison between flood records for the last century and those for the last 7000 years**

I examined the relationships between three proxies of flood events in this region before 1000 AD (950 yr BP). The frequency of events ranged from one to two times that in the last century, during which there were two flood events caused by rainfall of more than 400 mm over the last 80 years (~12 times in 500 years). Considering this result, the last century seems to be a period with a relatively frequent occurrence of “heavy flood” events (more than 400 mm precipitation within a few days). However, with respect to the thickness of the gray event layer, which corresponds to the scale of each flood event, it can be seen that there were about 10 event layers with a thickness of greater than 10 mm during the last 7000 years. Because gray event layers with thicknesses in excess of 1 cm are not found during the last century, it is not possible to estimate the scale of the precipitation that caused the flood and the deposition of extremely thick gray event layers. However, it is suggested that there were huge hazard events that caused the deposition of thick (more than ~1 cm) event layers about once per ~700 years over the last 7000 years, which cannot be observed over the last century.

##### **6-4-2. Correlation with other climatic records for the East Asia region**

From modern observations, it is known that precipitation patterns in the East Asia region (including the study site) are affected by the activity of the East Asian Summer Monsoon (EASM), which causes the rainy season on the East Asian continent and the Baiu season in the Japanese islands, which is

characterized by the frequent occurrence of moderately heavy rainfall [*Wang and Ho, 2002; Tada and Murray, 2016*]. On the other hand, it has been reported that the sea surface temperature (SST) in the East China Sea displays a positive relationship with precipitation patterns in central and western Japan on the basis of a numerical model [*Manda et al., 2014*] and observational records [*Fujibe, 2015*]. The SST is considered to affect rainfall by intensifying convective instability and the evaporation of seawater, which supplies water vapor to depressions. Considering that one cause of flood events in this region is the passage of typhoons near the coast of the Sea of Japan, the SST could increase the intensity and duration of typhoons (or depressions) sufficiently for them to cause floods in coastal regions by the Sea of Japan after passing over Honshu. To investigate the relationships between rainfall/flood events, regional rainfall, and SSTs observed or modeled in previous research, I have correlated these records with each other in this section.

When the flux of EM1 (Figure 40D: background frequency of heavy precipitation), the frequency of gray event layers with a thickness of >1 mm (black line in Figure 40C: frequency of large flood events), and the thickness of event layers (red lines in Figure 40C: magnitude of each flood) are correlated, it is expected that if the occurrence of floods and heavy precipitation are controlled by a simple mechanism, these three proxies would have a simple relationship. For instance, when the frequency of flood events increased, that of large flood events would also increase. However, as described in Section 6-3-1, the relationship between these three variables is not clear. This unclear relationship suggests that the precipitation pattern over the last 7000 years in this region was controlled by several different mechanisms such as the activity of summer/winter monsoon fronts, the occurrence of typhoons, the routes of typhoons, and other factors, in the same way as indicated by the observational records for this region (Figure 4).

To understand the spatiotemporal pattern of heavy precipitation in this region that causes flood events, I compared records of heavy precipitation

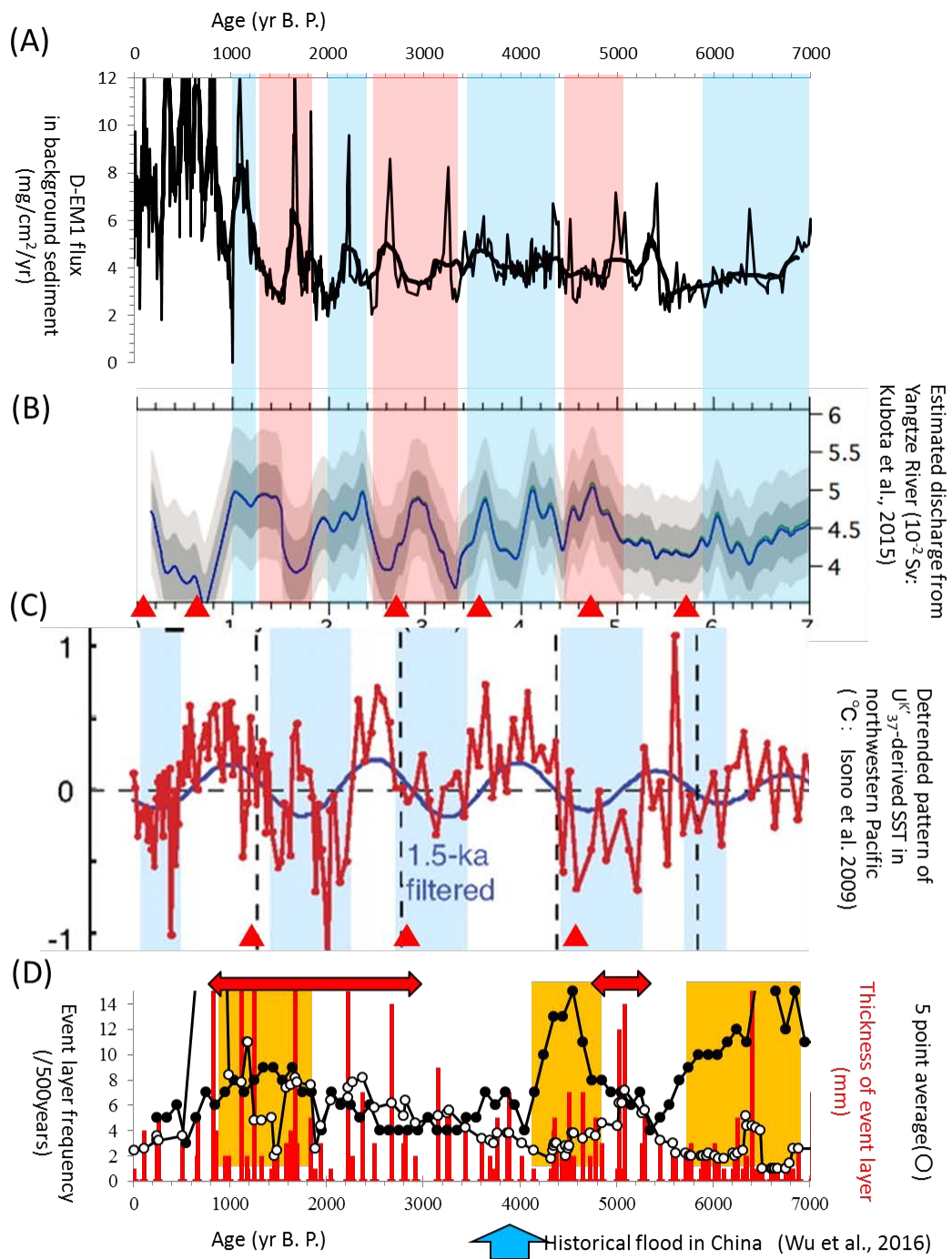


Figure 41  
 (A) D-EM1 flux in background sediment as a proxy for moderate string rainfall and thin event layers.  
 (B) Discharge from Yangtze River estimated based on  $\delta^{18}\text{O}_{\text{sw}}$  (Kubota et al. 2015)  
 (C) Detrended SST pattern in northwestern Pacific reconstructed by Isono et al. (2009)  
 (D) Event layer frequency and average thickness as a proxy for frequency and average magnitude of strong flood events.

and flood events in Lake Suigetsu with other climatic records.

Figure 41B shows the discharge from the Yangtze River in southern China during summer, which was estimated from reconstructions of changes in the  $^{18}\text{O}$  content of seawater ( $\delta^{18}\text{O}_{\text{sw}}$ ) in the northern East China Sea by *Kubota et al.* (2015). This discharge is significantly affected by rainfall in the drainage area, which is mainly produced by the EASM front [*Kubota et al.*, 2015; *Tada and Murray*, 2016]. A comparison of this discharge with the flux of D-EM1 (Figure 40A) revealed that these two variables tend to be positively correlated in the intervals (shaded blue in Figure 41 A and B) between 7.0 and 6.0, 4.4 and 3.4, and 2.4 and 2.0 ka but display the opposite trend in the intervals (shaded red in Figure 41A and B) of 5.0–4.6, 3.4–2.4, and 1.8–1.2 ka. It can be interpreted that these two types of precipitation distribution are affected by different mechanisms or climatic states. To characterize the intervals found by a comparison of precipitation patterns, I correlated these precipitation records with an SST record, which was derived from  $\text{U}^{\text{K}}_{37}$  values and reconstructed for the northeastern Pacific margin [*Isono et al.*, 2009], of which the detrended pattern is shown in Figure 41C. They found an oscillation in SSTs with a periodicity of around 1500 years. During cold periods (shaded blue in Figure 41C), the precipitation patterns in central Japan and the Yangtze drainage area displayed opposing trends, whereas during warm periods these precipitation patterns tended to exhibit similar patterns. The pattern of northwestern SSTs indicates another relationship with the patterns of flood and precipitation events found in this study. In Figure 41D, intervals with a high frequency of event layers (>1 mm: flood events with more than 300 mm precipitation) are shown in yellow (7–5.8, 4.8–4.2, and 1.8–0.8 ka). In particular, the intervals of 4.8–4.2 and 1.8–0.8 ka correspond to periods of sharp transition from a cold state to a warm state on the basis of the SST record (black arrows in Figure 41C). As it is known that there was a huge flood event in central China around 3.9 ka [*Wu et al.*, 2016], the interval of 4.8–4.2 ka could be characterized by a high frequency of flood events in the East Asia region.



## 7. Conclusion

Based on correlation between observational record and sedimentary record of Lake Suigetsu, it is revealed that fine-grained detrital material from the drainage area of Lake Mikata flows into Lake Suigetsu and deposits a gray event layer during flood events induced by strong rainfall of more than 100mm/day. The thickness of each event layer increases with the magnitude of flood event. It is also revealed that detrital flux increases with the frequency of moderately heavy precipitation of 30 to 100 mm/day, which does not result in deposition of gray event layer.

Based on Q-mode factor analysis of “detrital” elements of SG12 core samples and comparison of their chemical composition with that of detrital samples collected from the drainages of Lake Mikata and Lake Suigetsu, it is revealed that detrital material in SG12 core can be explained as a mixture of detrital material derived from four provenances. Namely, detrital material in the sediment of Lake Suigetsu is composed of fine particles from drainage area of Lake Mikata and Lake Suigetsu, eolian dust, and coarse particles from drainage area of Lake Suigetsu. Using multiple regression analysis of XRF bulk elemental composition data, contents and fluxes of detrital material from each source and other components in the sediment are estimated for the last 7000 years. The result of detrital flux reconstruction revealed that detrital flux increased for time scale of ~100 years after the occurrence of certain event layers possibly because of the increase of erosion level in drainage area. Based on correlation with historical earthquake record, it is also revealed that sudden increase and continuation of higher detrital flux have been caused by the change of morphology in the drainage area of Lake Suigetsu due to the fault movement.

Combining these results with occurrence and thickness of gray event layers thicker than 1mm, which correspond to large flood events (>300mm rainfall in total), semi-quantitative record of flood events and heavy precipitation in central Japan is reconstructed for the last 7000 years.

Comparing the flood record of Lake Suigetsu with precipitation and SST

records obtained from surrounding regions, it is revealed that change in spatial pattern of precipitation in EASM region could have been associated with the stage of cold/warm period, and that flood occurrence might be related with the change of climatic stage such as transition from cold to warm state, rather than the stable state. Spatio-temporal pattern of precipitation and flood events have such complex characteristics as is expected from the observational record. In this study, I established semi-quantitative proxy for reconstructing heavy precipitation and flood events, based on correlation between sedimentary record and observation, and focusing on the characteristic of sedimentation process sensitive to geologically instantaneous phenomenon such as deposition of event layers. This method can be applied to enclosed sedimentary basin such as lakes having varved sediment. More than 100 lakes and 50 marine basins in the world [Zolitschka *et al.*, 2015; Schimmelmann *et al.*, 2016] are able to correlate with observational record with annual resolution. Even if the sediment is not varved, sediment suffering only weak bioturbation could provide semi-quantitative event proxy such as detrital flux reconstructed in this study. Additionally, we could also determine whether the event layer is caused by tectonic activity by estimating the temporal change in detrital flux as is done in this study. For reconstructing flux of detrital material and correlation of the records with those from many sites, high-resolution age model is also necessary. By exploring this method to many sites in the world, we could reconstruct spatio-temporal variation of hazards such as floods and earthquakes.

## Acknowledgement

I would like to express my deep thanks to Professor R. Tada in University of Tokyo, for his helpful advice and discussion, revision of the manuscript, providing the occasion to join the sampling and field investigation, and financial support throughout this work. I would like to offer my special thanks to Professors E. Tajika, H. Kawahata, R. Tada, Y. Yokoyama and Y. Sekine in University of Tokyo for their critical comments and suggestive advices on the thesis as examiners. I would like to express many thanks to SG12 project members, the drilling team of Seibushisui Co. Ltd., and staffs at Jomon Museum in Wakasa town for sampling and safekeeping during the collection of the cores. I would also express many thanks to Professor T. Nakagawa in Ritsumeikan University, for instructing precise depth controlling and subsampling methods of core samples, having helpful advice and discussion of my research. I would like to thank Dr. K. Nagashima in JAMSTEC for her helping field survey, subsampling, constructing age model of LIMNOS core, and meaningful discussion about the research. I would express deep thanks to Dr. T. Irino in Hokkaido University for his providing many helps about sampling of riverbed and river water samples, measuring  $^{137}\text{Cs}$  and  $^{210}\text{Pb}$  isotopes in his laboratory, discussion about constructing age model and instruction for statistical analysis such as QFA and MRA. I would like to express my gratitude to Dr. K. Yamada in Museum of Natural and Environmental History, Shizuoka for conducting and teaching a technique for LIMNOS coring in field survey in 2014. I am deeply grateful to Dr. T. Omori in The University Museum of University Tokyo for helping the conduction of Bayesian analysis for validating the age model of LIMNOS core. I would express deep thanks to Mr. H. Kojima in Jomon Museum for giving me compiled data of historical floods in Wakasa town, providing much information about history of this region and supporting the field survey in research area. I also thank to Dr. J. Ashi and Dr. A. Omura of AORI, University of Tokyo for allowing me to use the He pycnometer. Dr. H. Yoshida and Mr. A. Kobayashi of the University of Tokyo helped me for operating the

XRF spectrometer. Dr. Kitagawa of Fukui Prefecture Satoyama-Satoumi Research Institute and Ms. Y. Nakai, a graduate of Hokkaido University, provided many help about field survey and LIMNOS core sampling conducted in 2014. Mr. T. Kanzaki, Dr. S. Inoue, Ms. H. Kobayashi, Mr. Y. Komori, Mr. T. Tada and Ms. K. Yoshizawa, graduate students of the University of Tokyo, provided valuable help about subsampling of SG12 core. I would like to thank Enago ([www.enago.jp](http://www.enago.jp)) for the English language review. This research is supported by the JSPS KAKENHI Grant KIBAN-S Number 23221002.

## References

- Alfieri, L., P. Burek, L. Feyen, and G. Forzieri (2015), Global warming increases the frequency of river floods in Europe, *Hydrol. Earth Syst. Sci.*, 19(5), 2247–2260, doi:10.5194/hess-19-2247-2015.
- Bronk Ramsey, C. (2009), Bayesian Analysis of Radiocarbon Dates, *Radiocarbon*, 51(1), 337–360, doi:10.2458/azu\_js\_rc.v51i1.3494.
- Bronk Ramsey, C. et al. (2012), A complete terrestrial radiocarbon record for 11.2 to 52.8 kyr B.P., *Science*, 338(6105), 370–4, doi:10.1126/science.1226660.
- Cai, W. et al. (2014), Increasing frequency of extreme El Niño events due to greenhouse warming, *Nat. Clim. Chang.*, 5(2), 1–6, doi:10.1038/nclimate2100.
- Center of Kaminaka-Town residents (2004), *Memoric magazine of 50th anniversary of Kaminaka-Town organization*
- Cohen, J. et al. (2014), Recent Arctic amplification and extreme mid-latitude weather, *Nat. Geosci.*, 7(9), 627–637, doi:10.1038/ngeo2234.
- Davis, J. A. (1982), Adsorption of natural dissolved organic matter at the oxide/water interface, *Geochim. Cosmochim. Acta*, 46(11), 2381–2393, doi:10.1016/0016-7037(82)90209-5.
- Delaune, R. D., W. H. Patrick, and R. J. Buresh (1978), Sedimentation rates determined by <sup>137</sup>Cs dating in a rapidly accreting salt marsh, *Nature*, 275(5680), 532–533, doi:10.1038/275532a0.
- Editing Committee of Mikata-Town history (1990), *Mikata Town History*
- Fudeyasu, H., K. Ichianagi, a. Sugimoto, K. Yoshimura, a. Ueta, M. D. Yamanaka, and K. Ozawa (2008), Isotope ratios of precipitation and water vapor observed in Typhoon Shanshan, *J. Geophys. Res.*, 113(D12), D12113, doi:10.1029/2007JD009313.
- Fujibe, F. (2015), Relationship between Interannual Variations of Extreme Hourly Precipitation and Air/Sea-Surface Temperature in Japan, *Sola*, 11(0), 5–9, doi:10.2151/sola.2015-002.
- Fukui Prefecture (1993), *Overview of history of Fukui Prefecture*
- Fukusawa, H., I. Koizumi, M. Okamura, and Y. Yasuda (1994), Historical earthquake, flood and human activity events recorded in the Holocene sediments of Lake Suigetsu, Fukui Prefecture, central Japan, *J. Geog.*, 103(2), 127–139.

- Gale, E. L., and M. A. Saunders (2013), The 2011 Thailand flood: Climate causes and return periods, *Weather*, 68(9), 233–237, doi:10.1002/wea.2133.
- Gee, G. W., and D. Or (2002), 2.4 Particle-Size Analysis, in *Methods of soil analysis. Part, 4*, pp. 255–293.
- Glaser, R., and H. Stangl (2004), Climate and floods in central Europe since AD 1000: Data, methods, results and consequences, *Surv. Geophys.*, 25(5–6), 485–510, doi:10.1007/s10712-004-6201-y.
- Hirabayashi, Y., R. Mahendran, S. Koirala, L. Konoshima, D. Yamazaki, S. Watanabe, H. Kim, and S. Kanae (2013), Global flood risk under climate change, *Nat. Clim. Chang.*, 3(9), 816–821, doi:10.1038/nclimate1911.
- IPCC: Summary for Policymakers, in: *Climate Change 2013: The Physical Science Basis, Contribution of Working Group I to the Fifth Assessment Report of the Intergovernmental Panel on Climate Change*, edited by: Stocker, T. F., Qin, D., Plattner, G.-K., Tignor, M., Allen, S. K., Boschung, J., Nauels, A., Xia, Y., Bex, V., and Midgley, P. M., Cambridge University Press, Cambridge, UK and New York, NY, USA, 2013
- Irino, T., and R. Tada (2000), Quantification of aeolian dust (Kosa) contribution to the Japan Sea sediments and its variation during the last 200 ky, *Geochem. J.*, 34, 59–93.
- Isono, D., M. Yamamoto, T. Irino, T. Oba, M. Murayama, T. Nakamura, and H. Kawahata (2009), The 1500-year climate oscillation in the midlatitude North Pacific during the Holocene, *Geology*, 37(7), 591–594, doi:10.1130/G25667A.1.
- Kaji, J., and Y. Nihei (2014), Evaluation of freshwater discharge and suspended sediment transport into Pacific Ocean from Tohoku and Kanto districts, , 70(4), 979–984.
- Kamatani, A., and O. Oku (2000), Measuring biogenic silica in marine sediments, *Mar. Chem.*, 68(3), 219–229, doi:10.1016/S0304-4203(99)00079-1.
- Kansanen, P. H., T. Jaakkola, S. Kulmala, and R. Suutarinen (1991), Sedimentation and distribution of gamma-emitting radionuclides in bottom sediments of southern Lake Päijänne, Finland, after the Chernobyl accident, *Hydrobiologia*, 222(2), 121–140, doi:10.1007/BF00006100.
- Kato, Y., H. Kitazato, M. Shimanaga, T. Nakatsuka, Y. Shirayama, and T.

- Masuzawa (2003),  $^{210}\text{Pb}$  and  $^{137}\text{Cs}$  in sediments from Sagami Bay, Japan: Sedimentation rates and inventories, *Prog. Oceanogr.*, 57(1), 77–95, doi:10.1016/S0079-6611(03)00052-1.
- Kay, A. L., H. N. Davies, V. A. Bell, and R. G. Jones (2009), Comparison of uncertainty sources for climate change impacts: Flood frequency in England, *Clim. Change*, 92(1–2), 41–63, doi:10.1007/s10584-008-9471-4.
- Kazama, S., K. Suzuki, and M. Sawamoto (2005), Estimation of rating-curve parameters for sedimentation using a physical model, *Hydrol. Process.*, 19(19), 3863–3871, doi:10.1002/hyp.5986.
- Kitagawa, H., and J. van der Plicht (2006), A 40,000-year varve chronology from Lake Suigetsu, Japan; extension of the (super 14) C calibration curve., *Radiocarbon*, 40(1), 505–515, doi:10.2458/azu\_js\_rc.40.2037.
- Kitagawa, H., H. Fukuzawa, T. Nakamura, M. Okamura, K. Takemura, A. Hayashida, and Y. Yasuda (1995), AMS (super 14) C dating of varved sediments from Lake Suigetsu, central Japan and atmospheric (super 14) C change during the late Pleistocene., *Radiocarbon*, 37(2), 371–378, doi:10.2458/azu\_js\_rc.37.1684.
- Klovan, J., and J. Imbrie (1971), An algorithm and Fortran-iv program for large-scale Q-mode factor analysis and calculation of factor scores, *Mathematical Geology*, Vol. 3, No. 1, 61-67
- Klovan, J., and A. Miesch (1976), Extended cabfac and Q model computer programs for Q-mode factor analysis of compositional data, *Comput. Geosci.* Vol. 1, 161-178
- Komatsubara, T. (2006), 寛文二年 (1662) 近江・若狭地震の地震像と被災地区の歴史地理的考察, *京都歴史災害研究*, 5, 21-38.
- Kubota, Y., R. Tada, and K. Kimoto (2015), Changes in East Asian summer monsoon precipitation during the Holocene deduced from a freshwater flux reconstruction of the Changjiang (Yangtze River) based on the oxygen isotope mass balance in the northern East China Sea, *Clim. Past*, 11(2), 265–281, doi:10.5194/cp-11-265-2015.
- Leinen, M., and N. Pisiias (1984), An objective technique for determining end-member compositions and for partitioning sediments according to their sources, *Geochim. Cosmochim. Acta*, 48, 47–62.
- Luo, P., B. He, K. Takara, Y. E. Xiong, D. Nover, W. Duan, and K. Fukushi (2015), Historical assessment of Chinese and Japanese flood management policies and implications for managing future floods,

- Environ. Sci. Policy, 48, 265–277, doi:10.1016/j.envsci.2014.12.015.
- Manda, A., H. Nakamura, N. Asano, S. Iizuka, T. Miyama, Q. Moteki, M. K. Yoshioka, K. Nishii, and T. Miyasaka (2014), Impacts of a warming marginal sea on torrential rainfall organized under the Asian summer monsoon., *Sci. Rep.*, 4, 5741, doi:10.1038/srep05741.
- Marshall, M. et al. (2012), A novel approach to varve counting using  $\mu$ XRF and X-radiography in combination with thin-section microscopy, applied to the Late Glacial chronology from Lake Suigetsu, Japan, *Quat. Geochronol.*, 13, 70–80, doi:10.1016/j.quageo.2012.06.002.
- McDonald, R. E., D. G. Bleaken, D. R. Cresswell, V. D. Pope, and C. A. Senior (2005), Tropical storms: Representation and diagnosis in climate models and the impacts of climate change, *Clim. Dyn.*, 25(1), 19–36, doi:10.1007/s00382-004-0491-0.
- Milliman, J. D., and J. P. M. Syvitski (1992), Geomorphic/Tectonic Control of Sediment Discharge to the Ocean: The Importance of Small Mountainous Rivers<sup>1</sup>, *J. Geol.*, 100, 525–544.
- Morton, R. A., G. Gelfenbaum, and B. E. Jaffe (2007), Physical criteria for distinguishing sandy tsunami and storm deposits using modern examples, *Sediment. Geol.*, 200(3–4), 184–207, doi:10.1016/j.sedgeo.2007.01.003.
- Nagashima, K., R. Tada, H. Matsui, and T. Irino (2007), Orbital-and millennial-scale variations in Asian dust transport path to the Japan Sea, *Palaeogeogr. Palaeoclimatol. Palaeoecol.*, 247, 144–161.
- Nagashima, K., Y. Suzuki, T. Irino, T. Nakagawa, R. Tada, Y. Hara, K. Yamada, and Y. Kurosaki (2016), Asian dust transport during the last century recorded in Lake Suigetsu sediments, *Geophys. Res. Lett.*, 43(6), 2835–2842, doi:10.1002/2015GL067589.
- Nakae, S., T. Komatsubara, and K. Naito (2002), Geology of the Nishizu District, *Quadrang. Ser. 150,000*, Geol. Surv. Japan, AIST, 10(78), 1–6.
- Nakagawa, T. et al. (2012), SG06, a fully continuous and varved sediment core from Lake Suigetsu, Japan: stratigraphy and potential for improving the radiocarbon calibration model and understanding of late Quaternary climate changes, *Quat. Sci. Rev.*, 36, 164–176, doi:10.1016/j.quascirev.2010.12.013.
- Nakai, Y. (2016MS), 過去1万5千年間における水月湖湖底堆積物への元素状炭素供給量の変動要因. 北海道大学大学院環境科学院地球圏科学専攻

- Nishiyama, A., T. Komatsubara, S. Azuma, S. Mizuno, I. Kitahara, M. Takemura, and A. Sangawa (2005), Source Faults and Processes of the AD1662 Kanbun Ohmi-Wakasa Earthquake, *Hist. Earthq.*, 20, 257–266.
- Okada, A., S. Katoh, D. Ishimura, and S. Saito (2010), Subsurface Geology at the Lake Mikata and Nakayama Lowlands, Fukui Prefecture, Central Japan: Implications on the Late Pleistocene Activity for the Mikata Fault Zone, *J. Geog.*, 119(5), 878–891.
- Oouchi, K., J. Yoshimura, H. Yoshimura, R. Mizuta, S. Kusunoki, and A. Noda (2006), Tropical Cyclone Climatology in a Global-Warming Climate as Simulated in a 20 km-Mesh Global Atmospheric Model: Frequency and Wind Intensity Analyses, *J. Meteorol. Soc. Japan*, 84(2), 259–276, doi:10.2151/jmsj.84.259.
- Osada, K. et al. (2014), Wet and dry deposition of mineral dust particles in Japan: factors related to temporal variation and spatial distribution, *Atmos. Chem. Phys.*, 14(2), 1107–1121, doi:10.5194/acp-14-1107-2014.
- Pennington, W., T. G. Tutin, R. S. Cambray, and E. M. Fisher (1973), Observations on Lake Sediments using Fallout Cs-137 as a Tracer, *Nature*, 242, 324–326, doi:10.1038/242324a0.
- PR magazine of Mikata-Town (2005), Looking back the history of Mikata-Town
- Sadeghi, S. H. R., T. Mizuyama, S. Miyata, T. Gomi, K. Kosugi, T. Fukushima, S. Mizugaki, and Y. Onda (2008), Development, evaluation and interpretation of sediment rating curves for a Japanese small mountainous reforested watershed, *Geoderma*, 144(1–2), 198–211, doi:10.1016/j.geoderma.2007.11.008.
- Saito-Kato, M., K. Yamada, R. A. Staff, T. Nakagawa, H. Yonenobu, T. Haraguchi, K. Takemura, and C. B. Ramsey (2013), An Assessment of the Magnitude of the AD1586 Tensho Tsunami Inferred from Lake Suigetsu Sediment Cores, *J. Geogr. (Chigaku Zasshi)*, 122(3), 493–501, doi:10.5026/jgeography.122.493.
- Schillereff, D. N., R. C. Chiverrell, N. Macdonald, and J. M. Hooke (2014), Flood stratigraphies in lake sediments: A review, *Earth-Science Rev.*, 135, 17–37, doi:10.1016/j.earscirev.2014.03.011.
- Schimmelmann, A., C. B. Lange, J. Schieber, P. Francus, A. E. K. Ojala, and B. Zolitschka (2016), Varves in marine sediments: A review, *Earth-Science Rev.*, 159, 215–246, doi:10.1016/j.earscirev.2016.04.009.

- Schlolaut, G. et al. (2012), An automated method for varve interpolation and its application to the Late Glacial chronology from Lake Suigetsu, Japan, *Quat. Geochronol.*, 13, 52–69.
- Schlolaut, G. et al. (2014), Event layers in the Japanese Lake Suigetsu “SG06” sediment core: description, interpretation and climatic implications, *Quat. Sci. Rev.*, 83, 157–170.
- Smith, V. C., R. a. Staff, S. P. E. Blockley, C. Bronk Ramsey, T. Nakagawa, D. F. Mark, K. Takemura, and T. Danhara (2013), Identification and correlation of visible tephras in the Lake Suigetsu SG06 sedimentary archive, Japan: chronostratigraphic markers for synchronising of east Asian/west Pacific palaeoclimatic records across the last 150 ka, *Quat. Sci. Rev.*, 67, 121–137, doi:10.1016/j.quascirev.2013.01.026.
- Staff, R., G. Schlolaut, and C. Ramsey (2013), Integration of the Old and New Lake Suigetsu (Japan) Terrestrial Radiocarbon Calibration Data Sets, *Radiocarbon*, 55(4), 2049–2058.
- Staff, R. a et al. (2011), New 14C Determinations from Lake Suigetsu, Japan: 12,000 to 0 cal BP, *Radiocarbon*, 53(3), 511–528, doi:10.2458/azu\_js\_rc.53.12340.
- Staff, R. a., C. Bronk Ramsey, and T. Nakagawa (2010), A re-analysis of the Lake Suigetsu terrestrial radiocarbon calibration dataset, *Nucl. Instruments Methods Phys. Res. Sect. B Beam Interact. with Mater. Atoms*, 268(7–8), 960–965, doi:10.1016/j.nimb.2009.10.074.
- Sturm, M., and A. Matter (1978), Turbidites and varves in Lake Brienz (Switzerland): deposition of clastic detritus by density currents, in *Special Publications of the International Association of Sedimentologists* 2, pp. 147–168.
- Tada, R., and R. W. Murray (2016), Preface for the article collection “Land–Ocean Linkages under the Influence of the Asian Monsoon,” *Prog. Earth Planet. Sci.*, 3(1), 24, doi:10.1186/s40645-016-0100-y.
- Tang, Q., X. Zhang, and A. Francis, Jennifer (2014), Extreme summer weather in northern mid-latitudes linked to a vanishing cryosphere, *Nat. Clim. Chang.*, 4(1), 45–50, doi:10.1038/nclimate2065.
- Toomey, M. R., J. P. Donnelly, and J. D. Woodruff (2013), Reconstructing mid-late Holocene cyclone variability in the Central Pacific using sedimentary records from Tahaa, French Polynesia, *Quat. Sci. Rev.*, 77, 181–189, doi:10.1016/j.quascirev.2013.07.019.

- Usami, T. (2003), *Materials for Comprehensive List of Destructive Earthquakes in Japan*. Tokyo University Press.
- Walden, J., J. Smith, and R. Dackombe (1992), The use of simultaneous R-and Q-mode factor analysis as a tool for assisting interpretation of mineral magnetic data, *Math. Geol.*
- Wang, B., and L. Ho (2002), Rainy season of the Asian-Pacific summer monsoon, *J. Clim.*, 15(4), 386–398, doi:10.1175/1520-0442(2002)015.
- Williams, A. G. B., and M. M. Scherer (2004), Spectroscopic evidence for Fe(II)-Fe(III) electron transfer at the iron oxide-water interface, *Environ. Sci. Technol.*, 38(18), 4782–4790, doi:10.1021/es049373g.
- Wu, Q. et al. (2016), Outburst flood at 1920 BCE supports historicity of Chinas Great Flood and the Xia dynasty, *Science (80- .)*, 353(6299), 579–582, doi:10.1126/science.aaf0842.
- Yang, G., Z. Chen, F. Yu, Z. Wang, and Y. Zhao (2007), Sediment rating parameters and their implications: Yangtze River, China, *Geomorphology*, 85(3–4), 166–175.
- Yasuda, Y., K. Yamaguchi, T. Nakagawa, H. Fukusawa, J. Kitagawa, and M. Okamura (2004), Environmental variability and human adaptation during the Lateglacial/Holocene transition in Japan with reference to pollen analysis of the SG4 core from Lake Suigetsu, *Quat. Int.*, 123–125, 11–19, doi:10.1016/j.quaint.2004.02.003.
- Yin, H., and C. Li (2001), Human impact on floods and flood disasters on the Yangtze River, *Geomorphology*, 41(2), 105–109, doi:10.1016/S0169-555X(01)00108-8.
- Zolitschka, B., P. Francus, A. E. K. Ojala, and A. Schimmelmann (2015), Varves in lake sediments - a review, *Quat. Sci. Rev.*, 117, 1–41, doi:10.1016/j.quascirev.2015.03.019.



## Supplementary Data

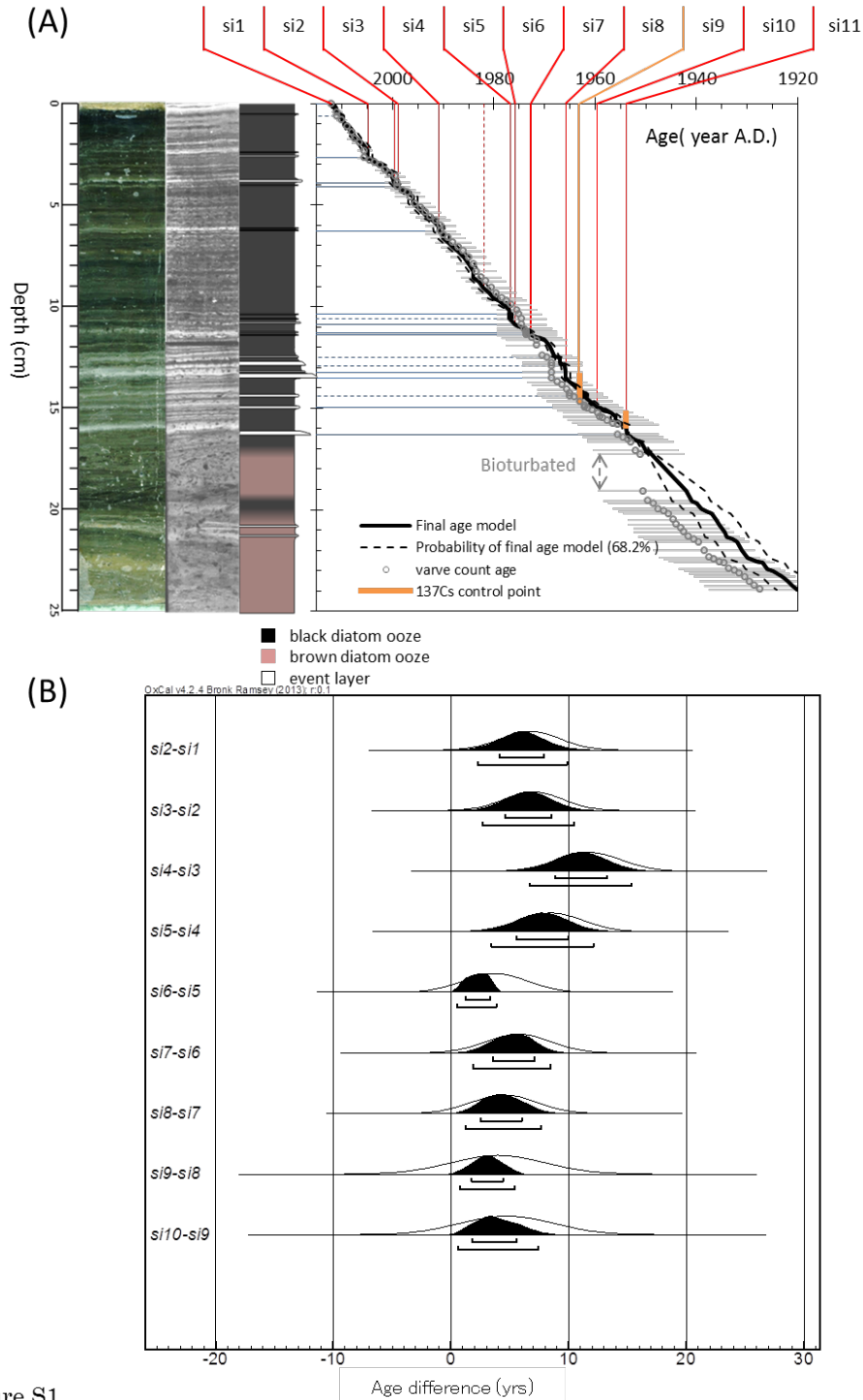


Figure S1  
 (A) Sample intervals of SG12LM3 used for Bayesian analysis and (B) estimated age differences between the centers of neighboring sample intervals using Bayesian analysis. Open and close ranges show probabilities of age differences based on varve counting and its coupling with Bayesian analysis, respectively.

Table S1 Varve count age model and fine-tuned age model with distance from core top of SG12LM3 core.

depth (distance from core top: cm)	Varve count		Fine tuned age model		
	varve count age (yr A.D.)	varve count error	median (yr A.D.)	68.2% probability (younger)	68.2% probability (older)
0.0	2012.0	1.0	2012.0	2012.5	2011.5
0.4	2011.0	1.0	2011.0	2011.5	2010.5
0.6	2011.0	1.0	2010.0	2010.5	2009.5
0.8	2010.0	1.0	2010.0	2010.5	2009.5
1.1	2009.0	1.0	2009.0	2009.5	2008.5
1.4	2008.0	1.0	2008.0	2009.0	2007.1
1.7	2007.5	1.5	2007.0	2008.0	2006.1
1.9	2006.5	1.5	2006.0	2007.0	2005.1
2.3	2005.5	1.5	2005.0	2006.0	2004.1
2.7	2005.5	1.5	2004.9	2005.8	2003.9
2.8	2004.5	1.5	2004.0	2005.0	2003.1
2.9	2003.5	1.5	2003.0	2004.0	2002.1
3.0	2002.5	1.5	2002.0	2003.0	2001.1
3.3	2001.5	2.0	2001.0	2002.0	2000.1
3.4	2000.5	2.0	2000.0	2001.0	1999.1
3.6	1999.5	2.0	2000.0	2001.0	1999.1
3.9	1999.0	2.5	1999.7	2000.7	1998.8
4.1	1999.0	2.5	1998.8	1999.8	1997.9
4.3	1998.0	2.5	1998.0	1999.0	1997.1
4.4	1997.0	2.5	1997.0	1998.0	1996.1
4.6	1996.5	3.0	1996.0	1997.0	1995.1
4.9	1995.5	3.0	1996.0	1997.0	1995.1
5.1	1994.5	3.0	1995.0	1996.1	1993.9
5.4	1993.5	3.0	1994.0	1995.1	1992.9
5.6	1992.5	3.0	1993.0	1994.1	1991.9
5.8	1991.5	3.0	1992.0	1993.1	1990.9
6.0	1990.5	3.0	1991.0	1992.1	1989.9
6.3	1990.5	3.0	1990.8	1991.9	1989.7
6.4	1990.0	3.5	1990.0	1991.1	1988.9
6.6	1989.0	3.5	1990.0	1991.1	1988.9
6.9	1988.0	3.5	1989.0	1990.1	1987.9
7.1	1987.0	3.5	1988.0	1989.1	1986.9
7.3	1986.0	3.5	1987.0	1988.1	1985.9
7.6	1985.0	3.5	1986.0	1987.1	1984.9
7.9	1984.0	3.5	1985.0	1986.1	1983.9
8.3	1983.5	4.0	1984.0	1985.1	1982.9
8.6	1982.5	4.0	1984.0	1985.1	1982.9
8.8	1981.5	4.0	1983.0	1984.1	1981.9
9.1	1980.5	4.0	1982.0	1983.1	1980.9
9.3	1979.5	4.0	1981.0	1982.1	1979.9
9.6	1978.5	4.0	1980.0	1981.1	1978.9
9.7	1977.5	4.0	1979.0	1980.1	1977.9
9.9	1976.5	4.0	1978.0	1979.1	1976.9
10.2	1975.5	4.0	1977.0	1977.5	1976.6
10.4	1975.0	4.5	1976.8	1977.2	1976.3
10.6	1974.5	5.0	1976.8	1977.2	1976.3
10.9	1974.5	5.0	1975.7	1976.2	1975.3
11.1	1974.0	5.5	1974.0	1974.9	1973.2
11.2	1973.5	6.0	1973.0	1973.9	1972.2
11.3	1973.5	6.0	1972.8	1973.6	1971.9
11.4	1973.5	6.0	1972.6	1973.5	1971.8
11.5	1972.5	6.0	1971.0	1971.9	1970.2
11.7	1971.5	6.0	1970.0	1970.9	1969.2
11.9	1971.5	6.0	1969.0	1969.9	1968.2
12.4	1970.5	6.0	1968.0	1968.9	1967.2
12.5	1969.5	6.0	1967.0	1967.9	1966.2
12.8	1968.5	6.0	1967.0	1967.9	1966.2
12.9	1968.5	6.0	1966.0	1966.9	1965.2
13.2	1968.5	6.0	1965.8	1966.7	1965.0

(Continued)

Table S1 Varve count age model and fine-tuned age model with distance from core top of SG12LM3 core.

depth (distance from core top: cm)	Varve count		Fine tuned age model		
	varve count age (yr A.D.)	varve count error	median (yr A.D.)	68.2% probability (younger)	68.2% probability (older)
13.5	1968.5	6.0	1965.8	1966.6	1964.9
13.7	1967.5	6.0	1965.0	1965.6	1964.4
13.9	1966.5	6.0	1964.0	1964.6	1963.4
14.1	1965.5	6.0	1963.0	1963.6	1962.4
14.3	1965.0	6.5	1962.0	1962.6	1961.4
14.4	1965.0	6.5	1962.0	1962.6	1961.4
14.5	1964.0	6.5	1962.0	1962.6	1961.4
14.7	1963.0	6.5	1961.0	1961.9	1960.2
14.9	1962.0	6.5	1960.0	1960.9	1959.2
15.0	1962.0	6.5	1959.7	1960.6	1958.9
15.0	1961.5	7.0	1959.0	1959.9	1958.2
15.1	1960.5	7.0	1958.0	1958.9	1957.2
15.2	1959.5	7.0	1957.0	1957.9	1956.2
15.4	1959.0	7.5	1956.0	1956.9	1955.2
15.5	1958.5	8.0	1956.0	1956.9	1955.2
15.6	1957.5	8.0	1956.0	1956.9	1955.2
15.7	1956.5	8.0	1955.0	1955.9	1954.2
15.8	1955.5	8.0	1954.0	1954.9	1953.2
16.3	1955.5	8.0	1953.8	1954.3	1953.3
16.4	1954.5	8.0	1953.0	1953.5	1952.5
16.6	1953.5	8.0	1952.0	1952.5	1951.5
16.7	1953.0	8.5	1951.0	1951.8	1950.3
17.1	1952.0	8.5	1950.0	1950.8	1949.3
17.3	1951.0	8.5	1949.0	1949.8	1948.3
19.1	1950.5	9.0	1942.0	1945.8	1938.3
19.6	1949.5	9.0	1941.0	1944.8	1937.3
19.7	1948.5	9.0	1940.0	1943.8	1936.3
20.0	1947.5	9.0	1939.0	1942.8	1935.3
20.1	1946.5	9.0	1938.0	1941.8	1934.3
20.2	1945.5	9.0	1937.0	1940.8	1933.3
20.5	1944.5	9.0	1936.0	1939.8	1932.3
20.7	1944.0	9.5	1935.5	1939.5	1931.5
20.9	1943.0	9.5	1935.0	1939.0	1931.0
21.1	1942.5	10.0	1934.5	1938.8	1930.3
21.3	1941.5	10.0	1934.0	1938.3	1929.8
21.5	1940.5	10.0	1933.0	1937.3	1928.8
21.6	1939.5	10.0	1932.0	1936.3	1927.8
22.0	1938.5	10.0	1931.0	1935.3	1926.8
22.3	1937.5	10.0	1930.0	1934.3	1925.8
22.4	1936.5	10.0	1929.0	1933.3	1924.8
22.6	1935.5	10.0	1928.0	1932.3	1923.8
22.6	1934.5	10.0	1927.0	1931.3	1922.8
22.9	1933.5	10.0	1926.0	1930.3	1921.8
23.0	1932.5	10.0	1925.0	1929.3	1920.8
23.1	1931.5	10.0	1924.0	1928.3	1919.8
23.3	1930.5	10.0	1923.0	1927.3	1918.8
23.5	1929.5	10.0	1922.0	1926.3	1917.8
23.7	1928.5	10.0	1921.0	1925.3	1916.8
23.9	1927.5	10.0	1920.0	1924.3	1915.8

Table S2 List of  $^{137}\text{Cs}$ ,  $\text{Excess } ^{210}\text{Pb}$ ,  $^{210}\text{Pb}$  and  $^{214}\text{Pb}$  measurement in SGI2LM3 core.

No.	Dpeth		$^{137}\text{Cs}$		$\text{Excess } ^{210}\text{Pb}$		$^{210}\text{Pb}$		$^{214}\text{Pb}$	
	top (cm)	bottom(cm)	(Bq/g)	error	(Bq/g)	error	(Bq/g)	error	(Bq/g)	error
4	1.7	2.2	0.015646	0.005864	12.00046	0.010213	12.06161	0.334591	0.921587	0.061149
8	4	4.6	0.026823	0.004997	8.341919	0.010913	8.400838	0.343597	0.970915	0.05892
12	6.4	7	0.045893	0.00493	7.710803	0.01178	7.779793	0.373391	1.070899	0.068989
16	8.9	9.5	0.050151	0.005987	5.958494	0.009501	6.014487	0.288823	0.825909	0.055993
19	10.7	11.3	0.057887	0.006545	3.685787	0.009709	3.772909	0.29379	0.857085	0.087122
20	11.3	11.9	0.087351	0.008809	3.674778	0.012963	3.758719	0.341701	0.988531	0.083941
21	11.9	12.55	0.079691	0.004663	2.704556	0.008604	2.758637	0.248651	0.727843	0.054081
22	12.55	13.1	0.079975	0.004988	1.490902	0.007715	1.568555	0.204747	0.605907	0.077653
24	13.7	14.3	0.147119	0.009447	2.558034	0.011254	2.631133	0.324609	0.953167	0.073099
26	14.95	15.55	0.08695	0.007651	3.32477	0.011048	3.386543	0.337639	0.99069	0.061772
28	16.2	16.7	0.002151	0.005408	0.509398	0.009567	0.598029	0.137976	0.876341	0.088631
30	17.3	17.9	0.000795	0.005758	1.946509	0.010087	2.01088	0.178355	0.514267	0.06437
32	18.55	19.2	-0.00404	0.006443	3.005995	0.010212	3.096402	0.27231	0.795211	0.090407
34	19.75	20.4	-0.00256	0.006716	2.304908	0.013472	2.319237	0.234471	0.688137	0.014328
36	21	21.6	-0.00471	0.005218	1.044071	0.007513	1.085675	0.243662	0.727747	0.041604

Table S3 List of top and bottom age, varve count and its error of each "si" input as prior probability of Bayesian analysis.

Sample Name	top age (yr A.D.) constrained by flood and $^{137}\text{Cs}$	bottom age (yr A.D.) constraint by flood and $^{137}\text{Cs}$	varve counts in each si (yr)	varve count error (yr)
SG12LM3-si01	2012	2004.9	8	2.5
SG12LM3-si02	2004.9	1998.8	5.5	2.5
SG12LM3-si03	1998.8	1990.8	8.5	2.5
SG12LM3-si04	1990.8	1976.8	15	3
SG12LM3-si05	1976.8	1975.7	2	2.5
SG12LM3-si06	1975.7	1972.6	5.5	3
SG12LM3-si07	1972.6	1965.8	6	2.5
SG12LM3-si08	1965.8	1963	3	3
SG12LM3-si09	1963	1959.7	5	5
SG12LM3-si10	1959.7	1954	4.5	3
SG12LM3-si11	1954	-	32.5	4.5

Table S4 List of age differences for SG12LM3 estimated by Bayesian analysis.

Sample Name	unmodelled		modelled age difference					agreement index (%)						
	varve count age difference (yr)	varve count error (yr)	median (yr)	mean (yr)	error (yr)	68.2% probability	95.4% probability							
SG12LM3-si01	-	SG12LM3-si02	6.75	2.5	6.0	6.0	1.9	4.1	-	7.9	2.3	-	9.9	110.1
SG12LM3-si02	-	SG12LM3-si03	7	2.5	6.6	6.6	1.9	4.6	-	8.6	2.7	-	10.4	111.0
SG12LM3-si03	-	SG12LM3-si04	11.75	2.75	11.0	11.0	2.2	8.8	-	13.2	6.7	-	15.3	108.8
SG12LM3-si04	-	SG12LM3-si05	8.5	2.75	7.8	7.8	2.2	5.6	-	10.0	3.4	-	12.1	108.8
SG12LM3-si05	-	SG12LM3-si06	3.75	2.75	2.3	2.2	0.9	1.3	-	3.3	0.5	-	3.9	117.0
SG12LM3-si06	-	SG12LM3-si07	5.75	2.75	5.3	5.2	1.7	3.6	-	7.1	1.9	-	8.5	118.8
SG12LM3-si07	-	SG12LM3-si08	4.5	2.75	4.3	4.4	1.7	2.5	-	6.0	1.2	-	7.8	120.2
SG12LM3-si08	-	SG12LM3-si09	4	4	3.1	3.1	1.2	1.8	-	4.4	0.7	-	5.4	132.2
SG12LM3-si09	-	SG12LM3-si10	4.75	4	3.8	3.9	1.7	1.8	-	5.6	0.6	-	7.4	126.8

Table S5 List of depth, age and physical property of SG12core samples.

Sample Number	Hole	Section	top	bottom	center	facies*	center	center	age	WC	DBD	GD
			distance from section top (cm)	distance from section top (cm)	distance from section top (cm)	0: BG 1: including EL-G 2: including EL-B 3: Tephra	composite depth (cm)	age (yr BP)	error (yr)			
SG12_YS_XRF_1	X	1	9.81	10.89	10.35	1	30.3741	-30	2	81.01	0.19	0.90
SG12_YS_XRF_2	X	1	10.89	11.97	11.43	0	31.4941	-27	2	81.92	0.18	0.97
SG12_YS_XRF_3	X	1	11.97	13	12.485	1	32.585	-24	2	81.15	0.18	0.87
SG12_YS_XRF_4	X	1	13	14.01	13.505	0	33.605	-18	3	82.93	0.17	0.92
SG12_YS_XRF_5	X	1	14.01	15.01	14.51	0	34.61	-13	3	82.55	0.17	0.89
SG12_YS_XRF_6	X	1	15.01	16.01	15.51	0	35.61	-7	4	84.83	0.14	0.76
SG12_YS_XRF_7	X	1	16.01	17.02	16.515	0	36.615	-1	5	84.97	0.14	0.76
SG12_YS_XRF_8	X	1	17.02	18.02	17.52	0	37.62	5	5	82.55	0.17	0.91
SG12_YS_XRF_9	X	1	18.02	19.03	18.525	0	38.625	11	6	80.59	0.19	0.95
SG12_YS_XRF_10	X	1	19.03	20.03	19.53	0	39.63	17	7	82.51	0.17	0.88
SG12_YS_XRF_11	X	1	20.03	21.03	20.53	0	40.63	23	7	78.82	0.22	1.14
SG12_YS_XRF_12	X	1	21.03	22.04	21.535	0	41.635	29	8	81.68	0.18	0.98
SG12_YS_XRF_13	X	1	22.04	23.04	22.54	0	42.64	34	8	81.65	0.18	0.87
SG12_YS_XRF_14	X	1	23.04	24.05	23.545	0	43.645	39	8	84.26	0.15	0.89
SG12_YS_XRF_15	X	1	24.05	25.05	24.55	0	44.65	45	8	82.02	0.18	1.06
SG12_YS_XRF_16	X	1	25.05	26.05	25.55	0	45.65	50	8	80.69	0.19	1.00
SG12_YS_XRF_17	X	1	26.05	27.06	26.555	0	46.655	55	7	81.95	0.17	0.84
SG12_YS_XRF_18	X	1	27.06	28.06	27.56	0	47.66	60	7	86.45	0.13	0.71
SG12_YS_XRF_19	X	1	28.06	29.07	28.565	0	48.665	65	7	82.02	0.18	1.00
SG12_YS_XRF_20	X	1	29.07	30.07	29.57	0	49.67	70	7	82.05	0.18	0.91
SG12_YS_XRF_21	X	1	30.07	31.07	30.57	0	50.67	76	7	81.42	0.19	1.26
SG12_YS_XRF_22	X	1	31.07	32.08	31.575	0	51.675	81	7	83.71	0.16	0.90
SG12_YS_XRF_23	X	1	32.08	33.08	32.58	0	52.68	86	7	82.70	0.17	0.88
SG12_YS_XRF_24	X	1	33.08	34.09	33.585	0	53.685	91	7	82.11	0.18	1.13
SG12_YS_XRF_25	X	1	34.09	35.09	34.59	0	54.69	96	7	79.82	0.21	1.26
SG12_YS_XRF_26	X	1	35.09	36.09	35.59	0	55.69	101	6	79.38	0.25	8.32
SG12_YS_XRF_27	X	1	36.09	37.1	36.595	1	56.695	106	6	72.19	0.30	1.43
SG12_YS_XRF_28	X	1	37.1	38.07	37.585	0	57.7052	112	6	79.10	0.20	0.85
SG12_YS_XRF_29	X	1	38.07	39.03	38.55	0	58.7754	117	6	80.09	0.20	1.08
SG12_YS_XRF_30	X	1	39.03	39.99	39.51	0	59.84	123	6	79.43	0.21	1.07
SG12_YS_XRF_31	X	1	39.99	40.95	40.47	0	60.9047	128	6	78.15	0.23	1.19
SG12_YS_XRF_32	X	1	40.95	41.91	41.43	0	61.9694	134	6	78.58	0.22	1.04
SG12_YS_XRF_33	X	1	41.91	42.87	42.39	0	63.034	139	6	81.43	0.18	0.92
SG12_YS_XRF_34	X	1	42.87	43.83	43.35	0	64.0987	145	5	76.24	0.27	1.83
SG12_YS_XRF_35	X	1	43.83	44.79	44.31	0	65.1633	150	5	80.66	0.19	0.92
SG12_YS_XRF_36	X	1	44.79	45.75	45.27	0	66.228	155	5	80.06	0.20	1.01
SG12_YS_XRF_37	X	1	45.75	46.71	46.23	0	67.2927	161	5	81.42	0.20	1.50
SG12_YS_XRF_38	X	1	46.71	47.68	47.195	0	68.3629	167	5	80.12	0.20	1.15
SG12_YS_XRF_39	X	1	47.68	48.64	48.16	0	69.4331	174	5	81.14	0.19	1.04
SG12_YS_XRF_40	X	1	48.64	49.6	49.12	0	70.4977	180	5	80.57	0.20	1.10
SG12_YS_XRF_41	X	1	49.6	50.56	50.08	0	71.5624	186	5	81.77	0.19	1.17
SG12_YS_XRF_42	X	1	50.56	51.52	51.04	0	72.6271	193	5	81.28	0.19	1.04
SG12_YS_XRF_43	X	1	51.52	52.48	52	0	73.6917	199	5	81.41	0.19	1.17
SG12_YS_XRF_44	X	1	52.48	53.44	52.96	0	74.7564	205	5	79.99	0.22	1.71
SG12_YS_XRF_45	X	1	53.44	54.4	53.92	0	75.8211	212	5	81.01	0.20	1.39
SG12_YS_XRF_46	X	1	54.4	55.36	54.88	0	76.8857	218	5	79.65	0.20	0.97
SG12_YS_XRF_47	X	1	55.36	56.32	55.84	0	77.9504	224	5	81.47	0.19	1.10
SG12_YS_XRF_48	X	1	56.32	57.28	56.8	0	79.015	231	5	80.60	0.20	1.32
SG12_YS_XRF_49	X	1	57.28	58.24	57.76	0	80.0797	237	5	84.43	0.16	0.99
SG12_YS_XRF_50	X	1	58.24	59.2	58.72	1	81.1444	243	5	81.58	0.19	1.11
SG12_YS_XRF_51	X	1	59.2	60.16	59.68	0	82.209	250	5	83.60	0.18	1.65
SG12_YS_XRF_52	X	1	60.16	61.12	60.64	0	83.2737	256	5	82.45	0.17	0.85
SG12_YS_XRF_53	X	1	61.12	62.08	61.6	0	84.3383	262	5	81.99	0.19	1.22
SG12_YS_XRF_54	X	1	62.08	63.04	62.56	0	85.403	269	5	81.67	0.20	1.54
SG12_YS_XRF_55	X	1	63.04	64	63.52	0	86.4677	275	5	82.39	0.18	1.07
SG12_YS_XRF_56	X	1	64	65.15	64.575	0	87.6053	282	5	84.41	0.16	1.13
SG12_YS_XRF_57	X	1	65.15	66.3	65.725	0	88.8158	287	5	85.99	0.15	2.03
SG12_YS_XRF_58	X	1	66.3	67.45	66.875	0	90.0263	292	6	83.11	0.17	1.01
SG12_YS_XRF_59	Y	1	19.8	20.8	20.3	0	90.6	295	6	83.35	0.17	1.28
SG12_YS_XRF_60	X	1	67.45	68.6	68.025	0	91.225	297	6	84.35	0.16	0.96
SG12_YS_XRF_61	Y	1	20.8	21.81	21.305	0	91.68	299	6	82.09	0.18	1.07

(Continued)

Table S5 List of depth, age and physical property of SG12core samples.

Sample Number	Hole	Section	top	bottom	center	facies*	center	center	age	WC	DBD	GD
			distance from section top (cm)	distance from section top (cm)	distance from section top (cm)	0: BG 1: including EL-G 2: including EL-B 3: Tephra	composite depth (cm)	age (yr BP)	error (yr)			
SG12_YS_XRF_62	X	1	68.6	69.75	69.175	0	92.375	302	6	82.67	0.18	1.11
SG12_YS_XRF_63	Y	1	21.81	22.82	22.315	0	92.6542	303	6	79.93	0.20	0.98
SG12_YS_XRF_64	Y	1	22.82	23.82	23.32	0	93.6235	307	6	80.95	0.20	1.32
SG12_YS_XRF_65	Y	1	23.82	24.83	24.325	0	94.5929	311	7	80.96	0.20	1.46
SG12_YS_XRF_66	Y	1	24.83	25.84	25.335	0	95.5671	315	7	82.29	0.18	0.98
SG12_YS_XRF_67	Y	1	25.84	26.84	26.34	0	96.5365	319	7	80.77	0.20	1.40
SG12_YS_XRF_68	Y	1	26.84	27.85	27.345	0	97.5058	323	7	78.26	0.24	1.62
SG12_YS_XRF_69	Y	1	27.85	28.86	28.355	0	98.48	327	8	75.87	0.28	2.07
SG12_YS_XRF_70	Y	1	28.86	29.87	29.365	0	99.4542	331	8	74.48	0.28	1.54
SG12_YS_XRF_71	Y	1	29.87	30.87	30.37	0	100.4235	335	8	78.71	0.23	1.43
SG12_YS_XRF_72	Y	1	30.87	31.88	31.375	0	101.3929	339	8	78.11	0.24	1.50
SG12_YS_XRF_73	Y	1	31.88	32.89	32.385	0	102.3671	343	9	77.28	0.25	1.57
SG12_YS_XRF_74	Y	1	32.89	33.89	33.39	0	103.3365	347	9	78.37	0.27	7.04
SG12_YS_XRF_75	Y	1	33.89	34.9	34.395	0	104.3058	351	9	77.81	0.24	1.46
SG12_YS_XRF_76	Y	1	34.9	35.9	35.4	0	105.3022	356	10	76.23	0.26	1.48
SG12_YS_XRF_77	Y	1	35.9	36.91	36.405	0	106.3103	360	10	73.57	0.31	2.02
SG12_YS_XRF_78	Y	1	36.91	37.91	37.41	0	107.3184	365	11	74.80	0.28	1.69
SG12_YS_XRF_79	Y	1	37.91	38.91	38.41	0	108.3215	370	11	73.93	0.30	1.86
SG12_YS_XRF_80	Y	1	38.91	39.92	39.415	0	109.3296	374	11	79.66	0.22	1.63
SG12_YS_XRF_81	Y	1	39.92	40.92	40.42	0	110.3377	379	11	79.76	0.22	1.42
SG12_YS_XRF_82	Y	1	40.92	41.92	41.42	0	111.3408	384	12	78.47	0.24	2.07
SG12_YS_XRF_83	Y	1	41.92	42.93	42.425	0	112.3489	389	12	79.01	0.22	1.45
SG12_YS_XRF_84	Y	1	42.93	43.93	43.43	0	113.357	394	12	79.11	0.22	1.49
SG12_YS_XRF_85	Y	1	43.93	44.93	44.43	0	114.3601	399	12	79.22	0.22	1.46
SG12_YS_XRF_86	Y	1	44.93	45.93	45.43	0	115.3632	404	12	79.03	0.23	1.84
SG12_YS_XRF_87	Y	1	45.93	46.94	46.435	0	116.3713	408	12	79.01	0.23	1.53
SG12_YS_XRF_88	Y	1	46.94	47.94	47.44	0	117.3794	413	11	79.31	0.23	2.02
SG12_YS_XRF_89	Y	1	47.94	48.94	48.44	0	118.3825	418	11	78.20	0.24	1.59
SG12_YS_XRF_90	Y	1	48.94	49.95	49.445	0	119.3906	423	11	79.34	0.22	1.59
SG12_YS_XRF_91	Y	1	49.95	50.95	50.45	0	120.3988	428	11	79.85	0.21	1.38
SG12_YS_XRF_92	Y	1	50.95	51.95	51.45	0	121.4019	433	11	79.49	0.22	1.49
SG12_YS_XRF_93	Y	1	51.95	52.96	52.455	0	122.41	438	10	79.29	0.22	1.54
SG12_YS_XRF_94	Y	1	52.96	53.96	53.46	0	123.4181	442	10	79.43	0.22	1.57
SG12_YS_XRF_95	Y	1	53.96	54.96	54.46	0	124.4212	447	10	79.10	0.22	1.44
SG12_YS_XRF_96	Y	1	54.96	55.97	55.465	0	125.4293	452	10	79.62	0.22	1.51
SG12_YS_XRF_97	Y	1	55.97	56.97	56.47	0	126.4374	457	10	78.10	0.23	1.44
SG12_YS_XRF_98	Y	1	56.97	57.97	57.47	0	127.4405	462	10	80.05	0.22	1.76
SG12_YS_XRF_99	Y	1	57.97	58.98	58.475	0	128.4486	467	9	78.93	0.23	1.69
SG12_YS_XRF_100	Y	1	58.98	59.98	59.48	0	129.4567	472	9	81.00	0.20	1.44
SG12_YS_XRF_101	Y	1	59.98	60.98	60.48	0	130.4598	476	9	78.90	0.23	1.65
SG12_YS_XRF_102	Y	1	60.98	61.98	61.48	0	131.4629	481	9	80.79	0.21	1.76
SG12_YS_XRF_103	Y	1	61.98	62.99	62.485	0	132.471	486	9	79.32	0.23	1.76
SG12_YS_XRF_104	Y	1	62.99	63.99	63.49	0	133.4791	491	9	76.87	0.25	1.62
SG12_YS_XRF_105	Y	1	63.99	64.99	64.49	0	134.4822	496	8	75.74	0.27	1.71
SG12_YS_XRF_106	Z	2	14.91	15.91	15.41	0	135.31	500	8	74.11	0.28	1.54
SG12_YS_XRF_107	Y	1	64.99	66	65.495	0	135.4903	501	8	74.46	0.28	1.44
SG12_YS_XRF_108	Z	2	15.91	16.9	16.405	1	136.305	505	8	72.57	0.33	2.61
SG12_YS_XRF_109	Y	1	66	67	66.5	1	136.4985	505	8	72.32	0.32	1.93
SG12_YS_XRF_110	Z	2	16.9	17.9	17.4	0	137.3027	509	8	78.70	0.23	1.40
SG12_YS_XRF_111	Y	1	67	68.01	67.505	0	137.505	510	8	79.04	0.22	1.37
SG12_YS_XRF_112	Z	2	17.9	18.91	18.405	0	138.3169	514	8	78.17	0.23	1.42
SG12_YS_XRF_113	Z	2	18.91	19.92	19.415	0	139.3362	518	8	77.37	0.25	1.66
SG12_YS_XRF_114	Z	2	19.92	20.92	20.42	0	140.3504	523	8	79.57	0.22	1.38
SG12_YS_XRF_115	Z	2	20.92	21.93	21.425	0	141.3646	527	8	79.44	0.22	1.51
SG12_YS_XRF_116	Z	2	21.93	22.94	22.435	0	142.3838	532	8	78.29	0.24	1.98
SG12_YS_XRF_117	Z	2	22.94	23.94	23.44	0	143.398	536	8	79.51	0.22	1.36
SG12_YS_XRF_118	Z	2	23.94	24.95	24.445	0	144.4122	541	7	80.11	0.21	1.33
SG12_YS_XRF_119	Z	2	24.95	25.95	25.45	0	145.4264	546	7	79.62	0.21	1.20
SG12_YS_XRF_120	Z	2	25.95	26.96	26.455	0	146.4406	550	7	79.39	0.23	1.70
SG12_YS_XRF_121	Z	2	26.96	27.97	27.465	0	147.4598	555	7	78.17	0.23	1.39
SG12_YS_XRF_122	Z	2	27.97	28.97	28.47	0	148.474	559	7	78.15	0.23	1.47

(Continued)

Table S5 List of depth, age and physical property of SG12core samples.

Sample Number	Hole	Section	top	bottom	center	facies*	center composite depth (cm)	center age (yr BP)	age error (yr)	WC (wt %)	DBD (g/cm <sup>3</sup> )	GD (g/cm <sup>3</sup> )
			distance from section top (cm)	distance from section top (cm)	distance from section top (cm)	0: BG 1: including EL-G 2: including EL-B 3: Tephra						
SG12_YS_XRF_123	Z	2	28.97	29.98	29.475	0	149.4882	564	7	75.97	0.26	1.56
SG12_YS_XRF_124	Z	2	29.98	30.98	30.48	0	150.5024	568	7	77.96	0.24	1.63
SG12_YS_XRF_125	Z	2	30.98	32.99	31.985	0	152.0211	575	7	81.06	0.20	1.29
SG12_YS_XRF_126	Z	2	32.99	33	32.995	0	153.0404	580	7	80.61	0.20	1.19
SG12_YS_XRF_127	Z	2	33	34	33.5	0	153.55	582	8	77.25	0.25	1.81
SG12_YS_XRF_128	Z	2	34	35.01	34.505	0	154.5642	587	8	77.02	0.25	1.58
SG12_YS_XRF_129	Z	2	35.01	36.02	35.515	0	155.5834	592	8	77.83	0.24	1.56
SG12_YS_XRF_130	Z	2	36.02	37.02	36.52	0	156.5976	596	9	78.70	0.23	1.54
SG12_YS_XRF_131	Z	2	37.02	38.03	37.525	0	157.6118	601	9	77.34	0.25	1.80
SG12_YS_XRF_132	Z	2	38.03	39.03	38.53	0	158.626	606	9	77.00	0.25	1.74
SG12_YS_XRF_133	Z	2	39.03	40.04	39.535	0	159.6402	611	10	76.47	0.26	1.58
SG12_YS_XRF_134	Z	2	40.04	41.05	40.545	0	160.6594	615	10	77.67	0.24	1.46
SG12_YS_XRF_135	Z	2	41.05	42.05	41.55	0	161.6736	620	10	78.53	0.23	1.47
SG12_YS_XRF_136	Z	2	42.05	43.06	42.555	0	162.6878	625	11	78.42	0.23	1.53
SG12_YS_XRF_137	Z	2	43.06	44.06	43.56	0	163.702	630	11	75.49	0.27	1.70
SG12_YS_XRF_138	Z	2	44.06	45.07	44.565	0	164.7162	634	12	72.91	0.31	1.71
SG12_YS_XRF_139	Z	2	45.07	46.08	45.575	0	165.7354	639	12	73.95	0.29	1.71
SG12_YS_XRF_140	Z	2	46.08	47.08	46.58	0	166.7496	644	12	72.09	0.32	1.75
SG12_YS_XRF_141	Z	2	47.08	48.09	47.585	0	167.7638	649	13	72.35	0.30	1.44
SG12_YS_XRF_142	Z	2	48.09	49.1	48.595	1	168.7831	653	13	68.87	0.36	1.80
SG12_YS_XRF_143	Z	2	49.1	50.11	49.605	1	169.8023	658	13	64.85	0.42	1.94
SG12_YS_XRF_144	Z	2	50.11	51.16	50.635	0	170.7982	663	14	73.09	0.30	1.61
SG12_YS_XRF_145	Z	2	51.16	52.2	51.68	1	171.791	666	14	71.61	0.32	1.74
SG12_YS_XRF_146	Z	2	52.2	53.22	52.71	0	172.7581	669	14	76.70	0.26	1.69
SG12_YS_XRF_147	Z	2	53.22	54.23	53.725	0	173.7081	674	15	76.46	0.26	1.55
SG12_YS_XRF_148	Z	2	54.23	55.25	54.74	0	174.6581	678	15	75.53	0.27	1.75
SG12_YS_XRF_149	Z	2	55.25	56.26	55.755	0	175.6081	683	15	76.09	0.27	1.81
SG12_YS_XRF_150	Z	2	56.26	57.28	56.77	0	176.5581	687	16	76.80	0.26	1.80
SG12_YS_XRF_151	Z	2	57.28	58.29	57.785	0	177.5081	692	16	77.36	0.25	1.73
SG12_YS_XRF_152	Z	2	58.29	59.31	58.8	0	178.4581	699	16	77.06	0.25	1.74
SG12_YS_XRF_153	Z	2	59.31	60.32	59.815	0	179.4081	706	16	77.10	0.26	1.94
SG12_YS_XRF_154	Z	2	60.32	61.34	60.83	0	180.3581	714	16	76.11	0.26	1.66
SG12_YS_XRF_155	Z	2	61.34	62.35	61.845	0	181.3081	721	15	76.19	0.26	1.59
SG12_YS_XRF_156	Z	2	62.35	63.37	62.86	0	182.2581	728	15	76.06	0.25	1.34
SG12_YS_XRF_157	Z	2	63.37	64.38	63.875	0	183.2081	736	15	75.84	0.28	2.17
SG12_YS_XRF_158	Z	2	64.38	65.4	64.89	0	184.1581	743	15	75.15	0.28	2.05
SG12_YS_XRF_159	Z	2	65.4	66.41	65.905	0	185.1081	751	15	75.05	0.28	1.95
SG12_YS_XRF_160	Z	2	66.41	67.43	66.92	0	186.0581	758	15	74.64	0.29	1.84
SG12_YS_XRF_161	Z	2	67.43	68.44	67.935	0	187.0081	766	15	74.49	0.29	1.77
SG12_YS_XRF_162	Z	2	68.44	69.46	68.95	0	187.9581	773	15	74.79	0.27	1.46
SG12_YS_XRF_163	Z	2	69.46	70.47	69.965	0	188.9081	780	14	71.96	0.32	1.89
SG12_YS_XRF_164	Z	2	70.47	71.49	70.98	0	189.8581	788	14	70.42	0.35	2.03
SG12_YS_XRF_165	Z	2	71.49	72.5	71.995	0	190.8081	795	14	71.01	0.33	1.84
SG12_YS_XRF_166	Y	2	13.42	14.4	13.91	0	190.91	796	14	73.40	0.31	2.06
SG12_YS_XRF_167	Z	2	72.5	73.48	72.99	0	191.4971	801	14	74.81	0.28	1.71
SG12_YS_XRF_168	Y	2	14.4	15.4	14.9	0	191.84	803	14	73.62	0.30	1.79
SG12_YS_XRF_169	Y	2	15.4	16.4	15.9	0	192.7733	811	14	72.89	0.30	1.68
SG12_YS_XRF_170	Y	2	16.4	17.4	16.9	0	193.7067	818	14	71.50	0.32	1.69
SG12_YS_XRF_171	Y	2	17.4	18.4	17.9	0	194.64	825	14	67.65	0.39	2.09
SG12_YS_XRF_172	Y	2	18.4	19.4	18.9	1	195.5733	832	13	57.87	0.53	1.99
SG12_YS_XRF_173	Y	2	19.4	20.4	19.9	1	196.5067	834	13	49.72	0.71	2.40
SG12_YS_XRF_174	Y	2	20.4	21.4	20.9	2	197.44	834	13	51.59	0.66	2.20
SG12_YS_XRF_175	Y	2	21.4	22.4	21.9	2	198.3733	834	13	55.09	0.58	1.99
SG12_YS_XRF_176	Y	2	22.4	23.4	22.9	2	199.3067	834	13	57.22	0.55	2.08
SG12_YS_XRF_177	Y	2	23.4	24.4	23.9	2	200.24	834	13	59.86	0.50	2.03
SG12_YS_XRF_178	Y	2	24.4	25.4	24.9	2	201.1733	834	13	62.87	0.47	2.33
SG12_YS_XRF_179	Y	2	25.4	26.4	25.9	2	202.1067	834	13	70.05	0.36	2.32
SG12_YS_XRF_180	Y	2	26.4	27.4	26.9	0	203.157	841	13	76.66	0.26	1.66
SG12_YS_XRF_181	Y	2	27.4	28.4	27.9	0	204.2203	850	13	75.31	0.28	2.00
SG12_YS_XRF_182	Y	2	28.4	29.4	28.9	1	205.2835	858	13	73.51	0.30	1.93
SG12_YS_XRF_183	Y	2	29.4	30.4	29.9	0	206.3468	866	13	78.02	0.24	1.70

(Continued)

Table S5 List of depth, age and physical property of SG12core samples.

Sample Number	Hole	Section	top	bottom	center	facies*	center composite depth (cm)	center age (yr BP)	age error (yr)	WC (wt %)	DBD (g/cm <sup>3</sup> )	GD (g/cm <sup>3</sup> )
			distance from section top (cm)	distance from section top (cm)	distance from section top (cm)	0: BG 1: including EL-G 2: including EL-B 3: Tephra						
SG12_YS_XRF_184	Y	2	30.4	31.4	30.9	0	207.4101	875	13	79.59	0.22	1.42
SG12_YS_XRF_185	Y	2	31.4	32.4	31.9	0	208.4734	883	12	78.08	0.24	1.90
SG12_YS_XRF_186	Y	2	32.4	33.4	32.9	0	209.5367	891	12	76.87	0.26	2.20
SG12_YS_XRF_187	Y	2	33.4	34.4	33.9	0	210.6	900	12	77.15	0.25	1.81
SG12_YS_XRF_188	Y	2	34.4	35.4	34.9	0	211.6633	908	12	77.22	0.25	1.58
SG12_YS_XRF_189	Y	2	35.4	36.4	35.9	0	212.7266	917	13	77.00	0.25	1.36
SG12_YS_XRF_190	Y	2	36.4	37.4	36.9	0	213.7899	927	13	76.99	0.26	1.86
SG12_YS_XRF_191	Y	2	37.4	38.4	37.9	0	214.8532	936	14	76.14	0.26	1.47
SG12_YS_XRF_192	Y	2	38.4	39.4	38.9	1	215.9165	946	15	74.46	0.29	1.84
SG12_YS_XRF_193	Y	2	39.4	40.4	39.9	0	216.9797	955	15	77.82	0.24	1.62
SG12_YS_XRF_194	Y	2	40.4	41.4	40.9	0	218.043	964	16	78.29	0.24	1.87
SG12_YS_XRF_195	Y	2	41.4	42.4	41.9	0	219.1063	974	17	79.70	0.22	1.64
SG12_YS_XRF_196	Y	2	42.4	43.4	42.9	0	220.1696	983	17	78.96	0.23	1.63
SG12_YS_XRF_197	Y	2	43.4	44.4	43.9	1	221.2329	993	18	77.86	0.24	1.67
SG12_YS_XRF_198	Y	2	44.4	45.4	44.9	0	222.2962	1002	19	78.26	0.24	1.89
SG12_YS_XRF_199	Y	2	45.4	46.4	45.9	0	223.3595	1012	19	79.29	0.23	2.23
SG12_YS_XRF_200	Y	2	46.4	47.4	46.9	0	224.4228	1022	20			
SG12_YS_XRF_201	Y	2	47.4	48.4	47.9	0	225.4861	1032	20	75.10	0.29	2.15
SG12_YS_XRF_202	Y	2	48.4	49.4	48.9	0	226.5494	1041	20	75.00	0.28	1.81
SG12_YS_XRF_203	Y	2	49.4	50.4	49.9	0	227.6127	1051	20	75.05	0.28	1.67
SG12_YS_XRF_204	Y	2	50.4	51.4	50.9	0	228.676	1061	21	74.59	0.29	1.86
SG12_YS_XRF_205	Y	2	51.4	52.4	51.9	0	229.7392	1071	21	73.11	0.32	2.26
SG12_YS_XRF_206	Y	2	52.4	53.4	52.9	0	230.8025	1080	21	72.45	0.32	2.02
SG12_YS_XRF_207	Y	2	53.4	54.4	53.9	0	231.8658	1090	21	72.33	0.32	2.14
SG12_YS_XRF_208	Y	2	54.4	55.4	54.9	1	232.9291	1100	22	66.06	0.41	2.07
SG12_YS_XRF_209	Y	2	55.4	56.4	55.9	1	233.9924	1110	22	62.55	0.47	2.23
SG12_YS_XRF_210	Y	2	56.4	57.4	56.9	1	235.0557	1119	22	56.34	0.58	2.24
SG12_YS_XRF_211	Y	2	57.4	58.4	57.905	0	236.1155	1128	22	75.45	0.27	1.76
SG12_YS_XRF_212	Y	2	58.4	59.4	58.92	0	237.1655	1137	22	73.89	0.30	2.00
SG12_YS_XRF_213	Y	2	59.4	60.4	59.94	0	238.2207	1146	22	75.26	0.28	1.97
SG12_YS_XRF_214	Y	2	60.4	61.4	60.96	0	239.2759	1155	22	74.44	0.29	1.92
SG12_YS_XRF_215	Y	2	61.4	62.4	61.975	0	240.3259	1164	22	72.83	0.32	2.04
SG12_YS_XRF_216	Y	2	62.4	63.4	62.99	1	241.3759	1173	22	72.11	0.33	2.21
SG12_YS_XRF_217	Y	2	63.4	64.4	64.005	0	242.3378	1181	22	75.02	0.28	1.88
SG12_YS_XRF_218	Y	2	64.4	65.4	65.015	1	243.2356	1189	21	78.16	0.25	2.20
SG12_YS_XRF_219	Y	2	65.4	66.4	66.025	0	244.1333	1196	21	78.64	0.23	1.52
SG12_YS_XRF_220	Y	2	66.4	67.4	67.035	0	245.0311	1204	21	79.36	0.23	1.80
SG12_YS_XRF_221	Y	2	67.4	68.4	68.045	0	245.9289	1212	21	77.51	0.24	1.47
SG12_YS_XRF_222	Y	2	68.4	69.4	69.055	0	246.8267	1219	21	77.89	0.24	1.79
SG12_YS_XRF_223	Y	2	69.4	70.4	70.065	0	247.7244	1227	21	76.04	0.27	1.72
SG12_YS_XRF_224	Y	2	70.4	71.4	71.075	0	248.6222	1235	21	75.50	0.28	1.84
SG12_YS_XRF_225	Z	3	31.3	32.3	31.8	1	249.4759	1242	21	68.69	0.37	1.90
SG12_YS_XRF_226	Y	2	71.4	72.4	72.085	1	249.52	1243	21	69.48	0.36	2.12
SG12_YS_XRF_227	Z	3	32.3	33.3	32.8	1	250.4127	1250	21	78.23	0.27	5.85
SG12_YS_XRF_228	Y	2	72.4	73.4	73.1	1	250.4222	1250	21	65.07	0.44	2.37
SG12_YS_XRF_229	Z	3	33.3	34.3	33.8	0	251.3518	1258	21	66.09	0.39	1.62
SG12_YS_XRF_230	Y	2	73.4	74.4	74.125	0	251.425	1259	21	77.75	0.25	1.89
SG12_YS_XRF_231	Z	3	34.3	35.3	34.8	0	252.2915	1266	21	76.07	0.26	1.56
SG12_YS_XRF_232	Y	2	74.4	75.4	75.15	0	252.45	1267	21	77.93	0.26	2.68
SG12_YS_XRF_233	Z	3	35.3	36.3	35.8	0	253.2312	1273	21	77.43	0.25	1.98
SG12_YS_XRF_234	Z	3	36.3	37.3	36.8	0	254.1709	1280	20	80.89	0.22	3.79
SG12_YS_XRF_235	Z	3	37.3	38.3	37.8	0	255.1106	1287	20	77.33	0.26	2.26
SG12_YS_XRF_236	Z	3	38.3	39.3	38.8	0	256.0504	1294	20	77.37	0.25	1.87
SG12_YS_XRF_237	Z	3	39.3	40.3	39.8	0	256.9901	1301	19	77.34	0.25	1.80
SG12_YS_XRF_238	Z	3	40.3	41.3	40.8	0	257.9298	1309	19	77.21	0.26	1.97
SG12_YS_XRF_239	Z	3	41.3	42.3	41.8	0	258.8695	1316	19	77.71	0.26	2.49
SG12_YS_XRF_240	Z	3	42.3	43.3	42.8	1	259.8092	1323	18	75.78	0.27	1.74
SG12_YS_XRF_241	Z	3	43.3	44.3	43.8	0	260.7489	1330	18	77.75	0.25	1.78
SG12_YS_XRF_242	Z	3	44.3	45.3	44.8	0	261.6887	1337	18	77.62	0.25	1.66
SG12_YS_XRF_243	Z	3	45.3	46.3	45.8	0	262.6284	1344	17	77.54	0.24	1.57
SG12_YS_XRF_244	Z	3	46.3	47.3	46.8	0	263.5681	1351	17	77.88	0.25	1.84

(Continued)

Table S5 List of depth, age and physical property of SG12core samples.

Sample Number	Hole	Section	top	bottom	center	facies*	center composite depth (cm)	center age (yr BP)	age error (yr)	WC (wt %)	DBD (g/cm <sup>3</sup> )	GD (g/cm <sup>3</sup> )
			distance from section top (cm)	distance from section top (cm)	distance from section top (cm)	0: BG 1: including EL-G 2: including EL-B 3: Tephra						
SG12_YS_XRF_245	Z	3	47.3	48.3	47.8	0	264.5078	1359	17	77.47	0.25	1.93
SG12_YS_XRF_246	Z	3	48.3	49.3	48.8	0	265.4475	1367	17	79.08	0.21	1.14
SG12_YS_XRF_247	Z	3	49.3	50.3	49.8	0	266.3872	1375	17	79.27	0.23	1.66
SG12_YS_XRF_248	Z	3	50.3	51.3	50.8	0	267.3269	1383	18	78.04	0.24	1.67
SG12_YS_XRF_249	Z	3	51.3	52.3	51.8	0	268.2667	1391	18	77.22	0.27	2.64
SG12_YS_XRF_250	Z	3	52.3	53.3	52.8	0	269.2064	1398	18	77.10	0.25	1.70
SG12_YS_XRF_251	Z	3	53.3	54.3	53.8	0	270.1461	1406	18	76.47	0.27	1.98
SG12_YS_XRF_252	Z	3	54.3	55.3	54.8	0	271.0858	1414	18	76.63	0.26	1.83
SG12_YS_XRF_253	Z	3	55.3	56.3	55.8	1	272.0255	1422	19	76.10	0.27	1.89
SG12_YS_XRF_254	Z	3	56.3	57.3	56.8	0	272.9652	1430	19	78.38	0.24	1.78
SG12_YS_XRF_255	Z	3	57.3	58.3	57.8	0	273.905	1437	19	78.41	0.24	1.76
SG12_YS_XRF_256	Z	3	58.3	59.3	58.8	0	274.8447	1445	19	77.98	0.25	2.41
SG12_YS_XRF_257	Z	3	59.3	60.3	59.8	0	275.7844	1453	20	79.27	0.23	1.63
SG12_YS_XRF_258	Z	3	60.3	61.3	60.8	1	276.7241	1461	20	78.45	0.24	1.96
SG12_YS_XRF_259	Z	3	61.3	62.3	61.8	0	277.7222	1469	20	78.94	0.23	1.67
SG12_YS_XRF_260	Z	3	62.3	63.3	62.8	1	278.7593	1478	20	77.17	0.26	2.07
SG12_YS_XRF_261	Z	3	63.3	64.3	63.8	0	279.7963	1486	20	79.68	0.22	1.59
SG12_YS_XRF_262	Z	3	64.3	65.3	64.8	0	280.77	1494	21	79.95	0.23	2.38
SG12_YS_XRF_263	Z	3	65.3	66.3	65.8	0	281.7367	1502	21	80.05	0.22	1.98
SG12_YS_XRF_264	Z	3	66.3	67.3	66.8	0	282.7033	1510	21	79.50	0.23	1.92
SG12_YS_XRF_265	Z	3	67.3	68.3	67.8	0	283.67	1518	21	79.52	0.23	1.89
SG12_YS_XRF_266	Z	3	68.3	69.3	68.8	0	284.6367	1526	22	79.67	0.23	2.46
SG12_YS_XRF_267	Z	3	69.3	70.3	69.8	0	285.6033	1535	22	79.84	0.22	1.86
SG12_YS_XRF_268	Z	3	70.3	71.3	70.8	0	286.57	1543	22	80.00	0.22	1.69
SG12_YS_XRF_269	Z	3	71.3	72.3	71.8	0	287.5367	1551	22	80.40	0.21	1.52
SG12_YS_XRF_270	Z	3	72.3	73.3	72.8	0	288.5033	1559	23	79.74	0.22	1.75
SG12_YS_XRF_271	Z	3	73.3	74.3	73.8	0	289.47	1567	23	78.72	0.23	1.76
SG12_YS_XRF_272	Z	3	74.3	75.3	74.8	1	290.4367	1575	23	77.31	0.25	1.57
SG12_YS_XRF_273	Z	3	75.3	76.3	75.8	0	291.4033	1582	23	78.00	0.24	1.54
SG12_YS_XRF_274	Z	3	76.3	77.3	76.8	0	292.37	1590	23	77.85	0.25	1.77
SG12_YS_XRF_275	Z	3	77.3	78.3	77.8	0	293.3367	1597	22	78.94	0.23	1.67
SG12_YS_XRF_276	Z	3	78.3	79.3	78.8	0	294.3033	1604	22	78.59	0.23	1.67
SG12_YS_XRF_277	Z	3	79.3	80.3	79.8	0	295.27	1612	22	77.05	0.24	1.21
SG12_YS_XRF_278	Y	3	25.29	26.3	25.795	1	296.1847	1619	22	76.36	0.27	1.86
SG12_YS_XRF_279	Z	3	80.3	81.3	80.8	1	296.2367	1619	22	76.67	0.26	1.67
SG12_YS_XRF_280	Y	3	26.3	27.3	26.8	0	297.1149	1626	21	77.22	0.25	1.66
SG12_YS_XRF_281	Z	3	81.3	82.26	81.78	0	297.184	1627	21	77.98	0.24	1.80
SG12_YS_XRF_282	Y	3	27.3	28.32	27.81	0	298.0705	1633	21	77.28	0.25	1.88
SG12_YS_XRF_283	Z	3	82.26	83.15	82.705	0	298.105	1634	21	78.12	0.24	1.70
SG12_YS_XRF_284	Z	3	83.15	84.04	83.595	0	298.995	1640	21	77.88	0.24	1.75
SG12_YS_XRF_285	Y	3	28.32	29.33	28.825	0	299.036	1641	21	77.65	0.25	1.66
SG12_YS_XRF_286	Y	3	29.33	30.34	29.835	0	299.9967	1647	21	74.89	0.29	2.12
SG12_YS_XRF_287	Y	3	30.34	31.35	30.845	0	300.9574	1654	21	74.87	0.29	2.11
SG12_YS_XRF_288	Y	3	31.35	32.37	31.86	0	301.9229	1661	21	73.00	0.31	2.00
SG12_YS_XRF_289	Y	3	32.37	33.38	32.875	1	302.8884	1667	21	66.20	0.42	2.25
SG12_YS_XRF_290	Y	3	33.38	34.39	33.885	1	303.8491	1674	21	57.56	0.56	2.36
SG12_YS_XRF_291	Y	3	34.39	35.38	34.885	1	304.8004	1680	21	59.86	0.49	1.78
SG12_YS_XRF_292	Y	3	35.38	36.31	35.845	1	305.9063	1688	21	74.67	0.28	1.70
SG12_YS_XRF_293	Y	3	36.31	37.3	36.805	0	306.9617	1695	21	79.56	0.23	1.82
SG12_YS_XRF_294	Y	3	37.3	38.31	37.805	0	307.8547	1702	21	79.37	0.23	1.93
SG12_YS_XRF_295	Y	3	38.31	39.31	38.81	0	308.7522	1709	22	80.08	0.20	1.09
SG12_YS_XRF_296	Y	3	39.31	40.32	39.815	0	309.6497	1716	22	79.11	0.23	2.05
SG12_YS_XRF_297	Y	3	40.32	41.32	40.82	0	310.5472	1723	23	80.37	0.21	1.56
SG12_YS_XRF_298	Y	3	41.32	42.33	41.825	0	311.4447	1730	23	80.90	0.21	1.60
SG12_YS_XRF_299	Y	3	42.33	43.33	42.83	0	312.3421	1737	24	80.64	0.20	1.09
SG12_YS_XRF_300	Y	3	43.33	44.34	43.835	0	313.2396	1744	24	81.63	0.18	1.00
SG12_YS_XRF_301	Y	3	44.34	45.34	44.84	0	314.1371	1751	25	80.20	0.20	0.96
SG12_YS_XRF_302	Y	3	46.35	47.35	46.85	0	315.9321	1765	26	81.32	0.19	0.98
SG12_YS_XRF_303	Y	3	47.35	48.36	47.855	0	316.8296	1772	26	79.75	0.22	1.58
SG12_YS_XRF_304	Y	3	48.36	49.36	48.86	0	317.7271	1779	27	81.16	0.20	1.24
SG12_YS_XRF_305	Y	3	49.36	50.36	49.86	0	318.6201	1786	27	81.47	0.19	1.21

(Continued)

Table S5 List of depth, age and physical property of SG12core samples.

Sample Number	Hole	Section	top	bottom	center	facies*	center composite depth (cm)	center age (yr BP)	age error (yr)	WC (wt %)	DBD (g/cm <sup>3</sup> )	GD (g/cm <sup>3</sup> )
			distance from section top (cm)	distance from section top (cm)	distance from section top (cm)	0: BG 1: including EL-G 2: including EL-B 3: Tephra						
SG12_YS_XRF_306	Y	3	50.36	51.37	50.865	0	319.5176	1793	28	80.14	0.21	1.59
SG12_YS_XRF_307	Y	3	51.37	52.37	51.87	0	320.4151	1800	28	79.21	0.23	1.60
SG12_YS_XRF_308	Y	3	52.37	53.38	52.875	0	321.3126	1807	29	79.05	0.22	1.37
SG12_YS_XRF_309	Y	3	53.38	54.38	53.88	0	322.21	1813	29	80.07	0.23	2.34
SG12_YS_XRF_310	Y	3	54.38	55.39	54.885	0	323.1075	1819	29	80.40	0.21	1.64
SG12_YS_XRF_311	Y	3	55.39	56.39	55.89	0	324.005	1825	29	78.98	0.23	1.50
SG12_YS_XRF_312	Y	3	56.39	57.4	56.895	0	324.9025	1831	29	77.79	0.25	1.76
SG12_YS_XRF_313	Y	3	57.4	58.41	57.905	1	325.8045	1837	29	70.07	0.35	1.82
SG12_YS_XRF_314	Y	3	59.43	60.45	59.94	0	327.6246	1849	29	80.77	0.21	1.57
SG12_YS_XRF_315	Y	3	60.45	61.47	60.96	0	328.5369	1856	29	80.81	0.21	1.80
SG12_YS_XRF_316	Y	3	61.47	62.49	61.98	0	329.4492	1862	29	81.35	0.19	1.24
SG12_YS_XRF_317	Y	3	62.49	63.5	62.995	0	330.357	1868	29	82.89	0.18	1.60
SG12_YS_XRF_318	Y	3	63.5	64.52	64.01	0	331.2648	1874	29	81.93	0.18	0.99
SG12_YS_XRF_319	Y	3	64.52	65.54	65.03	0	332.1771	1880	29	83.88	0.17	1.21
SG12_YS_XRF_320	Y	3	65.54	66.56	66.05	1	333.0894	1886	29	80.34	0.20	1.17
SG12_YS_XRF_321	Y	3	66.56	67.58	67.07	0	334.0017	1892	29	81.20	0.20	1.60
SG12_YS_XRF_322	Y	3	67.58	68.6	68.09	0	334.914	1898	29	80.42	0.22	2.03
SG12_YS_XRF_323	Y	3	68.6	69.62	69.11	0	335.8263	1904	29	80.23	0.21	1.48
SG12_YS_XRF_324	Y	3	69.62	70.64	70.13	0	336.7386	1910	29	79.47	0.22	1.63
SG12_YS_XRF_325	Y	3	70.64	71.66	71.15	0	337.6509	1917	29	79.45	0.22	1.57
SG12_YS_XRF_326	Z	4	29.6	30.6	30.1	0	338.3772	1923	29	79.16	0.22	1.51
SG12_YS_XRF_327	Y	3	71.66	72.68	72.17	0	338.5632	1924	29	78.19	0.24	1.73
SG12_YS_XRF_328	Z	4	30.6	31.6	31.1	0	339.2886	1930	30	78.71	0.23	1.77
SG12_YS_XRF_329	Y	3	72.68	73.69	73.185	0	339.4711	1931	30	79.08	0.23	1.72
SG12_YS_XRF_330	Z	4	31.6	32.6	32.1	0	340.2	1937	30	79.51	0.22	1.42
SG12_YS_XRF_331	Y	3	73.69	74.71	74.2	1	340.4	1938	30	79.55	0.22	1.66
SG12_YS_XRF_332	Z	4	32.6	33.61	33.105	0	341.2503	1945	30	79.56	0.23	1.82
SG12_YS_XRF_333	Y	3	74.71	75.71	75.21	0	341.41	1946	30	79.83	0.21	1.41
SG12_YS_XRF_334	Z	4	33.61	34.62	34.115	0	342.3059	1953	30	81.84	0.19	1.22
SG12_YS_XRF_335	Z	4	34.62	35.63	35.125	0	343.3615	1961	31	81.18	0.20	1.35
SG12_YS_XRF_336	Z	4	35.63	36.63	36.13	0	344.4118	1970	31	80.57	0.20	1.15
SG12_YS_XRF_337	Z	4	36.63	37.64	37.135	0	345.4621	1977	31	82.56	0.17	0.96
SG12_YS_XRF_338	Z	4	37.64	38.65	38.145	0	346.5177	1985	32	80.84	0.20	1.45
SG12_YS_XRF_339	Z	4	38.65	39.66	39.155	0	347.5733	1993	33	81.32	0.19	1.03
SG12_YS_XRF_340	Z	4	39.66	40.66	40.16	0	348.6236	2001	33	81.92	0.18	0.97
SG12_YS_XRF_341	Z	4	40.66	41.67	41.165	0	349.6739	2009	34	81.78	0.18	0.88
SG12_YS_XRF_342	Z	4	41.67	42.68	42.175	0	350.7295	2016	34	81.49	0.19	1.20
SG12_YS_XRF_343	Z	4	42.68	43.69	43.185	0	351.7851	2024	35	81.77	0.19	1.37
SG12_YS_XRF_344	Z	4	43.69	44.69	44.19	0	352.8354	2032	36	75.79	0.26	1.55
SG12_YS_XRF_345	Z	4	44.69	45.7	45.195	1	353.8858	2040	36	74.02	0.29	1.71
SG12_YS_XRF_346	Z	4	45.7	46.7	46.2	0	354.8904	2047	37	75.68	0.26	1.40
SG12_YS_XRF_347	Z	4	46.7	47.7	47.2	0	355.8784	2054	37	75.00	0.27	1.51
SG12_YS_XRF_348	Z	4	47.7	48.7	48.2	0	356.8664	2062	38	74.89	0.29	2.13
SG12_YS_XRF_349	Z	4	48.7	49.7	49.2	0	357.8544	2069	38	76.00	0.27	1.65
SG12_YS_XRF_350	Z	4	49.7	50.7	50.2	0	358.8424	2076	39	78.39	0.23	1.50
SG12_YS_XRF_351	Z	4	50.7	51.7	51.2	0	359.8304	2084	39	76.39	0.27	1.88
SG12_YS_XRF_352	Z	4	51.7	52.7	52.2	0	360.8184	2091	40	75.69	0.26	1.33
SG12_YS_XRF_353	Z	4	52.7	53.7	53.2	0	361.8064	2098	41	75.29	0.26	1.34
SG12_YS_XRF_354	Z	4	53.7	54.7	54.2	0	362.7944	2106	41	75.33	0.25	1.10
SG12_YS_XRF_355	Z	4	54.7	55.7	55.2	0	363.7824	2112	41	74.29	0.30	2.11
SG12_YS_XRF_356	Z	4	55.7	56.7	56.2	0	364.7704	2119	41	74.21	0.29	1.63
SG12_YS_XRF_357	Z	4	56.7	57.7	57.2	0	365.7584	2126	41	74.33	0.29	1.93
SG12_YS_XRF_358	Z	4	57.7	58.7	58.2	0	366.7464	2133	41	74.71	0.28	1.64
SG12_YS_XRF_359	Z	4	58.7	59.7	59.2	0	367.7344	2139	41	74.07	0.29	1.54
SG12_YS_XRF_360	Z	4	59.7	60.7	60.2	0	368.7224	2146	41	74.07	0.29	1.65
SG12_YS_XRF_361	Z	4	60.7	61.7	61.2	0	369.7104	2154	41	74.56	0.29	1.97
SG12_YS_XRF_362	Z	4	61.7	62.7	62.2	0	370.6984	2161	41	76.04	0.26	1.57
SG12_YS_XRF_363	Z	4	62.7	63.7	63.2	0	371.6864	2169	41	77.36	0.25	1.79
SG12_YS_XRF_364	Z	4	63.7	64.7	64.2	0	372.6744	2177	41	74.87	0.28	1.63
SG12_YS_XRF_365	Z	4	64.7	65.7	65.2	0	373.6624	2184	40	73.95	0.30	1.90
SG12_YS_XRF_366	Z	4	65.7	66.7	66.2	0	374.6504	2192	40	73.32	0.31	1.92

(Continued)

Table S5 List of depth, age and physical property of SG12core samples.

Sample Number	Hole	Section	top	bottom	center	facies*	center composite depth (cm)	center age (yr BP)	age error (yr)	WC (wt %)	DBD (g/cm <sup>3</sup> )	GD (g/cm <sup>3</sup> )
			distance from section top (cm)	distance from section top (cm)	distance from section top (cm)	0: BG 1: including EL-G 2: including EL-B 3: Tephra						
SG12_YS_XRF_367	Z	4	66.7	67.7	67.2	0	375.6384	2200	40	73.85	0.30	1.82
SG12_YS_XRF_368	Z	4	67.7	68.7	68.2	0	376.6264	2207	40	74.05	0.29	1.77
SG12_YS_XRF_369	Z	4	68.7	69.7	69.2	1	377.6144	2215	40	71.36	0.33	1.87
SG12_YS_XRF_370	Z	4	69.7	70.69	70.195	1	378.5975	2222	40	73.11	0.32	2.29
SG12_YS_XRF_371	Y	4	8.269663	10.3	9.284831	0	378.893	2225	40	72.36	0.32	2.10
SG12_YS_XRF_372	Z	4	70.69	71.68	71.185	0	379.585	2230	40	74.38	0.29	1.83
SG12_YS_XRF_373	Y	4	10.3	12.3	11.3	0	381.1019	2242	40	73.44	0.29	1.49
SG12_YS_XRF_374	Y	4	12.3	14.3	13.3	1	383.2942	2259	39	72.49	0.32	2.05
SG12_YS_XRF_375	Y	4	14.3	16.3	15.3	0	385.4366	2276	39	73.25	0.29	1.38
SG12_YS_XRF_376	Y	4	16.3	18.3	17.3	0	387.5179	2292	39	73.42	0.30	1.92
SG12_YS_XRF_377	Y	4	18.3	20.3	19.3	0	389.5992	2309	38	72.76	0.31	1.85
SG12_YS_XRF_378	Y	4	20.3	22.3	21.3	0	391.6805	2327	37	72.53	0.32	1.88
SG12_YS_XRF_379	Y	4	22.3	24.34562	23.32281	0	393.7855	2345	36	73.19	0.30	1.64
SG12_YS_XRF_380	Y	4	24.34562	26.35484	25.35023	1	395.8954	2364	35	73.06	0.30	1.60
SG12_YS_XRF_381	Y	4	26.35484	28.36406	27.35945	1	397.9942	2383	34	73.83	0.32	3.17
SG12_YS_XRF_382	Y	4	28.36406	30.37327	29.36866	0	400.1091	2401	34	73.87	0.30	2.03
SG12_YS_XRF_383	Y	4	30.37327	32.38249	31.37788	0	402.2241	2419	35	74.17	0.29	1.88
SG12_YS_XRF_384	Y	4	32.38249	34.39171	33.3871	0	404.339	2437	36	74.87	0.28	1.70
SG12_YS_XRF_385	Y	4	34.39171	36.40952	35.40061	0	406.4585	2455	37	77.87	0.24	1.54
SG12_YS_XRF_386	Y	4	36.40952	38.50476	37.45714	0	408.5	2472	37	74.66	0.28	1.47
SG12_YS_XRF_387	Y	4	38.50476	40.6	39.55238	1	410.5	2488	38	72.96	0.31	1.96
SG12_YS_XRF_388	Y	4	40.6	42.69524	41.64762	0	412.519	2505	38	73.64	0.31	2.19
SG12_YS_XRF_389	Y	4	42.69524	44.79048	43.74286	0	414.5571	2521	38	73.16	0.31	2.11
SG12_YS_XRF_390	Y	4	44.79048	46.88571	45.8381	0	416.5952	2538	38	72.57	0.33	2.86
SG12_YS_XRF_391	Y	4	46.88571	48.98095	47.93333	0	418.6333	2554	39	72.74	0.32	2.19
SG12_YS_XRF_392	Y	4	48.98095	50.55475	49.76785	0	420.4178	2568	39	72.06	0.33	2.08
SG12_YS_XRF_393	Y	4	50.55475	52.5457	51.55023	0	422.1516	2582	39	72.40	0.31	1.59
SG12_YS_XRF_394	Y	4	52.5457	54.53665	53.54118	0	424.0882	2598	39	66.35	0.29	0.69
SG12_YS_XRF_395	Y	4	54.53665	56.5276	55.53213	0	426.0249	2613	40	71.95	0.32	1.82
SG12_YS_XRF_396	Y	4	56.5276	58.51855	57.52308	0	427.9615	2628	40	71.86	0.33	1.93
SG12_YS_XRF_397	Y	4	58.51855	60.5095	59.51403	0	429.8982	2646	40	70.24	0.36	2.49
SG12_YS_XRF_398	Y	4	60.5095	62.50045	61.50498	1	431.8348	2664	40	67.30	0.40	2.26
SG12_YS_XRF_399	Y	4	62.50045	64.51166	63.50605	0	433.784	2681	39	72.20	0.31	1.64
SG12_YS_XRF_400	Y	4	64.51166	66.52393	65.51779	0	435.7466	2700	39	72.09	0.32	1.83
SG12_YS_XRF_401	Y	4	66.52393	68.5362	67.53006	0	437.7098	2718	39	72.80	0.31	1.72
SG12_YS_XRF_402	Y	4	68.5362	70.54847	69.54233	0	439.673	2736	39	72.81	0.31	1.89
SG12_YS_XRF_403	Y	4	70.54847	72.56074	71.5546	0	441.6362	2754	39	72.57	0.31	1.79
SG12_YS_XRF_404	Y	4	72.56074	74.57301	73.56687	0	443.5994	2772	39	72.08	0.31	1.55
SG12_YS_XRF_405	Y	4	74.57301	76.58528	75.57914	1	445.5626	2790	38	71.37	0.34	2.08
SG12_YS_XRF_406	Y	4	76.58528	78.59755	77.59141	1	447.5258	2808	38	71.41	0.32	1.62
SG12_YS_XRF_407	Y	4	78.59755	80.79439	79.69597	0	449.596	2827	38	73.64	0.31	2.38
SG12_YS_XRF_408	X	5	27.72336	29.70467	28.71402	1	457.9634	2911	39	73.38	0.29	1.46
SG12_YS_XRF_409	X	5	29.70467	31.68598	30.69533	0	459.9337	2930	40	73.89	0.28	1.37
SG12_YS_XRF_410	X	5	31.68598	33.66729	32.67664	0	461.904	2950	40	74.88	0.27	1.52
SG12_YS_XRF_411	X	5	33.66729	35.6486	34.65794	0	463.8743	2968	39	73.42	0.31	1.96
SG12_YS_XRF_412	X	5	35.6486	37.7	36.6743	0	465.8794	2986	38	73.57	0.28	1.27
SG12_YS_XRF_413	X	5	37.7	39.7	38.7	0	467.8939	3004	37	74.07	0.28	1.45
SG12_YS_XRF_414	X	5	39.7	41.7	40.7	0	469.8828	3022	36	73.12	0.29	1.34
SG12_YS_XRF_415	X	5	41.7	43.7	42.7	0	471.8717	3040	35	73.38	0.29	1.43
SG12_YS_XRF_416	X	5	43.7	45.7	44.7	0	473.8606	3058	35	73.39	0.29	1.42
SG12_YS_XRF_417	X	5	45.7	47.7	46.7	0	475.8494	3076	34	73.00	0.30	1.68
SG12_YS_XRF_418	X	5	47.7	49.7	48.7	0	477.8383	3094	33	72.43	0.29	1.28
SG12_YS_XRF_419	X	5	49.7	51.7	50.7	0	479.8272	3111	32	73.23	0.29	1.45
SG12_YS_XRF_420	X	5	51.7	53.7	52.7	0	481.8161	3128	31	72.49	0.31	1.69
SG12_YS_XRF_421	X	5	53.7	55.7	54.7	1	483.805	3145	30	68.28	0.34	1.28
SG12_YS_XRF_422	X	5	55.7	57.7	56.7	0	485.7899	3163	30	72.15	0.32	1.92
SG12_YS_XRF_423	X	5	57.7	59.7	58.7	0	487.7716	3181	29	73.19	0.30	1.61
SG12_YS_XRF_424	X	5	59.7	61.7	60.7	0	489.7532	3199	29	72.49	0.30	1.45
SG12_YS_XRF_425	X	5	61.7	63.7	62.7	0	491.7349	3218	28	72.38	0.31	1.76
SG12_YS_XRF_426	X	5	63.7	65.7	64.7	1	493.7165	3236	28	71.33	0.32	1.55
SG12_YS_XRF_427	X	5	65.7	67.82632	66.76316	0	495.7381	3254	27	71.39	0.32	1.56

(Continued)

Table S5 List of depth, age and physical property of SG12core samples.

Sample Number	Hole	Section	top	bottom	center	facies*	center composite depth (cm)	center age (yr BP)	age error (yr)	WC (wt %)	DBD (g/cm <sup>3</sup> )	GD (g/cm <sup>3</sup> )
			distance from section top (cm)	distance from section top (cm)	distance from section top (cm)	0: BG 1: including EL-G 2: including EL-B 3: Tephra						
SG12_YS_XRF_428	Y	5	22.07083	23.9875	23.02917	1	496.8458	3264	27	70.40	0.34	1.81
SG12_YS_XRF_429	X	5	67.82632	70.03684	68.93158	1	497.7316	3273	27	70.26	0.35	1.93
SG12_YS_XRF_430	Y	5	23.9875	25.90417	24.94583	0	498.6521	3281	26	74.10	0.29	1.82
SG12_YS_XRF_431	Y	5	25.90417	27.82083	26.8625	0	500.5784	3299	26	73.92	0.28	1.43
SG12_YS_XRF_432	Y	5	27.82083	29.7375	28.77917	0	502.5047	3316	24	68.84	0.29	0.82
SG12_YS_XRF_433	Y	5	29.7375	31.65417	30.69583	0	504.431	3333	23	74.04	0.29	1.60
SG12_YS_XRF_434	Y	5	31.65417	33.89751	32.77584	0	506.5214	3352	21	74.47	0.28	1.45
SG12_YS_XRF_435	Y	5	33.89751	35.87761	34.88756	0	508.6438	3371	20	74.99	0.28	1.68
SG12_YS_XRF_436	Y	5	35.87761	37.85771	36.86766	0	510.6338	3387	20	74.69	0.29	1.93
SG12_YS_XRF_437	Y	5	37.85771	39.83781	38.84776	0	512.6239	3403	21	73.92	0.30	2.02
SG12_YS_XRF_438	Y	5	39.83781	41.81791	40.82786	0	514.6139	3420	21	74.03	0.28	1.40
SG12_YS_XRF_439	Y	5	41.81791	43.8	42.80896	1	516.605	3436	21	72.90	0.30	1.53
SG12_YS_XRF_440	Y	5	43.8	45.8	44.8	0	518.6	3452	22	74.89	0.28	1.61
SG12_YS_XRF_441	Y	5	45.8	47.8	46.8	0	520.6	3469	22	75.14	0.28	1.90
SG12_YS_XRF_442	Y	5	47.8	49.8	48.8	0	522.6	3485	22	74.64	0.28	1.52
SG12_YS_XRF_443	Y	5	49.8	51.8	50.8	0	524.6	3501	23	75.53	0.27	1.50
SG12_YS_XRF_444	Y	5	51.8	53.8	52.8	0	526.6	3518	23	75.24	0.27	1.36
SG12_YS_XRF_445	Y	5	53.8	55.8	54.8	0	528.6	3534	23	74.26	0.28	1.40
SG12_YS_XRF_446	Y	5	55.8	57.8	56.8	0	530.6	3550	23	73.76	0.29	1.48
SG12_YS_XRF_447	Y	5	57.8	59.8	58.8	0	532.6	3566	22	73.44	0.29	1.43
SG12_YS_XRF_448	Y	5	59.8	61.8	60.8	0	534.6	3583	22	73.81	0.28	1.42
SG12_YS_XRF_449	Y	5	61.8	63.8	62.8	1	536.6	3599	22	72.46	0.30	1.51
SG12_YS_XRF_450	Y	5	63.8	65.81731	64.80865	0	538.5778	3615	22	74.23	0.29	1.90
SG12_YS_XRF_451	Y	5	65.81731	67.83654	66.82692	0	540.5192	3631	22	74.63	0.28	1.64
SG12_YS_XRF_452	Y	5	67.83654	69.85577	68.84615	0	542.4615	3647	22	75.09	0.27	1.60
SG12_YS_XRF_453	Y	5	69.85577	71.875	70.86538	0	544.4038	3662	22	74.14	0.28	1.44
SG12_YS_XRF_454	Y	5	71.875	73.89423	72.88462	1	546.3462	3678	22	74.07	0.29	1.63
SG12_YS_XRF_455	Y	5	73.89423	76.03509	74.96466	0	548.3647	3695	22	74.46	0.28	1.64
SG12_YS_XRF_456	Y	5	76.03509	78.22807	77.13158	0	550.5316	3713	22	75.17	0.26	1.23
SG12_YS_XRF_457	Y	5	78.22807	80.42105	79.32456	1	552.7323	3732	23	75.56	0.27	1.59
SG12_YS_XRF_458	Y	5	80.42105	82.61404	81.51754	0	554.9775	3751	23	75.18	0.27	1.51
SG12_YS_XRF_459	Y	5	82.61404	84.80702	83.71053	0	557.21	3770	24	72.54	0.27	0.92
SG12_YS_XRF_460	X	6	26.87755	27.87302	27.37528	1	560.1473	3795	25	76.21	0.26	1.46
SG12_YS_XRF_461	X	6	27.87302	28.86848	28.37075	0	561.1347	3804	25	75.63	0.27	1.69
SG12_YS_XRF_462	X	6	28.86848	29.86395	29.36621	0	562.1221	3812	25	75.86	0.27	1.68
SG12_YS_XRF_463	X	6	29.86395	30.85941	30.36168	0	563.1096	3821	25	75.40	0.29	2.41
SG12_YS_XRF_464	X	6	30.85941	31.85488	31.35714	0	564.097	3829	24	76.20	0.26	1.59
SG12_YS_XRF_465	X	6	31.85488	32.85034	32.35261	0	565.0844	3837	24	75.34	0.28	1.94
SG12_YS_XRF_466	X	6	32.85034	33.8458	33.34807	0	566.0719	3846	24	75.64	0.27	1.80
SG12_YS_XRF_467	X	6	33.8458	34.84127	34.34354	0	567.0593	3854	24	75.82	0.27	1.68
SG12_YS_XRF_468	X	6	34.84127	35.83673	35.339	0	568.0468	3863	24	74.76	0.28	1.64
SG12_YS_XRF_469	X	6	35.83673	36.8322	36.33447	1	569.0345	3871	24	71.51	0.33	1.82
SG12_YS_XRF_470	X	6	36.8322	37.82766	37.32993	0	570.0299	3880	23	75.51	0.27	1.58
SG12_YS_XRF_471	X	6	37.82766	38.82313	38.3254	1	571.0254	3888	23	73.33	0.31	1.94
SG12_YS_XRF_472	X	6	38.82313	39.81859	39.32086	0	572.0308	3897	23	76.64	0.27	2.11
SG12_YS_XRF_473	X	6	39.81859	40.81406	40.31633	0	573.0383	3905	23	75.14	0.27	1.50
SG12_YS_XRF_474	X	6	40.81406	41.80952	41.31179	0	574.0459	3913	23	74.62	0.28	1.69
SG12_YS_XRF_475	X	6	41.80952	42.80499	42.30726	0	575.0534	3921	23	74.83	0.29	1.88
SG12_YS_XRF_476	X	6	42.80499	43.80045	43.30272	0	576.0609	3929	23	75.55	0.28	2.04
SG12_YS_XRF_477	X	6	43.80045	44.79592	44.29819	0	577.0685	3937	23	75.17	0.28	1.94
SG12_YS_XRF_478	X	6	44.79592	45.79138	45.29365	0	578.076	3945	23	75.67	0.27	1.72
SG12_YS_XRF_479	X	6	45.79138	46.78685	46.28912	0	579.0835	3953	23	75.98	0.26	1.54
SG12_YS_XRF_480	X	6	46.78685	47.78231	47.28458	0	580.0911	3961	23	75.59	0.28	1.89
SG12_YS_XRF_481	X	6	47.78231	48.77778	48.28005	0	581.0986	3970	23	74.79	0.28	1.66
SG12_YS_XRF_482	X	6	48.77778	49.77324	49.27551	0	582.1061	3978	23	76.15	0.27	1.73
SG12_YS_XRF_483	X	6	49.77324	50.76871	50.27098	0	583.1137	3986	24	75.80	0.26	1.47
SG12_YS_XRF_484	X	6	50.76871	51.76417	51.26644	0	584.1212	3994	24	75.39	0.28	1.78
SG12_YS_XRF_485	X	6	51.76417	52.75964	52.2619	0	585.1287	4002	24	75.71	0.27	1.57
SG12_YS_XRF_486	X	6	52.75964	53.7551	53.25737	0	586.1362	4010	24	74.74	0.28	1.77
SG12_YS_XRF_487	X	6	53.7551	54.75057	54.25283	3	587.1438	4018	24	71.48	0.31	1.43
SG12_YS_XRF_488	X	6	54.75057	55.74603	55.2483	3	588.1439	4026	25	72.12	0.32	1.72

(Continued)

Table S5 List of depth, age and physical property of SG12core samples.

Sample Number	Hole	Section	top	bottom	center	facies*	center composite depth (cm)	center age (yr BP)	age error (yr)	WC (wt %)	DBD (g/cm <sup>3</sup> )	GD (g/cm <sup>3</sup> )
			distance from section top (cm)	distance from section top (cm)	distance from section top (cm)	0: BG 1: including EL-G 2: including EL-B 3: Tephra						
SG12_YS_XRF_489	X	6	55.74603	56.7415	56.24376	0	589.1219	4033	25	77.00	0.26	1.97
SG12_YS_XRF_490	X	6	56.7415	57.73696	57.23923	0	590.0999	4041	25	76.26	0.26	1.76
SG12_YS_XRF_491	X	6	57.73696	58.73243	58.23469	0	591.0779	4049	25	76.56	0.26	1.69
SG12_YS_XRF_492	X	6	58.73243	59.72789	59.23016	0	592.0559	4057	25	76.88	0.25	1.42
SG12_YS_XRF_493	X	6	59.72789	60.72336	60.22562	0	593.0339	4064	25	76.73	0.26	1.82
SG12_YS_XRF_494	X	6	60.72336	61.71882	61.22109	0	594.0119	4072	26	75.56	0.28	2.25
SG12_YS_XRF_495	X	6	61.71882	62.71429	62.21655	0	594.9899	4080	26	75.93	0.28	2.23
SG12_YS_XRF_496	X	6	62.71429	63.70975	63.21202	0	595.9679	4088	26	76.35	0.26	1.61
SG12_YS_XRF_497	X	6	63.70975	64.70522	64.20748	0	596.9459	4094	26	76.73	0.25	1.50
SG12_YS_XRF_498	X	6	64.70522	65.70068	65.20295	0	597.924	4100	25	76.83	0.26	2.12
SG12_YS_XRF_499	X	6	65.70068	66.69615	66.19841	0	598.9019	4106	25	76.02	0.26	1.60
SG12_YS_XRF_500	X	6	66.69615	67.69161	67.19388	0	599.88	4112	25	74.94	0.29	1.95
SG12_YS_XRF_501	X	6	67.69161	68.68707	68.18934	0	600.8579	4118	24	75.31	0.27	1.68
SG12_YS_XRF_502	X	6	68.68707	69.68254	69.18481	0	601.836	4124	24	75.80	0.27	1.94
SG12_YS_XRF_503	X	6	69.68254	70.678	70.18027	0	602.814	4131	24	76.50	0.25	1.45
SG12_YS_XRF_504	X	6	70.678	71.67347	71.17574	0	603.792	4138	24	75.78	0.27	1.94
SG12_YS_XRF_505	X	6	71.67347	72.66893	72.1712	1	604.7772	4144	24	68.15	0.37	1.80
SG12_YS_XRF_506	X	6	72.66893	73.6644	73.16667	0	605.8563	4152	24	74.06	0.30	1.97
SG12_YS_XRF_507	X	6	73.6644	74.65986	74.16213	0	606.9354	4159	24	75.07	0.28	1.73
SG12_YS_XRF_508	X	6	74.65986	75.65533	75.1576	0	608.0145	4167	24	75.28	0.28	1.88
SG12_YS_XRF_509	X	6	75.65533	76.65079	76.15306	0	609.0937	4174	23	75.98	0.27	1.97
SG12_YS_XRF_510	X	6	76.65079	77.64626	77.14853	0	610.1728	4182	23	74.83	0.30	2.40
SG12_YS_XRF_511	Y	6	42.73086	43.74826	43.23956	0	617.1992	4231	23	74.71	0.25	1.02
SG12_YS_XRF_512	Y	6	43.74826	44.76566	44.25696	0	618.2154	4238	23	70.84	0.32	1.38
SG12_YS_XRF_513	Y	6	44.76566	45.78306	45.27436	0	619.1684	4245	23	74.20	0.29	1.78
SG12_YS_XRF_514	Y	6	45.78306	46.80046	46.29176	0	620.1214	4252	23	75.79	0.26	1.50
SG12_YS_XRF_515	Y	6	46.80046	47.81787	47.30916	0	621.0744	4259	23	76.67	0.25	1.44
SG12_YS_XRF_516	Y	6	47.81787	48.83527	48.32657	0	622.0274	4266	23	73.79	0.29	1.66
SG12_YS_XRF_517	Y	6	48.83527	49.85267	49.34397	0	622.9804	4273	23	75.07	0.27	1.56
SG12_YS_XRF_518	Y	6	49.85267	50.87007	50.36137	0	623.9334	4280	24	75.11	0.27	1.55
SG12_YS_XRF_519	Y	6	50.87007	51.88747	51.37877	0	624.8864	4287	24	73.09	0.29	1.39
SG12_YS_XRF_520	Y	6	51.88747	52.90487	52.39617	0	625.8395	4294	24	74.85	0.28	1.78
SG12_YS_XRF_521	Y	6	52.90487	53.92227	53.41357	0	626.7925	4301	24	73.62	0.30	1.85
SG12_YS_XRF_522	Y	6	53.92227	54.93968	54.43097	0	627.7455	4308	24	74.11	0.29	1.67
SG12_YS_XRF_523	Y	6	54.93968	55.95708	55.44838	0	628.6985	4315	24	75.27	0.28	1.88
SG12_YS_XRF_524	Y	6	55.95708	56.97448	56.46578	0	629.6515	4322	24	74.92	0.27	1.47
SG12_YS_XRF_525	Y	6	56.97448	57.99188	57.48318	1	630.6045	4329	24	73.91	0.30	2.17
SG12_YS_XRF_526	Y	6	57.99188	59.00928	58.50058	0	631.5575	4336	24	71.83	0.33	1.92
SG12_YS_XRF_527	Y	6	59.00928	60.02668	59.51798	1	632.5038	4343	24	72.01	0.31	1.65
SG12_YS_XRF_528	Y	6	60.02668	61.04408	60.53538	1	633.3991	4349	24	70.91	0.34	1.89
SG12_YS_XRF_529	Y	6	61.04408	62.06148	61.55278	1	634.2944	4355	25	68.17	0.38	2.18
SG12_YS_XRF_530	Y	6	62.06148	63.07889	62.57019	1	635.3717	4363	25	68.99	0.37	2.00
SG12_YS_XRF_531	Y	6	63.07889	64.09629	63.58759	0	636.5433	4372	25	72.85	0.30	1.61
SG12_YS_XRF_532	Y	6	64.09629	65.11369	64.60499	1	637.7148	4380	25	73.81	0.30	1.83
SG12_YS_XRF_533	Y	6	65.11369	66.13109	65.62239	0	638.839	4388	25	73.87	0.30	2.20
SG12_YS_XRF_534	Y	6	66.13109	67.14849	66.63979	0	639.8965	4396	25	74.16	0.28	1.44
SG12_YS_XRF_535	Y	6	67.14849	68.16589	67.65719	0	640.9539	4403	25	73.14	0.30	1.72
SG12_YS_XRF_536	Y	6	68.16589	69.18329	68.67459	0	642.0114	4411	25	73.60	0.30	1.79
SG12_YS_XRF_537	Y	6	69.18329	70.2007	69.692	0	643.0688	4418	25	72.72	0.30	1.40
SG12_YS_XRF_538	Y	6	70.2007	71.2181	70.7094	0	644.1263	4426	25	72.35	0.32	1.88
SG12_YS_XRF_539	Y	6	71.2181	72.2355	71.7268	0	645.1838	4433	26	72.87	0.30	1.59
SG12_YS_XRF_540	Y	6	72.2355	73.2529	72.7442	1	646.2412	4441	26	72.89	0.31	2.01
SG12_YS_XRF_541	Y	6	73.2529	74.2703	73.7616	0	647.2987	4448	26	73.54	0.30	1.80
SG12_YS_XRF_542	Y	6	74.2703	75.2877	74.779	0	648.3561	4456	26	73.85	0.29	1.71
SG12_YS_XRF_543	Y	6	75.2877	76.3051	75.7964	0	649.4136	4464	26	74.85	0.27	1.45
SG12_YS_XRF_544	Y	6	76.3051	77.32251	76.81381	1	650.471	4471	26	74.23	0.29	1.71
SG12_YS_XRF_545	Y	6	77.32251	78.33991	77.83121	0	651.5285	4479	26	72.01	0.32	1.86
SG12_YS_XRF_546	Y	6	78.33991	79.35731	78.84861	1	652.4949	4486	26	78.55	0.24	2.17
SG12_YS_XRF_547	Y	6	79.35731	80.37471	79.86601	0	653.4547	4492	26	72.38	0.32	2.04
SG12_YS_XRF_548	Y	6	80.37471	81.39211	80.88341	1	654.4145	4500	26	72.81	0.31	1.90
SG12_YS_XRF_549	Y	6	81.39211	82.40951	81.90081	0	655.3743	4507	26	72.15	0.32	1.76

(Continued)

Table S5 List of depth, age and physical property of SG12core samples.

Sample Number	Hole	Section	top	bottom	center	facies*	center composite depth (cm)	center age (yr BP)	age error (yr)	WC (wt %)	DBD (g/cm <sup>3</sup> )	GD (g/cm <sup>3</sup> )
			distance from section top (cm)	distance from section top (cm)	distance from section top (cm)	0: BG 1: including EL-G 2: including EL-B 3: Tephra						
SG12_YS_XRF_550	Y	6	82.40951	83.42691	82.91821	0	656.3342	4514	25	71.71	0.33	1.91
SG12_YS_XRF_551	Z	7	40.8	42.8	41.8	1	656.9375	4519	25	70.00	0.34	1.61
SG12_YS_XRF_552	Y	6	83.42691	84.44432	83.93561	1	657.3356	4522	25	67.04	0.40	2.13
SG12_YS_XRF_553	Z	7	42.8	44.8	43.8	0	659.1875	4537	25	72.80	0.29	1.40
SG12_YS_XRF_554	Z	7	44.8	46.76467	45.78233	1	661.4176	4556	25	71.06	0.31	1.31
SG12_YS_XRF_555	Z	7	46.76467	48.75133	47.758	0	663.5879	4575	26	72.02	0.31	1.44
SG12_YS_XRF_556	Z	7	48.75133	50.738	49.74467	0	665.7516	4593	26	73.34	0.30	1.84
SG12_YS_XRF_557	Z	7	50.738	52.72467	51.73133	0	667.9153	4611	26	72.72	0.29	1.34
SG12_YS_XRF_558	Z	7	52.72467	54.71133	53.718	0	670.079	4627	25	71.93	0.31	1.47
SG12_YS_XRF_559	Z	7	54.71133	56.698	55.70467	1	672.2427	4643	25	64.05	0.43	1.88
SG12_YS_XRF_560	Z	7	56.698	58.72527	57.71164	0	674.2974	4659	24	73.76	0.30	1.74
SG12_YS_XRF_561	Z	7	58.72527	60.74725	59.73626	0	676.3	4674	24	72.61	0.29	1.34
SG12_YS_XRF_562	Z	7	60.74725	62.76923	61.75824	0	678.3	4689	23	73.76	0.30	1.93
SG12_YS_XRF_563	Z	7	62.76923	64.79121	63.78022	0	680.3	4703	21	73.47	0.29	1.40
SG12_YS_XRF_564	Z	7	64.79121	66.81319	65.8022	1	682.3	4718	18	72.49	0.30	1.55
SG12_YS_XRF_565	Z	7	66.81319	68.83516	67.82418	0	684.3	4733	16	72.80	0.30	1.58
SG12_YS_XRF_566	Z	7	68.83516	70.85714	69.84615	0	686.3	4748	15	71.38	0.32	1.55
SG12_YS_XRF_567	Z	7	70.85714	72.87912	71.86813	0	688.3	4764	15	72.70	0.29	1.34
SG12_YS_XRF_568	Z	7	72.87912	74.90065	73.88989	1	690.2998	4780	14	72.34	0.31	1.69
SG12_YS_XRF_569	Z	7	74.90065	76.91373	75.90719	0	692.3072	4796	14	74.27	0.29	1.63
SG12_YS_XRF_570	Z	7	76.91373	78.9268	77.92026	0	694.3203	4812	13	73.05	0.30	1.67
SG12_YS_XRF_571	Z	7	78.9268	80.93987	79.93333	0	696.3333	4830	14	73.29	0.30	1.61
SG12_YS_XRF_572	Y	7	21.72681	23.74574	22.73628	1	698.293	4847	15	71.04	0.32	1.58
SG12_YS_XRF_573	Z	7	80.93987	82.95294	81.94641	0	698.3464	4848	15	73.19	0.29	1.34
SG12_YS_XRF_574	Y	7	23.74574	25.76467	24.75521	0	699.2781	4856	15	70.76	0.33	1.66
SG12_YS_XRF_575	Z	7	82.95294	84.96601	83.95948	0	700.3595	4866	15	72.57	0.31	1.84
SG12_YS_XRF_576	Y	7	25.76467	27.7836	26.77413	0	702.1202	4882	16	70.93	0.32	1.43
SG12_YS_XRF_577	Z	7	84.96601	86.97908	85.97255	0	702.3725	4884	16	72.19	0.31	1.68
SG12_YS_XRF_578	Y	7	27.7836	29.80252	28.79306	0	705.0044	4908	17	72.35	0.30	1.40
SG12_YS_XRF_579	Y	7	29.80252	31.82145	30.81199	0	707.8886	4934	16	70.44	0.35	2.06
SG12_YS_XRF_580	Y	7	31.82145	33.84038	32.83091	0	710.7727	4960	16	71.22	0.32	1.61
SG12_YS_XRF_581	Y	7	33.84038	35.85931	34.84984	0	713.6569	4986	15	68.95	0.36	1.74
SG12_YS_XRF_582	Y	7	35.85931	37.87823	36.86877	1	716.5411	5008	15	67.65	0.37	1.67
SG12_YS_XRF_583	Y	7	37.87823	39.89716	38.8877	1	719.4253	5031	15	66.02	0.41	2.06
SG12_YS_XRF_584	Y	7	39.89716	41.92656	40.91186	0	722.1104	5038	15	73.42	0.29	1.38
SG12_YS_XRF_585	Y	7	41.92656	43.95781	42.94219	1	724.4219	5056	15	71.33	0.32	1.51
SG12_YS_XRF_586	Y	7	43.95781	45.98906	44.97344	0	726.7344	5074	16	71.41	0.32	1.52
SG12_YS_XRF_587	Y	7	45.98906	48.02031	47.00469	1	728.9758	5091	16	70.71	0.33	1.62
SG12_YS_XRF_588	Y	7	48.02031	50.05156	49.03594	0	730.8147	5106	16	71.44	0.33	1.75
SG12_YS_XRF_589	Y	7	50.05156	52.08281	51.06719	0	732.6536	5120	16	71.80	0.32	1.61
SG12_YS_XRF_590	Y	7	52.08281	54.11406	53.09844	0	734.4925	5134	16	71.57	0.32	1.77
SG12_YS_XRF_591	Y	7	54.11406	56.14531	55.12969	0	736.3314	5148	16	71.38	0.34	2.07
SG12_YS_XRF_592	Y	7	56.14531	58.08626	57.11579	0	738.1294	5162	16	70.06	0.32	1.20
SG12_YS_XRF_593	Y	7	58.08626	60.10153	59.09389	0	739.9202	5178	16	73.12	0.31	1.96
SG12_YS_XRF_594	Y	7	60.10153	62.11679	61.10916	0	741.7447	5194	16	71.50	0.32	1.52
SG12_YS_XRF_595	Y	7	62.11679	64.13206	63.12443	0	743.5691	5211	16	71.97	0.31	1.45
SG12_YS_XRF_596	Y	7	64.13206	66.14733	65.13969	0	745.3935	5227	16	71.59	0.32	1.54
SG12_YS_XRF_597	Y	7	66.14733	68.1626	67.15496	0	747.2179	5243	16	70.80	0.33	1.61
SG12_YS_XRF_598	Y	7	68.1626	70.17786	69.17023	1	749.0424	5260	16	70.82	0.33	1.59
SG12_YS_XRF_599	Y	7	70.17786	72.19313	71.1855	0	750.8668	5278	16	70.77	0.34	1.79
SG12_YS_XRF_600	Y	7	72.19313	74.27444	73.23378	1	752.7338	5296	16	70.46	0.28	0.85
SG12_YS_XRF_601	X	8	14.0979	16.1	15.09895	0	753.45	5303	16	70.23	0.34	1.62
SG12_YS_XRF_602	Y	7	74.27444	76.40977	75.34211	0	754.8421	5314	16	71.92	0.30	1.23
SG12_YS_XRF_603	X	8	16.1	18.1	17.1	0	755.57	5319	15	71.96	0.32	1.89
SG12_YS_XRF_604	X	8	18.1	20.1	19.1	0	757.69	5332	15	71.47	0.32	1.58
SG12_YS_XRF_605	X	8	20.1	22.1	21.1	0	759.81	5346	14	71.34	0.30	1.23
SG12_YS_XRF_606	X	8	22.1	24.1	23.1	0	761.93	5360	13	71.01	0.32	1.50
SG12_YS_XRF_607	X	8	24.1	26.1	25.1	0	764.05	5374	13	71.62	0.32	1.65
SG12_YS_XRF_608	X	8	26.1	28.1	27.1	0	766.17	5389	14	72.28	0.30	1.41
SG12_YS_XRF_609	X	8	28.1	30.1	29.1	0	768.29	5403	14	72.13	0.31	1.59
SG12_YS_XRF_610	X	8	30.1	32.11692	31.10846	0	770.37	5419	14	73.40	0.29	1.42

(Continued)

Table S5 List of depth, age and physical property of SG12core samples.

Sample Number	Hole	Section	top	bottom	center	facies*	center composite depth (cm)	center age (yr BP)	age error (yr)	WC (wt %)	DBD (g/cm <sup>3</sup> )	GD (g/cm <sup>3</sup> )
			distance from section top (cm)	distance from section top (cm)	distance from section top (cm)	0: BG 1: including EL-G 2: including EL-B 3: Tephra						
SG12_YS_XRF_611	X	8	32.11692	34.14769	33.13231	0	772.02	5431	13	74.48	0.26	1.05
SG12_YS_XRF_612	X	8	34.14769	36.17846	35.16308	0	773.68	5444	13	75.09	0.26	1.25
SG12_YS_XRF_613	X	8	36.17846	38.20923	37.19385	3	775.33	5458	12	67.29	0.38	1.67
SG12_YS_XRF_614	X	8	38.20923	40.24	39.22462	0	777.26	5474	12	76.17	0.25	1.18
SG12_YS_XRF_615	X	8	40.24	42.27077	41.25538	0	779.22	5490	11	75.77	0.26	1.35
SG12_YS_XRF_616	X	8	42.27077	44.30154	43.28615	0	781.19	5506	11	75.45	0.26	1.29
SG12_YS_XRF_617	X	8	44.30154	46.1165	45.20902	0	783.04	5521	11	77.05	0.25	1.69
SG12_YS_XRF_618	X	8	46.1165	48.09709	47.1068	0	784.88	5536	11	75.11	0.25	1.01
SG12_YS_XRF_619	X	8	48.09709	50.07767	49.08738	0	786.79	5552	10	74.42	0.27	1.37
SG12_YS_XRF_620	X	8	50.07767	52.05825	51.06796	0	788.7	5567	10	74.50	0.28	1.53
SG12_YS_XRF_621	X	8	52.05825	54.03883	53.04854	1	790.62	5582	10	74.14	0.28	1.38
SG12_YS_XRF_622	X	8	54.03883	56.01942	55.02913	0	792.53	5598	10	74.93	0.27	1.28
SG12_YS_XRF_623	X	8	56.01942	58	57.00971	0	794.44	5612	11	75.20	0.26	1.13
SG12_YS_XRF_624	X	8	58	60.04762	59.02381	1	796.28	5626	12	74.91	0.27	1.37
SG12_YS_XRF_625	X	8	60.04762	62.09524	61.07143	0	798.03	5639	13	74.26	0.27	1.28
SG12_YS_XRF_626	X	8	62.09524	64.14286	63.11905	0	800.25	5656	14	73.20	0.29	1.29
SG12_YS_XRF_627	X	8	64.14286	66.19048	65.16667	0	802.59	5672	14	73.59	0.30	1.68
SG12_YS_XRF_628	X	8	66.19048	68.2381	67.21429	0	804.93	5688	15	74.43	0.27	1.37
SG12_YS_XRF_629	X	8	68.2381	70.28571	69.2619	0	807.27	5704	15	74.45	0.28	1.42
SG12_YS_XRF_630	X	8	70.28571	72.32745	71.30658	1	809.52	5719	16	72.74	0.30	1.57
SG12_YS_XRF_631	X	8	72.32745	74.36667	73.34706	0	811.6	5733	16	73.63	0.28	1.29
SG12_YS_XRF_632	X	8	74.36667	76.40588	75.38627	0	813.68	5750	17	75.05	0.28	1.68
SG12_YS_XRF_633	Y	8	28.24457	30.22171	29.23314	1	814.03	5753	17	71.64	0.31	1.45
SG12_YS_XRF_634	Y	8	30.22171	32.19825	31.20998	1	815.86	5769	18	71.69	0.32	1.78
SG12_YS_XRF_635	Y	8	32.19825	34.16316	33.1807	0	817.89	5786	19	75.52	0.26	1.43
SG12_YS_XRF_636	Y	8	34.16316	36.12807	35.14561	0	820.03	5804	21	72.70	0.30	1.46
SG12_YS_XRF_637	Y	8	36.12807	38.09298	37.11053	0	822.17	5822	21	72.33	0.29	1.17
SG12_YS_XRF_638	Y	8	38.09298	40.05789	39.07544	0	824.3	5840	21	71.58	0.30	1.26
SG12_YS_XRF_639	Y	8	40.05789	42.02281	41.04035	0	826.44	5858	21	71.00	0.33	1.61
SG12_YS_XRF_640	Y	8	42.02281	44.02692	43.02487	1	828.6	5876	21	71.74	0.31	1.42
SG12_YS_XRF_641	Y	8	44.02692	46.10385	45.06538	1	830.53	5892	21	72.73	0.30	1.39
SG12_YS_XRF_642	Y	8	46.10385	48.1	47.10192	0	832.6	5910	21	72.46	0.29	1.30
SG12_YS_XRF_643	Y	8	48.1	50.1	49.1	1	834.76	5928	21	70.63	0.32	1.43
SG12_YS_XRF_644	Y	8	50.1	52.1	51.1	1	836.74	5944	21	71.71	0.33	1.85
SG12_YS_XRF_645	Y	8	52.1	54.1	53.1	0	838.67	5961	21	72.68	0.28	1.07
SG12_YS_XRF_646	Y	8	54.1	56.05762	55.07881	0	840.58	5977	21	73.18	0.29	1.37
SG12_YS_XRF_647	Y	8	56.05762	58.04437	57.05099	0	842.48	5993	22	74.59	0.28	1.43
SG12_YS_XRF_648	Y	8	58.04437	60.03113	59.03775	1	844.39	6010	22	72.51	0.30	1.34
SG12_YS_XRF_649	Y	8	60.03113	62.01788	61.0245	0	846.35	6027	22	74.06	0.28	1.51
SG12_YS_XRF_650	Z	9	13.82326	15.68372	14.75349	0	847.64	6038	23	71.11	0.33	1.72
SG12_YS_XRF_651	Y	8	62.01788	64.00464	63.01126	0	848.43	6045	23	71.85	0.31	1.42
SG12_YS_XRF_652	Z	9	15.68372	17.54419	16.61395	1	849.59	6055	23	71.00	0.30	1.15
SG12_YS_XRF_653	Z	9	17.54419	19.40465	18.47442	0	851.51	6072	23	71.92	0.30	1.25
SG12_YS_XRF_654	Z	9	19.40465	21.26512	20.33488	0	853.42	6088	24	70.03	0.34	1.69
SG12_YS_XRF_655	Z	9	21.26512	23.12558	22.19535	0	855.33	6105	24	70.08	0.33	1.42
SG12_YS_XRF_656	Z	9	23.12558	24.98605	24.05581	1	857.24	6121	23	69.81	0.34	1.61
SG12_YS_XRF_657	Z	9	24.98605	26.84651	25.91628	0	859.14	6137	23	69.66	0.34	1.52
SG12_YS_XRF_658	Z	9	26.84651	28.70698	27.77674	0	861.05	6153	22	69.64	0.33	1.36
SG12_YS_XRF_659	Z	9	28.70698	30.56744	29.63721	0	862.96	6170	21	69.46	0.33	1.28
SG12_YS_XRF_660	Z	9	30.56744	33.64492	32.10618	0	865.5	6192	20	69.20	0.34	1.43
SG12_YS_XRF_661	Z	9	33.64492	35.65027	34.64759	1	868.1	6215	18	69.56	0.35	1.79
SG12_YS_XRF_662	Z	9	35.65027	37.65561	36.65294	1	870.13	6233	17	69.34	0.34	1.54
SG12_YS_XRF_663	Z	9	37.65561	39.66096	38.65829	1	872	6249	16	69.42	0.34	1.54
SG12_YS_XRF_664	Z	9	39.66096	41.66631	40.66364	0	873.99	6267	15	70.19	0.32	1.25
SG12_YS_XRF_665	Z	9	41.66631	43.67166	42.66898	0	876.03	6284	14	68.90	0.35	1.54
SG12_YS_XRF_666	Z	9	43.67166	45.67701	44.67433	1	878.07	6304	15	67.39	0.36	1.42
SG12_YS_XRF_667	Z	9	45.67701	47.68235	46.67968	0	880.1	6326	16	67.23	0.36	1.32
SG12_YS_XRF_668	Z	9	47.68235	49.6877	48.68503	1	882.12	6348	17	65.72	0.40	1.64
SG12_YS_XRF_669	Z	9	49.6877	51.69305	50.69037	0	884.15	6369	18	66.33	0.39	1.77
SG12_YS_XRF_670	Z	9	51.69305	53.6984	52.69572	1	886.18	6391	19	60.80	0.49	2.06
SG12_YS_XRF_671	Z	9	53.6984	55.7	54.6992	1	888.19	6405	19	67.91	0.37	1.67

(Continued)

Table S5 List of depth, age and physical property of SG12core samples.

Sample Number	Hole	Section	top	bottom	center	facies*	center composite depth (cm)	center age (yr BP)	age error (yr)	WC (wt %)	DBD (g/cm <sup>3</sup> )	GD (g/cm <sup>3</sup> )
			distance from section top (cm)	distance from section top (cm)	distance from section top (cm)	0: BG 1: including EL-G 2: including EL-B 3: Tephra						
SG12_YS_XRF_672	Z	9	55.7	57.7	56.7	0	890	6424	20	67.51	0.37	1.59
SG12_YS_XRF_673	Z	9	57.7	59.7	58.7	1	891.82	6444	21	66.46	0.38	1.57
SG12_YS_XRF_674	Z	9	59.7	61.7	60.7	0	893.88	6466	22	68.83	0.36	1.77
SG12_YS_XRF_675	Z	9	61.7	63.7	62.7	1	895.96	6488	23	69.14	0.34	1.51
SG12_YS_XRF_676	Z	9	63.7	65.7	64.7	1	898.05	6510	24	70.74	0.33	1.63
SG12_YS_XRF_677	Z	9	65.7	67.7	66.7	0	900.13	6533	24	70.04	0.34	1.56
SG12_YS_XRF_678	Y	9	9.869281	11.84314	10.85621	0	902.16	6556	25	69.91	0.33	1.44
SG12_YS_XRF_679	Z	9	67.7	69.7	68.7	0	902.22	6557	25	69.76	0.34	1.52
SG12_YS_XRF_680	Y	9	11.84314	13.81699	12.83007	0	904.13	6578	25	69.26	0.35	1.57
SG12_YS_XRF_681	Y	9	13.81699	15.79085	14.80392	1	906.1	6599	26	66.82	0.38	1.71
SG12_YS_XRF_682	Y	9	15.79085	17.76471	16.77778	1	907.62	6616	26	70.12	0.34	1.57
SG12_YS_XRF_683	Y	9	17.76471	19.8	18.78235	1	908.99	6632	26	70.87	0.32	1.39
SG12_YS_XRF_684	Y	9	19.8	21.8	20.8	1	910.38	6648	26	70.58	0.32	1.36
SG12_YS_XRF_685	Y	9	21.8	23.8	22.8	1	911.75	6663	26	74.53	0.28	1.46
SG12_YS_XRF_686	Y	9	23.8	25.8	24.8	0	913.13	6678	26	76.12	0.25	1.29
SG12_YS_XRF_687	Y	9	25.8	27.8	26.8	0	914.5	6694	26	76.05	0.25	1.15
SG12_YS_XRF_688	Y	9	27.8	29.8	28.8	0	915.87	6709	26	75.41	0.26	1.29
SG12_YS_XRF_689	Y	9	29.8	31.8	30.8	0	917.25	6725	27	74.89	0.27	1.35
SG12_YS_XRF_690	Y	9	31.8	33.8	32.8	0	918.62	6740	27	75.09	0.28	1.62
SG12_YS_XRF_691	Y	9	33.8	35.8	34.8	1	920	6756	27	74.07	0.29	1.54
SG12_YS_XRF_692	Y	9	35.8	37.8	36.8	0	921.37	6771	27	74.25	0.27	1.24
SG12_YS_XRF_693	Y	9	37.8	39.8	38.8	1	922.74	6787	27	72.94	0.29	1.33
SG12_YS_XRF_694	Y	9	39.8	41.8	40.8	1	924.42	6806	27	73.85	0.29	1.58
SG12_YS_XRF_695	Y	9	41.8	43.8	42.8	1	926.47	6828	27	74.19	0.28	1.35
SG12_YS_XRF_696	Y	9	43.8	45.8	44.8	0	928.51	6849	27	74.15	0.28	1.56
SG12_YS_XRF_697	Y	9	45.8	47.8	46.8	0	930.56	6871	27	73.40	0.30	1.60
SG12_YS_XRF_698	Y	9	47.8	49.8	48.8	1	932.6	6892	28	73.86	0.29	1.52
SG12_YS_XRF_699	Y	9	49.8	51.8	50.8	0	934.65	6914	28	74.30	0.27	1.28
SG12_YS_XRF_700	Y	9	51.8	53.8	52.8	0	936.7	6935	28	73.94	0.29	1.51
SG12_YS_XRF_701	Y	9	53.8	55.8	54.8	0	938.74	6956	28	74.89	0.27	1.39
SG12_YS_XRF_702	Y	9	55.8	57.8	56.8	0	940.79	6978	29	74.10	0.29	1.57
SG12_YS_XRF_703	Y	9	57.8	59.8	58.8	0	942.83	7000	30	72.33	0.31	1.51
SG12_YS_XRF_704	Y	9	59.8	61.79341	60.7967	1	944.88	7021	31	62.14	0.45	1.76
SG12_YS_XRF_705	Y	9	61.79341	63.74945	62.77143	1	946.74	7041	32	59.15	0.46	1.34
SG12_YS_XRF_706	Y	9	63.74945	65.70549	64.72747	1	948.46	7059	33	70.52	0.33	1.55
SG12_YS_XRF_707	Y	9	65.70549	67.66154	66.68352	1	950.27	7078	34	74.35	0.28	1.48
SG12_YS_XRF_708	Y	9	67.66154	69.61758	68.63956	0	952.18	7099	35	73.99	0.28	1.42
SG12_YS_XRF_709	Y	9	69.61758	71.6233	70.62044	1	954.12	7119	36	70.47	0.33	1.51
SG12_YS_XRF_710	Y	9	71.6233	73.66214	72.64272	0	956.12	7141	37	72.53	0.30	1.47
SG12_YS_XRF_711	Y	9	73.66214	75.70097	74.68155	0	958.14	7163	36	72.58	0.30	1.37
SG12_YS_XRF_712	Y	9	75.70097	77.73981	76.72039	1	960.16	7187	35	71.23	0.32	1.65
SG12_YS_XRF_713	Y	9	77.73981	79.77864	78.75922	0	962.18	7211	34	70.38	0.34	1.67
SG12_YS_XRF_714	Y	9	79.77864	81.8	80.78932	3	964.19	7235	33	48.60	0.60	1.39
SG12_YS_XRF_715	Y	9	81.8	83.8	82.8	3	965.94	7239	32	50.99	0.39	0.64

Table S6 List of age controlling point of Lake Suigetsu sediment used in chapter 5.

Name of Age controlling point	Sampling position in SG06 core			Composite depth (cm)	Event free depth (cm)	Age mid point (0 = 1950 AD)			Source
	Hole	Core	Distance from core top			Error +	Error -		
OxA-24328	A	1	22	42	42	8	31	8	Saito Kato et al. (2014)
OxA-24276	A	1	47.5	67.5	67.5	5	162	5	Saito Kato et al. (2015)
Urami Canal Construction, AD	---	---	---	87.8	87.8	5	283	5	Saito Kato et al. (2016)
SUERC-25980	C	1	18.5	103.6	103.5455	9	348	9	Saito Kato et al. (2017)
OxA-24231	A	1	88.4	108.4	108.4	11	370	11	Saito Kato et al. (2018)
SUERC-26727	C	1	30.8	113.8	113.8327	12	396	12	Saito Kato et al. (2019)
OxA-X-2270-49	A	1	116.4	136.4	136.4	8	505	8	Saito Kato et al. (2020)
SUERC-26355	C	1	76.4	152	154.9	7	575	7	Saito Kato et al. (2021)
SUERC-20471	D	1	56.8	177.6	176.8	16	692	16	Saito Kato et al. (2022)
OxA-24191	D	1	91	211.8	205.4	12	909	12	Saito Kato et al. (2023)
SUERC-23361	C	2	19.8	222.5	214.5	19	1004	19	Staff et al. (2011)
OxA-24233	D	1	113.1	233.9	227.5	22	1109	22	Staff et al. (2011)
SUERC-25981	A	2	23.5	251.8	245.4	21	1262	21	Staff et al. (2011)
OxA-24266	C	2	64	263.4	256.9841	17	1350	17	Staff et al. (2011)
SUERC-26356	C	2	70.3	269.4	263.0397	18	1400	18	Staff et al. (2011)
OxA-24299	C	2	91	290.6	283.5	23	1576	23	Staff et al. (2011)
SUERC-25982	A	2	70.5	298.8	292.4	21	1639	21	Staff et al. (2011)
OxA-	A	2	78.9	307.2	300.8	21	1697	21	Staff et al. (2011)
SUERC-20499	A	2	93.4	321.7	315.3	29	1810	29	Staff et al. (2011)
OxA-24319	C	3	35.6	337	330.6746	29	1912	29	Staff et al. (2011)
SUERC-26357	C	3	43.4	344.6	338.1909	31	1971	31	Staff et al. (2011)
SUERC-25983	A	2	134.4	362.7	356.3	41	2105	41	Staff et al. (2011)
OxA-24243/OxA-	A	2	140.7	369	362.6	41	2148	41	Staff et al. (2011)
SUERC-26358	D	2	64.6	387.3	380.9	39	2290	39	Staff et al. (2011)
OxA-X-2347-43	D	2	70.2	392.9	386.5	36	2337	36	Staff et al. (2011)
SUERC-25984	A	2	170.2	399	392.6419	34	2392	34	Staff et al. (2011)
OxA-	A	2	177.7	406.3	399.9	37	2454	37	Staff et al. (2011)
24183/SUERC-	A	2	182.3	413.9	404.9	38	2516	38	Staff et al. (2011)
SUERC-	D	2	105.7	428.4	422	40	2632	40	Staff et al. (2011)
20472/OxA-	D	2	126.7	449.4	443	38	2825	38	Staff et al. (2011)
SUERC-26359	D	2	138.9	461.6	455.2	40	2947	40	Staff et al. (2011)
OxA-24308	D	2	154.8	477.5	471.1	33	3091	33	Staff et al. (2011)
SUERC-28200	D	2	162	484.7	478.3	30	3153	30	Staff et al. (2011)
OxA-24232	D	2	178.8	500.4	495	26	3297	26	Staff et al. (2011)
SUERC-26729	A	3	81.7	508.4	502	20	3369	20	Staff et al. (2011)
OxA-24320	A	3	100.8	527.5	521.1	23	3525	23	Staff et al. (2011)
SUERC-28201	A	3	108.3	535	528.6	22	3586	22	Staff et al. (2011)
SUERC-20473	D	3	15.6	548.9	542.4814	22	3699	22	Staff et al. (2011)
OxA-24300	D	3	28.2	561.3	554.8469	25	3805	25	Staff et al. (2011)
SUERC-25985	A	3	144.9	571.8	565.4036	23	3895	23	Staff et al. (2011)
OxA-24321	A	3	152.5	579.4	573.0494	23	3956	23	Staff et al. (2011)
SUERC-20474	A	3	169	596	589.6	26	4088	26	Staff et al. (2011)
OxA-24194	A	3	175	602.1	595.6	24	4126	24	Staff et al. (2011)
SUERC-26360	C	6	19	616	609.7	23	4222	23	Staff et al. (2011)
SUERC-20475	C	6	34.3	631.6	625.2706	24	4336	24	Staff et al. (2011)
OxA-	C	6	37.8	635.2	628.8392	25	4362	25	Staff et al. (2011)
24237/SUERC-	D	3	120.5	653.4	647	26	4492	26	Staff et al. (2011)
OxA-24277/OxA-	C	6	60.5	657.6	651.2861	25	4524	25	Staff et al. (2011)
24278	D	3	135	667.9	661.5	26	4611	26	Staff et al. (2011)
SUERC-25988	C	6	79.4	678.2	671.4	23	4688	23	Staff et al. (2011)
OxA-24271	C	6	86	685.4	678	15	4741	15	Staff et al. (2011)
SUERC-26361	A	4	55.9	691.9	685.5	14	4793	14	Staff et al. (2011)
SUERC-26730	A	4	57.7	693.7	687.3	13	4806	13	Staff et al. (2011)
OxA-24284	A	4	69.8	705.8	699.4	17	4915	17	Staff et al. (2011)
SUERC-20476	D	3	182.3	713.5	707.7	15	4985	15	Staff et al. (2011)
OxA-24195	A	4	102	738	730.3	16	5161	16	Staff et al. (2011)
OxA-24285	A	4	102	738	730.3	16	5161	16	Staff et al. (2011)
SUERC-25989	D	3	182.3	713.5	707.7	15	4985	15	Staff et al. (2011)
SUERC-23354	A	4	102	738	730.3	16	5161	16	Staff et al. (2011)

(Continued)

Table S6 List of age controlling point of Lake Suigetsu sediment used in chapter 5.

Name of Age controlling point	Sampling position in SG06 core			Composit e depth (cm)	Event free depth (cm)	Age mid point (0 = 1950 AD)			Source
	Hole	Core	Distance from core top			Error +	Error -		
OxA-X-2360-44	B	4	4.7	748.3	740.6	16	5253	16	Staff et al. (2011)
OxA-24238	A	4	118.1	754.1	746.4	16	5309	16	Staff et al. (2011)
SUERC-25990	B	4	18.1	761.8	754.052	13	5359	13	Staff et al. (2011)
SUERC-28202	B	4	24.4	768.1	760.3881	14	5402	14	Staff et al. (2011)
OxA-24351	B	4	29.5	773	765.2415	13	5438	13	Staff et al. (2011)
SUERC-28206	B	4	36.8	780	772.3	11	5497	11	Staff et al. (2011)
OxA-24220	B	4	49.5	792.7	785	10	5599	10	Staff et al. (2011)
SUERC-25992	B	4	57.6	800.8	793.1	14	5660	14	Staff et al. (2011)
SUERC-20479	A	4	176	812	804.2561	16	5736	16	Staff et al. (2011)
SUERC-28228	B	4	77.4	820.6	812.9	21	5809	21	Staff et al. (2011)
SUERC-26362	B	4	96.7	839.9	832.2001	21	5971	21	Staff et al. (2011)
OxA-24262	A	5	5.8	854.9	848.2001	24	6101	24	Staff et al. (2011)
SUERC-23355	A	5	11.6	861	854	22	6153	22	Staff et al. (2011)
SUERC- 13332/OxA-	A	5	26.9	876.9	869.3	14	6292	14	Staff et al. (2011)
OxA-24255	A	5	47.6	898.1	889.6	24	6511	24	Staff et al. (2011)
SUERC-26731	A	5	56.1	906.6	898.1	26	6605	26	Staff et al. (2011)
SUERC-20480	B	5	23.2	925.7	917.2001	27	6820	27	Staff et al. (2011)
OxA-24279	B	5	36.5	939	930.5	28	6959	28	Staff et al. (2011)
SUERC-25993	C	7	56.3	957.1	948.5638	37	7151	37	Staff et al. (2011)
SUERC-26365	C	7	82.4	983.8	972.1001	22	7435	22	Staff et al. (2011)

Table S7 List of XRF data of SG12core samples (Total value including LOI is normalized to 100 wt%) and LSR

Sample Number	SiO <sub>2</sub>	TiO <sub>2</sub>	Al <sub>2</sub> O <sub>3</sub>	Fe <sub>2</sub> O <sub>3</sub>	MnO	MgO	CaO	Na <sub>2</sub> O	K <sub>2</sub> O	P <sub>2</sub> O <sub>5</sub>	LOI	LSR (cm/yr)
SG_YS_XRF_1	43.16	0.78	14.91	9.11	0.41	2.46	0.62	2.58	2.07	0.25	23.64	0.19
SG_YS_XRF_2	41.97	0.70	14.19	9.16	0.49	2.19	0.61	2.65	2.01	0.25	25.78	0.19
SG_YS_XRF_3	40.21	0.69	14.45	9.75	0.55	2.14	0.56	2.59	1.99	0.26	26.82	0.19
SG_YS_XRF_4	38.86	0.62	12.71	10.26	0.52	2.06	0.61	2.81	1.92	0.25	29.37	0.19
SG_YS_XRF_5	36.45	0.59	11.75	10.74	0.50	1.88	0.60	2.60	1.92	0.27	32.70	0.19
SG_YS_XRF_6	36.39	0.56	11.88	9.42	0.38	1.94	0.58	2.93	1.82	0.28	33.81	0.19
SG_YS_XRF_7	39.07	0.60	11.91	8.61	0.33	2.00	0.58	2.87	1.92	0.24	31.88	0.19
SG_YS_XRF_8	42.34	0.66	12.76	8.99	0.33	2.09	0.59	2.66	1.94	0.24	27.40	0.19
SG_YS_XRF_9	43.15	0.69	14.12	9.76	0.33	2.18	0.57	2.53	1.91	0.23	24.52	0.19
SG_YS_XRF_10	46.31	0.54	11.11	8.02	0.25	1.80	0.49	2.53	1.74	0.21	26.99	0.19
SG_YS_XRF_11	58.83	0.52	9.73	6.54	0.17	1.62	0.43	2.26	1.42	0.18	18.32	0.19
SG_YS_XRF_12	45.76	0.65	12.76	9.43	0.27	2.07	0.57	2.67	1.79	0.24	23.79	0.19
SG_YS_XRF_13	48.29	0.64	12.57	8.75	0.24	1.96	0.51	2.61	1.79	0.22	22.43	0.19
SG_YS_XRF_14	50.56	0.48	9.63	7.42	0.19	1.65	0.45	2.77	1.52	0.20	25.14	0.19
SG_YS_XRF_15	53.47	0.52	9.98	7.32	0.18	1.67	0.44	2.43	1.59	0.20	22.20	0.19
SG_YS_XRF_16	48.30	0.64	12.25	9.08	0.23	1.96	0.52	2.51	1.75	0.21	22.56	0.19
SG_YS_XRF_17	52.60	0.52	10.39	7.55	0.21	1.66	0.44	2.49	1.64	0.19	22.32	0.19
SG_YS_XRF_18	48.08	0.49	9.61	7.75	0.25	1.74	0.51	3.08	1.76	0.21	26.52	0.19
SG_YS_XRF_19	45.61	0.62	12.14	9.83	0.33	1.92	0.53	2.66	1.90	0.22	24.24	0.19
SG_YS_XRF_20	44.84	0.61	12.04	9.88	0.34	1.91	0.51	2.67	1.80	0.22	25.18	0.19
SG_YS_XRF_21	42.69	0.75	14.38	10.14	0.36	2.25	0.57	2.70	2.04	0.25	23.88	0.19
SG_YS_XRF_22	45.56	0.61	13.07	8.93	0.29	1.95	0.53	2.90	1.92	0.24	24.00	0.19
SG_YS_XRF_23	44.17	0.59	12.24	9.87	0.35	1.88	0.55	2.76	1.82	0.24	25.52	0.19
SG_YS_XRF_24	40.87	0.65	13.53	10.37	0.38	2.06	0.55	2.84	1.87	0.23	26.65	0.19
SG_YS_XRF_25	42.64	0.65	13.64	10.71	0.38	2.02	0.53	2.58	1.88	0.22	24.74	0.19
SG_YS_XRF_26	45.66	0.69	14.87	9.91	0.34	2.15	0.54	2.57	2.01	0.20	21.06	0.19
SG_YS_XRF_27	44.03	0.86	20.49	9.83	0.35	2.36	0.54	2.12	2.25	0.31	16.87	0.19
SG_YS_XRF_28	43.92	0.65	13.52	12.14	0.37	2.04	0.52	2.47	1.85	0.18	22.33	0.19
SG_YS_XRF_29	50.53	0.52	10.89	12.23	0.28	1.69	0.42	2.38	1.66	0.14	19.26	0.19
SG_YS_XRF_30	50.17	0.53	11.12	12.65	0.16	1.71	0.41	2.30	1.67	0.14	19.14	0.19
SG_YS_XRF_31	53.10	0.61	12.87	9.17	0.16	1.89	0.46	2.34	1.83	0.15	17.41	0.19
SG_YS_XRF_32	49.98	0.56	11.67	12.86	0.15	1.78	0.43	2.28	1.69	0.15	18.46	0.19
SG_YS_XRF_33	52.42	0.49	10.45	11.48	0.14	1.63	0.41	2.49	1.50	0.14	18.87	0.19
SG_YS_XRF_34	57.78	0.45	9.34	11.16	0.11	1.43	0.34	1.96	1.37	0.11	15.94	0.19
SG_YS_XRF_35	50.89	0.46	9.71	13.41	0.13	1.54	0.38	2.29	1.48	0.13	19.58	0.19
SG_YS_XRF_36	46.14	0.41	8.76	17.47	0.33	1.39	0.35	2.12	1.40	0.12	21.52	0.19
SG_YS_XRF_37	52.83	0.61	12.97	8.18	0.25	1.91	0.48	2.65	1.81	0.17	18.15	0.19
SG_YS_XRF_38	46.86	0.56	11.73	11.39	1.25	1.81	0.51	2.44	1.67	0.19	21.59	0.17
SG_YS_XRF_39	48.76	0.62	12.79	9.75	0.36	1.97	0.50	2.61	1.86	0.17	20.61	0.17
SG_YS_XRF_40	48.53	0.65	13.51	9.84	0.20	2.08	0.50	2.58	1.91	0.17	20.01	0.17
SG_YS_XRF_41	47.60	0.55	11.66	11.78	0.74	1.83	0.49	2.55	1.79	0.17	20.83	0.17
SG_YS_XRF_42	50.14	0.58	12.06	10.85	0.20	1.85	0.45	2.47	1.79	0.15	19.46	0.17
SG_YS_XRF_43	47.66	0.62	12.45	11.22	0.24	1.91	0.49	2.61	1.87	0.16	20.79	0.17
SG_YS_XRF_44	58.31	0.59	12.41	6.46	0.17	1.87	0.44	2.43	1.72	0.16	15.44	0.17
SG_YS_XRF_45	58.71	0.55	11.78	6.42	0.17	1.74	0.43	2.54	1.62	0.16	15.88	0.17
SG_YS_XRF_46	56.37	0.57	12.27	7.79	0.17	1.74	0.42	2.32	1.69	0.16	16.50	0.17
SG_YS_XRF_47	58.68	0.53	11.59	6.63	0.15	1.67	0.41	2.48	1.77	0.15	15.95	0.17
SG_YS_XRF_48	58.75	0.50	12.80	6.37	0.14	1.57	0.35	2.40	1.79	0.16	15.16	0.17
SG_YS_XRF_49	56.88	0.46	9.69	8.34	0.14	1.53	0.39	2.73	1.58	0.14	18.12	0.17
SG_YS_XRF_50	57.00	0.58	12.72	6.76	0.20	1.77	0.42	2.60	1.71	0.17	16.06	0.17
SG_YS_XRF_51	55.58	0.54	10.88	7.44	0.18	1.73	0.44	2.81	1.70	0.17	18.53	0.17
SG_YS_XRF_52	57.10	0.57	11.50	6.78	0.16	1.76	0.44	2.73	1.72	0.16	17.08	0.17
SG_YS_XRF_53	59.00	0.52	10.43	6.79	0.15	1.61	0.44	2.48	1.65	0.16	16.76	0.17
SG_YS_XRF_54	58.60	0.55	10.80	6.17	0.14	1.63	0.43	2.53	1.64	0.16	17.34	0.17
SG_YS_XRF_55	59.54	0.47	9.51	6.89	0.27	1.49	0.44	2.45	1.45	0.15	17.34	0.17
SG_YS_XRF_56	50.71	0.51	9.88	9.48	0.53	1.67	0.42	2.75	1.72	0.19	22.14	0.17
SG_YS_XRF_57	40.01	0.38	7.30	20.99	0.20	1.37	0.40	2.81	1.45	0.14	24.95	0.24
SG_YS_XRF_58	56.14	0.58	11.34	6.81	0.22	1.77	0.44	2.75	1.68	0.19	18.09	0.24
SG_YS_XRF_61	53.85	0.61	12.26	6.34	0.44	1.83	0.47	2.63	1.75	0.49	19.34	0.24
SG_YS_XRF_59	55.69	0.59	11.64	5.83	0.35	1.83	0.43	2.84	1.83	0.39	18.59	0.24
SG_YS_XRF_62	57.65	0.58	11.50	5.89	0.46	1.69	0.44	2.43	1.67	0.74	16.95	0.24
SG_YS_XRF_60	58.05	0.55	10.82	6.01	0.46	1.66	0.44	2.63	1.66	0.96	16.76	0.24
SG_YS_XRF_63	58.81	0.59	11.42	6.63	0.41	1.67	0.40	2.17	1.58	1.21	15.12	0.24
SG_YS_XRF_64	60.49	0.56	10.68	6.12	0.34	1.58	0.39	2.23	1.54	0.93	15.13	0.24
SG_YS_XRF_65	60.12	0.52	10.41	6.45	0.39	1.56	0.38	2.22	1.47	1.14	15.32	0.24
SG_YS_XRF_66	62.04	0.54	10.66	5.56	0.26	1.61	0.39	2.32	1.49	0.52	14.61	0.24
SG_YS_XRF_67	61.09	0.57	11.01	6.10	0.26	1.64	0.39	2.22	1.53	0.65	14.55	0.24
SG_YS_XRF_68	60.51	0.61	11.74	6.37	0.28	1.67	0.40	2.07	1.61	0.76	13.98	0.24

(Continued)

Table S7 List of XRF data of SG12core samples (Total value including LOI is normalized to 100 wt%) and LSR

Sample Number	SiO <sub>2</sub>	TiO <sub>2</sub>	Al <sub>2</sub> O <sub>3</sub>	Fe <sub>2</sub> O <sub>3</sub>	MnO	MgO	CaO	Na <sub>2</sub> O	K <sub>2</sub> O	P <sub>2</sub> O <sub>5</sub>	LOI	LSR (cm/yr)
SG_YS_XRF_69	61.43	0.65	12.40	6.20	0.24	1.72	0.38	1.92	1.67	0.66	12.72	0.24
SG_YS_XRF_70	58.61	0.77	14.34	6.79	0.25	1.95	0.42	1.89	1.88	0.56	12.55	0.24
SG_YS_XRF_71	59.21	0.62	12.01	7.09	0.33	1.71	0.39	2.09	1.65	1.02	13.88	0.24
SG_YS_XRF_72	60.38	0.64	12.46	6.61	0.24	1.73	0.38	2.05	1.68	0.56	13.26	0.24
SG_YS_XRF_73	57.20	0.70	13.26	7.79	0.31	1.82	0.41	2.04	1.80	0.89	13.78	0.24
SG_YS_XRF_74	57.77	0.67	12.38	7.93	0.29	1.72	0.39	2.08	1.68	0.89	14.19	0.24
SG_YS_XRF_75	59.08	0.72	13.26	7.06	0.19	1.74	0.39	2.06	1.69	0.37	13.43	0.22
SG_YS_XRF_76	59.95	0.75	13.52	6.45	0.21	1.71	0.37	1.97	1.78	0.34	12.94	0.22
SG_YS_XRF_77	58.89	0.79	14.25	6.37	0.24	1.69	0.37	1.87	1.85	0.45	13.23	0.22
SG_YS_XRF_78	59.06	0.67	12.57	6.70	0.26	1.66	0.39	1.90	1.93	0.62	14.25	0.22
SG_YS_XRF_79	63.00	0.56	11.41	5.97	0.25	1.43	0.35	1.81	2.11	0.56	12.55	0.22
SG_YS_XRF_80	61.65	0.54	9.84	6.50	0.29	1.49	0.37	2.06	1.42	0.78	15.07	0.21
SG_YS_XRF_81	60.89	0.54	10.13	6.72	0.30	1.51	0.36	2.05	1.43	0.79	15.28	0.21
SG_YS_XRF_82	60.17	0.59	10.93	6.94	0.32	1.50	0.36	2.06	1.55	0.79	14.79	0.21
SG_YS_XRF_83	61.04	0.58	10.58	6.78	0.30	1.50	0.36	2.04	1.51	0.77	14.53	0.21
SG_YS_XRF_84	61.22	0.55	9.82	6.72	0.31	1.49	0.36	1.97	1.38	0.74	15.44	0.21
SG_YS_XRF_85	61.34	0.53	9.53	7.34	0.30	1.49	0.37	2.00	1.37	0.83	14.90	0.21
SG_YS_XRF_86	61.39	0.54	9.69	6.73	0.27	1.49	0.37	1.97	1.38	0.73	15.45	0.21
SG_YS_XRF_87	61.22	0.52	9.40	6.63	0.30	1.43	0.36	2.00	1.34	0.76	16.05	0.21
SG_YS_XRF_88	62.39	0.50	9.06	6.62	0.32	1.39	0.35	1.97	1.32	0.88	15.21	0.21
SG_YS_XRF_89	61.71	0.59	10.32	6.44	0.25	1.53	0.38	1.93	1.40	0.61	14.85	0.21
SG_YS_XRF_90	61.84	0.53	9.68	6.41	0.28	1.43	0.35	2.03	1.36	0.71	15.38	0.21
SG_YS_XRF_91	62.90	0.50	9.14	6.18	0.26	1.42	0.36	1.99	1.30	0.69	15.26	0.21
SG_YS_XRF_92	62.09	0.53	9.33	6.42	0.29	1.48	0.37	1.98	1.32	0.74	15.46	0.21
SG_YS_XRF_93	61.96	0.54	9.59	6.38	0.28	1.52	0.38	1.98	1.35	0.67	15.34	0.21
SG_YS_XRF_94	61.90	0.55	9.78	6.24	0.26	1.55	0.39	1.98	1.38	0.59	15.39	0.21
SG_YS_XRF_95	61.03	0.58	10.13	6.58	0.28	1.61	0.40	1.99	1.41	0.64	15.34	0.21
SG_YS_XRF_96	60.64	0.56	9.77	6.94	0.35	1.57	0.40	2.08	1.37	0.83	15.50	0.21
SG_YS_XRF_97	59.54	0.65	11.25	7.15	0.31	1.81	0.43	1.94	1.50	0.63	14.79	0.21
SG_YS_XRF_98	62.20	0.51	9.35	6.32	0.32	1.42	0.36	2.02	1.25	0.73	15.51	0.21
SG_YS_XRF_99	61.23	0.58	10.52	6.11	0.23	1.56	0.37	1.98	1.39	0.53	15.50	0.21
SG_YS_XRF_100	60.52	0.49	8.71	6.49	0.36	1.36	0.36	1.99	1.34	0.88	17.50	0.21
SG_YS_XRF_101	59.67	0.57	10.23	6.66	0.34	1.52	0.38	1.96	1.35	0.83	16.48	0.21
SG_YS_XRF_102	61.58	0.52	9.74	6.04	0.29	1.45	0.37	2.09	1.29	0.72	15.92	0.21
SG_YS_XRF_103	60.49	0.56	10.26	6.56	0.33	1.54	0.39	1.97	1.36	0.78	15.75	0.21
SG_YS_XRF_104	59.58	0.63	11.25	6.90	0.30	1.64	0.41	1.90	1.48	0.68	15.22	0.21
SG_YS_XRF_105	61.10	0.65	12.06	6.13	0.23	1.69	0.40	1.82	1.50	0.47	13.96	0.21
SG_YS_XRF_106	60.15	0.73	13.82	6.44	0.21	1.83	0.41	1.66	1.63	0.40	12.73	0.21
SG_YS_XRF_109	60.08	0.71	13.31	6.25	0.19	1.79	0.41	1.76	1.66	0.39	13.47	0.21
SG_YS_XRF_107	57.99	0.78	15.13	6.82	0.21	1.94	0.42	1.63	1.74	0.40	12.94	0.21
SG_YS_XRF_110	57.99	0.79	15.09	6.79	0.19	1.96	0.43	1.71	1.78	0.39	12.89	0.26
SG_YS_XRF_108	62.31	0.55	9.89	6.62	0.36	1.47	0.37	1.83	1.33	0.71	14.56	0.26
SG_YS_XRF_111	62.93	0.54	9.82	6.26	0.29	1.47	0.37	1.89	1.38	0.64	14.41	0.26
SG_YS_XRF_112	62.85	0.54	9.81	6.65	0.33	1.47	0.36	1.78	1.32	0.69	14.18	0.26
SG_YS_XRF_113	61.39	0.57	10.72	6.99	0.38	1.54	0.38	1.76	1.36	0.77	14.13	0.26
SG_YS_XRF_114	61.77	0.52	9.25	7.67	0.57	1.42	0.37	1.79	1.34	0.87	14.43	0.26
SG_YS_XRF_115	62.88	0.51	9.20	7.07	0.45	1.41	0.35	1.85	1.29	0.72	14.27	0.26
SG_YS_XRF_116	61.23	0.58	10.29	7.32	0.41	1.54	0.37	1.81	1.38	0.66	14.42	0.26
SG_YS_XRF_117	63.57	0.47	8.62	6.59	0.43	1.32	0.34	1.80	1.21	0.75	14.90	0.26
SG_YS_XRF_118	65.61	0.47	8.24	6.04	0.40	1.28	0.34	1.79	1.23	0.61	13.98	0.26
SG_YS_XRF_119	64.63	0.47	8.26	6.64	0.53	1.27	0.34	1.71	1.18	0.64	14.34	0.26
SG_YS_XRF_120	64.28	0.53	9.28	6.44	0.38	1.40	0.36	1.80	1.29	0.46	13.78	0.26
SG_YS_XRF_121	62.52	0.56	9.71	7.00	0.49	1.45	0.37	1.76	1.32	0.66	14.17	0.26
SG_YS_XRF_122	63.93	0.58	9.82	7.16	0.52	1.47	0.37	1.76	1.38	0.77	12.25	0.26
SG_YS_XRF_123	62.24	0.64	10.61	7.22	0.52	1.56	0.38	1.68	1.37	0.61	13.18	0.26
SG_YS_XRF_124	63.06	0.57	9.72	6.93	0.55	1.43	0.37	1.69	1.28	0.65	13.77	0.26
SG_YS_XRF_125	62.47	0.49	8.51	7.61	0.75	1.28	0.36	1.90	1.19	0.85	14.59	0.19
SG_YS_XRF_126	64.39	0.50	8.80	6.69	0.45	1.32	0.34	1.87	1.26	0.85	13.52	0.19
SG_YS_XRF_127	63.19	0.57	9.94	6.75	0.41	1.44	0.35	1.69	1.34	0.65	13.68	0.19
SG_YS_XRF_128	61.37	0.58	10.11	7.02	0.42	1.44	0.34	1.67	1.32	0.72	15.01	0.19
SG_YS_XRF_129	60.79	0.59	10.18	7.34	0.46	1.54	0.37	1.75	1.36	0.69	14.95	0.19
SG_YS_XRF_130	61.40	0.56	9.72	7.12	0.47	1.42	0.36	1.74	1.33	0.59	15.29	0.19
SG_YS_XRF_131	61.16	0.56	10.04	6.73	0.37	1.45	0.35	1.69	1.32	0.60	15.74	0.19
SG_YS_XRF_132	62.55	0.57	10.13	6.61	0.37	1.47	0.36	1.65	1.30	0.56	14.43	0.19
SG_YS_XRF_133	62.67	0.56	10.21	6.55	0.43	1.46	0.35	1.62	1.29	0.59	14.28	0.19
SG_YS_XRF_134	62.83	0.54	9.73	6.76	0.40	1.40	0.35	1.65	1.26	0.78	14.29	0.19
SG_YS_XRF_135	63.20	0.55	9.83	6.49	0.35	1.43	0.34	1.69	1.25	0.58	14.29	0.19
SG_YS_XRF_136	62.60	0.56	9.83	6.87	0.44	1.42	0.35	1.66	1.29	0.67	14.31	0.19

(Continued)

Table S7 List of XRF data of SG12core samples (Total value including LOI is normalized to 100 wt%) and LSR

Sample Number	SiO <sub>2</sub>	TiO <sub>2</sub>	Al <sub>2</sub> O <sub>3</sub>	Fe <sub>2</sub> O <sub>3</sub>	MnO	MgO	CaO	Na <sub>2</sub> O	K <sub>2</sub> O	P <sub>2</sub> O <sub>5</sub>	LOI	LSR (cm/yr)
SG_YS_XRF_137	59.98	0.67	11.80	7.31	0.33	1.71	0.40	1.62	1.48	0.59	14.10	0.19
SG_YS_XRF_138	58.71	0.78	13.46	7.71	0.35	1.98	0.44	1.54	1.73	0.52	12.79	0.19
SG_YS_XRF_139	60.91	0.68	12.01	7.29	0.33	1.66	0.39	1.56	1.52	0.56	13.08	0.19
SG_YS_XRF_140	59.10	0.76	13.44	7.45	0.28	1.85	0.42	1.52	1.68	0.46	13.03	0.19
SG_YS_XRF_141	57.65	0.77	14.64	7.28	0.24	1.90	0.43	1.58	1.82	0.38	13.33	0.19
SG_YS_XRF_142	56.20	0.83	16.45	7.50	0.19	2.05	0.43	1.46	1.97	0.31	12.60	0.19
SG_YS_XRF_143	51.77	0.86	19.80	8.07	0.21	2.26	0.42	1.34	2.17	0.35	12.75	0.19
SG_YS_XRF_144	55.80	0.71	14.48	8.04	0.38	1.76	0.38	1.50	1.69	0.69	14.59	0.19
SG_YS_XRF_145	55.66	0.72	15.24	7.87	0.32	1.84	0.38	1.43	1.77	0.62	14.15	0.19
SG_YS_XRF_146	61.31	0.52	9.24	7.70	0.53	1.26	0.31	1.48	1.19	0.85	15.61	0.19
SG_YS_XRF_147	62.89	0.52	9.31	7.00	0.41	1.28	0.30	1.51	1.22	0.76	14.80	0.19
SG_YS_XRF_148	62.71	0.57	10.24	6.84	0.34	1.36	0.31	1.44	1.33	0.65	14.21	0.19
SG_YS_XRF_149	62.82	0.52	9.47	7.05	0.36	1.28	0.31	1.45	1.26	0.71	14.75	0.19
SG_YS_XRF_150	62.84	0.50	8.95	7.30	0.39	1.23	0.31	1.44	1.21	0.74	15.09	0.19
SG_YS_XRF_151	63.15	0.48	8.40	7.27	0.44	1.17	0.30	1.47	1.13	0.82	15.36	0.19
SG_YS_XRF_152	62.96	0.46	8.11	7.28	0.44	1.15	0.30	1.44	1.06	0.83	15.97	0.13
SG_YS_XRF_153	62.96	0.49	8.50	7.13	0.39	1.21	0.30	1.46	1.12	0.75	15.68	0.13
SG_YS_XRF_154	62.71	0.52	8.88	7.29	0.41	1.25	0.31	1.45	1.15	0.75	15.28	0.13
SG_YS_XRF_155	61.86	0.50	8.80	7.51	0.50	1.24	0.33	1.44	1.13	0.73	15.97	0.13
SG_YS_XRF_156	61.57	0.52	9.50	7.47	0.45	1.28	0.33	1.44	1.19	0.67	15.56	0.13
SG_YS_XRF_157	61.90	0.53	9.56	7.21	0.39	1.30	0.33	1.44	1.20	0.63	15.50	0.13
SG_YS_XRF_158	61.84	0.54	9.72	7.37	0.41	1.32	0.33	1.42	1.22	0.66	15.18	0.13
SG_YS_XRF_159	61.53	0.54	9.87	7.25	0.36	1.32	0.32	1.38	1.22	0.69	15.52	0.13
SG_YS_XRF_160	62.85	0.55	9.99	7.12	0.35	1.33	0.31	1.39	1.23	0.64	14.24	0.13
SG_YS_XRF_161	62.47	0.54	10.44	6.96	0.32	1.35	0.31	1.38	1.26	0.63	14.32	0.13
SG_YS_XRF_162	62.12	0.55	10.56	7.09	0.35	1.34	0.32	1.39	1.29	0.66	14.33	0.13
SG_YS_XRF_163	58.47	0.63	13.06	6.86	0.26	1.51	0.33	1.33	1.49	0.49	15.56	0.13
SG_YS_XRF_164	58.26	0.67	14.74	6.98	0.23	1.56	0.34	1.30	1.61	0.47	13.85	0.13
SG_YS_XRF_167	57.14	0.67	14.38	7.13	0.27	1.56	0.33	1.29	1.56	0.46	15.20	0.13
SG_YS_XRF_165	60.69	0.59	11.04	7.71	0.40	1.36	0.31	1.19	1.30	0.66	14.75	0.13
SG_YS_XRF_166	57.79	0.55	9.66	7.18	0.38	1.28	0.30	1.34	1.22	0.69	19.61	0.13
SG_YS_XRF_168	62.73	0.58	10.04	8.31	0.61	1.32	0.32	1.19	1.23	0.79	12.89	0.13
SG_YS_XRF_169	61.83	0.61	10.65	6.65	0.29	1.36	0.30	1.15	1.29	0.52	15.36	0.13
SG_YS_XRF_170	62.16	0.69	12.04	6.99	0.31	1.48	0.31	1.15	1.42	0.49	12.98	0.13
SG_YS_XRF_171	58.90	0.85	14.76	7.08	0.24	1.73	0.33	1.12	1.70	0.31	12.97	0.13
SG_YS_XRF_172	54.74	1.09	19.11	7.45	0.20	2.16	0.36	0.98	2.05	0.21	11.64	0.13
SG_YS_XRF_173	54.96	1.39	19.25	7.87	0.18	2.30	0.50	1.03	1.96	0.23	10.32	0.13
SG_YS_XRF_174	52.70	1.32	18.99	8.32	0.17	2.66	1.14	1.06	1.73	0.22	11.68	0.13
SG_YS_XRF_175	54.53	1.22	17.96	7.71	0.19	2.29	0.85	1.06	1.79	0.21	12.19	0.13
SG_YS_XRF_176	55.42	1.15	17.39	7.38	0.17	2.15	0.80	1.12	1.77	0.21	12.45	0.13
SG_YS_XRF_177	56.39	0.66	12.50	7.87	0.41	1.82	0.41	1.23	1.30	0.61	16.82	0.13
SG_YS_XRF_178	55.55	1.04	15.67	7.35	0.17	2.07	0.90	1.18	1.68	0.18	14.22	0.13
SG_YS_XRF_179	57.50	0.83	13.01	7.51	0.28	1.77	0.68	1.22	1.42	0.49	15.30	0.13
SG_YS_XRF_180	61.31	0.52	9.20	7.37	0.38	1.34	0.35	1.24	1.11	0.77	16.43	0.13
SG_YS_XRF_181	58.37	0.60	11.03	7.86	0.38	1.57	0.39	1.25	1.25	0.74	16.57	0.13
SG_YS_XRF_182	52.66	1.04	15.69	6.81	0.15	1.96	0.77	1.08	1.61	0.18	18.05	0.13
SG_YS_XRF_183	57.46	0.50	8.58	8.50	0.55	1.25	0.37	1.30	1.10	0.86	19.51	0.13
SG_YS_XRF_184	57.35	0.46	8.10	8.82	0.72	1.19	0.34	1.33	1.05	0.89	19.75	0.13
SG_YS_XRF_185	55.54	0.48	8.28	9.36	0.66	1.21	0.35	1.27	1.07	1.04	20.73	0.13
SG_YS_XRF_186	57.84	0.51	8.77	8.57	0.50	1.30	0.36	1.27	1.13	0.96	18.77	0.13
SG_YS_XRF_187	58.59	0.50	8.71	8.44	0.47	1.28	0.36	1.27	1.11	0.91	18.35	0.13
SG_YS_XRF_188	56.96	0.54	9.38	8.87	0.48	1.38	0.37	1.30	1.19	0.88	18.64	0.13
SG_YS_XRF_189	55.74	0.58	10.13	9.16	0.48	1.46	0.39	1.31	1.27	0.88	18.59	0.10
SG_YS_XRF_190	54.35	0.60	10.53	9.53	0.55	1.55	0.41	1.35	1.32	0.86	18.98	0.10
SG_YS_XRF_191	53.51	0.65	11.67	9.73	0.53	1.67	0.42	1.33	1.40	0.88	18.20	0.10
SG_YS_XRF_192	52.30	0.72	13.25	9.55	0.51	1.87	0.45	1.31	1.51	0.76	17.77	0.10
SG_YS_XRF_193	49.52	0.65	11.25	11.17	0.57	1.56	0.43	1.40	1.43	1.04	20.98	0.10
SG_YS_XRF_194	49.48	0.62	10.83	11.76	0.69	1.54	0.42	1.38	1.36	1.00	20.91	0.10
SG_YS_XRF_195	49.44	0.53	9.21	12.56	1.62	1.30	0.41	1.37	1.20	1.09	21.26	0.10
SG_YS_XRF_196	48.94	0.61	10.96	11.93	1.50	1.53	0.45	1.39	1.30	1.11	20.27	0.10
SG_YS_XRF_197	48.31	0.62	10.89	12.08	2.16	1.57	0.47	1.34	1.33	0.99	20.24	0.10
SG_YS_XRF_198	46.17	0.35	6.08	17.02	4.06	0.91	0.46	1.13	0.79	1.22	21.80	0.10
SG_YS_XRF_199	55.40	0.38	6.55	12.23	2.33	1.00	0.38	1.20	0.89	1.01	18.63	0.12
SG_YS_XRF_200	56.25	0.46	8.13	11.31	1.46	1.15	0.38	1.31	1.07	0.86	17.62	0.12
SG_YS_XRF_201	57.44	0.61	10.38	9.92	0.66	1.56	0.41	1.20	1.27	0.80	15.76	0.12
SG_YS_XRF_202	56.72	0.66	11.29	9.84	0.54	1.69	0.43	1.24	1.38	0.77	15.45	0.12
SG_YS_XRF_203	57.73	0.63	11.08	9.51	0.50	1.66	0.41	1.24	1.34	0.78	15.12	0.12
SG_YS_XRF_204	57.91	0.65	11.21	9.64	0.46	1.70	0.41	1.23	1.37	0.79	14.62	0.12

(Continued)

Table S7 List of XRF data of SG12core samples (Total value including LOI is normalized to 100 wt%) and LSR

Sample Number	SiO <sub>2</sub>	TiO <sub>2</sub>	Al <sub>2</sub> O <sub>3</sub>	Fe <sub>2</sub> O <sub>3</sub>	MnO	MgO	CaO	Na <sub>2</sub> O	K <sub>2</sub> O	P <sub>2</sub> O <sub>5</sub>	LOI	LSR (cm/yr)
SG_YS_XRF_205	57.09	0.73	12.71	9.56	0.41	1.88	0.43	1.23	1.51	0.68	13.77	0.12
SG_YS_XRF_206	57.63	0.76	13.37	9.06	0.35	1.94	0.43	1.21	1.58	0.58	13.11	0.12
SG_YS_XRF_207	58.20	0.78	13.86	8.61	0.30	1.91	0.41	1.18	1.58	0.51	12.65	0.12
SG_YS_XRF_208	55.27	0.93	17.61	8.30	0.20	2.22	0.41	1.06	1.88	0.30	11.81	0.12
SG_YS_XRF_209	51.01	0.99	21.15	8.65	0.17	2.29	0.38	0.96	2.03	0.31	12.08	0.12
SG_YS_XRF_210	49.50	1.10	22.34	8.96	0.16	2.61	0.43	0.97	2.27	0.37	11.29	0.12
SG_YS_XRF_211	59.83	0.62	10.23	8.74	0.38	1.51	0.38	1.19	1.27	0.72	15.13	0.12
SG_YS_XRF_212	59.38	0.69	11.35	8.68	0.38	1.66	0.40	1.18	1.37	0.70	14.21	0.12
SG_YS_XRF_213	60.48	0.61	10.24	8.53	0.43	1.46	0.37	1.19	1.28	0.74	14.67	0.12
SG_YS_XRF_214	61.49	0.64	10.75	8.27	0.37	1.55	0.37	1.17	1.31	0.67	13.41	0.12
SG_YS_XRF_215	63.08	0.66	11.11	7.60	0.30	1.56	0.35	1.09	1.31	0.65	12.29	0.12
SG_YS_XRF_216	60.85	0.71	12.22	8.03	0.33	1.63	0.36	1.09	1.40	0.61	12.78	0.12
SG_YS_XRF_217	60.82	0.64	10.51	8.64	0.45	1.44	0.33	1.12	1.26	0.73	14.06	0.12
SG_YS_XRF_218	57.84	0.61	9.89	9.35	0.79	1.30	0.34	1.20	1.20	0.79	16.71	0.12
SG_YS_XRF_219	60.00	0.53	8.77	8.73	0.72	1.14	0.32	1.18	1.09	0.78	16.76	0.12
SG_YS_XRF_220	62.03	0.46	8.04	8.19	0.56	1.06	0.29	1.16	1.01	0.84	16.36	0.12
SG_YS_XRF_221	62.77	0.51	8.72	7.85	0.44	1.15	0.31	1.14	1.08	0.66	15.37	0.12
SG_YS_XRF_222	62.40	0.49	8.27	8.18	0.47	1.13	0.32	1.15	1.04	0.71	15.85	0.12
SG_YS_XRF_223	63.89	0.51	8.64	7.93	0.40	1.17	0.31	1.09	1.07	0.71	14.28	0.12
SG_YS_XRF_224	64.28	0.56	9.00	7.71	0.52	1.26	0.34	1.06	1.07	0.62	13.57	0.12
SG_YS_XRF_229	60.68	0.79	12.20	7.49	0.33	1.77	0.44	0.99	1.35	0.52	13.46	0.12
SG_YS_XRF_225	61.41	0.80	12.67	7.44	0.30	1.80	0.44	1.06	1.41	0.48	12.20	0.12
SG_YS_XRF_230	58.59	0.88	13.39	7.89	0.28	2.00	0.52	1.03	1.45	0.48	13.48	0.12
SG_YS_XRF_226	58.10	0.97	15.16	7.98	0.26	2.24	0.54	1.05	1.61	0.38	11.70	0.12
SG_YS_XRF_231	62.20	0.38	6.28	9.04	0.58	0.93	0.27	0.95	0.79	1.02	17.56	0.12
SG_YS_XRF_227	62.69	0.41	6.88	9.40	0.57	1.00	0.28	1.05	0.85	1.05	15.82	0.12
SG_YS_XRF_232	60.24	0.45	7.37	9.27	0.56	1.09	0.30	1.03	0.90	0.97	17.82	0.13
SG_YS_XRF_228	62.12	0.42	7.15	9.46	0.60	1.03	0.29	1.07	0.87	1.08	15.92	0.13
SG_YS_XRF_233	60.14	0.40	6.63	9.46	0.59	0.97	0.30	1.00	0.84	1.09	18.57	0.13
SG_YS_XRF_234	58.31	0.44	7.35	10.20	0.75	1.04	0.32	1.01	0.90	1.08	18.61	0.13
SG_YS_XRF_235	61.24	0.44	7.38	8.41	0.41	1.04	0.29	0.97	0.92	0.87	18.03	0.13
SG_YS_XRF_236	61.78	0.41	6.82	8.26	0.40	0.98	0.29	0.97	0.90	0.86	18.34	0.13
SG_YS_XRF_237	62.27	0.40	6.39	8.20	0.37	0.96	0.28	0.97	0.82	0.91	18.45	0.13
SG_YS_XRF_238	61.48	0.42	6.89	8.15	0.39	1.01	0.30	0.95	0.90	0.77	18.74	0.13
SG_YS_XRF_239	62.98	0.40	6.56	8.18	0.38	0.96	0.29	0.96	0.87	0.90	17.53	0.13
SG_YS_XRF_240	63.67	0.45	7.66	7.59	0.34	1.05	0.29	0.93	0.95	0.77	16.31	0.13
SG_YS_XRF_241	62.11	0.44	7.21	8.36	0.38	1.00	0.31	0.95	0.93	0.81	17.50	0.13
SG_YS_XRF_242	61.79	0.43	7.11	8.05	0.33	1.02	0.31	0.96	0.93	0.81	18.26	0.13
SG_YS_XRF_243	61.79	0.43	7.04	8.30	0.35	1.00	0.30	0.95	0.91	0.80	18.15	0.13
SG_YS_XRF_244	61.93	0.42	6.98	8.12	0.35	0.98	0.30	0.96	0.91	0.86	18.20	0.12
SG_YS_XRF_245	60.07	0.43	7.08	8.46	0.37	1.00	0.32	0.94	0.92	0.89	19.51	0.12
SG_YS_XRF_246	60.13	0.41	6.75	8.86	0.47	0.98	0.32	0.97	0.90	0.96	19.23	0.12
SG_YS_XRF_247	62.11	0.37	6.01	8.21	0.50	0.90	0.30	0.94	0.79	0.95	18.92	0.12
SG_YS_XRF_248	64.00	0.38	6.27	7.64	0.38	0.92	0.29	0.91	0.82	0.86	17.52	0.12
SG_YS_XRF_249	65.10	0.38	6.38	7.27	0.35	0.93	0.29	0.86	0.82	0.69	16.92	0.12
SG_YS_XRF_250	64.81	0.40	6.48	7.30	0.34	0.95	0.31	0.88	0.83	0.75	16.94	0.12
SG_YS_XRF_251	64.01	0.40	6.87	7.52	0.33	0.98	0.34	0.88	0.86	0.73	17.08	0.12
SG_YS_XRF_252	64.37	0.40	6.69	7.51	0.33	0.99	0.42	0.90	0.85	0.80	16.74	0.12
SG_YS_XRF_253	62.81	0.46	7.63	7.92	0.33	1.14	0.33	0.87	0.96	0.83	16.70	0.12
SG_YS_XRF_254	62.42	0.37	6.22	8.46	0.42	0.91	0.29	0.89	0.81	1.04	18.17	0.12
SG_YS_XRF_255	62.20	0.35	5.73	8.97	0.52	0.87	0.28	0.87	0.77	1.03	18.41	0.12
SG_YS_XRF_256	62.90	0.35	5.78	8.68	0.52	0.87	0.28	0.87	0.76	0.93	18.05	0.12
SG_YS_XRF_257	57.15	0.43	6.88	11.12	0.83	1.04	0.32	0.94	0.92	1.11	19.25	0.12
SG_YS_XRF_258	58.56	0.47	7.59	9.92	0.71	1.12	0.33	0.91	0.99	1.07	18.33	0.12
SG_YS_XRF_259	60.06	0.39	6.17	9.50	0.55	0.98	0.31	0.90	0.80	1.16	19.18	0.12
SG_YS_XRF_260	59.16	0.53	8.16	8.91	0.45	1.30	0.35	0.91	1.00	0.91	18.32	0.12
SG_YS_XRF_261	58.99	0.41	6.45	9.54	0.53	0.99	0.31	0.90	0.82	1.06	19.99	0.12
SG_YS_XRF_262	59.03	0.36	5.84	9.84	0.59	0.88	0.29	0.88	0.79	1.21	20.30	0.12
SG_YS_XRF_263	58.30	0.36	5.89	9.97	0.63	0.89	0.29	0.90	0.78	1.16	20.83	0.12
SG_YS_XRF_264	58.77	0.38	6.17	10.44	0.82	0.91	0.30	0.87	0.81	1.21	19.33	0.12
SG_YS_XRF_265	62.34	0.35	5.80	8.91	0.65	0.86	0.28	0.84	0.77	1.06	18.15	0.12
SG_YS_XRF_266	61.97	0.34	5.53	8.65	0.60	0.87	0.29	0.84	0.74	0.90	19.27	0.12
SG_YS_XRF_267	59.51	0.36	5.74	9.44	0.82	0.90	0.31	0.86	0.73	1.08	20.25	0.12
SG_YS_XRF_268	58.77	0.36	5.75	9.68	1.37	0.90	0.32	0.86	0.75	1.19	20.07	0.12
SG_YS_XRF_269	59.75	0.38	6.15	9.40	0.67	0.97	0.31	0.88	0.79	1.26	19.45	0.12
SG_YS_XRF_270	61.16	0.39	6.31	8.62	0.58	0.99	0.31	0.86	0.80	1.04	18.93	0.12
SG_YS_XRF_271	60.66	0.46	7.39	8.33	0.53	1.17	0.36	0.88	0.92	0.92	18.39	0.12
SG_YS_XRF_272	60.05	0.57	9.02	7.90	0.42	1.40	0.41	0.89	1.10	0.70	17.53	0.12

(Continued)

Table S7 List of XRF data of SG12core samples (Total value including LOI is normalized to 100 wt%) and LSR

Sample Number	SiO <sub>2</sub>	TiO <sub>2</sub>	Al <sub>2</sub> O <sub>3</sub>	Fe <sub>2</sub> O <sub>3</sub>	MnO	MgO	CaO	Na <sub>2</sub> O	K <sub>2</sub> O	P <sub>2</sub> O <sub>5</sub>	LOI	LSR (cm/yr)
SG_YS_XRF_273	60.27	0.49	7.86	8.22	0.46	1.25	0.39	0.90	0.99	0.75	18.41	0.14
SG_YS_XRF_274	61.45	0.48	7.56	8.15	0.46	1.22	0.38	0.87	0.93	0.81	17.69	0.14
SG_YS_XRF_275	60.63	0.45	7.08	8.82	0.67	1.13	0.36	0.85	0.89	0.90	18.22	0.14
SG_YS_XRF_276	59.76	0.45	7.20	9.10	0.68	1.15	0.36	0.86	0.91	1.04	18.51	0.14
SG_YS_XRF_277	60.20	0.50	7.95	8.51	0.50	1.24	0.39	0.87	1.00	0.95	17.91	0.14
SG_YS_XRF_282	59.60	0.55	8.84	8.69	0.52	1.36	0.40	0.89	1.09	0.86	17.19	0.14
SG_YS_XRF_278	59.20	0.54	8.88	8.70	0.54	1.38	0.41	0.88	1.08	0.84	17.56	0.14
SG_YS_XRF_283	58.93	0.51	8.27	9.29	0.67	1.30	0.40	0.79	0.99	0.93	17.92	0.14
SG_YS_XRF_279	58.63	0.49	8.16	9.41	0.64	1.29	0.40	0.86	0.98	1.07	18.07	0.14
SG_YS_XRF_284	59.63	0.48	7.93	9.19	0.60	1.30	0.39	0.78	0.97	1.05	17.69	0.14
SG_YS_XRF_280	58.86	0.48	8.10	9.20	0.61	1.32	0.41	0.88	0.98	1.04	18.12	0.14
SG_YS_XRF_281	58.65	0.52	8.84	9.02	0.50	1.42	0.42	0.90	1.06	0.98	17.67	0.14
SG_YS_XRF_285	58.30	0.52	8.72	9.40	0.54	1.42	0.41	0.83	1.05	1.02	17.79	0.14
SG_YS_XRF_286	58.77	0.62	10.85	8.79	0.39	1.70	0.45	0.85	1.23	0.70	15.66	0.14
SG_YS_XRF_287	60.36	0.59	10.26	8.40	0.37	1.67	0.44	0.83	1.18	0.71	15.20	0.14
SG_YS_XRF_288	57.59	0.68	12.71	8.64	0.33	1.99	0.48	0.85	1.35	0.67	14.71	0.14
SG_YS_XRF_289	51.70	0.90	18.61	8.92	0.22	2.70	0.54	0.84	1.83	0.37	13.36	0.14
SG_YS_XRF_290	46.14	1.10	22.75	9.81	0.17	3.24	0.60	0.80	2.16	0.38	12.85	0.14
SG_YS_XRF_291	50.82	1.02	18.49	9.23	0.23	3.27	0.72	0.90	1.98	0.44	12.91	0.14
SG_YS_XRF_292	54.46	0.67	13.05	8.01	0.34	1.66	0.38	0.82	1.39	0.73	18.50	0.14
SG_YS_XRF_293	58.41	0.42	7.22	8.73	0.40	1.03	0.32	0.81	0.88	1.04	20.75	0.14
SG_YS_XRF_294	60.77	0.39	6.82	7.76	0.39	0.99	0.29	0.79	0.85	1.02	19.93	0.13
SG_YS_XRF_295	60.34	0.41	7.22	7.66	0.36	1.03	0.34	0.81	0.87	1.00	19.97	0.13
SG_YS_XRF_296	58.46	0.45	7.82	8.02	0.31	1.14	0.32	0.80	0.95	1.14	20.58	0.13
SG_YS_XRF_297	59.72	0.39	6.51	8.17	0.36	1.01	0.29	0.81	0.80	1.10	20.85	0.13
SG_YS_XRF_298	59.41	0.35	6.06	9.21	0.42	0.92	0.28	0.81	0.76	1.20	20.58	0.13
SG_YS_XRF_299	61.31	0.34	5.85	8.63	0.35	0.89	0.26	0.77	0.72	1.29	19.59	0.13
SG_YS_XRF_300	58.27	0.37	6.52	9.18	0.43	0.99	0.30	0.83	0.80	1.27	21.04	0.13
SG_YS_XRF_301	58.30	0.37	6.38	9.44	0.58	0.98	0.29	0.77	0.79	1.45	20.66	0.13
SG_YS_XRF_302	55.28	0.39	6.74	10.85	0.53	1.04	0.31	0.83	0.84	1.43	21.76	0.13
SG_YS_XRF_303	53.44	0.46	7.59	11.13	0.65	1.13	0.34	0.81	0.88	1.46	22.12	0.13
SG_YS_XRF_304	57.40	0.36	6.37	10.02	0.49	0.98	0.27	0.79	0.78	1.41	21.11	0.13
SG_YS_XRF_305	54.99	0.37	6.43	10.99	0.82	1.01	0.30	0.84	0.81	1.51	21.93	0.13
SG_YS_XRF_306	57.09	0.42	7.37	10.17	0.51	1.14	0.31	0.79	0.90	1.19	20.11	0.13
SG_YS_XRF_307	58.29	0.43	7.36	9.48	0.56	1.15	0.31	0.77	0.89	1.07	19.68	0.13
SG_YS_XRF_308	57.89	0.38	6.74	9.69	0.70	1.06	0.30	0.74	0.80	1.29	20.42	0.13
SG_YS_XRF_309	59.98	0.37	6.75	8.93	0.68	1.05	0.28	0.77	0.79	0.98	19.41	0.15
SG_YS_XRF_310	55.10	0.46	8.36	9.84	0.69	1.29	0.33	0.82	0.95	1.02	21.13	0.15
SG_YS_XRF_311	56.90	0.54	10.15	9.24	0.49	1.36	0.35	0.85	1.15	0.83	18.14	0.15
SG_YS_XRF_312	54.83	0.64	12.38	8.99	0.66	1.60	0.39	0.85	1.35	0.67	17.64	0.15
SG_YS_XRF_313	49.23	0.88	18.26	9.07	0.27	2.23	0.43	0.78	1.85	0.47	16.53	0.15
SG_YS_XRF_314	57.41	0.29	5.09	8.94	0.60	0.71	0.26	0.70	0.63	1.25	24.11	0.15
SG_YS_XRF_315	59.45	0.31	5.46	9.25	0.55	0.76	0.26	0.71	0.67	1.07	21.51	0.15
SG_YS_XRF_316	57.94	0.33	5.66	9.88	0.89	0.80	0.27	0.72	0.69	1.05	21.77	0.15
SG_YS_XRF_317	63.30	0.28	4.78	8.44	0.52	0.67	0.23	0.72	0.59	1.13	19.33	0.15
SG_YS_XRF_318	60.15	0.29	4.96	9.11	0.67	0.70	0.26	0.71	0.62	1.27	21.28	0.15
SG_YS_XRF_319	60.87	0.24	4.08	9.34	0.68	0.60	0.23	0.73	0.52	1.41	21.30	0.15
SG_YS_XRF_320	57.47	0.26	4.62	10.35	1.46	0.65	0.26	0.66	0.58	1.79	21.91	0.15
SG_YS_XRF_321	59.85	0.32	5.31	9.97	0.65	0.73	0.27	0.71	0.68	1.35	20.16	0.15
SG_YS_XRF_322	58.94	0.34	5.77	9.89	0.56	0.77	0.26	0.71	0.74	1.43	20.59	0.15
SG_YS_XRF_323	58.67	0.33	5.86	9.34	0.56	0.78	0.27	0.69	0.75	1.29	21.46	0.15
SG_YS_XRF_324	59.74	0.38	6.71	9.22	0.54	0.87	0.28	0.72	0.84	1.11	19.60	0.15
SG_YS_XRF_325	58.14	0.40	6.88	9.82	0.49	0.89	0.28	0.71	0.84	1.17	20.39	0.13
SG_YS_XRF_330	59.82	0.39	6.95	8.38	0.48	0.89	0.27	0.67	0.86	0.93	20.36	0.13
SG_YS_XRF_326	61.46	0.39	7.26	8.04	0.43	0.88	0.29	0.80	1.04	0.92	18.49	0.13
SG_YS_XRF_331	59.61	0.42	7.54	8.49	0.48	0.93	0.27	0.67	0.92	0.96	19.72	0.13
SG_YS_XRF_327	60.13	0.40	7.06	8.49	0.54	0.89	0.28	0.70	0.88	0.94	19.70	0.13
SG_YS_XRF_332	58.94	0.40	7.00	8.69	0.47	0.89	0.27	0.66	0.85	0.95	20.88	0.13
SG_YS_XRF_328	59.13	0.41	7.27	8.54	0.43	0.91	0.28	0.70	0.90	0.94	20.49	0.13
SG_YS_XRF_333	58.78	0.36	5.90	9.50	0.56	0.82	0.27	0.62	0.73	1.17	21.29	0.13
SG_YS_XRF_329	57.33	0.35	5.63	9.29	0.61	0.77	0.27	0.65	0.71	1.19	23.21	0.13
SG_YS_XRF_334	59.38	0.32	5.19	9.02	0.61	0.73	0.26	0.63	0.65	1.20	22.03	0.13
SG_YS_XRF_335	58.58	0.33	5.49	7.42	0.57	0.74	0.25	0.63	0.70	0.95	24.32	0.13
SG_YS_XRF_336	61.55	0.33	5.50	7.41	0.43	0.75	0.25	0.65	0.69	1.04	21.39	0.13
SG_YS_XRF_337	60.71	0.33	5.38	6.92	0.45	0.73	0.25	0.68	0.68	0.96	22.91	0.14
SG_YS_XRF_338	63.04	0.34	5.59	6.77	0.47	0.75	0.25	0.65	0.68	0.98	20.48	0.14
SG_YS_XRF_339	63.16	0.34	5.81	6.63	0.42	0.78	0.25	0.66	0.72	0.99	20.25	0.14
SG_YS_XRF_340	65.29	0.27	4.46	6.82	0.53	0.62	0.23	0.61	0.55	1.09	19.53	0.14

(Continued)

Table S7 List of XRF data of SG12core samples (Total value including LOI is normalized to 100 wt%) and LSR

Sample Number	SiO <sub>2</sub>	TiO <sub>2</sub>	Al <sub>2</sub> O <sub>3</sub>	Fe <sub>2</sub> O <sub>3</sub>	MnO	MgO	CaO	Na <sub>2</sub> O	K <sub>2</sub> O	P <sub>2</sub> O <sub>5</sub>	LOI	LSR (cm/yr)
SG_YS_XRF_341	64.32	0.26	4.49	6.80	0.48	0.62	0.22	0.62	0.58	1.10	20.50	0.14
SG_YS_XRF_342	63.56	0.29	4.95	7.34	0.50	0.68	0.25	0.64	0.62	1.14	20.03	0.14
SG_YS_XRF_343	60.60	0.34	5.74	7.67	0.59	0.78	0.26	0.66	0.70	0.95	21.71	0.14
SG_YS_XRF_344	69.72	0.27	4.72	6.48	0.46	0.63	0.21	0.53	0.57	0.82	15.60	0.14
SG_YS_XRF_345	66.36	0.37	7.15	7.00	0.51	0.85	0.24	0.54	0.79	0.74	15.45	0.14
SG_YS_XRF_346	68.88	0.27	4.38	6.99	0.56	0.61	0.20	0.50	0.55	0.90	16.18	0.14
SG_YS_XRF_347	69.90	0.30	4.91	6.19	0.43	0.67	0.21	0.50	0.59	0.83	15.47	0.14
SG_YS_XRF_348	71.42	0.27	4.36	5.75	0.33	0.61	0.19	0.50	0.55	0.84	15.17	0.14
SG_YS_XRF_349	72.46	0.23	3.75	5.50	0.39	0.55	0.18	0.49	0.47	0.71	15.27	0.14
SG_YS_XRF_350	68.83	0.22	3.81	6.29	0.67	0.53	0.19	0.51	0.46	0.91	17.56	0.14
SG_YS_XRF_351	67.65	0.25	4.13	6.95	0.58	0.60	0.21	0.51	0.52	1.09	17.52	0.14
SG_YS_XRF_352	69.80	0.25	4.15	6.62	0.51	0.59	0.20	0.48	0.52	0.98	15.90	0.14
SG_YS_XRF_353	70.56	0.24	4.12	6.41	0.54	0.59	0.19	0.48	0.51	0.92	15.45	0.14
SG_YS_XRF_354	71.94	0.23	4.00	6.11	0.46	0.57	0.19	0.47	0.50	0.85	14.68	0.15
SG_YS_XRF_355	72.81	0.23	3.87	5.61	0.42	0.56	0.18	0.45	0.48	0.75	14.63	0.15
SG_YS_XRF_356	70.39	0.27	4.63	5.93	0.42	0.66	0.21	0.50	0.56	0.92	15.50	0.15
SG_YS_XRF_357	71.13	0.28	4.73	5.68	0.41	0.67	0.21	0.49	0.59	0.74	15.08	0.15
SG_YS_XRF_358	70.98	0.27	4.65	5.86	0.40	0.66	0.21	0.49	0.57	0.74	15.16	0.15
SG_YS_XRF_359	70.62	0.28	4.86	5.79	0.45	0.68	0.21	0.48	0.59	0.71	15.32	0.15
SG_YS_XRF_360	70.59	0.31	5.29	5.61	0.42	0.73	0.22	0.49	0.63	0.70	15.02	0.15
SG_YS_XRF_361	69.35	0.32	5.53	5.99	0.46	0.75	0.24	0.52	0.67	0.69	15.49	0.13
SG_YS_XRF_362	66.80	0.38	6.55	6.13	0.43	0.89	0.27	0.57	0.80	0.76	16.42	0.13
SG_YS_XRF_363	68.21	0.32	5.67	6.01	0.39	0.79	0.28	0.57	0.71	0.80	16.24	0.13
SG_YS_XRF_364	68.88	0.34	5.90	5.95	0.40	0.83	0.27	0.55	0.73	0.80	15.34	0.13
SG_YS_XRF_365	69.30	0.37	6.35	5.63	0.37	0.89	0.25	0.54	0.78	0.71	14.81	0.13
SG_YS_XRF_366	68.74	0.37	6.45	5.66	0.40	0.89	0.25	0.54	0.78	0.62	15.29	0.13
SG_YS_XRF_367	66.84	0.40	7.37	6.18	0.40	0.98	0.28	0.56	0.87	0.67	15.46	0.13
SG_YS_XRF_368	63.24	0.47	8.87	6.65	0.46	1.15	0.30	0.58	0.99	0.69	16.60	0.13
SG_YS_XRF_369	59.97	0.56	11.32	6.74	0.41	1.28	0.32	0.61	1.16	0.57	17.08	0.13
SG_YS_XRF_370	62.17	0.57	11.52	6.28	0.30	1.37	0.32	0.59	1.17	0.54	15.17	0.13
SG_YS_XRF_372	63.55	0.48	9.46	6.26	0.40	1.11	0.28	0.52	0.98	0.72	16.25	0.13
SG_YS_XRF_371	69.61	0.30	5.13	5.40	0.44	0.69	0.22	0.49	0.63	0.70	16.39	0.13
SG_YS_XRF_373	70.20	0.32	5.38	5.38	0.42	0.74	0.23	0.46	0.68	0.68	15.51	0.13
SG_YS_XRF_374	71.10	0.32	5.74	5.39	0.36	0.76	0.22	0.45	0.71	0.65	14.29	0.13
SG_YS_XRF_375	71.78	0.27	4.74	5.60	0.46	0.65	0.20	0.41	0.58	0.66	14.64	0.13
SG_YS_XRF_376	72.11	0.28	5.01	5.14	0.32	0.68	0.20	0.43	0.64	0.65	14.54	0.12
SG_YS_XRF_377	71.62	0.31	5.37	5.32	0.31	0.73	0.21	0.44	0.67	0.67	14.35	0.12
SG_YS_XRF_378	69.56	0.36	6.11	5.69	0.41	0.85	0.24	0.48	0.76	0.61	14.93	0.12
SG_YS_XRF_379	71.77	0.31	5.42	5.09	0.32	0.71	0.22	0.43	0.68	0.63	14.43	0.11
SG_YS_XRF_380	68.46	0.39	6.94	5.80	0.38	0.90	0.25	0.49	0.82	0.71	14.86	0.11
SG_YS_XRF_381	69.02	0.36	6.36	5.56	0.38	0.82	0.24	0.48	0.80	0.67	15.30	0.11
SG_YS_XRF_382	69.63	0.34	6.06	5.49	0.32	0.77	0.23	0.46	0.78	0.65	15.28	0.12
SG_YS_XRF_383	70.17	0.29	5.17	5.86	0.41	0.66	0.21	0.43	0.68	0.72	15.41	0.12
SG_YS_XRF_384	69.02	0.32	5.78	6.02	0.44	0.72	0.22	0.44	0.74	0.70	15.60	0.12
SG_YS_XRF_385	66.98	0.31	5.65	7.03	0.69	0.71	0.24	0.46	0.72	0.90	16.32	0.08
SG_YS_XRF_386	69.38	0.31	5.66	5.82	0.42	0.73	0.23	0.43	0.74	0.69	15.61	0.08
SG_YS_XRF_387	68.57	0.38	7.22	5.84	0.37	0.89	0.24	0.46	0.93	0.68	14.43	0.08
SG_YS_XRF_388	70.93	0.30	5.26	5.49	0.38	0.69	0.22	0.43	0.68	0.64	14.99	0.08
SG_YS_XRF_389	71.84	0.30	5.34	5.16	0.35	0.70	0.21	0.43	0.68	0.59	14.42	0.15
SG_YS_XRF_390	71.84	0.31	5.30	5.18	0.36	0.70	0.22	0.42	0.68	0.59	14.40	0.15
SG_YS_XRF_391	70.91	0.33	5.68	5.33	0.37	0.75	0.23	0.42	0.74	0.60	14.64	0.15
SG_YS_XRF_392	70.10	0.32	5.70	5.20	0.36	0.74	0.21	0.41	0.74	0.59	15.62	0.15
SG_YS_XRF_393	71.56	0.33	5.63	5.27	0.34	0.75	0.22	0.42	0.73	0.56	14.20	0.15
SG_YS_XRF_394	70.50	0.34	6.12	5.68	0.42	0.82	0.23	0.44	0.77	0.64	14.05	0.15
SG_YS_XRF_395	70.97	0.37	6.61	5.34	0.32	0.87	0.23	0.44	0.84	0.58	13.43	0.15
SG_YS_XRF_396	69.63	0.42	7.66	5.62	0.32	0.99	0.25	0.47	0.95	0.56	13.13	0.15
SG_YS_XRF_397	65.91	0.51	10.15	6.09	0.30	1.24	0.28	0.50	1.20	0.51	13.32	0.11
SG_YS_XRF_398	62.31	0.60	13.02	6.27	0.26	1.46	0.28	0.47	1.48	0.42	13.42	0.11
SG_YS_XRF_399	69.06	0.39	7.09	5.61	0.34	0.87	0.23	0.44	0.86	0.60	14.51	0.11
SG_YS_XRF_400	70.54	0.33	5.80	5.35	0.36	0.74	0.22	0.42	0.74	0.63	14.88	0.11
SG_YS_XRF_401	70.50	0.31	5.57	5.55	0.41	0.69	0.21	0.41	0.72	0.66	14.97	0.11
SG_YS_XRF_402	70.86	0.29	5.29	5.22	0.38	0.67	0.20	0.42	0.70	0.63	15.33	0.11
SG_YS_XRF_403	70.27	0.31	5.60	5.42	0.40	0.71	0.22	0.40	0.71	0.65	15.30	0.11
SG_YS_XRF_404	70.45	0.33	6.18	5.26	0.36	0.78	0.24	0.45	0.79	0.60	14.57	0.11
SG_YS_XRF_405	68.54	0.42	7.70	5.54	0.33	0.97	0.27	0.47	0.94	0.55	14.28	0.11
SG_YS_XRF_406	67.35	0.40	8.25	5.64	0.30	0.98	0.28	0.48	0.92	0.55	14.84	0.11
SG_YS_XRF_407	71.06	0.29	5.22	5.39	0.37	0.66	0.21	0.39	0.67	0.69	15.05	0.10
SG_YS_XRF_408	69.91	0.37	6.52	5.37	0.33	0.83	0.24	0.40	0.83	0.58	14.63	0.10

(Continued)

Table S7 List of XRF data of SG12core samples (Total value including LOI is normalized to 100 wt%) and LSR

Sample Number	SiO <sub>2</sub>	TiO <sub>2</sub>	Al <sub>2</sub> O <sub>3</sub>	Fe <sub>2</sub> O <sub>3</sub>	MnO	MgO	CaO	Na <sub>2</sub> O	K <sub>2</sub> O	P <sub>2</sub> O <sub>5</sub>	LOI	LSR (cm/yr)
SG_YS_XRF_409	70.71	0.33	5.67	5.36	0.35	0.73	0.23	0.39	0.73	0.64	14.86	0.10
SG_YS_XRF_410	69.06	0.34	5.91	5.73	0.41	0.76	0.24	0.41	0.76	0.68	15.70	0.11
SG_YS_XRF_411	69.58	0.34	5.87	5.56	0.40	0.76	0.23	0.39	0.77	0.67	15.43	0.11
SG_YS_XRF_412	71.44	0.33	5.84	5.31	0.35	0.74	0.22	0.37	0.74	0.60	14.06	0.11
SG_YS_XRF_413	70.35	0.34	5.90	5.74	0.42	0.73	0.22	0.37	0.74	0.67	14.53	0.11
SG_YS_XRF_414	70.54	0.36	6.22	5.34	0.35	0.80	0.23	0.40	0.81	0.59	14.36	0.11
SG_YS_XRF_415	71.77	0.31	5.51	5.25	0.37	0.70	0.21	0.38	0.72	0.60	14.18	0.11
SG_YS_XRF_416	71.54	0.32	5.52	5.33	0.35	0.70	0.21	0.36	0.73	0.63	14.32	0.11
SG_YS_XRF_417	71.10	0.34	6.12	5.42	0.35	0.76	0.23	0.40	0.80	0.62	13.85	0.11
SG_YS_XRF_418	70.71	0.32	5.68	5.88	0.43	0.73	0.22	0.36	0.72	0.68	14.27	0.12
SG_YS_XRF_419	71.85	0.34	6.09	5.65	0.36	0.75	0.24	0.41	0.80	0.62	12.89	0.12
SG_YS_XRF_420	70.27	0.35	6.67	5.79	0.34	0.82	0.26	0.45	0.88	0.62	13.55	0.12
SG_YS_XRF_421	65.67	0.51	10.83	6.00	0.28	1.16	0.41	0.68	1.28	0.54	12.64	0.12
SG_YS_XRF_422	70.12	0.33	6.59	5.64	0.36	0.68	0.36	0.64	0.93	0.58	13.77	0.12
SG_YS_XRF_423	68.59	0.38	6.84	6.11	0.41	0.78	0.22	0.39	0.90	0.68	14.71	0.12
SG_YS_XRF_424	69.08	0.38	7.17	5.78	0.34	0.79	0.21	0.40	0.94	0.54	14.36	0.12
SG_YS_XRF_425	65.98	0.46	8.94	6.31	0.35	0.97	0.26	0.46	1.14	0.56	14.56	0.12
SG_YS_XRF_426	63.22	0.53	11.08	6.51	0.31	1.14	0.29	0.47	1.29	0.52	14.65	0.12
SG_YS_XRF_427	65.25	0.51	10.09	6.27	0.30	1.12	0.28	0.44	1.15	0.55	14.05	0.12
SG_YS_XRF_429	63.97	0.58	11.38	6.34	0.27	1.34	0.31	0.45	1.26	0.49	13.60	0.12
SG_YS_XRF_428	62.71	0.61	11.92	6.40	0.27	1.40	0.31	0.47	1.30	0.47	14.14	0.12
SG_YS_XRF_430	70.70	0.31	5.71	5.46	0.34	0.66	0.20	0.34	0.74	0.65	14.89	0.12
SG_YS_XRF_431	69.80	0.29	5.38	6.03	0.43	0.63	0.20	0.33	0.70	0.74	15.47	0.10
SG_YS_XRF_432	70.24	0.30	5.92	5.70	0.34	0.66	0.21	0.36	0.77	0.70	14.79	0.10
SG_YS_XRF_433	70.36	0.28	5.10	6.12	0.44	0.61	0.23	0.35	0.66	0.77	15.10	0.10
SG_YS_XRF_434	69.66	0.32	5.94	6.05	0.37	0.70	0.29	0.45	0.77	0.69	14.76	0.10
SG_YS_XRF_435	69.13	0.31	5.60	6.19	0.44	0.66	0.21	0.35	0.73	0.77	15.62	0.12
SG_YS_XRF_436	68.86	0.32	5.89	6.01	0.39	0.69	0.21	0.35	0.77	0.71	15.81	0.12
SG_YS_XRF_437	68.57	0.35	6.74	6.01	0.36	0.75	0.22	0.38	0.87	0.68	15.08	0.12
SG_YS_XRF_438	67.14	0.41	8.08	6.34	0.37	0.85	0.25	0.44	1.00	0.69	14.44	0.12
SG_YS_XRF_439	64.66	0.43	10.49	5.78	0.28	0.90	0.25	0.45	1.11	0.55	15.10	0.12
SG_YS_XRF_440	66.41	0.40	7.01	6.16	0.35	0.87	0.25	0.38	0.88	0.76	16.53	0.12
SG_YS_XRF_441	67.23	0.38	6.44	6.08	0.37	0.82	0.25	0.38	0.83	0.81	16.41	0.12
SG_YS_XRF_442	66.69	0.41	6.99	6.07	0.36	0.89	0.25	0.39	0.89	0.73	16.33	0.12
SG_YS_XRF_443	67.72	0.37	6.29	6.01	0.38	0.80	0.24	0.37	0.81	0.83	16.18	0.12
SG_YS_XRF_444	66.37	0.40	6.97	6.24	0.40	0.88	0.26	0.42	0.92	0.78	16.36	0.12
SG_YS_XRF_445	66.79	0.43	7.51	6.22	0.35	0.95	0.26	0.41	0.96	0.73	15.39	0.12
SG_YS_XRF_446	66.14	0.46	8.26	6.17	0.33	1.02	0.27	0.43	1.06	0.66	15.22	0.12
SG_YS_XRF_447	67.14	0.42	7.46	6.49	0.35	0.96	0.26	0.42	0.96	0.75	14.79	0.12
SG_YS_XRF_448	68.24	0.41	7.37	6.16	0.31	0.96	0.25	0.39	0.93	0.72	14.25	0.12
SG_YS_XRF_449	65.16	0.55	10.21	6.24	0.27	1.27	0.30	0.45	1.20	0.55	13.79	0.12
SG_YS_XRF_450	66.80	0.46	8.58	6.06	0.33	1.02	0.26	0.42	1.05	0.67	14.35	0.12
SG_YS_XRF_451	68.48	0.40	7.39	5.64	0.32	0.86	0.24	0.42	0.96	0.63	14.68	0.12
SG_YS_XRF_452	67.31	0.39	7.25	6.28	0.41	0.81	0.23	0.40	0.94	0.76	15.23	0.12
SG_YS_XRF_453	68.21	0.42	7.97	5.72	0.32	0.84	0.23	0.42	1.02	0.69	14.15	0.12
SG_YS_XRF_454	68.77	0.40	7.92	5.49	0.31	0.79	0.22	0.41	0.99	0.65	14.05	0.12
SG_YS_XRF_455	68.09	0.36	7.12	6.26	0.39	0.77	0.22	0.38	0.88	0.79	14.74	0.12
SG_YS_XRF_456	68.45	0.33	6.64	6.46	0.40	0.72	0.21	0.36	0.80	0.70	14.93	0.12
SG_YS_XRF_457	68.64	0.35	6.56	6.22	0.41	0.80	0.23	0.36	0.82	0.76	14.85	0.12
SG_YS_XRF_458	68.86	0.34	5.91	6.34	0.40	0.76	0.23	0.34	0.75	0.84	15.24	0.12
SG_YS_XRF_459	68.24	0.38	6.67	6.30	0.36	0.90	0.25	0.37	0.85	0.85	14.82	0.12
SG_YS_XRF_460	69.88	0.36	6.15	5.73	0.28	0.83	0.24	0.37	0.80	0.73	14.63	0.12
SG_YS_XRF_461	69.46	0.35	6.33	5.92	0.34	0.84	0.24	0.35	0.81	0.87	14.47	0.12
SG_YS_XRF_462	69.22	0.36	6.30	6.08	0.35	0.85	0.24	0.36	0.79	0.86	14.59	0.12
SG_YS_XRF_463	69.84	0.35	6.22	5.93	0.32	0.84	0.24	0.36	0.79	0.77	14.35	0.12
SG_YS_XRF_464	70.40	0.34	5.97	5.84	0.30	0.79	0.23	0.34	0.77	0.75	14.27	0.12
SG_YS_XRF_465	70.59	0.34	5.93	5.92	0.31	0.80	0.23	0.32	0.74	0.80	14.01	0.12
SG_YS_XRF_466	69.53	0.35	5.98	6.26	0.42	0.81	0.24	0.34	0.76	0.77	14.55	0.12
SG_YS_XRF_467	67.47	0.43	7.42	6.25	0.28	1.03	0.29	0.39	0.92	0.65	14.87	0.12
SG_YS_XRF_468	65.72	0.48	8.50	6.57	0.30	1.18	0.32	0.42	1.04	0.67	14.81	0.12
SG_YS_XRF_469	63.13	0.62	11.25	6.68	0.23	1.50	0.36	0.43	1.24	0.56	13.99	0.12
SG_YS_XRF_470	67.85	0.42	7.42	6.10	0.26	0.98	0.27	0.37	0.90	0.76	14.67	0.12
SG_YS_XRF_471	64.93	0.55	10.59	5.93	0.20	1.34	0.33	0.43	1.17	0.47	14.07	0.12
SG_YS_XRF_472	68.45	0.35	5.99	6.06	0.36	0.78	0.26	0.34	0.74	0.78	15.89	0.13
SG_YS_XRF_473	68.96	0.38	6.56	5.58	0.27	0.87	0.28	0.37	0.82	0.68	15.24	0.13
SG_YS_XRF_474	69.96	0.37	6.42	5.46	0.26	0.86	0.27	0.35	0.80	0.76	14.49	0.13
SG_YS_XRF_475	69.86	0.36	6.20	5.52	0.27	0.86	0.26	0.36	0.78	0.75	14.78	0.13
SG_YS_XRF_476	69.67	0.34	5.77	5.47	0.27	0.78	0.26	0.36	0.74	0.78	15.57	0.13

(Continued)

Table S7 List of XRF data of SG12core samples (Total value including LOI is normalized to 100 wt%) and LSR

Sample Number	SiO <sub>2</sub>	TiO <sub>2</sub>	Al <sub>2</sub> O <sub>3</sub>	Fe <sub>2</sub> O <sub>3</sub>	MnO	MgO	CaO	Na <sub>2</sub> O	K <sub>2</sub> O	P <sub>2</sub> O <sub>5</sub>	LOI	LSR (cm/yr)
SG_YS_XRF_477	69.65	0.32	5.70	5.44	0.27	0.76	0.26	0.37	0.74	0.79	15.70	0.13
SG_YS_XRF_478	69.19	0.33	6.02	5.47	0.29	0.79	0.28	0.38	0.75	0.76	15.72	0.13
SG_YS_XRF_479	69.81	0.34	6.13	5.17	0.26	0.82	0.29	0.41	0.78	0.66	15.32	0.13
SG_YS_XRF_480	69.45	0.34	6.26	5.31	0.25	0.83	0.30	0.40	0.80	0.69	15.38	0.13
SG_YS_XRF_481	68.98	0.37	6.65	5.41	0.24	0.88	0.33	0.43	0.83	0.66	15.22	0.13
SG_YS_XRF_482	69.67	0.34	6.29	5.35	0.25	0.82	0.33	0.45	0.79	0.69	15.02	0.13
SG_YS_XRF_483	69.55	0.34	6.30	5.40	0.28	0.82	0.35	0.45	0.78	0.71	15.02	0.13
SG_YS_XRF_484	70.35	0.35	6.63	5.10	0.24	0.84	0.38	0.48	0.82	0.65	14.17	0.13
SG_YS_XRF_485	71.88	0.31	6.03	4.91	0.22	0.76	0.39	0.49	0.74	0.70	13.55	0.13
SG_YS_XRF_486	70.95	0.31	6.67	4.64	0.22	0.80	0.62	0.71	0.81	0.65	13.63	0.13
SG_YS_XRF_487	70.75	0.30	8.51	4.44	0.19	0.88	1.30	1.37	1.02	0.53	10.72	0.13
SG_YS_XRF_488	70.33	0.31	7.76	4.88	0.22	0.88	1.06	1.09	0.91	0.57	11.98	0.13
SG_YS_XRF_489	71.42	0.32	5.68	5.08	0.28	0.77	0.23	0.33	0.72	0.76	14.41	0.13
SG_YS_XRF_490	71.06	0.33	5.79	4.99	0.25	0.80	0.24	0.34	0.73	0.68	14.79	0.13
SG_YS_XRF_491	70.56	0.31	5.38	5.35	0.27	0.77	0.23	0.31	0.68	0.78	15.35	0.13
SG_YS_XRF_492	70.91	0.32	5.47	5.18	0.25	0.76	0.23	0.32	0.68	0.72	15.17	0.13
SG_YS_XRF_493	71.82	0.31	5.88	4.88	0.22	0.71	0.20	0.26	0.65	0.75	14.33	0.13
SG_YS_XRF_494	72.51	0.31	5.28	4.90	0.22	0.75	0.22	0.32	0.66	0.68	14.15	0.13
SG_YS_XRF_495	70.34	0.31	5.44	5.50	0.27	0.78	0.24	0.31	0.68	0.87	15.26	0.13
SG_YS_XRF_496	71.79	0.30	5.31	4.99	0.28	0.77	0.23	0.31	0.65	0.80	14.58	0.13
SG_YS_XRF_497	71.42	0.28	4.97	5.32	0.25	0.74	0.23	0.30	0.61	0.95	14.94	0.16
SG_YS_XRF_498	70.11	0.30	5.33	5.78	0.27	0.80	0.24	0.32	0.65	0.85	15.34	0.16
SG_YS_XRF_499	69.42	0.33	6.02	5.90	0.31	0.85	0.23	0.33	0.71	0.87	15.02	0.16
SG_YS_XRF_500	69.44	0.36	6.15	5.82	0.30	0.86	0.24	0.32	0.77	0.85	14.90	0.16
SG_YS_XRF_501	69.37	0.32	5.35	5.82	0.29	0.74	0.22	0.32	0.70	0.88	15.98	0.16
SG_YS_XRF_502	70.47	0.30	5.05	5.66	0.29	0.69	0.22	0.31	0.66	0.92	15.45	0.16
SG_YS_XRF_503	71.66	0.31	5.14	5.17	0.24	0.70	0.21	0.29	0.66	0.81	14.81	0.15
SG_YS_XRF_504	70.10	0.34	5.93	5.52	0.26	0.79	0.23	0.33	0.76	0.72	15.02	0.15
SG_YS_XRF_505	68.50	0.37	6.58	6.31	0.25	0.86	0.24	0.34	0.82	0.85	14.87	0.15
SG_YS_XRF_506	67.79	0.34	5.84	6.41	0.31	0.82	0.23	0.33	0.72	1.06	16.16	0.15
SG_YS_XRF_507	67.02	0.32	5.43	6.88	0.32	0.76	0.23	0.34	0.70	1.02	16.98	0.15
SG_YS_XRF_508	66.86	0.32	5.35	7.12	0.43	0.77	0.23	0.32	0.69	0.94	16.97	0.15
SG_YS_XRF_509	67.48	0.34	5.64	6.70	0.34	0.81	0.24	0.33	0.71	1.02	16.38	0.15
SG_YS_XRF_510	69.33	0.35	5.88	5.75	0.28	0.86	0.25	0.34	0.75	0.75	15.47	0.15
SG_YS_XRF_511	69.63	0.35	6.22	5.86	0.28	0.87	0.24	0.34	0.76	0.87	14.60	0.14
SG_YS_XRF_512	68.64	0.34	5.92	6.41	0.30	0.81	0.24	0.32	0.72	1.02	15.29	0.14
SG_YS_XRF_513	68.09	0.30	5.22	6.83	0.38	0.73	0.22	0.31	0.67	1.20	16.04	0.14
SG_YS_XRF_514	67.83	0.28	4.96	7.19	0.42	0.69	0.21	0.30	0.64	1.16	16.30	0.14
SG_YS_XRF_515	71.09	0.29	5.06	5.73	0.27	0.69	0.20	0.30	0.65	0.94	14.79	0.14
SG_YS_XRF_516	68.81	0.33	6.11	6.30	0.32	0.81	0.23	0.33	0.76	0.93	15.07	0.14
SG_YS_XRF_517	66.04	0.34	5.96	7.02	0.54	0.84	0.24	0.31	0.73	1.06	16.90	0.14
SG_YS_XRF_518	69.91	0.31	5.46	6.02	0.35	0.76	0.22	0.31	0.67	0.95	15.04	0.14
SG_YS_XRF_519	70.01	0.29	5.15	6.50	0.35	0.74	0.21	0.31	0.64	1.04	14.75	0.14
SG_YS_XRF_520	67.10	0.32	5.53	7.46	0.53	0.78	0.24	0.32	0.68	1.11	15.94	0.14
SG_YS_XRF_521	70.33	0.31	5.50	6.24	0.39	0.74	0.21	0.32	0.69	0.99	14.29	0.14
SG_YS_XRF_522	69.34	0.28	4.81	7.31	0.54	0.67	0.20	0.29	0.60	1.09	14.87	0.14
SG_YS_XRF_523	69.60	0.32	5.64	6.66	0.48	0.78	0.23	0.34	0.69	0.88	14.36	0.14
SG_YS_XRF_524	68.96	0.34	6.11	6.40	0.44	0.86	0.24	0.37	0.75	0.95	14.58	0.14
SG_YS_XRF_525	69.39	0.38	6.87	6.27	0.34	0.95	0.25	0.38	0.84	0.77	13.57	0.14
SG_YS_XRF_526	66.99	0.40	7.43	7.41	0.50	0.99	0.26	0.39	0.89	0.87	13.86	0.14
SG_YS_XRF_527	64.15	0.51	9.57	7.48	0.57	1.29	0.33	0.45	1.07	0.75	13.82	0.14
SG_YS_XRF_528	63.56	0.52	9.95	7.20	0.36	1.25	0.30	0.40	1.05	0.81	14.60	0.14
SG_YS_XRF_529	58.74	0.70	13.95	7.81	0.27	1.76	0.38	0.47	1.36	0.65	13.91	0.14
SG_YS_XRF_530	62.56	0.59	12.13	6.90	0.27	1.48	0.33	0.44	1.19	0.63	13.48	0.14
SG_YS_XRF_531	67.27	0.39	6.67	7.15	0.43	0.90	0.24	0.33	0.77	0.99	14.85	0.14
SG_YS_XRF_532	65.23	0.42	7.57	7.74	0.43	1.05	0.26	0.36	0.84	0.95	15.14	0.14
SG_YS_XRF_533	68.28	0.43	7.13	6.60	0.33	1.12	0.27	0.37	0.86	0.87	13.75	0.14
SG_YS_XRF_534	71.02	0.30	4.95	6.32	0.36	0.69	0.19	0.29	0.62	1.00	14.24	0.14
SG_YS_XRF_535	71.10	0.26	4.31	6.23	0.63	0.60	0.19	0.27	0.56	0.83	15.03	0.14
SG_YS_XRF_536	70.76	0.26	4.42	5.88	0.41	0.62	0.19	0.28	0.56	0.83	15.80	0.14
SG_YS_XRF_537	70.82	0.31	5.19	5.95	0.31	0.72	0.19	0.31	0.67	0.83	14.69	0.14
SG_YS_XRF_538	70.93	0.32	5.31	6.41	0.34	0.73	0.20	0.31	0.66	1.00	13.78	0.14
SG_YS_XRF_539	71.20	0.28	4.67	6.08	0.54	0.64	0.19	0.26	0.58	0.98	14.59	0.14
SG_YS_XRF_540	71.09	0.31	5.13	6.03	0.37	0.75	0.21	0.30	0.65	0.90	14.25	0.14
SG_YS_XRF_541	72.01	0.26	4.38	5.84	0.49	0.60	0.17	0.27	0.56	0.90	14.51	0.14
SG_YS_XRF_542	72.48	0.26	4.54	5.52	0.43	0.61	0.19	0.27	0.58	0.81	14.32	0.14
SG_YS_XRF_543	73.18	0.24	4.32	5.40	0.52	0.58	0.17	0.28	0.57	0.85	13.90	0.14
SG_YS_XRF_544	72.21	0.26	4.59	6.02	0.42	0.63	0.18	0.29	0.59	0.94	13.89	0.14

(Continued)

Table S7 List of XRF data of SG12core samples (Total value including LOI is normalized to 100 wt%) and LSR

Sample Number	SiO <sub>2</sub>	TiO <sub>2</sub>	Al <sub>2</sub> O <sub>3</sub>	Fe <sub>2</sub> O <sub>3</sub>	MnO	MgO	CaO	Na <sub>2</sub> O	K <sub>2</sub> O	P <sub>2</sub> O <sub>5</sub>	LOI	LSR (cm/yr)
SG_YS_XRF_545	71.60	0.28	4.76	6.48	0.54	0.65	0.18	0.28	0.61	0.88	13.73	0.14
SG_YS_XRF_546	70.35	0.37	6.60	6.08	0.46	0.88	0.22	0.33	0.81	0.70	13.20	0.14
SG_YS_XRF_547	72.02	0.28	4.95	5.68	0.40	0.64	0.18	0.29	0.63	0.91	14.00	0.13
SG_YS_XRF_548	70.00	0.31	5.59	6.51	0.43	0.69	0.20	0.32	0.72	0.88	14.33	0.13
SG_YS_XRF_549	69.87	0.37	6.48	6.38	0.36	0.80	0.21	0.32	0.82	0.79	13.59	0.13
SG_YS_XRF_550	70.07	0.38	7.02	6.03	0.31	0.80	0.20	0.33	0.87	0.72	13.26	0.13
SG_YS_XRF_552	69.13	0.42	8.03	6.28	0.48	0.90	0.22	0.33	0.93	0.76	12.51	0.13
SG_YS_XRF_551	62.55	0.63	12.97	6.42	0.36	1.38	0.28	0.44	1.41	0.47	13.10	0.13
SG_YS_XRF_553	72.63	0.28	4.61	6.17	0.52	0.63	0.19	0.27	0.61	0.88	13.21	0.12
SG_YS_XRF_554	71.86	0.30	5.01	6.61	0.61	0.69	0.20	0.27	0.65	0.89	12.92	0.12
SG_YS_XRF_555	74.11	0.25	4.11	5.87	0.53	0.58	0.17	0.25	0.54	0.82	12.76	0.12
SG_YS_XRF_556	72.18	0.30	4.97	6.30	0.53	0.66	0.20	0.28	0.64	0.90	13.02	0.12
SG_YS_XRF_557	71.16	0.27	4.41	7.00	0.82	0.60	0.20	0.26	0.58	0.89	13.80	0.13
SG_YS_XRF_558	71.44	0.35	5.65	6.34	0.47	0.77	0.22	0.31	0.73	0.81	12.91	0.13
SG_YS_XRF_559	62.98	0.80	13.77	6.56	0.30	1.87	0.35	0.48	1.47	0.35	11.07	0.13
SG_YS_XRF_560	69.60	0.35	5.62	7.18	0.70	0.78	0.24	0.29	0.69	0.83	13.73	0.13
SG_YS_XRF_561	71.60	0.37	6.01	5.92	0.50	0.86	0.24	0.34	0.77	0.69	12.70	0.13
SG_YS_XRF_562	71.57	0.34	5.53	6.07	0.51	0.76	0.22	0.29	0.70	0.79	13.22	0.12
SG_YS_XRF_563	68.72	0.39	6.25	7.23	0.90	0.88	0.26	0.33	0.81	0.80	13.44	0.12
SG_YS_XRF_564	66.89	0.35	5.39	9.31	1.31	0.75	0.25	0.29	0.68	0.83	13.96	0.12
SG_YS_XRF_565	68.69	0.30	5.01	8.84	0.94	0.65	0.21	0.28	0.65	0.75	13.68	0.12
SG_YS_XRF_566	67.79	0.31	5.32	9.02	0.96	0.61	0.21	0.28	0.69	0.71	14.11	0.14
SG_YS_XRF_567	68.57	0.34	5.70	7.72	0.65	0.71	0.21	0.30	0.75	0.80	14.26	0.14
SG_YS_XRF_568	67.04	0.42	8.24	7.47	0.58	0.82	0.24	0.33	1.02	0.66	13.17	0.14
SG_YS_XRF_569	69.55	0.28	4.70	8.12	0.81	0.66	0.22	0.27	0.60	0.76	14.02	0.14
SG_YS_XRF_570	71.05	0.36	6.06	5.95	0.44	0.84	0.24	0.32	0.78	0.63	13.34	0.11
SG_YS_XRF_571	68.12	0.32	5.38	8.32	0.77	0.74	0.23	0.28	0.68	0.77	14.37	0.11
SG_YS_XRF_575	67.83	0.40	7.06	8.52	0.74	0.86	0.25	0.33	0.90	0.58	12.52	0.11
SG_YS_XRF_572	69.73	0.32	5.47	7.47	0.68	0.75	0.23	0.29	0.70	0.65	13.72	0.11
SG_YS_XRF_576	70.22	0.35	5.84	7.99	0.75	0.75	0.22	0.35	0.73	0.61	12.19	0.11
SG_YS_XRF_573	69.87	0.31	5.32	7.73	0.68	0.71	0.22	0.31	0.70	0.70	13.46	0.11
SG_YS_XRF_577	71.67	0.33	5.48	7.24	0.70	0.74	0.22	0.29	0.71	0.58	12.05	0.11
SG_YS_XRF_574	68.17	0.34	5.89	8.28	0.79	0.77	0.24	0.31	0.77	0.78	13.65	0.11
SG_YS_XRF_578	71.57	0.35	6.03	6.99	0.62	0.77	0.22	0.31	0.78	0.63	11.74	0.11
SG_YS_XRF_579	65.67	0.35	5.88	10.24	1.25	0.78	0.26	0.32	0.73	0.74	13.78	0.12
SG_YS_XRF_580	63.87	0.39	6.74	10.23	1.13	0.98	0.30	0.35	0.83	0.90	14.27	0.13
SG_YS_XRF_581	67.73	0.46	8.01	7.81	0.69	1.20	0.30	0.40	0.98	0.66	11.76	0.13
SG_YS_XRF_582	61.64	0.69	12.49	7.87	0.51	1.77	0.37	0.49	1.36	0.50	12.31	0.13
SG_YS_XRF_583	62.60	0.61	14.75	6.25	0.22	1.50	0.33	0.48	1.41	0.34	11.51	0.13
SG_YS_XRF_584	67.29	0.35	6.20	8.56	0.79	0.72	0.22	0.29	0.73	0.96	13.88	0.13
SG_YS_XRF_585	73.31	0.27	4.73	6.65	0.59	0.59	0.17	0.25	0.60	0.74	12.10	0.13
SG_YS_XRF_586	70.80	0.42	7.69	5.89	0.32	0.96	0.24	0.37	0.93	0.56	11.81	0.13
SG_YS_XRF_587	73.12	0.36	6.52	5.14	0.32	0.77	0.19	0.29	0.81	0.60	11.90	0.13
SG_YS_XRF_588	75.71	0.29	5.27	4.62	0.27	0.64	0.16	0.28	0.68	0.60	11.47	0.13
SG_YS_XRF_589	73.98	0.27	4.70	5.63	0.40	0.60	0.17	0.25	0.62	0.70	12.68	0.13
SG_YS_XRF_590	74.06	0.26	4.62	5.52	0.45	0.57	0.17	0.24	0.60	0.71	12.81	0.13
SG_YS_XRF_591	75.73	0.26	4.65	4.93	0.33	0.59	0.16	0.24	0.61	0.68	11.82	0.13
SG_YS_XRF_592	74.05	0.28	5.04	5.40	0.40	0.60	0.16	0.27	0.66	0.68	12.45	0.11
SG_YS_XRF_593	74.39	0.29	5.24	5.23	0.38	0.64	0.17	0.27	0.68	0.61	12.10	0.11
SG_YS_XRF_594	74.87	0.28	4.99	5.17	0.35	0.60	0.16	0.28	0.67	0.73	11.90	0.11
SG_YS_XRF_595	73.28	0.29	5.29	5.62	0.43	0.64	0.18	0.28	0.70	0.65	12.64	0.11
SG_YS_XRF_596	73.70	0.30	5.48	5.34	0.38	0.67	0.18	0.30	0.75	0.64	12.26	0.11
SG_YS_XRF_597	74.73	0.30	5.23	5.26	0.32	0.67	0.17	0.28	0.68	0.68	11.68	0.11
SG_YS_XRF_598	75.37	0.35	6.20	4.66	0.26	0.80	0.19	0.33	0.80	0.54	10.51	0.10
SG_YS_XRF_599	73.79	0.37	6.89	4.41	0.21	0.79	0.19	0.33	0.88	0.48	11.65	0.10
SG_YS_XRF_600	71.12	0.43	7.89	5.28	0.27	0.95	0.21	0.33	0.97	0.54	12.01	0.10
SG_YS_XRF_602	73.75	0.38	7.17	3.96	0.29	0.83	0.18	0.33	0.88	0.19	12.03	0.10
SG_YS_XRF_601	75.31	0.30	5.43	4.41	0.28	0.62	0.16	0.30	0.72	0.55	11.91	0.15
SG_YS_XRF_603	75.13	0.30	5.70	3.97	0.36	0.63	0.16	0.28	0.72	0.19	12.55	0.15
SG_YS_XRF_604	75.50	0.30	5.68	3.54	0.30	0.63	0.16	0.28	0.73	0.17	12.71	0.15
SG_YS_XRF_605	75.08	0.30	5.61	3.66	0.27	0.62	0.16	0.30	0.73	0.22	13.04	0.15
SG_YS_XRF_606	74.25	0.34	6.16	3.92	0.26	0.65	0.17	0.33	0.80	0.26	12.87	0.15
SG_YS_XRF_607	72.39	0.35	6.52	4.47	0.26	0.67	0.19	0.35	0.84	0.29	13.66	0.15
SG_YS_XRF_608	69.55	0.41	7.83	4.22	0.27	0.77	0.24	0.40	0.99	0.18	15.14	0.15
SG_YS_XRF_609	65.92	0.48	9.18	5.21	0.33	0.84	0.26	0.44	1.15	0.30	15.89	0.13
SG_YS_XRF_610	66.13	0.41	8.30	5.31	0.35	0.74	0.31	0.46	1.02	0.36	16.60	0.13
SG_YS_XRF_611	69.99	0.26	4.88	4.66	0.31	0.59	0.31	0.37	0.59	0.48	17.54	0.13
SG_YS_XRF_612	69.88	0.22	4.16	5.68	0.34	0.52	0.25	0.31	0.50	0.84	17.29	0.12

(Continued)

Table S7 List of XRF data of SG12core samples (Total value including LOI is normalized to 100 wt%) and LSR

Sample Number	SiO <sub>2</sub>	TiO <sub>2</sub>	Al <sub>2</sub> O <sub>3</sub>	Fe <sub>2</sub> O <sub>3</sub>	MnO	MgO	CaO	Na <sub>2</sub> O	K <sub>2</sub> O	P <sub>2</sub> O <sub>5</sub>	LOI	LSR (cm/yr)
SG_YS_XRF_613	66.71	0.25	9.32	4.87	0.25	0.85	1.85	1.76	0.99	0.66	12.50	0.12
SG_YS_XRF_614	67.53	0.28	5.04	5.83	0.31	0.66	0.20	0.27	0.61	0.86	18.40	0.12
SG_YS_XRF_615	67.01	0.24	4.05	6.21	0.31	0.53	0.19	0.25	0.52	0.99	19.71	0.12
SG_YS_XRF_616	65.63	0.27	4.69	6.41	0.40	0.61	0.20	0.26	0.57	1.06	19.90	0.12
SG_YS_XRF_617	68.96	0.23	3.93	5.47	0.43	0.53	0.18	0.24	0.48	0.83	18.72	0.12
SG_YS_XRF_618	72.78	0.21	3.72	4.19	0.30	0.50	0.16	0.22	0.46	0.78	16.69	0.12
SG_YS_XRF_619	71.95	0.24	4.36	4.43	0.29	0.56	0.17	0.25	0.53	0.71	16.51	0.12
SG_YS_XRF_620	70.49	0.23	3.92	4.72	0.37	0.52	0.17	0.23	0.49	0.78	18.09	0.12
SG_YS_XRF_621	71.89	0.25	4.16	4.50	0.29	0.57	0.16	0.25	0.51	0.84	16.58	0.12
SG_YS_XRF_622	67.34	0.30	5.07	5.42	0.40	0.69	0.21	0.28	0.60	0.83	18.84	0.12
SG_YS_XRF_623	68.77	0.34	5.93	4.91	0.27	0.79	0.21	0.30	0.68	0.65	17.15	0.13
SG_YS_XRF_624	68.08	0.26	4.40	5.50	0.35	0.58	0.19	0.25	0.54	1.07	18.79	0.13
SG_YS_XRF_625	68.73	0.27	5.03	5.00	0.29	0.57	0.24	0.45	0.78	0.85	17.80	0.13
SG_YS_XRF_626	71.78	0.24	4.25	4.59	0.30	0.54	0.16	0.23	0.55	0.90	16.48	0.13
SG_YS_XRF_627	69.92	0.26	4.20	5.08	0.31	0.57	0.17	0.25	0.52	1.05	17.67	0.15
SG_YS_XRF_628	66.62	0.28	4.82	5.96	0.39	0.65	0.20	0.27	0.59	1.10	19.14	0.15
SG_YS_XRF_629	68.17	0.25	4.19	5.86	0.35	0.58	0.17	0.25	0.52	1.16	18.51	0.15
SG_YS_XRF_630	69.70	0.31	5.29	4.76	0.29	0.71	0.20	0.27	0.63	0.75	17.09	0.15
SG_YS_XRF_631	71.79	0.25	4.21	3.92	0.22	0.58	0.17	0.25	0.52	0.61	17.49	0.15
SG_YS_XRF_632	70.07	0.25	4.13	5.01	0.26	0.57	0.19	0.25	0.50	0.96	17.81	0.12
SG_YS_XRF_633	69.08	0.29	4.81	5.74	0.22	0.67	0.20	0.26	0.57	1.15	17.01	0.12
SG_YS_XRF_634	66.82	0.32	5.56	5.81	0.25	0.73	0.22	0.28	0.66	1.07	18.30	0.12
SG_YS_XRF_635	65.02	0.29	4.87	6.50	0.29	0.65	0.22	0.27	0.58	1.32	20.00	0.12
SG_YS_XRF_636	67.37	0.27	4.48	6.01	0.31	0.63	0.20	0.26	0.54	1.25	18.68	0.12
SG_YS_XRF_637	70.15	0.29	4.91	4.94	0.20	0.67	0.20	0.27	0.59	0.93	16.85	0.12
SG_YS_XRF_638	69.28	0.31	5.09	4.88	0.19	0.69	0.21	0.28	0.62	0.90	17.55	0.12
SG_YS_XRF_639	70.53	0.28	4.71	4.71	0.20	0.64	0.19	0.28	0.58	0.90	16.99	0.12
SG_YS_XRF_640	68.70	0.31	5.48	5.17	0.23	0.70	0.22	0.28	0.64	0.97	17.31	0.12
SG_YS_XRF_641	65.84	0.33	5.58	5.85	0.26	0.72	0.22	0.29	0.67	1.07	19.17	0.12
SG_YS_XRF_642	70.48	0.21	3.59	4.05	0.29	0.48	0.15	0.23	0.45	0.76	19.33	0.12
SG_YS_XRF_643	66.52	0.35	5.94	5.79	0.24	0.81	0.25	0.34	0.71	1.03	18.01	0.12
SG_YS_XRF_644	66.54	0.31	5.35	5.72	0.25	0.64	0.27	0.35	0.64	1.06	18.87	0.12
SG_YS_XRF_645	62.63	0.33	5.46	6.92	0.35	0.80	0.26	0.32	0.67	1.25	21.01	0.12
SG_YS_XRF_646	61.42	0.30	4.96	7.68	0.46	0.71	0.24	0.30	0.61	1.52	21.81	0.12
SG_YS_XRF_647	51.95	0.39	6.50	9.57	0.63	0.94	0.35	0.35	0.79	1.79	26.74	0.12
SG_YS_XRF_648	64.18	0.31	5.36	6.94	0.49	0.76	0.25	0.30	0.64	1.31	19.46	0.12
SG_YS_XRF_649	67.75	0.31	5.32	5.69	0.30	0.75	0.23	0.30	0.64	1.00	17.70	0.12
SG_YS_XRF_651	69.65	0.29	4.64	5.93	0.38	0.66	0.21	0.27	0.59	1.07	16.31	0.12
SG_YS_XRF_650	67.67	0.29	4.80	6.49	0.41	0.68	0.22	0.28	0.58	1.19	17.39	0.12
SG_YS_XRF_652	67.67	0.31	5.11	5.59	0.32	1.75	0.22	2.37	0.61	0.87	15.18	0.12
SG_YS_XRF_653	72.37	0.27	4.36	5.38	0.28	0.66	0.20	0.27	0.54	1.00	14.67	0.12
SG_YS_XRF_654	72.37	0.29	4.87	5.18	0.24	0.72	0.21	0.27	0.59	0.87	14.37	0.12
SG_YS_XRF_655	71.96	0.28	4.79	5.57	0.30	0.71	0.21	0.27	0.57	0.87	14.48	0.11
SG_YS_XRF_656	72.23	0.29	4.79	5.33	0.27	0.72	0.22	0.29	0.59	0.80	14.47	0.11
SG_YS_XRF_657	73.15	0.27	4.46	5.26	0.28	0.67	0.20	0.25	0.54	0.83	14.10	0.11
SG_YS_XRF_658	72.65	0.31	5.23	5.06	0.23	0.76	0.22	0.29	0.61	0.77	13.86	0.11
SG_YS_XRF_659	71.35	0.29	4.91	5.54	0.27	0.74	0.22	0.28	0.60	0.85	14.94	0.11
SG_YS_XRF_660	71.66	0.30	5.16	5.89	0.33	0.76	0.22	0.28	0.63	0.80	13.98	0.11
SG_YS_XRF_661	71.49	0.32	5.51	5.40	0.27	0.80	0.22	0.29	0.66	0.76	14.27	0.11
SG_YS_XRF_662	72.68	0.28	4.70	5.74	0.32	0.72	0.21	0.26	0.57	1.08	13.43	0.11
SG_YS_XRF_663	69.80	0.37	6.34	6.03	0.29	0.95	0.26	0.33	0.74	0.82	14.08	0.11
SG_YS_XRF_664	72.52	0.30	5.01	5.45	0.27	0.75	0.22	0.28	0.60	0.77	13.83	0.11
SG_YS_XRF_665	71.40	0.32	5.44	6.02	0.33	0.78	0.22	0.29	0.65	0.79	13.77	0.11
SG_YS_XRF_666	72.11	0.28	4.83	6.58	0.42	0.71	0.21	0.26	0.57	0.76	13.28	0.09
SG_YS_XRF_667	71.96	0.30	5.14	6.41	0.35	0.76	0.22	0.28	0.62	0.80	13.18	0.09
SG_YS_XRF_668	68.91	0.28	4.95	6.22	0.37	0.74	0.20	0.27	0.58	0.64	16.82	0.09
SG_YS_XRF_669	69.70	0.43	8.00	6.33	0.26	1.15	0.28	0.37	0.88	0.56	12.02	0.09
SG_YS_XRF_670	55.11	0.88	18.83	7.59	0.11	2.34	0.44	0.56	1.74	0.28	12.11	0.09
SG_YS_XRF_671	69.96	0.36	6.12	5.57	0.21	0.81	0.23	0.31	0.71	0.87	14.84	0.09
SG_YS_XRF_672	70.00	0.31	5.32	5.88	0.27	0.72	0.22	0.28	0.63	0.89	15.49	0.09
SG_YS_XRF_673	65.66	0.32	6.08	8.21	0.51	0.75	0.24	0.28	0.69	0.98	16.27	0.09
SG_YS_XRF_674	62.91	0.28	5.06	9.51	0.59	0.67	0.24	0.26	0.59	1.14	18.73	0.09
SG_YS_XRF_675	60.61	0.35	6.32	10.02	0.62	0.83	0.28	0.31	0.74	1.14	18.80	0.09
SG_YS_XRF_676	64.08	0.33	5.86	6.99	0.33	0.76	0.25	0.30	0.69	0.98	19.43	0.09
SG_YS_XRF_677	53.92	0.30	5.34	13.11	0.91	0.71	0.29	0.28	0.63	1.41	23.10	0.09
SG_YS_XRF_679	59.33	0.30	5.19	10.88	0.76	0.72	0.27	0.29	0.63	1.19	20.45	0.09
SG_YS_XRF_678	60.37	0.32	5.56	9.69	0.61	0.73	0.27	0.29	0.66	1.13	20.38	0.09
SG_YS_XRF_680	66.17	0.31	5.59	6.86	0.36	0.72	0.23	0.29	0.67	1.03	17.78	0.09

(Continued)

Table S7 List of XRF data of SG12core samples (Total value including LOI is normalized to 100 wt%) and LSR

Sample Number	SiO <sub>2</sub>	TiO <sub>2</sub>	Al <sub>2</sub> O <sub>3</sub>	Fe <sub>2</sub> O <sub>3</sub>	MnO	MgO	CaO	Na <sub>2</sub> O	K <sub>2</sub> O	P <sub>2</sub> O <sub>5</sub>	LOI	LSR (cm/yr)
SG_YS_XRF_681	67.06	0.30	5.50	7.05	0.41	0.72	0.22	0.26	0.64	0.88	16.97	0.09
SG_YS_XRF_682	59.37	0.31	5.81	9.64	0.63	0.73	0.25	0.28	0.68	1.16	21.12	0.09
SG_YS_XRF_683	58.59	0.32	6.10	9.96	0.66	0.75	0.26	0.29	0.72	1.32	21.03	0.09
SG_YS_XRF_684	63.01	0.28	5.11	8.00	0.49	0.64	0.22	0.27	0.62	1.17	20.19	0.09
SG_YS_XRF_685	48.08	0.51	9.70	10.34	0.52	1.18	0.36	0.43	1.15	1.16	26.56	0.09
SG_YS_XRF_686	45.64	0.42	8.09	10.91	0.63	0.95	0.34	0.38	0.98	1.57	30.08	0.09
SG_YS_XRF_687	45.70	0.41	7.71	11.25	0.78	0.92	0.35	0.38	0.92	1.63	29.97	0.09
SG_YS_XRF_688	50.39	0.34	6.58	10.25	0.64	0.79	0.31	0.33	0.80	1.57	28.00	0.09
SG_YS_XRF_689	47.17	0.42	8.02	12.67	0.90	0.96	0.35	0.38	0.98	1.67	26.50	0.09
SG_YS_XRF_690	48.93	0.45	8.62	11.73	0.88	0.98	0.33	0.39	1.04	1.51	25.14	0.09
SG_YS_XRF_691	47.20	0.40	7.89	13.16	1.22	0.88	0.32	0.36	0.94	1.58	26.05	0.09
SG_YS_XRF_692	49.38	0.46	8.85	11.11	0.81	1.03	0.32	0.41	1.06	1.57	25.00	0.09
SG_YS_XRF_693	50.47	0.60	12.18	9.81	0.47	1.34	0.35	0.47	1.38	1.07	21.87	0.09
SG_YS_XRF_694	50.21	0.56	10.80	9.58	0.43	1.26	0.35	0.46	1.28	1.15	23.91	0.09
SG_YS_XRF_695	50.27	0.51	9.76	10.02	0.50	1.13	0.36	0.45	1.15	1.34	24.50	0.10
SG_YS_XRF_696	53.73	0.47	8.86	9.03	0.48	1.05	0.34	0.45	1.08	1.19	23.31	0.10
SG_YS_XRF_697	58.00	0.48	9.18	7.75	0.34	1.12	0.34	0.45	1.09	1.02	20.23	0.10
SG_YS_XRF_698	57.66	0.43	8.24	7.34	0.34	0.92	0.31	0.43	1.00	1.14	22.18	0.10
SG_YS_XRF_699	51.93	0.45	8.85	9.65	0.47	1.00	0.33	0.44	1.06	1.43	24.38	0.10
SG_YS_XRF_700	52.45	0.45	9.01	9.63	0.50	0.99	0.34	0.46	1.07	1.37	23.73	0.10
SG_YS_XRF_701	49.76	0.46	9.20	10.78	0.54	1.03	0.36	0.45	1.09	1.44	24.88	0.10
SG_YS_XRF_702	54.76	0.45	9.00	9.43	0.46	1.00	0.34	0.46	1.07	1.36	21.67	0.09
SG_YS_XRF_703	58.40	0.50	10.09	7.88	0.31	1.11	0.35	0.48	1.20	1.04	18.64	0.09
SG_YS_XRF_704	52.75	0.86	18.21	8.16	0.17	2.02	0.40	0.57	2.02	0.55	14.29	0.09
SG_YS_XRF_705	53.33	0.49	9.11	9.78	0.47	0.96	0.36	0.50	1.12	1.31	22.57	0.09
SG_YS_XRF_706	52.89	0.67	13.24	8.67	0.35	1.44	0.41	0.55	1.50	0.84	19.45	0.09
SG_YS_XRF_707	54.28	0.43	8.17	9.61	0.58	0.84	0.37	0.49	1.01	1.31	22.91	0.09
SG_YS_XRF_708	62.74	0.33	6.10	8.23	0.62	0.64	0.31	0.43	0.77	1.25	18.59	0.09
SG_YS_XRF_709	61.29	0.50	9.24	7.15	0.34	1.01	0.36	0.54	1.12	0.88	17.55	0.09
SG_YS_XRF_710	60.37	0.37	7.48	7.64	0.36	0.73	0.45	0.66	0.98	1.20	19.77	0.09
SG_YS_XRF_711	60.88	0.39	7.80	6.94	0.29	0.76	0.53	0.85	1.09	1.18	19.29	0.08
SG_YS_XRF_712	63.73	0.43	8.53	6.01	0.26	0.84	0.63	1.00	1.21	0.84	16.52	0.08
SG_YS_XRF_713	65.26	0.37	8.12	6.32	0.35	0.56	0.87	1.50	1.38	0.81	14.48	0.08
SG_YS_XRF_714	70.06	0.53	12.62	3.38	0.11	0.60	1.88	3.44	2.71	0.13	4.55	0.08
SG_YS_XRF_715	67.59	0.56	12.36	4.50	0.18	0.69	1.82	3.15	2.50	0.31	6.33	0.08

Table S8 List of event layers thicker than 1mm observed in the top 10m of SG12 core.

Hole	Section	Bottom of event layer (distance from section top: cm)	Event layer thickness (mm)	Composite depth (correlation model: version 25 Jul. 2014)	Hole	Section	Bottom of event layer (distance from section top: cm)	Event layer thickness (mm)	Composite depth (correlation model: version 25 Jul. 2014)
X	1	9.7	2	29.7	X	7	41.6	7	673.9681
X	1	12.4	2	32.5	X	7	51.5	2	683.5521
X	1	19	1	39.1	X	7	59.5	5	691.2482
X	1	37.4	4	57.5	X	7	76	3	699.2036
Z	1	49.9	3	82.2957	Y	7	37.4	1	717.3
Z	1	51.9	5	84.2558	Y	7	40.2	12	721.3
Y	1	67	3	137	Y	7	43.6	1	725.1708
Z	2	49.9	2	170.1	Y	7	46.6	14	728.5862
Z	2	51.9	5	172	Y	7	69.8	3	749.6125
Y	2	26	70	202.2	Y	7	73.1	6	752.6
Y	2	29.4	4	205.8152	X	8	37.4	3	775.5
Y	2	39.6	2	216.6608	X	8	53	2	790.5699
Y	2	44	2	221.3392	X	8	58	2	795.4
Y	2	57.6	32	235.8	X	8	70.6	2	808.8
Y	2	63.4	2	241.8	X	8	75.7	2	814
Y	2	65	1	243.2222	Y	8	31.9	3	816.5
Y	2	73.3	18	250.6	Y	8	43.3	1	828.9
Z	3	43.8	2	260.7489	Y	8	45.9	2	831.3
Z	3	56.9	1	273.0592	Y	8	49.6	2	835.3
Z	3	61.2	2	277.1	Y	8	51.6	2	837.2259
Z	3	64	2	279.9967	Y	8	60.3	3	845.6037
Z	3	75.4	3	291.0167	Y	8	64.7	2	850.2
Z	3	81.9	4	297.3	Z	9	23.1	1	856.2545
Y	3	35.2	26	305.1	Z	9	34	1	867.4398
Y	3	36.4	3	306.6	Z	9	36.3	2	869.8
Y	3	57.9	5	325.8	Z	9	39.2	5	872.5
Y	3	66.2	1	333.2236	Z	9	45.1	1	878.5
Y	3	74	3	340.2	Z	9	48.1	2	881.5316
Z	4	45.4	1	354.1	Z	9	48.6	2	882.0368
Y	4	9.2	15	378.8	Z	9	54.6	16	888.1
Y	4	14.4	2	384.5	Z	9	58.9	1	892
Y	4	26.7	7	397.3	Z	9	63	1	896.2757
Y	4	40.6	3	411.5	Z	9	64.3	1	897.6314
Y	4	62.6	14	432.9	Z	9	72.9	1	906.6
Y	4	76.1	3	446.0707	Y	9	16.1	1	907.1496
Y	4	79	4	448.9	Y	9	18.3	1	908.661
X	5	30.2	2	459.4411	Y	9	19.7	1	909.6228
X	5	55.6	9	484.7	Y	9	20.5	1	910.1724
X	5	66.5	5	495.5	Y	9	23.4	1	912.1646
X	5	68.6	6	497.4	Y	9	34.1	1	919.5154
Y	5	43.6	5	517.4	Y	9	34.7	1	919.9276
Y	5	64	3	537.8	Y	9	39.9	1	923.5
Y	5	74.5	2	547.9	Y	9	42.7	1	926.3642
Y	5	79	1	552.4	Y	9	48.2	3	931.9904
Y	5	83.2	5	556.7					
X	6	36.3	4	569					
X	6	38.5	7	571.2					
X	6	55	2	587.9					
X	6	72.6	1	605.242					
Y	6	57.4	1	630.5266					
Y	6	59.4	1	632.4					
Y	6	60.5	4	633.368					
Y	6	61.9	5	634.6					
Y	6	65.2	3	638.4					
Y	6	72.1	2	645.5717					
Y	6	77	1	650.6646					
Y	6	77.9	2	651.6					
Y	6	81.5	2	654.9962					
Y	6	83.2	7	656.6					
X	7	29.2	1	659.9623					
X	7	31.2	2	662					